AD-A285 063

ASYMMETRIC VORTICAL FLOWS OVER SLENDER BODIES WITH APPENDAGES

FINAL REPORT

Mukund Acharya, John Kiedaisch, & Maskan Md Hassan

June 30, 1994

Sponsored by

U. S. ARMY RESEARCH OFFICE

Grant No. DAAL03-91-G-0043

DTIC
SEP 2 1 1994

Fluid Dynamics Research Center
Illinois Institute of Technology, Chicago

Approved for public release;
DISTRIBUTION STATEMENT A

25918

94-30964

THE VIEWS, OPINIONS, AND/OR FINDINGS CONTAINED IN THIS REPORT ARE THOSE OF THE AUTHORS AND SHOULD NOT BE CONSTRUED AS AN OFFICIAL DEPARTMENT OF THE ARMY POSITION, POLICY, OR DECISION, UNLESS SO DESIGNATED BY OTHER DOCUMENTATION.

REPORT DOCUMENTATION PAGE

Form Approved
OMB No. 0704-0188

Public reporting burden for this collection of information is estimated to average 1 hour per response, including the time for reviewing instructions, searching existing data sources, gathering and maintaining the data needed, and completing and reviewing the collection of information. Send comments regarding this burden estimate or any other aspect of this collection of information, including suggestions for reducing this burden, to Washington Headquarters Services, Directorate for Information Operations and Reports, 1215 Jefferson Davis Highway, Suite 1204, Arlington, VA 22202-4302, and to the Office of Management and Budget, Paperwork Reduction Project (0704-0188), Washington, DC 20503.

1. AGENCY USE ONLY (Leave blank)	2. REPORT DATE	3. REPORT TYPE AND DATES COVERED
	June 30, 1994	Final (2/15/91 - 5/31/94)

4. TITLE AND SUBTITLE
Asymmetric Vortical Flows Over Slender Bodies with Appendages

5. FUNDING NUMBERS
DAAL03-91-G-0043

6. AUTHOR(S)
Mukund Acharya, John W. Kiedaisch & Maskan Md Hassan

7. PERFORMING ORGANIZATION NAME(S) AND ADDRESS(ES)
Illinois Institute of Technology
Chicago, IL 60616

8. PERFORMING ORGANIZATION REPORT NUMBER

9. SPONSORING/MONITORING AGENCY NAME(S) AND ADDRESS(ES)
U. S. Army Research Office
P. O. Box 12211
Research Triangle Park, NC 27709-2211

10. SPONSORING/MONITORING AGENCY REPORT NUMBER

11. SUPPLEMENTARY NOTES
The view, opinions and/or findings contained in this report are those of the author(s) and should not be construed as an official Department of the Army position, policy, or decision, unless so designated by other documentation.

12a. DISTRIBUTION/AVAILABILITY STATEMENT
Approved for public release; distribution unlimited.

12b. DISTRIBUTION CODE

13. ABSTRACT *(Maximum 200 words)*

In part one of this study, the interaction between vortices forming at the tip of a missile model, and a single fin located down the axis of the model was investigated experimentally for a range of axial fin positions ($2.5 < (x/d)_f < 9$), azimuthal fin positions ($-180^o < \phi < -180^o$), and Reynolds number ($6000 < Re_d < 34{,}000$), for two angles of attack (30^o and 45^o). Symmetric, attached vortices formed over the model for the first angle of attack, while the vortex system was asymmetric for the second. The interaction was documented using flow visualization and mean-pressure measurements on the fin surfaces. The pressure data were used to compute the normal-force coefficients on the fin. The effects of the interaction on the fin are described. Results include a detailed examination of the fin interaction with the symmetric and asymmetric vortex systems, the azimuthal range of fin positions over which interaction occurs, and the effects of changing axial fin location and Reynolds number. In the second part, the vortical flow over a steady missile configuration with a tangent-ogive forebody was investigated for different angles of attack. The model was designed in a such a way to allow the tip and the aft body to be stationary and the body to roll. This enabled measurement of the pressure over the model surface without disturbing the flow field. The angle of attack and Reynolds number were varied from 0° to 85° and from 6000 to 34000, respectively. Flow visualization and pressure distributions acquired at several azimuthal angles were used to describe the flow regions and the onset of asymmetry. Local side force and normal force coefficients, derived from the pressure measurement, were used as a tool to further understand the flow development.

14. SUBJECT TERMS	15. NUMBER OF PAGES
Missile Aerodynamics, Asymmetric Vortices, Vortex-Surface Interaction	242
	16. PRICE CODE

DTIC QUALITY INSPECTED 3

17. SECURITY CLASSIFICATION OF REPORT	18. SECURITY CLASSIFICATION OF THIS PAGE	19. SECURITY CLASSIFICATION OF ABSTRACT	20. LIMITATION OF ABSTRACT
UNCLASSIFIED	UNCLASSIFIED	UNCLASSIFIED	UL

ASYMMETRIC VORTICAL FLOWS OVER SLENDER BODIES WITH APPENDAGES

FINAL REPORT

Mukund Acharya, John Kiedaisch, & Maskan Md Hassan

June 30, 1994

Sponsored by

U. S. ARMY RESEARCH OFFICE

Grant No. DAAL03-91-G-0043

Accesion For
NTIS CRA&I
DTIC TAB
Unannounced
Justification
By
Distribution /
Availability Codes
Dist | Avail and / or Special
A-1

Fluid Dynamics Research Center
Illinois Institute of Technology, Chicago

APPROVED FOR PUBLIC RELEASE;
DISTRIBUTION UNLIMITED

ACKNOWLEDGMENT

We would like to express our sincere thanks to Mr. Ed Nieman, Mr. Craig Johnson, and Mr. Ron Mashek of the MAE Department Machine Shop, and Mr. Dominic Deluca of the MAE Department Electronics Shop, for their skilled craftsmanship, patience and encouragement. Mr. Keith Downing, Mr. Dennis Tang, Ms. Tanya Taylor, and Mr. David Grossman assisted very ably during various phases of this work.

TABLE OF CONTENTS

LIST OF FIGURES

NOMENCLATURE

Symbol	Term
A	Reference area, dl
A/D	Analog to digital
C_{ff}	normal force coefficient, far-side surface of fin
C_{fn}	normal force coefficient, near-side surface of fin
C_{ft}	total normal force coefficient
C_n	Coefficient of local normal force, local normal force/qAsin$^2\alpha$
C_p	pressure coefficient
C_r	Coefficient of local resultant force, local resultant force/qAsin$^2\alpha$
C_y	Coefficient of local side force, local side force/qAsin$^2\alpha$
d	model diameter
D/A	Digital to analog
l	*Longitudinal* distance from one port to the next
q	Dynamic head, $0.5\rho_\infty U^2_\infty$
Re_d	Reynolds number based on model diameter
U_∞	Free stream velocity
x	axial distance along model from nose tip
x'	axial distance from leading edge of fin
x/d	Normalized distance
$(x/d)_f$	dimensionless distance from nose to leading edge of fin
y'	transverse (spanwise) distance from root of fin
α	pitch angle
Δp	Change in pressure
ρ_∞	Density of freestream air
ϕ	azimuthal angle, (measured from leeward ray in part A and from the windward ray in part B)

ABSTRACT

In part one of this study, the interaction between vortices forming at the tip of a missile model, and a single fin located down the axis of the model was investigated experimentally for a range of axial fin positions ($2.5 < (x/d)_f < 9$), azimuthal fin positions ($-180^o < \phi < -180^o$), and Reynolds number ($6000 < Re_d < 34{,}000$), for two angles of attack (30^o and 45^o). Symmetric, attached vortices formed over the model for the first angle of attack, while the vortex system was asymmetric for the second. The interaction was documented using flow visualization and mean-pressure measurements on the fin surfaces. The pressure data were used to compute the normal-force coefficients on the fin. The effects of the interaction on the fin are described. Results include a detailed examination of the fin interaction with the symmetric and asymmetric vortex systems, the azimuthal range of fin positions over which interaction occurs, and the effects of changing axial fin location and Reynolds number.

In the second part of this study, the vortical flow over a steady missile configuration with a tangent-ogive forebody was investigated for different angles of attack. The model was designed in a such a way to allow the tip and the aft body to be stationary and the body to roll. This enabled measurement of the pressure over the model surface without disturbing the flow field. The angle of attack and Reynolds number were varied from 0° to 85° and from 6000 to 34000, respectively. Flow visualization and pressure distributions acquired at several azimuthal angles were used to describe the flow regions and the onset of asymmetry. Local side force and normal force coefficients, derived from the pressure measurement, were used as a tool to further understand the flow development.

CHAPTER I
INTRODUCTION AND BACKGROUND

1.1 Introduction

Interactions between vortical flows and surfaces are seen in many situations, and understanding the effects of such interactions is important in many applications. The separation of the flowfield around the forebody of a maneuvering aircraft, for example, can create vortical structures that interact with the wings and tail. This causes significant handling and performance problems. The highly vortical flow in the wake of a helicopter rotor interacts to a great degree with the main body, creating unsteady loading which effects performance. Also, the interaction between a helicopter blade with the wake of the preceding blade, known as the "blade-vortex" interaction problem, can reduce the effectiveness of the rotor blade.

The flowfield on the leeward side of a missile at an angle of attack is also highly vortical in nature. As the angle of attack increases, the wake exhibits four basic flow regimes. At very low angles of attack, the flow is attached on the leeside. As the angle of attack in increased, three-dimensional flow separation occurs, resulting in the formation of well-defined, vortical structures on the leeward side of the body. At slightly higher angles, the flow separates and rolls up into a symmetric pair of vortices. As the angle of attack increases further, the vortices develop asymmetrically. At very high angles of attack, unsteady vortex shedding takes place. Fins placed at various locations along the missile body will interact with the separated, vortical, leeside flowfield in different ways. In many cases, the fins are used as control surfaces, and the changing loads due to the interaction with the vortex system can reduce the effectiveness of the fin as a control surface. Depending on the flow parameters such as angle of attack, tip configuration, control surfaces and other conditions, different flow regimes exist such as strong tip vortices, bound body vortices which can be either symmetric or asymmetric, and vortex shedding from some regions of the body. The separation and vortex shedding result in significant unsteady forces on the missile that determine its overall stability and performance in flight.

Previous work has led to a good understanding of the general features of the flow about slender bodies of revolution at angles of attack, but the underlying mechanisms are not completely understood. An excellent overview of this work is found in the reference by Ericsson and Reding (1986). However, little work has concentrated on the interaction between missile tip vortices and control surfaces. Further investigation is important for many reasons. Vortex-induced loads are difficult to predict, and cause changes in yaw, roll and pitch motions that can be coupled in a non-linear manner. Also, the placement of a surface in such a flowfield may alter its structure. An investigation to understand the nature and outcome of such interactions is therefore of great value.

1.2 Background

Vortex-surface interaction of the kind described above therefore continues to be the subject of investigation by both experiments and computational modeling. There has been quite a bit of recent work investigating the interaction between vortical flows and tail surfaces for aircraft configurations. Washburn et al. (1993) conducted experiments to examine the interaction between vortices forming over a sharp-edged delta wing and twin tails mounted at the rear. This work focused on the effect of the tails on the vortex trajectories and vortex breakdown, as well as fin loading and buffet. Unsteady pressure and load measurements were made on the tail fins of an F/A-18 aircraft by Lee and Tang (1993). More work has been done for helicopter configurations. The blade-vortex interaction problem was recently studied by Wittmer et al. (1994), who observed a large increase in turbulence in the vortex after it interacted with the blade. The blade-vortex interaction was also investigated by Poling et al. (1989). The interaction between the flowfield in the wake of a helicopter rotor and the helicopter body was recently investigated experimentally by Brand et al. (1989), who measured mean and unsteady pressures on the airframe for various flight speeds. Extreme unsteady fluctuations in pressure were seen on the airframe. Affes and Conlisk (1993) developed a simplified computational model for the interaction of a rotor tip vortex with a helicopter body, and

compared the results with experiments in the reference by Affes et al. (1993). Other computational work related to the present study was performed by Bodstein et al. (1993), who developed an analytical model for the interaction of a streamwise vortex with a long plate. Their results included spanwise variations of the vortex-induced pressures on the plate, and vortex trajectories over the plate. Computational work directly related to the missile problem was conducted by Mendenhall and Perkins (1989), who developed a calculation procedure for the prediction of nonlinear aerodynamic characteristics of missiles at high angles of attack in subsonic flow. Their results included predictions of the vortex-induced effects on the normal force coefficients for a single fin mounted approximately ten diameters from the missile nose.

The present status of knowledge on the aerodynamics of missiles was reviewed by Mendenhall et al. (1989). It is clear from their presentation and discussions, that several important issues are not understood clearly. Among these are the characteristics of flow around missiles, and the complex mechanisms that govern the effectiveness of missile control procedures. This area needs further investigation and documentation. In addition, not a single method exists that can predict the flow field around a missile in flight with sufficient accuracy, nor is there an adequate data base to guide efforts to develop and improve methods for this purpose.

The aerodynamics of tactical missiles is strongly dependent on the geometry, angle of attack, Reynolds number, Mach number, and boundary layer transition in the forebody region (Chapman and Keener, (1979), Peake and Tobak, (1980), Ericsson and Reding, (1986)). The separated vortical flow and body motion are strongly coupled. At low angles of attack, the flow is three-dimensional and there is an interaction between the fuselage and the lifting surfaces as well as an interference between the lifting surfaces themselves. Interaction and interference associated with symmetric vortices are present at all velocities. Although the vortex pair is symmetric, flow entrainment results in a highly non-uniform flow in the tail regions. Currently, not much definitive data are available on the

position and strength of these vortices or on the associated non-uniformity. At high angles of attack, the flow is highly three-dimensional, separated, and unsteady. A family of vortical structures exist. They originate from the tip, the main body, and also at the lifting surfaces. The nature of this vortical system is a function of the missile geometry, the angle of attack, and the Mach number. With increase in the angle of attack, the vortex system becomes asymmetric. One of the pair lifts away from the missile, while the other moves closer to the tip. Therefore, the resulting vortex-induced loads are highly complicated to predict. An increase in lift is seen together with a highly non-linear coupling between the yaw and pitch motions. The effects in the tail regions are even more complex because unsteady interference causes large unsteady cross-coupling effects. Wardlaw and Morrison (1975) showed that the side forces resulted from asymmetric vortex separation could be significant for cross-flow Mach number less than 0.8 with the largest effects occurring for Mach numbers less 0.4.

In transonic and supersonic regimes, the flow is further complicated by the presence of shocks. However, at Mach numbers greater than about 3, the flow field is insensitive to the vortical interaction. The density is very low over the leeward surfaces and the windward pressure distributions dominate significantly the overall forces (Hoeijmakers, (1989)). On the other hand, the vortical wake flow and the accompanying interactions and unsteady effects are clearly important during some portions of the flight, especially in the launch phase, the initial stages of flight, and during maneuvers. For a missile operating in this regime, it is very important to have a knowledge of the dynamics resulting from the unsteadiness in the vortical flow structure and the underlying mechanisms that cause this behavior.

1.3 Previous Work at IIT

The flowfield in the wake of a forebody at an angle of attack has been studied previously at the IIT Fluid Dynamics Research Center. Work reported by Montividas

(1988) and Montividas et al. (1989) investigated the behavior of the flowfield behind a circular cylinder with a conical nose for both steady and unsteady conditions. Attempts were made to control the asymmetric wake through the use of splitter plates, trapezoidal wings, and symmetric winglets. Control of the asymmetric vortices in the wake of a forebody was also investigated by Williams and Bernhardt (1990), who used suction to bleed fluid from selected regions near the nose tip.

1.4 Objectives

The objective of the first part of this work was to examine interactions between the tip vortices and surfaces for a typical missile geometry, and to understand the influence of these tip vortices on control surfaces, such as fins and canards, that may be placed at different locations along a missile body. The specific goals of the experiments were: (1) to document the interaction of the tip vortices and a single, generic, control surface through flow visualization and mean-pressure measurements, (2) identify and understand the physical mechanisms that play an important role in this interaction, (3) to determine the forces on the fin that result from interaction with the vortices, and (4) to examine the effects of fin placement on the development of the vortex system.

In the second part, surface-pressure measurements at various angles of attack were used to calculate local side and normal forces. The objectives of this phase were (1) fulfill the need for carefully controlled experiments that would provide documentation of the flow field over a steady missile configuration for selected flow conditions and establish a clearer understanding of the nature of such separated, vortical flow, (2) provide information on the pressure distributions on both windward and the leeward sides of the model for various angles of attack, (3) characterize the different flow regimes encountered as the angle of attack changed, and identify the important features and the mechanisms responsible for the change from one characteristic flow regime to another, (4) examine the conditions under which asymmetry develops in the flow field and the mechanism responsible for its appearance as well as the switching of vortices from one side to the other.

CHAPTER II

EXPERIMENTAL FACILITIES AND PROCEDURES

2.1 Flow Facility

The experiments were conducted in the Andrew Fejer Unsteady Wind Tunnel at the IIT Fluid Dynamics Research Center. The plan view of this tunnel is shown in Figure 1. This is a closed-circuit, low-speed facility that is driven by a axial-vane fan powered by a 40 horsepower synchronous motor. The flow velocity is adjusted by varying the excitation of a magnetic clutch, and velocities up to 40 m/s can be reached. A honeycomb, followed by seven screens and a 6.25 to 1 fifth-order square contraction condition the flow upstream of the test section. This results in a free-stream turbulence level of 0.03% in the test section at the maximum velocity. The test section itself is 0.61 meters square in cross-section and 3.1 meters in length. For this study, the removable front panel of the test section was constructed out of one sheet of 0.375 in. (0.953 cm.) thick plexiglass, and the entire top of the test section was replaced with a solid sheet of 0.75 in. (1.905 cm.) thick plexiglass to allow optical access for flow visualization. The model positioning system, which will be described later, entered the tunnel through a removable panel in the test-section floor. While this tunnel is equipped with a shutter mechanism which can be used to produce an unsteady flow component in the test section, this feature was not used in the present experiments.

2.2 Model and Positioning System Design

Figure 2 shows the model and its positioning system installed in the wind tunnel. The positioning system allowed the model to be placed in the central region of the test section, at the desired yaw and pitch angles, through the use of three stepper motors. The ability to roll the model was built directly into its design using one small stepper motor mounted internally. The positioning system consisted of a slider mechanism mounted on a large, vertical traversing mechanism. The slider housed two Bodine stepper motors which controlled the yaw and pitch angles of the model. The yaw motion was transmitted to the model through a 50 to 1 ratio worm gear to a 1.5 in. (3.81 cm.) diameter hollow shaft,

which ran vertically from the top of the slider into the wind tunnel. On top of this shaft, the pitch mechanism was mounted. This mechanism consisted of a housing and a 40 to 1 ratio worm gear, which was cut to a 90° arc. The model was mounted directly to this gear. The pitch gear was driven by a 0.5 in. (1.27 cm.) diameter shaft that ran inside the 1.5 in. yaw shaft down to the slider, where it connected to the pitch motor.

In order to keep the model in the center of the wind tunnel as the pitch angle was increased, the slider had to be traversed vertically. The traversing mechanism consisted of a dove-tail rail and an acme-threaded lead screw driven through a 10 to 1 ratio worm gear by a third Bodine stepper motor. Teflon strips were used to reduce friction between the slider and the rail, which were both constructed out of aluminum. The entire positioning system was stabilized and mounted to the floor by a 12×24 in. (0.3×0.6 m.) aluminum base plate.

The Bodine stepper motors used rotated 1.8° per step input. The Bodine controller used allowed the motors to move in half-step increments of 0.9°. This provided very accurate positioning of the model in the tunnel. The actual position of the model was monitored through the use of Hewlett Packard optical encoders and codewheels. A model HEDS 9100 encoder and a HEDS 5120 codewheel, which gave 500 counts per revolution, were mounted on the pitch gear shaft. A similar encoder and a 360 counts-per-revolution codewheel were mounted on the shaft of the yaw motor. Finally, a similar encoder and a 100 counts-per-revolution codewheel monitored the lead screw motion in the traversing mechanism. All encoders were powered by a Hewlett Packard model 6234 Dual Output Power Supply.

The model used in the present experiments had a diameter (d) of 1.44 in. (3.65 cm.) and a length of 20 in. (50.8 cm.), including a tangent-ogive nose, 3.75 in. (9.53 cm.) long. A modular construction, shown schematically in Figure 3, was used for several reasons. This allowed interchangeability of some of the sections, thereby minimizing the number of sensors and sensor locations required. It was possible, for instance, to map the pressure over the entire model surface with one axial row of pressure ports, by rolling the model and placing the ray containing the pressure ports at different azimuthal locations. The modular construction also enabled positioning of the control surface at different axial

locations relative to the model tip. Each body section was constructed from a hollow, aluminum tube with an inner diameter of 1.19 in. (3.02 cm.). A step machined into the end of each section allowed the sections to fit together tightly. The body sections were supported from the inside by a brass framework consisting of a hollow tube and four Y-shaped brass supports. Set screws in the supports locked the body sections in position.

The nose is a tangent ogive with a radius of 9.43 in. (23.95 cm.) and a length to diameter ratio of 2.6. An important feature of this nose is that the first 1.5 in. of the nose was constructed as a separate piece. It is well known that small variations in the surface microgeometry in the tip region can result in large changes in the flow state. For example, rolling the nose of the model can result in a flipping of the leeward flow asymmetry between the near and far (port and starboard) sides. To prevent such an occurrence, and yet be able to roll the model for measurements, the model was designed to keep the first 1.5 in. (3.81 cm.) of the model tip fixed while the rest of the model rolled. The effectiveness of this design was confirmed during the experiments. The base of the nose was mounted to one end of the hollow, brass tube described earlier, while the tip was connected to a steel shaft that ran inside the brass tube. At the base of the model, the other end of the brass tube was connected to the roll motor housing, while the steel shaft was coupled to the roll motor shaft. The roll motor shaft was also connected the model mounting plate. This arrangement allowed the motor housing, which was connected to the model body, to rotate around the motor shaft, which was held fixed by the model mounting plate. The roll motor was a Digital Motor model HY-200 3.6°/1.8° Hybrid M.A.E. stepping motor driven by a Compumotor Digiplan Type PK2 stepper motor driver. The roll position of the model was monitored by a Hewlett Packard model HEDS 9700 encoder module with a HEDS 5120 400 counts-per-revolution codewheel.

For surface pressure measurements, (Figure 3b) the base of the nose section was instrumented with 12 pressure ports, of which ten were located on rays 180° apart. The other two ports were positioned ninety degrees apart from these longitudinal rays. Each of the body sections had nine ports which were made from steel tabulations inserted flush with the surface with a tight fit. Six ports were arranged along a longitudinal ray, called the main ray, and the rest were located circumferentially ninety degrees apart, in line with

the third main ray port at x/d 3.6, 5.8, 8.1, and 10.3. The rear section was 3.25 in. long with two different configurations. One was without any fins to provide control measurements for a cylindrical body. The second had four equal, angular-spaced, clipped-delta type fins without pressure ports. A similar configuration was built but with forty-eight ports. Rotating the fin section forty-five degrees with respect to the body could generate two different fin orientations with respect to the flow.

The generic fin used in the vortex-surface interaction experiments was attached to an interchangeable body section that could be placed in any one of four axial locations along the body of the model (Figure 3). These locations are referred to as stations 1-4 in subsequent discussions. The fin had a tapered, clipped-delta shape with a chord length of 3.25 in. (8.26 cm.) and a span of 3.0 in. (6.72 cm.), or 2 diameters. The sweep angle of the leading edge was 28.4°. The fin was 0.5 in. (1.27 cm.) thick at the root and 0.19 in. (0.48 cm.) thick at the tip. Two identical fins were used in the experiments; one for flow visualization, and the second for pressure measurements. Both surfaces of the second fin, designated the near and far sides for purposes of identification, were instrumented with 18 pressure ports, as shown in Figure 4. This fin was constructed out of aluminum in two halves. The 18 pressure ports were drilled into each half, and slots were milled in the inner surface which transmitted the pressure from each port to a separate stainless steel tubulation at the fin root. The two halves were epoxied together with a thin sheet of brass in between. The tubulations at the fin root protruded into the body section, where they were each connected to a length of 0.04 in. ID nylon pressure transmission tubing. One row of pressure ports was also located axially on the model body, along the root of the fin. Each of these ports was also connected to a piece of nylon tubing. The tubing was routed through the center of the body and exited the model at the base.

The four motors used to position the model in the wind tunnel were controlled by computer. Also, the position data from the optical encoders was acquired and processed by the same routine. The electrical interface between the model and the positioning system to the computer is shown schematically in Figure 3c. The three Bodine stepper motors secured in the positioning system were driven by a Bodine driver which was connected to

the driver power supply. The driver received two signals from a D/A distribution box for directing the rotation and driving the motor. In order to utilize one driver to drive all three motors, a relay was used to channel the signal. The relay was activated by two channels from the D/A distribution box. The roll motor was connected directly to the PK2 driver which was activated by three D/A channels to energize/inhibit, direct, and drive from the D/A distribution box. The distribution box was connected to the DA12FA board at the Masscomp computer using a ribbon cable.

To detect the final model position, four encoders leads were connected to a distribution box. This distribution box channeled the voltage from a Hewlett Packard 6234 Dual Output power supply to the encoders. (This power supply also provided a 10 V supply to the Bodine relay mentioned above). In addition to channeling the power supply, the distribution box also connected a ribbon cable from encoder signals to the A/D board at the Masscomp computer.

2.2 Position Control and Pressure Acquisition Code

To move the model and monitor its final position, a computer code was developed following the flow chart shown in Figure 3d. Initially, the program read a look-up table which contained appropriate values of the number of pulses and the expected number of encoder cycles to pitch and translate the model. Then, a menu listing several commands, the current position, and pressure-acquisition parameters was displayed. Commands available to move the model could be accessed using a selection number and entering the desired yaw, pitch, and roll. In addition to the model-positioning tasks, other commands, such as changing the pressure-acquisition parameters, acquiring mean or fluctuating pressure signals at a particular port, acquiring mean pressure signal at all 48 ports at a particular azimuth angle and changing the default positions could also be activated.

For motion control, the selection number and the final positions were entered. Then, the computer code would generate an appropriate series of steps to yaw, pitch, and

roll the model. First, the nearest final position was calculated and displayed on the screen, because the model could be moved only to a set of predetermined positions. For yawing and rolling movements, the corresponding number of pulses to drive the motor and the expected number of encoder cycles were calculated. After that, the relays and direction of the motor, either clockwise or counter clockwise, were set up by sending the appropriate signals to the Bodine relay and driver, respectively. Before the motor was driven, the number of samples and acquisition frequency to acquire the encoder signal were calculated based on three factors: the time required for the motor to operate, any additional samples needed at the beginning and ending of the acquisition period, as well as the criterion that each encoder count would contain 25 samples. The number of encoder cycles was obtained from a count of the number of times the signal changed from a high (about 5 V) to a low (0 V) state. Then, the expected number of cycles and the detected number of encoder cycles were displayed. In most instances, the counts were equal, indicating that the model had been moved to the desired position. Finally, the code returned to the menu.

For a pitch movement, on the other hand, the number of swaps between pitching and translating motion was evaluated. Then, the number of pulses to drive the motor for each swap was referred to or interpolated from values contained in the look-up table. Based on the number of swaps, the process of setting up the relay and direction, calculating encoder parameters, driving the motor, and counting the encoder cycles were repeated until the entire swap was completed. The menu was displayed after the model positioning was completed. It was estimated that the uncertainty for moving the model would be $\pm$ 0.3% based on the Bodine motor positioning error.

In addition to moving the model, entering the selection number and zero could provide the facility to initialize the position to some angle, to change the pressure acquisition parameters, and to acquire a pressure signal. The initialization to some angle command was designed with the idea of changing the default position to the actual position, if the program unexpectedly aborted with the model at a known position.

Parameters of the pressure acquisition were a pressure transducer offset voltage, operational amplifier gain, number of samples to be acquired, sample acquisition frequency, x/d location, and option to store a fluctuating pressure signal.

The pressure acquisition command could be used to acquire the signal at either a single port or at all 48 ports at a particular azimuth angle. With acquisition at a single port, the mean value of pressure could be stored in one file and the fluctuating data in another file, if the option to store the fluctuating signal was selected. Acquisition of pressure at all 48 ports was accomplished automatically by sending a signal to a relay that moved the scanivalve to the next port, after acquiring and averaging of samples from the previous port had been completed. Before returning to the menu, the mean values from all 48 ports were stored in the file for further processing. Finally, the menu provided a normal exit from the code.

2.4 Flow Visualization Techniques

The smoke-wire technique was used for flow visualization. A detailed description of this technique can be found in the reference by Corke et al. (1977). For this study, two vertical smoke wires were placed about 50 cm. upstream of the model, and about 2 mm. on either side of the tunnel center line. The two 0.1 mm. nichrome wires were coated with oil droplets and heated electrically, causing the droplets to vaporize and produce uniform streaklines of smoke. This enabled introduction of smoke into the near-wall region at the tip of the model, on the near and far sides. Either one, or both wires could be operated, as desired. Cross-sectional views of the flow at various axial positions along the model were obtained by illuminating the smoke with a laser-light sheet placed at the appropriate location. The beam of a Continuum Surelite Series 10 YAG laser, with a wavelength of 532 nm., was routed to the top of the wind tunnel and aligned along the tunnel centerline. The beam passed through a 60 cm. focal length spherical lens and a 30 cm. focal length spherical lens places 30 cm. from the first lens. This simple arrangement focused the beam down to one half its original diameter, approximately 3 mm. Next, it passed through a

cylindrical lens which expanded it in the horizontal direction creating a 3 mm-thick sheet of light. This sheet was then reflected down through the plexiglass top of the test section at an angle perpendicular to the axis of the model. The axial position of the sheet along the model could be changed by traversing one mirror. A Nikon F2 camera with motor drive was mounted on a tripod on top of the test section and positioned so that its line of view was directly down the model axis. An 80-200 mm. f3.5 zoom lens was used to obtain the desired field of view, and the photographs were taken on Kodak T-MAX P3200 black and white print film. Great care was taken to minimize the reflections from the laser beam. The inside surfaces of the tunnel, as well as the model and all optical mounts, were painted flat black. The laser sheet entered the tunnel through a 3 mm. wide horizontal slot masked onto the plexiglass top. For the side-view visualizations, the laser light source was replaced by a stroboscopic light source that could be triggered by an external command signal.

2.5 Surface Pressure Measurement

A Setra model 239 pressure transducer was used for the pressure measurements. During a measurement, the pressure transmission lines from the pressure ports on the fin surface were routed out of the wind tunnel test section and connected in sequence to the pressure transducer through a 48-channel Scanivalve (model JS4-48). The reference-pressure port of the transducer was connected to a wall-mounted static pressure port at the upstream end of the wind-tunnel test section. The Scanivalve was controlled by a model CTLR10/S2-S6 Solenoid Controller and a model OED2/BINY Odd-Even Decoder. The Setra pressure transducer was powered by a Hewlett Packard 6234 Dual Output Power Supply. The output of the transducer was passed through an Ithaco 4212 Electronic Filter set to a low-pass cut-off frequency of 500 Hz. for anti-aliasing purposes. The filtered signal was then amplified by a Teledyne Philbrick Nexus operational amplifier to fall in a ±5 volt range. Data acquisition was handled by a Masscomp minicomputer, which will be described in the following section. Two Philips PM2519 auto-ranging multimeters and a Philips PM3055 dual-channel oscilloscope were used to monitor both the non-amplified and the amplified pressure signals throughout the experiments. At the

lowest Reynolds number, the sensitivity of the Setra transducer was inadequate, and it was replaced by a Validyne DP103 differential pressure transducer connected to a CD15 Carrier Demodulator.

2.6 Computer Facilities

A Masscomp model MC-5500 minicomputer was used to control the positioning motors, control the Scanivalve, acquire model position data from the optical encoders, and acquire the pressure data. The computer was fitted with a DA08F digital-to-analog conversion board, and a AD12FA twelve-bit analog-to-digital conversion board, which had a maximum aggregate sampling rate of 1 MHz and a bipolar input range of ±5 volts. These boards provided eight analog output channels, used for motor and Scanivalve control, and eight differential analog input channels, used for data acquisition. Both the Masscomp computer and a Gateway 2000 model 4DX2-66V personal computer with a 486 DX2 66MHz processor were used to process the pressure data.

2.6 Experimental Procedures and Parameter Ranges

2.6.1 Vortex-fin interaction Experiments were performed for two pitch angles (α), 30° and 45°. This selection was based upon earlier work described in Part B of this report, performed using the same facilities and model. The tip vortices are symmetric at 30°, and asymmetric at 45°. Care was taken to ensure that flowfield conditions remained the same throughout the experiments. Improper positioning of the model, dust on the tip of the model's nose, or improper positioning of the smoke wires upstream of the model could cause the asymmetry to flip sides at $\alpha = 45°$.

A standard procedure for aligning the model in the wind tunnel was used prior to each flow visualization or pressure data run. First, the model was set to $\alpha = 0°$ in the center of the wind tunnel test section. This was checked by placing a level on the upper surface of the body of the model. Next, the model was pitched to the chosen angle of attack. The position was verified by the optical encoder output signals. The yaw was set to 0° for all cases in this project. This was verified by measuring the perpendicular distance of the nose tip from the back wall of the test section. Finally, the azimuthal fin position (ϕ)

was set to 0° by measuring the perpendicular distance of its tip from the back wall of the test section. At this point, the front of the tunnel was sealed, the tunnel flow was turned on, and the test run began.

The first phase involved a detailed flow-visualization study of the vortex system and its interaction with the control surface (fin) using the laser-sheet/smoke-wire technique mentioned earlier. All flow visualization was performed at a Reynolds number based on model diameter (Re_d) of 6000, due to limitations of the smoke-wire technique at higher flow speeds. Experiments were conducted for four axial locations of the fin (see Figure 3), identified by the axial position of the fin's leading edge ($(x/d)_f$). At station 1, $(x/d)_f = 2.6$. At stations 2, 3, and 4, $(x/d)_f = 4.9$, 7.1, and 9.4, respectively. For each axial location of the fin, flow visualization was performed at a section through the middle of the fin for azimuthal fin positions 5.4° apart, over the range -92° to +92°. Development of the vortices ahead of the fin was documented at several axial locations (the number varied with the axial location of the fin) for three azimuthal fin positions (ϕ = 0° and ±54°). At the leading and trailing edges of the fin, flow development was documented for five azimuthal fin positions (ϕ = 0°, ±22°, and ±54°).

Pressure data were obtained on both surfaces of the fin at Reynolds numbers based on model diameter of 6000, 20000, and 34000 for the four axial locations of the fin and two angles of attack described above. Data sets were acquired at azimuthal fin positions every 5.4° from -178° to +178°, along with one set at 180°. The raw voltage data were converted to pressure data and non-dimensionalized by the approach-flow dynamic pressure, to obtain coefficients of pressure. This was done on the Masscomp computer. The data were then transferred to the personal computer for further processing. The data were split into two separate data files, each containing the 24 data points on one side of the fin, and these files were input into a software package by Golden Software named Surfer. This package was used to take the input data and, through user-chosen interpolation methods and parameters, create a 116×96 grid of pressure values for each surface of the fin. These data were then plotted in the form of pressure-coefficient contours. Several tests of the interpolation method and parameters chosen were

performed. Known linear spanwise and chordwise pressure distributions, as well as circular pressure distributions, were input into the software using only 24 data points at locations corresponding to the locations of the actual pressure data on the fin surface. The resulting interpolated values compared well to the input distributions in all cases.

These dense grids of pressure data were also used to calculate the normal forces acting on each side of the fin. The fin was divided up into 116×96 differential areas, corresponding to the pressure values in the grid. Each pressure value was multiplied by the differential area to get a differential force. These forces were summed up over each surface of the fin, and the total force was non-dimensionalized by the planform area of the fin to get the normal force coefficient on each side of the fin. The fact that the area near the leading edge of the fin is heavily tapered, and that the entire fin is slightly tapered in the spanwise direction, were taken into account when the calculations were performed, and only the proper normal components were included in the summation.

2.6.2 Surface-pressure measurements During the experiment the following procedure was followed. First the model was set up to zero angle of attack. The distance from the model to the back wall of the test section was measured and adjusted to align the model correctly with the flow. The measurement was checked each time the model was set to this zero pitch position. Then the body of model was rotated until the main ray of the pressure port was aligned to zero degrees in the azimuthal position, if the pressure measurement was to be carried out. For the flow visualization, the main ray was adjusted to 90°. Then, the model was pitched up to the desired position. The final position would place the model at the center of test section. After that, either flow visualization or pressure measurement was implemented. If pressure measurement was chosen, the model was rolled in an increment of 5.4° or higher until the main ray reached the final position at 360°. Next, the body was rolled back to the zero roll position and the model was pitched up again. At this new pitch angle either the pressure measurement or the flow visualization was repeated. After above procedures were completed, the model was positioned back to zero pitch angle. The pressure data recorded during the measurement were used to obtain,

among other parameters of interest, the coefficient of pressure and local forces. Experiments were carried out for angles of attack between 0 and 85 degrees, and Reynolds numbers between 6,000 and 34,000.

PART A

CHAPTER III
SYMMETRIC FLOWFIELD INTERACTION

3.1 Flowfield Development

We first consider the data at $\alpha = 30°$. At this angle of attack, a pair of steady, symmetric vortices dominates the wake on the leeward side of the model. The development of this flowfield ahead of the fin as well as its structure in the fin region were documented for each of the four fin locations, using the cross-sectional laser-sheet flow-visualization technique described earlier.

Figure 5 shows the development of the vortex system at seven axial locations along the model with the fin positioned at station 3 ($(x/d)_f = 7.1$). All flow visualization was performed at $Re_d = 6000$. Each view in this figure is a cross-sectional plane perpendicular to the model axis, looking down along the axis from the tip. Flow is from left to right, and the fin is at $\phi = 0°$, corresponding to the leeward ray of the model. The "far" side is toward the top of each view, and the "near" side is toward the bottom. There are some important points to consider when viewing these cross-sectional flow visualization photographs. First, the vortex system is steady and three-dimensional. The laser sheet is perpendicular to the model axis, which is at an angle to the flow direction. Therefore, there is a large component of velocity in the plane of the photograph. Slight differences in the appearance of the vortices in some of the photographs at this angle of attack are not due to asymmetry in the flowfield. Rather, they are due to slight differences in the positions of the smoke wires to either side of the stagnation line upstream of the model. Also, due to the system used to distribute oil on the wires, the quantity of oil on each wire may not be equal in all cases. Finally, the two lines visible along the centerline of the model just beyond the vortices are streaklines in the outer flow passing above the tip of the model nose.

Figure 5 shows that the pair of vortices has started to form at x/d = 1.0. By x/d = 1.8, the vortices have formed and are clearly symmetric. They remain symmetric, coherent,

and attached to the body through x/d = 7.1, the leading edge of the fin. At this location, the vortices become slightly less coherent, presumably an influence of the fin. At x/d = 8.8, the middle of the fin, the vortices remain symmetric, but are clearly less coherent, and start to lift away from the body. The centers of the vortices are further from the leeward ray at this location due to the presence of the fin. At the trailing edge of the fin, x/d = 9.4, the vortices are further away from the body but otherwise unchanged. This indicates that the vortices remain symmetric and close to the body as they pass the fin section.

The flowfield develops similarly with the fin placed at the other three axial locations. Figure 6 shows the development of the vortex system with the fin at station 4 ($(x/d)_f = 9.4$). The vortex development from x/d = 1.0 through x/d = 7.1 is very similar to that shown in Figure 5. The vortices continue to grow symmetrically and remain attached to the body up to the leading edge of the fin (x/d = 9.4). As the vortices come in contact with the fin, they become less coherent, lift away from the body, and move away from the leeward ray, again as shown in Figure 5, however, since the fin is positioned further downstream, the vortices are larger in size. The development of the vortex system with the fin at station 2 ($(x/d)_f = 4.9$) and with the fin at station 1 ($(x/d)_f = 2.6$) is shown in Figures 7 and 8, respectively. Again, in both these cases the vortices remain symmetric, coherent, and attached to the body until they come in contact with the fin. At the fin, the vortices remain symmetric, but become less coherent, lift away from the body, and their centers are displaced away from the leeward ray by the presence of the fin. As the fin is positioned closer to the nose, the vortices are smaller in size when they come in contact with the fin.

Figures 9 and 10 show side and top views, respectively, of the vortex-center trajectories for the four axial positions of the fin with $\alpha = 30°$, $\phi = 0°$, and $Re_d = 6000$. The vortex centers in these two figures were obtained from the cross-sectional flow visualization photographs shown in Figures 5 to 8. The data ends at the trailing edge of the fin because no flow visualization was performed beyond this point. X/d is aligned with the axis of the model, z/d is radially outward from the model axis, and y/d is the transverse coordinate, mutually orthogonal to x/d and z/d. Positive z/d is away from the model, and y/d is positive in the direction toward the near side of the wind tunnel. In order to show

the top view data correctly, -y/d was plotted versus x/d in Figure 10. These figures clearly show the paths of the vortices as they pass over the fin section in each case. Figure 9 shows that the trajectories of the near- and far-side vortices are the same in each case, confirming the symmetry of the flowfield. The vortices begin to separate from the body as they contact the fin. As the fin is placed closer to the nose, the vortices lift from the body at a lower x/d. The trajectories of the vortices ahead of the fin section in each case are nearly identical. The top view, Figure 10, again shows the symmetry of the flowfield. The trajectories of the near- and far-side vortices are symmetric about the leeward ray (y/d = 0). The vortex trajectories in each case are nearly identical until the vortices contact the fin, where they are displaced away from the leeward ray. These figures clearly show that at this angle of attack, the axial position of the fin does not effect the development of the flowfield.

Figures 11 through 14 combine the cross-sectional flow visualizations with the vortex trajectories to show the development of the flowfield in a three dimensional perspective view for $\alpha = 30°$, $\phi = 0°$, and $Re_d = 6000$. This representation helps further visualize the flowfield that exists under these conditions. The larger view is from the near side of the wind tunnel, and the smaller view is from the far side. The view angles and perspective were chosen to show the most information about the flowfield. The angle of attack and azimuthal fin position are indicated in the lower right corner. For each of the four axial locations of the fin, the vortices are large, symmetric, and their trajectories run close to the body in the region of the fin. Therefore, there is a substantial interaction between the vortex system and the fin at these axial locations.

3.2 Characteristics of the Interaction

3.2.1 Vortex Signature on the Fin Surface. Now that the structure of the flowfield in the region of the fin and ahead of it has been described, characteristics of the interaction between the fin and the vortex system will be shown. Figure 15 shows the pressure-coefficient (C_p) contours on the near- and far-side surfaces of the fin with the fin at station 3, for the same flow conditions described in the previous section, enabling a direct comparison with the x/d = 8.8 view in Figure 5. Flow is from left to right in Figure 15.

The fin is attached to the body at y' = 0, and its leading and trailing edges are at x' = 0 and x' = 3.25, respectively. A projection of part of the missile body is also seen between y' = 0 and -0.375. In this figure and in all following contour plots, dashed lines indicate a negative C_p, or suction, while solid lines indicate a positive C_p. The pressure contours on the two sides of the fin in this figure are almost identical, confirming the symmetry of the flowfield. The most striking feature is the large low-pressure region near the fin-body junction. At half span, the concentration of pressure contours represents a rapid rise in pressure in the spanwise (y') direction due to flow toward the fin surface. Near the tip of the fin, there is a region of higher pressure. This pressure distribution across the surface of the fin is a characteristic signature of a vortex near the surface. As seen in Figure 5, x/d = 8.8, the centers of the two vortices pass on either side of the fin slightly inboard of half span. Further inboard of this location, near the fin-body junction, fluid is flowing away from the fin surface, creating a region of low pressure. Outboard of this location, near the tip, fluid is flowing toward the fin surface, creating a region of high pressure. Figure 16 shows five spanwise slices of the pressure data on the near side of the fin. The conditions are the same as in Figure 15. These show more clearly the spanwise variation in pressure. Close to the leading edge of the fin (x' = 1.09), a strong suction peak is seen at y' = 0.375 in the spanwise pressure distribution, due to the presence of the vortex over the fin. With increasing x', the magnitude of this peak diminishes, and its spanwise extent increases. The pressure traces at different chordwise locations are very similar for y' > 1.5. Due to the symmetry of the flowfield, the spanwise pressure distribution on the far side of the fin for these conditions is nearly identical to the near-side distribution.

For comparison, Figure 17 shows the C_p contours on the near- and far-side surfaces of the fin for all four fin stations for the same flow conditions previously described. Figure 17(c) is the same as Figure 15. The pressure distribution shown in Figure 17(d) (fin at station 4) is similar to that in Figure 17(c) (station 3), however the low-pressure region near the fin-body junction is larger in the spanwise direction, with the concentration of pressure contours slightly outboard on half span. This is due to the growth in size of the vortices with increasing x/d and the separation of the vortices from the body. The magnitudes of the low-pressure region near the fin-body junction and the

region of higher pressure near the fin tip are comparable with those at station 3. Figures 17(b) and 17(a) show the C_p contours on both sides of the fin with the fin at stations 2 and 1 respectively. Again, the features are similar to those shown in Figure 17(c); however the size of the low-pressure region near the fin-body junction is smaller in Figure 17(b) and smaller yet in Figure 17(a). This is due to the smaller size of the vortices closer to the nose. The magnitudes of the low-pressure region near the fin-body junction and the higher-pressure region near the tip at stations 2 and 1 are again similar to those at station 3.

Figure 18 compares the spanwise pressure distributions on the near side of the fin for the four different axial fin positions. Again, since the fin is at $\phi = 0°$ and the flowfield is symmetric, the pressure distributions on the far side of the fin are nearly identical to those on the near side. The $(x/d)_f = 7.1$ graph is the same as Figure 16. At station 1 ($(x/d)_f = 2.6$), the low pressure peak is small in spanwise extent and its magnitude decreases rapidly with increasing x'. The pressure traces at $x' \leq 1.64$ are nearly identical. As $(x/d)_f$ increases, it is clear that the low pressure peak remains in the same location, but its spanwise extent increases and its magnitude decreases at a slower rate in the x' direction.

3.2.2 Symmetry with Changing Azimuthal Fin Position. When the fin is positioned along the leeward ray of the model, as is the case for Figures 5 through 18, the near- and far-side vortices are located at equal distances from the near and far sides of the fin surface, respectively. Therefore, any effect of the vortex system on the two surfaces of the fin will be symmetric. The pressure distributions of Figure 17 confirm this. As the azimuthal position of the fin changes, however, the position of the fin relative to the vortex system changes, and the effect of the vortex system on the two surfaces of the fin is no longer symmetric. However, since the overall flowfield is still symmetric, the effects of the vortex system at azimuthal positions of the fin to one side of the leeward ray ($+\phi$) are the same as those for azimuthal fin positions to the other side of the leeward ray ($-\phi$), if one compares the near-side surface pressure distribution at $+\phi$ to the far-side surface at $-\phi$ and vice-versa. This is clearly seen in Figures 19 and 20 with the fin at station 3. Figures

19(a) and (b) show the pressure-coefficient contours on the two sides of the fin for azimuthal fin positions of ϕ = -22° and ϕ = +22°, respectively, and Figures 20(a) and (b), show the C_p contours on the two sides of the fin for ϕ = -54° and ϕ = +54°, respectively. Note from the flow visualization that these fin positions show a case where the fin is in the path of each vortex (ϕ = ±22°) and a case where the fin is at the edges of the vortex system (ϕ = ±54°).

Figures 17 and Figure 18 also show that the flowfield is very similar for the four axial fin positions, with the only significant difference being the size of the vortices as they pass the fin. Hence the interactions between the fin and the vortex system at various azimuthal fin positions for stations 1, 2, and 4, exhibit similar characteristics to those at station 3. These similarities are seen by comparing Figures 21 and 22 (station 1, ϕ = ±22° and ϕ = ±54°, respectively), Figures 23 and 24 (station 2, ϕ = ±22° and ϕ = ±54°, respectively), and Figures 25 and 26 (station 4, ϕ = ±22° and ϕ = ±54°, respectively) with Figures 19 and 20.

3.2.3 Azimuthal Fin Position Effects on the Symmetric Flowfield It is clear that the symmetry in the flowfield causes an interaction that is symmetric about the leeward ray with changing azimuthal fin position. Likewise, the effect of the azimuthal fin position on the structures and trajectories of the vortices is symmetric at equal azimuthal positions to either side of the leeward ray. Figures 27 and 28 show side and top views, respectively, of the vortex trajectories with the fin at ϕ = -54° for the same conditions and coordinate system as in Figures 9 and 10. Figures 29 and 30 show the same for ϕ = +54°. It is clear that at both azimuthal fin positions, for each axial fin location, the vortex trajectories remain symmetric until the vortices reach the fin section. At the fin section, in each case, the vortex on the same side of the body as the fin remains close to the body and moves away from the leeward ray and towards the fin. The vortex on the side of the body opposite the fin lifts away from the body, but also moves slightly towards the leeward ray. These four figures show that there is no apparent effect of the azimuthal fin position on

the trajectories of the vortices upstream of the fin section. However, for all four axial fin locations, the trajectories change at the fin section.

Figures 31 through 34 show cross-sectional flow-visualization sequences at ϕ = +54° for the four axial fin locations. Figures 5 through 8 show the corresponding flow-visualization sequences at ϕ = 0°. These figures will show if any upstream influence of the azimuthal fin position on the structures of the vortices exists. In Figure 31, the fin is at station 1. This figure shows no change in the structures of the vortices until they reach the leading edge of the fin (x/d = 2.6). At this location, and at the following two locations, the near-side vortex is greatly distorted by the presence of the fin section. It appears that at axial locations ahead of fin station 1, the vortices are not affected by the azimuthal fin position. Figures 32, 33, and 34, where the fin is at stations 2, 3, and 4, respectively, show similar results. In these figures, at axial locations ahead of fin's leading edge, the vortices appear very similar to those shown at the same axial locations in the flow visualizations at ϕ = 0°. The slight differences between the near- and far-side vortices in some of the views is due to slight differences in the positions of the smoke wires upstream of the model.

3.3 Effects of the Interaction

3.3.1 Normal-Force Coefficients on the Fin. The effects of the vortex system are best shown by studying the forces on the fin. When the fin is positioned on the leeward ray of the model, the forces on each side of the fin have the same magnitude and are opposite in direction, due to the symmetry of the flowfield. As the azimuthal position of the fin is changed, however, the forces on each side of the fin due to the mean flow are no longer equal, and a net force and rolling moment are created. Calculations using potential-flow theory with no separation result in a total normal force coefficient (C_{fi}) on the fin that exhibits a nearly sinusoidal variation with azimuthal fin position. The coefficient is zero when the fin is positioned along either the leeward ray or the windward ray of the model, reaches a maximum approximately 90° from the windward ray, and is at a minimum approximately 90° from the leeward ray (Mendenhall & Perkins, 1989). Therefore, the magnitude of the total normal force on the fin at a given azimuthal position to one side of the leeward ray should be equal to the magnitude of the total normal force on the fin at the

same azimuthal position on the other side of the leeward ray. However, these forces will act in opposite directions. For the coordinate system defined in Figure 3, $C_{ft} = 0$ at $\phi = 0°$ and 180°. The maximum force in the positive direction should occur near $\phi = -90°$, and the maximum force in the negative direction should occur near $\phi = +90°$. The actual flowfield, however, is separated and contains the vortex system, and the effect of each vortex on the forces changes as the azimuthal position of the fin changes. Therefore, any differences between the forces obtained experimentally and the potential flow results may be attributed to the interaction of the fin with the vortex system.

Figure 35 shows the variation of C_{ft} with ϕ for $\alpha = 30°$, $Re_d = 6000$, at each of the four fin stations. Also shown are the components for the near-side and far-side surfaces (C_{fn} and C_{ff}, respectively). The outward normal to the near side of the fin is the positive direction for the force coefficients. For each fin station, the forces are nearly perfectly anti-symmetric about $\phi = 0°$, where $C_{ft} = 0$ as expected. Also, $C_{ft} = 0$ at $\phi = \pm 180°$ in each case. At azimuthal angles toward the far side of the leeward ray (negative ϕ), the forces act on the fin in the positive direction. At azimuthal angles toward the near side of the leeward ray (positive ϕ), the forces act on the fin in the negative direction. Each C_{ft} curve is approximately sinusoidal; however, three pairs of peaks are present. Each pair consists of a peak at some negative azimuthal angle and a corresponding peak at the complimentary positive azimuthal angle. The two peaks in each pair correspond to forces that are identical in magnitude, but opposite in direction. One pair of peaks is seen in each case at about $\phi = \pm 49°$. A second pair is seen at about $\phi = \pm 108°$, and a third, smaller pair of peaks occurs at about $\phi = \pm 151°$. Since the variation in C_f is similar at each axial fin station, and we have shown in Figures 19 through 26 that the interaction is similar at each axial fin location with varying azimuthal fin position, the case with the fin at station 3 ($(x/d)_f = 7.1$) and $Re_d = 6000$, shown in Figure 35(c), is presented in detail. This case shows all the important features of the interaction, and provides a base from which the effects of change in fin axial location and Reynolds number can be seen.

The pair of peaks at $\phi = \pm 108°$ represent the maximum positive and negative forces on the fin due to the mean flow, not changes due to the vortex system. The surface

pressure contour plots in Figure 36 substantiate this conclusion. Figures 36(a), 36(b), and 36(c) show the pressure contours on both surfaces of the fin at azimuthal fin positions of $\phi = +97°$, $+108°$, and $+119°$, respectively. All other conditions are the same as in Figure 35(c). The near side of the fin in these figures is the windward side, and the far side of the fin is the leeward side. At these azimuthal angles, the fin is in the mean flow and not affected by the vortex system. There is very little change in the pressure distributions on the fin over this range of angles. The large low-pressure cell due to flow separation on the leeward side and the high pressure on the windward side of the fin combine to create the large forces on the fin seen over this range of angles in Figure 35. Since the flowfield is symmetric, the pressure contour plots for $\phi = -97°$, $-108°$, and $-119°$ are very similar, although in this case, the near side is leeward and the far side is windward.

The most interesting pair of peaks occurs at about $\phi = \pm 49°$. These features are attributable to interaction between the fin and the vortex system. Between these peaks, over the range $\phi = -49°$ to $+49°$, the total force on the fin is changed by the presence of the vortex system. At azimuthal angles beyond this range, the effects of the vortex system diminish. This conclusion is established by studying the flow visualization, surface-pressure contour plots, and spanwise pressure distributions for azimuthal fin positions in this range. Figure 37 shows a sequence of surface-pressure contours and the corresponding flow-visualization photographs, taken in a cross-sectional plane at $x' = 2.4$, for a range of azimuthal angles ϕ. Again, all conditions are the same as for Figure 35(c). (Recall that Figures 5 and 15 showed this information for $\phi = 0°$.) Figure 37(a) shows that at $\phi = +11°$, the near-side vortex is greatly distorted by the fin, although the vortex core is visible on the near side of the fin. The far-side vortex remains coherent and positioned slightly to the far side of the leeward ray. The pressure contours on the far-side surface resemble those at $\phi = 0°$, except for the beginning of a second low-pressure region about half way up the span, reflecting the influence of the near-side vortex on this surface. A comparison of Figures 14 and 37(a) shows that the signature of the near-side vortex has become weaker in the pressure contours on the near-side surface. At $\phi = +22°$ (Figure 37(b)), the near-side vortex core has moved to the far side of the fin. It is still greatly distorted by the fin. The far-side vortex remains coherent and in the same position. At this

azimuthal position, the pressure contours show that the far side of the fin is affected by both vortices, and the effects of the near-side vortex on the near side of the fin decrease further. Figure 37(c) represents $\phi = +32°$. The near-side vortex is still very distorted and the far-side vortex is unchanged. Both vortices have an effect on the far side of the fin; the two low-pressure signatures seen at $\phi = +22°$ have merged into a single, strong low-pressure cell on the far side of the fin. Also, the near-side vortex no longer has an effect on the near side of the fin. In Figure 37(d), where $\phi = +43°$, the fin is no longer directly in the path of the near-side vortex. The near-side vortex is less distorted, but still incoherent. The core is seen clearly over the far-side surface. The far-side vortex is unchanged, but is located relatively further away from the fin, so that its effect on the pressure distribution is diminished. The relative location of the near-side vortex at this fin position is almost the same as that of the far-side vortex at $\phi = 0°$. The dominant influence on the far-side pressure distribution is now due to the near-side vortex. A comparison of the far-side pressure distributions in Figures 37(d) and 15 show similar signatures, although the contours are more diffuse at $\phi = +43°$. The near side of the fin at this azimuthal position sees only the external flow; it is not affected by the vortex system. In Figure 37(e), where $\phi = +54°$, the near-side vortex remains distorted and slightly incoherent, while the far-side vortex appears to have grown slightly in size. This increase in size is due to increased flow around the far side of the body. The fin poses an obstacle to the flow on the near side of the body, shifting the windward stagnation line towards the far side. The fin is farther away from the vortex system at this position, and the effects of the vortex system on the far side of the fin are greatly decreased. The near-side pressure contours are largely unchanged. Finally, in Figure 37(f), where $\phi = +65°$, the effects of the vortex system have diminished, and external flow dominates. The pressure distributions change very little beyond this position.

Figure 38 shows a series of spanwise pressure distributions on the far (leeward) and near (windward) sides of the fin for the same azimuthal fin positions and flow conditions as in Figure 37. These plots show in more detail the influence of each vortex on the fin surface pressure. At $\phi = 0°$, the pressure distributions on the far and near sides of the fin are identical as expected. The vortices are at equal distances from opposite sides of

the fin. At $\phi = +11°$, a second suction peak begins to form near the tip of the fin on the far side. This indicates that the near-side vortex is beginning to affect the pressure on the far side of the fin. The suction peak in the near-side pressure distribution is diminished, indicating a reduced effect of the vortex on this side of the fin. At $\phi = +22°$, the suction peak near the fin-body junction has decreased in magnitude and extent on the far side of the fin, while the suction peak near the tip is larger. This indicates the increasing effect of the near-side vortex on the far side of the fin as the vortex moves to that side of the fin, and the decreasing effect of the far-side vortex as the fin moves further away. The effect of the near-side vortex on the near side of the fin is small at this angle. The far-side pressure distribution at $\phi = +32°$ shows that the suction peak associated with the near-side vortex is larger and closer to the fin-body junction, while the suction peak associated with the far-side vortex continues to shrink. The near-side vortex has moved between the fin and the far-side vortex as the fin moves to the near side. The effect of the near-side vortex on the near side of the fin has diminished, and the pressure distribution on the near side of the fin at this angle and beyond is indicative of the mean flow, high near the leading edge and steadily decreasing in the chordwise (x') direction. At $\phi = +43°$, the fin is further away from the pair of vortices, and their effect on the far side has decreased. At $\phi = +54°$ and beyond, the vortices no longer interact with the fin, and the pressure distributions vary little in the spanwise and chordwise directions. These plots clearly show the effects of each individual vortex on the fin surface pressure as well as the azimuthal fin positions where the effects of the vortices diminish and the mean flow dominates.

Figure 35 shows a third pair of peaks in the C_{ft} curve at about $\phi = \pm 151°$. Since these peaks occur at such high roll angles, they are believed to be a feature of the external flow around the fin. The C_{fn} and C_{ff} curves in Figure 35 show that these peaks are caused by a change in the forces on the leeward side of the fin. Figures 39(a), 39(b), and 39(c) show surface-pressure contours for $\phi = +140°$, $+151°$, and $+162°$, respectively. These show a large change in the pressure on the far side of the fin which, in this case, is the leeward side of the fin. Figure 39(b) shows a strong low-pressure cell at the leading edge

and a sudden increase in pressure in the chordwise direction. In Figure 39(c), this chordwise increase in pressure is even greater.

3.3.2 Determining the Range of Interaction. A better understanding of the forces on the fin can be gained by studying the contributions to the normal forces on each side of the fin separately. Figure 35 shows that when the fin is positioned at negative azimuthal angles, peaks are present in the C_{fn} curve which correspond to the peaks in the C_{ft} curve described earlier. However, the C_{ff} curve is smooth and convex past a certain azimuthal angle. The opposite is true for positive azimuthal angles, where the C_{fn} curve is smooth and concave past a certain azimuthal angle and the C_{ff} curve exhibits the three peaks. These azimuthal angles represent the limits of the interaction between the fin and the vortex system. Once the fin is positioned past a certain azimuthal angle, the windward side of the fin is not affected by the vortex system. The leeward side of the fin, however, is affected by the vortices over a wider range of azimuthal angles. Over a certain range of azimuthal angles to either side of $\phi = 0°$, the vortex system interacts with both sides of the fin. By examining the C_{fn} and C_{ff} curves in Figure 35, the pressure-contour plots in Figure 37, and the spanwise pressure distributions in Figure 38, the range of azimuthal angles over which the vortex system interacts with each side of the fin can be defined. For this case, as the fin is moved toward the near side, Figures 37(b) and 37(c), along with Figures 35 and 38, show that interaction with the near side of the fin ends around $\phi = +32°$. Figures 37(d) and 37(e), along with Figures 35 and 38, show that interaction with the far side of the fin ends around $\phi = +54°$. As the fin is moved toward the far side, a similar analysis of the pressure data and Figure 35 shows that interaction with the far side ends around $\phi = -32°$ and interaction with the near side ends around $\phi = -54°$. Therefore, with the fin at station 3 for $\alpha = 30°$ and $Re_d = 6000$, the near side of the fin is influenced by the vortex system over the range $-54° < \phi < +32°$. The far side of the fin is influenced by the vortex system over the range $-32° < \phi < +54°$. The changes in this range of interaction with fin axial location and Reynolds number will be discussed later.

3.4 Effects of Change in Fin Axial Location

As mentioned earlier, data were taken at four different axial locations of the fin. The detailed discussion of the effects of the interaction in the previous section has concentrated on the third location. We now turn to an examination of the differences in the interaction between the vortex system and the fin that occur as the axial location of the fin is changed. The flow visualizations of Figures 5, 6, 7, and 8 show that for $\alpha = 30°$, the vortices remain symmetric, grow in size, become less coherent, and move slightly away from the body as they progress down the model. Figure 40 shows C_{ft} versus azimuthal angle at the four different axial locations for the three Reynolds numbers based on model diameter studied. The overall force coefficients increase in magnitude as $(x/d)_f$ increases for each of the Reynolds numbers. Also, for each Re_d, the magnitudes of the peaks associated with the vortex interaction increase only slightly. As the fin moves further down the axis from the nose, the effect of the vortex system on the forces on the fin does not change substantially. It should also be noted that as fin axial location changes, the peaks occurring at high azimuthal angles remain in the same position and at nearly the same magnitude for each fin location at each Re_d. This is further evidence that they are features of the external flow, rather than due to the vortex system. Figure 41 shows the change in range of interaction of the vortex system with increasing $(x/d)_f$ for each Re_d. The dark shaded area labeled "Both" indicates the range of azimuthal angles over which both sides of the fin are affected by the vortex system. Likewise, the shaded areas labeled "Near" and "Far" indicate the range of azimuthal angles over which the specified side of the fin alone is affected by the vortex system. It should be noted that these ranges of interaction were determined qualitatively from the surface-pressure contours and spanwise pressure distributions at the four axial fin locations as described in the previous section. The results agree with the locations of the peaks in the total normal force results described earlier. Figure 41 shows that the interaction is symmetric for all axial locations for the three Reynolds numbers studied. Figures 41(a) and (b), where Re_d = 6000 and 20000 respectively, show that the overall range of interaction increases slightly beyond $(x/d)_f$ = 7.1, and the range in which both sides of the fin interact with the vortex system increases

as $(x/d)_f$ increases. Figure 41(c) shows that the overall range of interaction increases for each $(x/d)_f$ at $Re_d = 34000$. This growth in range is due to the growth of the vortices with increasing x/d.

3.5 Effects of Increasing Reynolds Number

Figure 42 shows the influence of Reynolds number on the variation of C_{ft} with azimuthal angle for each of the four axial fin locations. As Re_d increases, the magnitudes of the force coefficients on the fin increase at each fin location, however the increase is larger from $Re_d = 6000$ to 20000 than from 20000 to 34000. Figure 43 shows the change in range of vortex interaction with increasing Re_d for each of the axial fin locations. Note that these results come from data at only three Reynolds numbers. At stations 2, 3, and 4, Figures 43(b), (c), and (d) respectively, the range of interaction appears to increase with increasing Re_d. Figure 43(a) shows that when the fin is at station 1 ($(x/d)_f = 2.6$), the overall range of interaction increases only at lower Reynolds numbers, and the range over which both sides of the fin are effected does not appear to change at all. This may be because only three Reynolds numbers were studied. In general, it appears that the range of interaction increases slightly as Re_d increases for the Reynolds numbers studied, and as $(x/d)_f$ increases, the increase in range is more pronounced.

CHAPTER IV
ASYMMETRIC FLOWFIELD INTERACTION

4.1 Flowfield Development

When the angle of attack in increased to 45°, the flowfield changes significantly. The vortex system becomes asymmetric, with the vortex on one side of the body separating from the body at a lower x/d location than the other vortex. The latter remains attached to the body and generally grows much larger than the first vortex, until it also separates from the body. This was shown by the results described in Part II of this report, using the same model with no fin section installed. The following results will show that when the fin section is installed at certain axial locations, significant changes occur in the flowfield.

Figure 44 shows the development of the vortex system when the fin is placed at axial station 3 ($(x/d)_f$ = 7.1). As in Figure 5, views at different cross-sectional planes perpendicular to the model axis are shown. The asymmetry in the flowfield with the fin at this axial location is clear. The vortices become asymmetric very close to the nose tip. At x/d = 1.0, the vortices are just beginning to form. At x/d = 1.8, the vortices are very coherent and the asymmetry is evident. The near-side vortex is clearly larger than the far-side vortex. This trend continues in the view at x/d = 2.6. By x/d = 4.9, the near-side vortex is less coherent, distorted, and is beginning to lift away from the body. The vortex on the far side remains coherent, attached to the body, and continues to grow. At x/d = 7.1, the leading edge of the fin, the near-side vortex is separated from the body and is much less coherent. The far-side vortex is much larger in size and still attached to the body. Its core is now located directly above the leeward ray of the model. At x/d = 8.8, the middle of the fin, the far-side vortex envelops the fin. It is even less coherent, slightly distorted, and its core is hard to locate. Also, it has separated from the body. The near-side vortex changes little and is located further away from the body. At the trailing edge of the fin, x/d = 9.4, the near-side vortex is faint and far away from the body. The far-side vortex has grown. It is separated from the body, and has been distorted further by the presence of the fin. At this angle of attack and fin location, the fin interacts with the far-

side vortex to a much greater degree than with the near-side vortex. Because the latter is weak, and far from the body at axial locations near the fin, its effect on the fin is minimal.

In Figure 45, the fin is further from the nose at station 4 ($(x/d)_f = 9.4$), and the flowfield is very similar to that for station 3 through x/d = 7.1. At x/d = 9.4 (leading edge of the fin), the far-side vortex is very large and separated from the body. A recirculation region exists between the far-side vortex and the body. The near side vortex is weak and far from the body at this location. In the views at the middle and trailing edge of the fin, x/d = 11.1 and 11.7 respectively, the near-side vortex is out of the field of view. The far-side vortex has grown in size, is less coherent due to contact with the fin, and has moved rapidly away from the body. It is clear that the far-side vortex dominates the interaction with the fin at this axial location, and the near side vortex no longer interacts with the fin.

When the fin is located closer to the nose at station 2 ($(x/d)_f = 4.9$), only a moderate degree of asymmetry is present in the wake vortices as they contact the fin section. The flowfield development for this case is shown in Figure 46. Ahead of the fin, the asymmetric development is clear and similar to the two previously described cases. When the vortices contact the fin at this location, however, both vortices are much smaller and closer to the body. The view at x/d = 4.9 (leading edge of the fin) shows that the near-side vortex has just started to separate from the body. At x/d = 6.6 and 7.1 (middle and trailing edge of the fin, respectively), the far-side vortex is greatly distorted by the presence of the fin. With the fin at this location, both vortices interact substantially with the fin.

Large changes in the flowfield result when the fin is located at station 1 ($(x/d)_f = 2.6$). Figure 47 shows that the vortices develop and remain symmetric as they pass the fin. The flowfield is very similar to that shown in Figure 8 where $\alpha = 30°$, however the vortices are larger in size. At this location, the fin is directly behind the nose section of the model. Its location and size greatly affect the formation of the tip vortices, causing the flowfield to develop symmetrically.

Figures 48 and 49 show side and top views, respectively, of the vortex center trajectories for $\alpha = 45°$, $Re_d = 6000$, and $\phi = 0°$ for each axial fin location. In Figure 48,

the last two plots, $(x/d)_f = 7.1$ and $(x/d)_f = 9.4$, show that the near-side vortex separates from the body around x/d = 4.9. The far-side vortex remains attached to the body until about x/d = 7.1. Once a vortex separates, it quickly moves away from the body. When the fin is at station 4 ($(x/d)_f = 9.4$), the center of the far-side vortex passes the fin outboard of the fin tip, and the near-side vortex is out of the field of view. When the fin is at station 3 ($(x/d)_f = 7.1$), the center of the far-side vortex passes across the central portion of the fin. The near-side vortex passes close to the leading edge of the fin tip, but rapidly moves away further downstream. The trajectories for station 2 ($(x/d)_f = 4.9$) are slightly different. The far-side vortex appears to remain closer to the body until just before the trailing edge of the fin. The near-side vortex is further away from the body at x/d = 4.9 than when the fin is at stations 3 and 4, but as it passes the fin, it does not move away from the body as quickly. At this fin station, the centers of both vortices pass across the central portion of the fin. Finally, for station 1 ($(x/d)_f = 2.6$), the trajectories of the near- and far-side vortices are nearly identical, indicating the symmetry in the flowfield with the fin at this axial location. Both vortices pass the fin close to the fin-body junction, similar to the $\alpha = 30°$ case shown in Figure 9.

In Figure 49, the first plot, $(x/d)_f = 2.6$, again shows the vortex trajectories are symmetric. The second plot, where $(x/d)_f = 4.9$, shows that the far-side vortex moves toward the leeward ray of the model (y/d = 0) as the near-side vortex begins to separate from the body. When it reaches the fin section, it moves away from the leeward ray and passes the fin on the far side. When the fin is at station 3 ($(x/d)_f = 7.1$) and station 4 ($(x/d)_f = 9.4$), the far-side vortex once again moves to the leeward ray as the near-side vortex separates, however in these cases, it remains there, and appears to pass the fin on the near side.

Recall that these trajectories were determined from the cross-sectional flow visualization photographs. It should be noted that it was difficult to determine the exact center of the far-side vortex at the middle and trailing edge of the fin in the last two cases, because the vortex was greatly distorted due to contact with the fin, as seen in Figures 44 and 45, at x/d = 8.8 and 11.1, respectively. Both Figures 48 and 49 show that at this angle

of attack, the axial location of the fin section has a significant effect on the development of the flowfield.

Figures 50 through 53 combine the cross-sectional flow visualizations with the vortex trajectories to show the development of the flowfield in three-dimensional views for $\alpha = 45°$, $\phi = 0°$, and $Re_d = 6000$. As for the $\alpha = 30°$ case, the larger view is from the near side of the model, and the smaller view is from the far side. Once again, these views provide an excellent overall picture of the flowfield structure.

4.2 Characteristics of the Interaction

4.2.1 Changes in Vortex Signatures with Increasing Flowfield Asymmetry. In the previous section, it was shown that the structure of the flowfield at the fin section is significantly different for each of the four axial fin locations. These differences result in interactions with different features in each case. Figure 54 shows the surface pressure-coefficient contours on both sides of the fin at $\phi = 0°$ and $Re_d = 6000$ for the four fin stations. As in Figure 5, flow is from left to right, the fin-body junction is at $y' = 0$, and the leading and trailing edges of the fin are at $x' = 0$ and $x' = 3.25$, respectively. At station 1, the C_p contours on the near and far sides of the fin are nearly identical, indicating the symmetry in the flowfield at this axial fin location. The contours are very similar to those shown in Figure 17 where $\alpha = 30°$. The vortices, which pass on either side of the fin slightly inboard of half span, create a strong low-pressure region near the fin-body junction with a rapid spanwise increase in pressure to about half span. The next plot is for fin station 2. The C_p contours on either side of the fin now show slight differences. On the far side of the fin, there is a low-pressure region near the fin-body junction that is larger and stronger than the one on the near side. This is a result of the moderate degree of asymmetry present in the flowfield. As shown in Figure 46 at $x/d = 6.6$, the near-side vortex at this axial location is less coherent and beginning to separate from the body, causing a weaker signature in the near-side pressure distribution. The far-side vortex, on the other hand, is larger, stronger, and attached to the body, resulting in the strong signature seen in the far-side pressure distribution. When the fin is at station 3 (Figure

54(c)), the pressure distributions on the two sides of the fin are significantly different, due to the larger degree of asymmetry in the flowfield at this axial location. This is in sharp contrast to the symmetric pressure distributions at $\alpha = 30°$ (Figure 15). On the far side of the fin, the pressure is low near the fin-body junction due to separation of the flow from the body and a secondary recirculation. The pressure increases to a high-pressure region at half span. The view at x/d = 8.8 in Figure 44 shows inward flow toward the fin at this location. Further outboard of this location, the pressure decreases due to the presence of the far-side vortex. On the near side of the fin, the pressure is low near the fin-body junction, and steadily increases in the spanwise direction to a region of higher pressure at the fin tip, caused by fluid from the far-side vortex flowing around the tip of the fin. No significant effect of the weak near-side vortex is seen. The fourth plot, representing the pressure distribution on the fin at station 4, is similar to that at station 3. The near-side vortex is much further from the body at this axial location, and does not influence the pressure on the fin. Because the large far-side vortex is separated from the body, as shown in Figure 45 at x/d = 11.1, the high-pressure region at half span is located further outboard than in the previous plot. There is a strong recirculation between the far-side vortex and the body. This results in the low-pressure region and rapid spanwise increase in pressure near the fin-body junction on the near side of the fin.

Figure 55 shows five spanwise slices of the pressure data on the near and far sides of the fin for each of the four axial fin locations. For station 1 ($(x/d)_f = 2.6$), the distributions are similar to those shown in Figure 18 ($\alpha = 30°$) at $(x/d)_f = 2.6$ and 4.9. The near- and far-side distributions are nearly identical, confirming the symmetry in the flowfield at this axial location. The suction peak near the fin-body junction ($y' = 0.375$) on each side is the influence of the vortex above each surface. The near-side pressure distribution at $(x/d)_f = 4.9$ in Figure 55 is very similar to that in Figure 18 at $(x/d)_f = 7.1$, while the corresponding far-side pressure distribution in Figure 55 is very similar to that in Figure 18 at $(x/d)_f = 9.4$. Both show a suction peak at $y' = 0.375$, but the peak on the near side diminishes in the chordwise direction faster than the peak on the far side. Also, the far-side suction peak is greater in spanwise extent at lower x' locations. At this axial

location for $\alpha = 45°$, where the flowfield is asymmetric, the near-side vortex is smaller and weaker than the far-side vortex. This is comparable to the difference between the flowfields at $(x/d)_f = 7.1$ and $(x/d)_f = 9.4$ for $\alpha = 30°$, where the vortices are close to the body in both cases, but are smaller in size at $(x/d)_f = 7.1$ than they are at $(x/d)_f = 9.4$. The pressure distributions in Figure 55 for station 3 ($(x/d)_f = 7.1$) show some significant differences. The pressure increases steadily in the spanwise and chordwise directions on the near side of the fin with a weak minimum at $y' = 0.375$. The far side distribution shows the increase in pressure at around half span and subsequent decrease in pressure toward the tip described earlier in Figure 54. At the fin-body junction in the separated region beneath the vortex, the pressure decreases in the chordwise direction; while at the tip, the behavior is similar to that on the near side, with the pressure increasing in the chordwise direction. At station 4 ($(x/d)_f = 9.4$), the near-side pressure distribution shows a low-pressure area near the fin-body junction due to the strong secondary recirculation under the far-side vortex. The far-side distribution is similar to the one for station 3, however there is a greater chordwise variation in pressure near the tip of the fin.

4.2.2 Effects of Azimuthal Fin Position on the Asymmetric Flowfield. As the azimuthal position of the fin is changed, the features and effects of the interaction between the vortex system and the fin at each axial location also change. At all axial fin locations, changing the azimuthal position of the fin changes the relative distance between each vortex and the fin surface. The trajectories of the vortices are also affected by the azimuthal position ot the fin, especially at the fin axial locations close to the nose, stations 1 and 2. This is shown by the vortex center trajectories plotted in Figures 56 through 59. Figure 56 shows the side view of the trajectories with $\phi = -54°$ for each of the four axial fin locations. No data is shown for the far-side vortex in the first plot ($(x/d)_f = 2.6$) because this vortex was difficult to see in the flow-visualization photographs. Comparing this figure to Figure 48 ($\phi = 0°$), we see that the distance of the near-side vortex trajectory from the body is the same for station 1. At station 2 ($(x/d)_f = 4.9$), however, both the near-and far-side trajectories are different. The near-side vortex moves further away from

the body once it separates, and the far-side vortex remains close to the body and moves closer at the trailing edge of the fin. At station 3 and 4 ($(x/d)_f$ = 7.1 and 9.4, respectively), the trajectories of both vortices appear unchanged. The top views for ϕ = -54° in Figure 57, when compared to Figure 49 (ϕ = 0°), show that at station 1, the near-side vortex moves across the leeward ray to the far side of the model at the fin section. At station 2, the near-side vortex, once it has separated, moves further toward the near side than it did for ϕ = 0°. The far-side vortex moves to the leeward ray ahead of the fin section, but then moves back toward the far side at the fin section. At stations 3 and 4, the near-side vortex trajectories appear the same as in Figure 49; however, there are slight changes in the far-side vortex trajectories at the middle and trailing edge of the fin in both cases. At station 3, the far-side vortex suddenly moves from the near side of the leeward ray back toward the far side at the trailing edge of the fin. At station 4, the far-side vortex is slightly further toward the near side at the fin section than it was at ϕ = 0°.

Figure 58 shows the side view of the vortex center trajectories at the four axial fin locations for ϕ = +54°. Again, these are compared to the trajectories at ϕ = 0° shown in Figure 48. At station 1, the far-side vortex trajectory appears unchanged, while the near-side vortex lifts further from the body between x/d = 2.6 and 4.9. At station 2, the trajectories of both vortices are similar to those at ϕ = 0°; however, the near-side vortex is slightly farther from the body. At station 3, the trajectories of both vortices are very similar to those at ϕ = 0° up to the trailing edge of the fin, where the far-side vortex, which was moving away from the body, begins to move back toward the body. At station 4, the trajectories of both vortices appear unchanged by the azimuthal position of the fin. Figure 59 shows the top view of the trajectories at each fin location for ϕ = +54°. A comparison with the trajectories at ϕ = 0° shown in Figure 49 shows that at station 1, the paths of both vortices are changed by the azimuthal position of the fin. Both vortices move toward the near side of the body at the fin section. Similar changes are seen at station 2, however it appears that the far-side vortex is affected to a greater degree than the near-side vortex. At stations 3 and 4, the near-side vortex trajectories appear unchanged, however the far-side vortex trajectories show changes at the middle and trailing edge of

the fin section. At station 3, the far-side vortex moves further to the near side over the last half of the fin section. At station 4, the far-side vortex moves from the near side of the model back toward the leeward ray at the trailing edge of the fin.

Figures 56 through 59 also show that there is very little change in the trajectory of either vortex ahead of the fin. This indicates that there is no upstream influence of the azimuthal position of the fin on the trajectories of the vortices. The paths of the vortices are only altered once they reach the fin section. While there is no upstream influence of the fin on the trajectories of the vortices, the structures of the vortices upstream of the fin section do show some changes. Figures 60 through 67 show cross-sectional flow visualization sequences at $\phi = \pm 54°$ for the four axial fin locations. The views are the same as in Figures 44 through 47, in which the fin is at $\phi = 0°$. In Figures 60 and 61, the fin is at axial station 1. Recall that the flowfield is symmetric with the fin at $\phi = 0°$ for this axial location. The slightly different appearances between the near-side vortex at $\phi = -54°$ and the far-side vortex at $\phi = +54°$ are due to slight differences in the positions of the smoke wires to either side of the upstream stagnation line. When the fin is at $\phi = -54°$ (Figure 60), the far-side vortex is barely visible at all five x/d locations, again due to the smoke-wire position. The near-side vortex at x/d = 1.0 through 2.6 appears similar to the $\phi = 0°$ case shown in Figure 47. At x/d = 4.3 and 4.9, the middle and trailing edge of the fin, respectively, the near-side vortex is much larger, and its center has moved across the leeward ray to the far side of the model. The structure of the far-side vortex at $\phi = +54°$ in Figure 61 is similar. Here, the near-side vortex is visible. At x/d = 1.0 through 2.6, it is smaller and less coherent than the far-side vortex. At x/d = 4.3 and 4.9, it is greatly distorted as it comes in contact with the fin. Details of the changes in the flowfield at the fin, as the azimuthal fin position is changed for all four axial fin locations, will be discussed later in this chapter. This section will concentrate on the upstream x/d locations. The first two x/d locations are upstream of the fin, and the azimuthal position of the fin to one side clearly affects the structure of the vortex on the same side of the body as itself.

Figures 62 and 63 show the development of the flowfield at $\phi = -54°$ and $+54°$, respectively, for fin station 2. Figure 46 shows the corresponding sequence for $\phi = 0°$. Recall that with the fin at this axial location, a moderate degree of asymmetry is present in

the flowfield. In Figure 62, the vortices are unchanged at x/d = 1.0 and 1.8. At x/d = 2.6, however, the near-side vortex appears slightly distorted, but still coherent. Along the fin section, from x/d = 4.9 to 7.1, the far-side vortex is much more distorted than it was when $\phi = 0°$, and the near-side vortex is larger in size and separates from the body. In Figure 63, the vortices in the views at x/d = 1.0 and 1.8 are again similar to the $\phi = 0°$ case. At x/d = 2.6, the near-side vortex is slightly distorted but coherent. Along the fin section, the near-side vortex separates from the body while the far-side vortex grows in size and moves across the leeward ray to the near side of the model. The azimuthal position of the fin has less of an upstream influence at this axial fin location, but the effect is clear at x/d = 2.6 in both figures.

Figures 64 and 65 show the flowfield development at $\phi = -54°$ and $+54°$, respectively, for the third axial fin location. Comparison with the $\phi = 0°$ case in Figure 15 shows that at x/d locations upstream of the fin (x/d = 1.0 through 4.9), no significant differences are present in the structures of the vortices. Similar behavior is observed in Figures 66 and 67, which show the flowfield development at $\phi = -54°$ and $+54°$, respectively, for fin station 4 (Figure 45 shows the corresponding $\phi = 0°$ case). At x/d locations upstream of the fin section (x/d = 1.0 through 7.1), no significant upstream effects are seen. As mentioned earlier, the flowfield changes at the fin section for different azimuthal fin positions will be discussed in detail later in this chapter. These figures show that when the fin is at axial locations farther from the nose, its azimuthal position has no upstream effect on the structures of the vortices. However, as it is positioned axially closer to the nose, an increasing degree of influence on the vortex structures is seen.

4.3 Effects of the Interaction

The results presented in the previous section show that the flowfield, and hence the interaction between the fin and the vortex system, are significantly different at each of the four axial fin locations. At the first location (station 1, $(x/d)_f = 2.6$), the vortex system develops symmetrically due to the presence of the fin close to the nose. At the second location (station 2, $(x/d)_f = 4.9$), the flowfield develops asymmetrically, but since the fin is

still relatively close to the nose, the degree of asymmetry is small and both vortices remain close to the body throughout the interaction. At the third location (station 3, $(x/d)_f = 7.1$), a larger degree of asymmetry exists in the flowfield. The near-side vortex separates from the body ahead of the fin section, while the far-side vortex remains attached to the body until it reaches the fin and grows very large. The interaction is dominated by the far-side vortex, but the near-side vortex is still close enough to the fin to possibly have a small effect. Finally, at the fourth location (station 4, $(x/d)_f = 9.4$), the flowfield is dominated by the large, far-side vortex, which begins to separate from the body ahead of the fin section. The near-side vortex is very far from the body in this case, and does not interact with the fin. The details of the interaction for selected ranges of azimuthal fin positions at each of these four axial fin locations are presented in the following sections.

Figure 68 shows the total normal-force coefficient (C_{ft}) variations with azimuthal fin position for each of the four axial fin locations at $Re_d = 6000$. The components for the near-side and far-side surfaces (C_{fn} and C_{ff}, respectively) are also shown. As expected, distinct differences are apparent between the four axial fin locations. Recall that the corresponding plots at $\alpha = 30°$ were shown in Figure 35. For the results of Figure 68(a), the fin is at station 1. This plot shows that the C_{ft} variation with ϕ is almost perfectly anti-symmetric about the leeward ray ($\phi = 0°$), as it was at all axial fin locations for $\alpha = 30°$. This confirms that the flowfield is symmetric as it contacts the fin at this axial location. The coefficient is zero when the fin is on the leeward and windward rays of the model, and the variation is somewhat sinusoidal in nature. However, the variation is slightly different from those seen at $\alpha = 30°$. Recall that at $\alpha = 30°$, three pairs of peaks were seen. At fin station 1 for $\alpha = 45°$, we see one pair of large, broad peaks at about $\phi = \pm 65°$ and one pair of small peaks at about $\phi = \pm 162°$. The reasons for this difference will be discussed later. Again, as for $\alpha = 30°$, the two peaks in each pair are identical in magnitude, but opposite in direction.

The large pair of peaks at $\phi = \pm 65°$ indicate the effect of the vortex system on the normal force acting on the fin. This is shown by examining in detail the coefficient of pressure contour plots and the cross-sectional flow visualizations over this range of

azimuthal fin positions. Figure 69 shows a sequence of C_p contours and the corresponding flow-visualization photographs for a range of azimuthal angles on the near side of the model (positive ϕ). Since the flowfield is symmetric, azimuthal angles on the far side of the model (negative ϕ) show very similar results to the corresponding azimuthal angles on the near side and, therefore, will not be shown. Recall that Figures 47 (x/d = 4.3) and 54(a) show this information for $\phi = 0°$. All conditions in these figures are the same as in Figure 68(a). The photograph in Figure 69(a), where $\phi = +11°$, shows that the near-side vortex is distorted by the fin, and its center, while in the shadow of the fin, still appears to be on the near side of the fin. The far-side vortex is more coherent than it was at $\phi = 0°$. The pressure contours are similar to those shown in Figure 54(a) ($\phi = 0°$), but on the near side, the low-pressure region at the fin-body junction is weaker. On the far side, there is a second smaller low-pressure region forming at $y' = 1.875$, indicating a small influence of the near-side vortex on the far side of the fin. At $\phi = +22°$ (Figure 69(b)), the flow visualization shows an incoherent accumulation of fluid on the far side of the fin tip, apparently part of the greatly distorted near-side vortex. The far-side vortex is larger and coherent, and its center is closer to the leeward ray. The pressure contours on the near side of the fin show a decreasing effect of the near-side vortex, and the contours on the far side of the fin show changes along the leading edge and the tip. This is due to the increasing influence of the near-side vortex on that side of the fin. Figure 69(c), where $\phi = +32°$, shows that the near-side vortex is beginning to re-form near the tip on the far side of the fin. The far-side vortex is larger and is centered along the leeward ray. The near-side vortex no longer effects the near side of the fin, as shown by the near-side pressure contours. The far-side contours show a strong low-pressure region along the leading edge at about half-span. This is the influence of the near-side vortex. The far-side vortex continues to significantly effect the pressure on the far side of the fin along the fin-body junction. At $\phi = +43°$ (Figure 69(d)), the near-side vortex is spread out along the far side of the fin, and the far-side vortex has moved across the leeward ray to the near side of the model. The pressure contours on the far side indicate the decreased effect of the far-side vortex as the near-side vortex moves closer to the body, increasing its effect. The pressure

on the near side of the fin is representative of the external flow over the fin surface. At ϕ = +54° (Figure 69(e)), the near-side vortex is less spread out and has moved between the far-side vortex and the fin. The far-side vortex is still large and coherent, centered along the leeward ray of the model. The far-side pressure contours no longer show the large low-pressure region at the fin-body junction due to the far-side vortex. Only the more diffuse effect of the incoherent near-side vortex is seen. As the azimuthal angle of the fin is increased to ϕ = +65° (Figure 69(f)), the positions of the vortices remain essentially the same, and their relative distances from the fin surface increase. The pressure contours on the far side of the fin indicate that the near-side vortex has an effect that is large in extent, but less intense. The pressure contours on the far side of the fin at ϕ = +76° (Figure 69(g)) show that the effect of the vortex system has diminished greatly. The flow visualization shows that the fin is farther from the vortices, but the near-side vortex is still distorted and a portion of it makes contact with the fin. This trend continues at ϕ = +86° and +97° (Figures 69(h) and (i)), where the far-side pressure contours show very little change in pressure across the fin surface. The fin is no longer effected by the vortex system and the external flow dominates at these azimuthal positions. Note that there is no flow-visualization photograph for ϕ = +97° because no flow visualization was performed beyond $\phi = \pm 92°$.

The trends and details of the interaction are easier to see by looking at the spanwise pressure distributions on each surface of the fin at these same nine azimuthal positions. These, along with the spanwise pressure distribution at ϕ = 0°, which was shown earlier in Figure 55 ($(x/d)_f$ = 2.6), are shown in Figure 70. Each graph shows the spanwise pressure distribution at five positions along the fin chord (x'). The pressure distributions on the near side of the fin at each azimuthal fin position are shown in the left-hand column, and the far-side pressure distributions are shown in the right-hand column. Looking down each column from ϕ = 0° to ϕ = +97°, we can see how the pressure distributions change in both the spanwise and chordwise directions as the fin is moved to different azimuthal positions in the vortex system. The pressure distributions on the near and far sides of the fin at ϕ = 0° are nearly identical. There is a suction peak at about y' =

0.375 on each side, which decreases in magnitude as x' increases. This peak on each side is the signature of the vortex passing over each surface. As the fin moves further from the leeward ray, this suction peak in the near-side pressure distributions decreases in magnitude and spanwise extent through $\phi = +22°$, showing the decreasing effect of the near side vortex. Past this angle, the entire near-side vortex is on the far side of the fin. From $\phi = +32°$ to $\phi = +97°$, the near-side pressure distributions change little, and reflect the external flow across the fin surface. On the far side of the fin, the interaction is more complicated. At $\phi = +11°$, changes are seen in the distribution at $x' = 0.68$ and at the outboard end (higher y') of the distribution at $x' = 1.09$, both of which are close to the leading edge of the fin. This reflects the beginning of the influence of the near-side vortex on the far side of the fin. The suction peak at $y' = 0.375$, which is the effect of the far-side vortex, is still large in magnitude, but slightly smaller in spanwise extent. At $\phi = +22°$, this suction peak is much smaller in magnitude, indicating that the effect of the far-side vortex has decreased. A new suction peak at about $y' = 1.125$ has formed, indicating the increasing effect of the near-side vortex as is moves to the far side of the fin. The far-side pressure distributions at $\phi = +32°$ and $\phi = +43°$ are similar because the trajectories of the vortices are effected by the azimuthal position of the fin, as shown earlier in Section 4.2.2. Even though the fin is moving further from the leeward ray, the relative distance between it and the vortex system is not changing. These two pressure distributions show the large effect of the near-side vortex, which is now located on the far side of the fin, and the decreasing effect of the far-side vortex as the near-side vortex moves between it and the fin surface. At $\phi = +54°$ and $\phi = +65°$, the pressure distributions on the far side of the fin indicate that the far-side vortex no longer has an effect, and the effect of the near-side vortex is decreasing and moving closer to the fin-body junction. The trajectories of the vortices no longer change at these azimuthal angles, and the distance of the vortices from the fin is increasing as ϕ increases. Beyond $\phi = +76°$, the pressure on the far side of the fin changes little in the spanwise and chordwise directions, indicating that the interaction with the vortex system has ended.

From Figure 70, along with Figure 69, and the C_{fn} and C_{ff} variations in Figure 68(a), we can determine the range of azimuthal fin positions over which each side of the fin interacts with the vortex system. This process was explained in Section 3.3.2 for α = 30°. At this axial fin location (station 1, $(x/d)_f = 2.6$), for α = 45° and Re_d = 6000, the near side of the fin is influenced by the vortex system over the range $-70° < \phi < +32°$. The far side of the fin interacted with the vortex system over the range $-32° < \phi < +70°$. The overall range is symmetric about ϕ = 0°, like the ranges at each of the four axial fin locations for α = 30°. However, due to the effect of the azimuthal position of the fin on the vortex trajectories, this range is larger than any at α = 30°.

The pair of small peaks seen at about $\phi = \pm 162°$ in Figure 68(a) are similar to those seen at $\phi = \pm 151°$ in the four cases at α = 30° shown in Figure 35. These are features of the external flow around the fin, and are not due to the interaction with the vortex system.

The variations of the normal-force coefficients with azimuthal fin position for axial fin station 2 ($(x/d)_f$ = 4.9) are shown in Figure 68(b). The C_{ft} variation exhibits many irregularly spaced peaks over a large range of ϕ, but the overall variation is sinusoidal in nature. C_{ft} is no longer zero at ϕ = 0°, but is zero at $\phi = \pm 180°$. In order to help explain this unusual behavior, it is necessary to look in detail at the cross-sectional flow visualization and pressure-coefficient contours at certain azimuthal fin positions in this range. Figure 71 shows the C_p contours with the corresponding flow visualizations for twelve azimuthal fin positions to the near side of the leeward ray (positive ϕ). Note that no flow visualization is available beyond $\phi = \pm 92°$, so only the pressure contours are shown in the last four figures. Recall that Figures 46 (x/d = 6.6) and 54(b) show this information for ϕ = 0°. Comparing the sequence of flow visualization and C_p contours shown in Figure 71 with the sequence shown for fin station 1 in Figure 69, we see surprising similarities. Even though the flowfield, which was symmetric for fin station 1, is asymmetric for fin station 2, the trends and changes seen as the azimuthal fin position is changed are the same in the flow visualization and surface pressures. However, these changes are spread out over a much wider range of azimuthal fin positions at fin station 2. Figures 71(a) and (b), where

ϕ = +11° and +22°, respectively, are similar to Figure 69(a) (ϕ = +11°). The near-side vortex is on the near side of the fin and is distorted and incoherent. The far-side vortex is more coherent than at ϕ = 0°, and is positioned over the fin near the fin-body junction. The pressure contours on the near side show a decreased effect of the near-side vortex on that side of the fin, and the effect of the near-side vortex is now seen on the far side of the fin. Figures 71(c) and (d) (ϕ = +32° and +43°, respectively) are comparable to Figures 69 (b) and (c) (ϕ = +22° and +32°, respectively). The flow visualization in Figure 71(c) shows part of the incoherent near-side vortex at the tip of the fin. The far-side vortex is larger and centered above the leeward ray. The effect of the near-side vortex on the near-side pressure has greatly decreased, and a low-pressure region near the leading edge of the far side of the fin is stronger due to the increased influence of the near-side vortex on that side of the fin. In Figure 71(d), these trends continue, and the near-side vortex no longer has an effect on the near-side pressure contours. Figure 71(e) and (f) (ϕ = +54° and +65°, respectively) show similar trends to those in Figure 69(d) (ϕ = +43°). The near-side vortex is incoherent and entirely on the far side of the fin. The center of the far-side vortex has moved to the near side of the leeward ray, allowing the far-side vortex to remain in contact with the far-side surface of the fin. The effect of the far-side vortex on the far-side pressure contours has decreased, however, the influence of the near-side vortex is still strong. Figure 71(g) (ϕ = +76°) is similar to Figure 69(e) (ϕ = +54°). The far-side vortex is further away from the surface and its effect is no longer obvious in the far-side pressure contours. The near-side vortex appears less distorted, and is positioned above the far-side surface of the fin closer to the fin-body junction. Figures 71(h), (i), and (j) (ϕ = +86°, +97°, and +108°, respectively) can be compared to Figure 69(f), where ϕ = +65°. The flow-visualization in Figure 71(h) is different than in Figure 69(f), but the pressure contours at these three azimuthal positions are similar to that shown in Figure 69(f). In Figure 71(h), the flow-visualization shows that while the far-side vortex is no longer in contact with the fin surface, its center has moved further to the near side of the leeward ray. The near-side vortex is weak and farther from the fin. The far-side pressure contours in Figures 71(h), (i), and (j) show a decreasing effect of the vortex system as ϕ increases.

Finally, Figures 71(k) and (l) (ϕ = +119° and +130°, respectively) show similarities to Figures 69(g), (h), and (i), where ϕ = +76°, +86°, and +97°, respectively. No flow visualization is available at these large azimuthal angles, but the pressure contours show that the vortex system no longer has an effect on the fin surface pressure.

These similarities in the effects of the interaction at fin stations 1 and 2 are more evident in the spanwise pressure distributions shown in Figure 72. Again, the left-hand column shows five spanwise slices in the pressure data on the near-side surface of the fin, while the right-hand column shows the same for the far-side surface of the fin. Comparing this figure to Figure 70, where the fin is at station 1, we see that the spanwise pressure distributions in Figure 72 exhibit the same characteristics and trends as previously described for Figure 70. Slight differences do exist, however, which can be attributed to the asymmetry present in the flowfield at fin station 2. These differences are most apparent at azimuthal fin positions close to the leeward ray. At ϕ = 0° in Figure 72, there are obvious differences in the spanwise pressure distributions on the near and far sides of the fin. This was described earlier in Figure 55 ($(x/d)_f = 4.9$). The pressure distributions on the near side in Figure 72 indicate that the near-side vortex affects the near side of the fin through ϕ = +32°, beyond which it is located entirely on the far side of the fin. Therefore, it affects the near side of the fin over a slightly larger range of azimuthal angles at station 2 than it did at station 1. The range of azimuthal angles over which the far side of the fin is affected by the vortex system is much larger for station 2 than it was for station 1. This can be seen by comparing the far-side pressure distributions in Figure 72 with those in Figure 70. In Figure 72, the effect of the far-side vortex begins decreasing at ϕ = +32°, where the near-side vortex begins to have a large effect. The distributions at ϕ = +43° through +65° are similar, and they show the large effect of the near-side vortex and the decreasing effect of the far-side vortex as ϕ increases. The interaction continues through ϕ = +119°, where the effects of the vortex system diminish. At ϕ = +130°, the pressure distribution characteristic of the external flow is seen.

It is evident from Figures 71 and 72 that the interaction with the asymmetric flowfield at fin station 2, as the fin is moved toward the near side of the leeward ray

(positive ϕ), is very similar to the interaction with the symmetric flowfield seen at station 1. However, because the flowfield is asymmetric at station 2, we would expect the interaction to be different as the fin is moved toward the far side of the leeward ray (negative ϕ). Figure 73 shows a sequence of cross-sectional flow visualizations at azimuthal angles to the far side of the leeward ray corresponding to those shown in Figure 71, which are at azimuthal angles to the near side of the leeward ray. It is clear from these views that the structure of the vortex system differs as the fin is positioned to the far side due to the asymmetry in the flowfield. From ϕ = -11° through -65°, the azimuthal position of the fin greatly effects the structure of the far-side vortex, which remains close to the body. The position of the near-side vortex, which has separated from the body, does not change over this range of azimuthal angles, but it grows slightly in size. Beginning at $\phi \approx$ -22°, a small amount of fluid is seen coming around the body on the near side. This fluid forms a small, secondary recirculation on the lee side of the body. As the azimuthal angle increases, the amount of fluid coming around the body also increases and the recirculation grows in size. At these azimuthal angles, the fin poses an obstruction to the flow around the far side of the body. This causes a shift in the windward stagnation line towards the near side. It appears that at ϕ = -76° and beyond, this shift is so great that the flowfield undergoes a sudden change. The flow around the near side of the body creates a large vortex which dominates the wake. This is similar to the conditions that exist at ϕ = +76° and +86° in Figure 71.

While the structure of the flowfield appears different at azimuthal fin positions to the far side of the leeward ray, the pressure-coefficient contours at these angles are very similar to those shown in Figure 71. Figure 74 shows, for comparison, the C_p contours at four azimuthal fin positions on the far side of the body. The contours in Figure 74(a), where ϕ = -22°, are very similar to those in Figure 71(b) (ϕ = +22°) if we compare the near side in the former with the far side in the latter, and vice versa. However, there are slight differences in the magnitudes of C_p between the two cases. On the near side in Figure 74(a), the pressure is slightly higher in the low-pressure region near the fin-body junction, and is consistently higher across the fin surface than it is on the far side in Figure

71(b). The pressures across the far-side surface of the fin in Figure 74(a) are consistently lower than those in Figure 71(b) on the near side. In Figure 74(b), where ϕ = -54°, both the distribution and magnitudes of C_p on both surfaces of the fin are similar to those shown in Figure 71(e) (ϕ = +54°). At ϕ = -86°, shown in Figure 74(c), the contours on the far side of the fin appear the same and are the same magnitude as those on the near side of the fin in Figure 71(h) (ϕ = +86°). However, the contours on the near side of the fin appear slightly different from those on the far side of the fin in Figure 71(h). This is because the low-pressure region at the leading edge near the fin-body junction is at a lower pressure and the high-pressure region at the trailing edge near the fin-body junction is at a higher pressure than in Figure 71(h). The result is a greater change in pressure along the chord of the fin at the fin-body junction. Figure 74(d) shows the C_p contours at ϕ = -119°. Again, the far-side contours are similar to those on the near side of the fin in Figure 71(k) (ϕ = +119°), however the near-side contours show one significant difference. The low-pressure region, which had diminished before ϕ = +119°, is still present at ϕ = -119°. Otherwise, the pressures across the near-side surface of the fin at ϕ = -119° are similar to those at ϕ = +119°.

The ranges of azimuthal fin positions over which each side of the fin interacts with the vortex system can once again be determined for this case by studying the C_{fn} and C_{ff} variations in Figure 68(b) along with the pressure contours and spanwise distributions shown in Figures 71 and 72, respectively. For α = 45°, Re_d = 6000, and the fin at axial station 2 ($(x/d)_f$ = 4.9), the near side of the fin is influenced by the vortex system over the range -124° < ϕ < +32°. The far side of the fin is influenced by the vortex system over the range -32° < ϕ < +124°. Even though the flowfield develops asymmetrically for this axial fin station, the large effects of the azimuthal fin position on the structures and trajectories of the vortices, described earlier in Section 4.2.2, causes a range of interaction that is symmetric about ϕ = 0° for these flow conditions. This range of interaction changes significantly with increasing Reynolds number, as shown later in this chapter.

When the fin is placed axially at station 3 ($(x/d)_f$ = 7.1), there is a large degree of asymmetry in the flowfield, and the far-side vortex interacts with the fin to a much greater

degree than does the near-side vortex. The vortex system has a smaller effect on the fin for azimuthal fin positions toward the near side than for fin positions toward the far side. This is clearly seen by studying the forces on the fin at different azimuthal positions. Figure 68(c) shows the total normal-force coefficient variation versus azimuthal angle for α = 45°, Re_d = 6000, and fin station 3. The forces on the fin are clearly asymmetric about the leeward ray, ϕ = 0°, where the coefficient is non-zero. As the fin moves toward the far side (negative ϕ), there is a sharp peak in the C_{ft} curve at about ϕ = -43°. This is the effect of the large, far-side vortex. As the fin moves toward the near side (positive ϕ), the C_{ft} curve is relatively smooth. There is a broader dip in the curve around ϕ = +59°, indicating that the vortex-induced forces are smaller, but that the effect of the vortices persists over a wider range of azimuthal angles to this side of the leeward ray.

Examination of the surface-pressure contours and flow-visualization photographs provides additional information. Figure 75 shows a sequence of pressure contours along with the corresponding flow visualizations at x/d = 8.8, for the same conditions as in Figure 68(c), as the fin is moved toward the far side. Figure 44 (x/d = 8.8) and Figure 54(c) show this information for ϕ = 0°. In Figure 75(a), for ϕ = -11°, the flow visualization shows that the far-side vortex is positioned above the near side of the fin. It is large and fairly coherent, but slightly distorted around the fin tip. The pressure contours are very similar to those shown in Figure 54(c), where ϕ = 0°. In Figure 75(b), where ϕ = -22°, the far-side vortex is more distorted and appears larger. The fin interferes with the flow feeding the vortex from the far side of the body. Comparison of the pressure contours with those at ϕ = -11° shows that while the pressure on the far side of the fin changes little, the pressure on the near side changes significantly due to the presence of the vortex. At ϕ = 0°, the far-side vortex has a small effect on the near side of the fin. At angles between 0° and -22°, the fin is directly in the path of the far-side vortex and the vortex is distorted and incoherent. When ϕ increases to -22°, as shown in this figure, the far side vortex is no longer broken up by the presence of the fin, and begins to have a significant effect on the near side of the fin. In Figure 75(c), where ϕ = -32°, the interaction with the far side of the fin diminishes, while the interaction with the near side intensifies. At ϕ = -43°, shown in

Figure 75(d), and beyond, there is no longer any interaction with the far side of the fin. The far-side vortex is located further from the near side of the fin, and its effect on the near-side pressures is decreased. At ϕ = -54°, shown in Figure 75(e), the flow visualization shows that the far-side vortex is no longer in contact with the fin and is not distorted by it. There is a considerable increase in flow around the near side of the body, however, which separates and forms a secondary recirculation in the low-pressure region on the leeward side of the body. As for the previous case at fin station 2, the fin poses an obstruction to flow around the far side of the body, causing a shift in the windward stagnation line towards the near side. The pressure contours on both surfaces of the fin indicate that the fin no longer interacts with the vortex system at this azimuthal position. Figures 75(f) and (g), where ϕ = -65° and -76°, respectively, further support this conclusion, showing that the pressure changes little with azimuthal position beyond -54°. The pressure distributions are representative of the external flow around the fin. The flow visualization also shows that flow around the near side of the body continues to increase as ϕ increases.

The pressure on the fin is affected differently for azimuthal positions toward the near side of the model. Figure 76 shows the surface-pressure contours and corresponding flow visualizations at a few such positions. In Figure 76(a), where ϕ = +11°, the flow visualization shows that the far-side vortex is large, incoherent, distorted, and close to the body. It contacts the entire far side of the fin, and part of the near side near the fin tip. The near-side vortex is far from the body, distorted, and smaller than the far-side vortex. The pressure contours on the far side of the fin are very similar to those shown in Figure 54(c) at ϕ = 0°, with a low pressure region over the fin-body junction and a rapid increase in pressure in the spanwise direction to a high-pressure region near the tip. This is representative of contact of the far-side vortex with this side of the fin. The near-side pressure contours are also similar to the ϕ = 0° case, except for a small low pressure cell near the fin-body junction at the trailing edge. Figure 76(b), where ϕ = +22°, shows that the far-side vortex is more coherent and closer to the body, making contact with the far side of the fin. The near-side vortex is distorted around the tip of the fin. The pressure on the far side of the fin is similar to that at ϕ = +11°. The pressure on the near side shows a region of low pressure where the flow separates near the fin-body junction. The pressure

increases rapidly to a high-pressure region at half span where the flow attaches to the surface of the fin. The pressure then decreases toward the tip, due to the presence of the near-side vortex. At $\phi = +32°$, shown in Figure 76(c), the center of the far-side vortex has moved across the leeward ray, indicating that its path is affected by the azimuthal position of the fin. The vortex remains close to the body and still makes contact with the fin. The far-side surface pressure shows trends similar to those shown at $\phi = +22°$. The near-side pressure shows no signs of interaction. There is a stagnation region near the fin-body junction, and the pressure decreases steadily in the spanwise and chordwise directions. Again, this is characteristic of the external flow along this side of the fin. In Figure 76(d), where $\phi = +43°$, the near-side vortex is unchanged, and the near-side pressure changes little. The far-side vortex no longer makes contact with the far side of the fin. The surface pressure distribution on the far side is similar to that at $\phi = +32°$. In Figure 76(e), where $\phi = +54°$, the fin is further away from the far-side vortex. The interaction has decreased, and this is reflected in the pressure contours on the far side of the fin. The far-side vortex is larger in size due to increased flow around the far side of the body caused by shifting of the windward stagnation line. At $\phi = +65°$ and $+76°$ (Figures 76(f) and (g), respectively), the far-side vortex is larger, distorted, and less coherent. The fin is far away from the vortex system, and the surface pressure contours show no signs of interaction.

Once again, the spanwise pressure distributions provide more details of the effects of each vortex on the fin. Figure 77 shows the spanwise pressure distributions at five x' locations for the seven azimuthal fin locations described in Figure 75, as well as for $\phi = 0°$. All flow conditions are the same as in Figures 68 and 75. The plots for $\phi = 0°$ are the same as shown in Figure 55 ($(x/d)_f = 7.1$). The near-side pressure distributions are shown in the left-hand column and the far-side pressure distributions are shown in the right-hand column. The degree of asymmetry is evident at $\phi = 0°$. The near- and far-side pressure distributions show significant differences, which were described earlier. As the azimuthal position of the fin is changed from $\phi = -11°$ through $-32°$, the near-side distributions show the growth of a large suction peak at about $y' = 0.375$. This peak decreases in magnitude and increases in spanwise extent as x' increases. This is the signature of the large far-side

vortex, which is centered above the leeward ray throughout this range of ϕ. As ϕ increases, and thus the distance between the near-side surface of the fin and the far-side vortex increases, the effect of the vortex on the near side of the fin increases. At $\phi = -43°$, the effect of the far-side vortex on the near side of the fin begins to decrease, and there is a large gradient in the pressure in the chordwise direction near the fin tip. The interaction with the near side of the fin ends before $\phi = -54°$, and the pressure across the fin changes little in the spanwise and chordwise directions through $\phi = -76°$. The pressure distributions on the far side of the fin show the effect of the far-side vortex through $\phi = -32°$. From $\phi = -43°$ to $-76°$, the pressure distributions on the far side of the fin represent the external flow over that surface.

Figure 78 shows the spanwise pressure distributions at the same five x' locations for the seven azimuthal fin positions described in Figure 76 and for $\phi = 0°$. The plots at $\phi = 0°$ are the same as those in Figure 77. The near-side pressure distributions at $\phi = +11°$ and $+22°$ show a weak suction peak at about $y' = 0.375$. This is caused by separation of the flow around the near side of the body, which re-attaches around $y' = 1.125$. There is a slight effect of the far-side vortex near $y' = 1.5$ at $\phi = +11°$, but there is no obvious effect of the weak near-side vortex, which is located slightly outboard of the fin tip. From $\phi = +32°$ to $\phi = +76°$, the near-side pressure data show typical external flow pressure distributions. The pressure distributions on the far side of the fin are much different from those seen on the near side of the fin in Figure 77. At $\phi = +11°$ and $+22°$, the distributions are similar to those at $\phi = 0°$. The pressure is lower near the body due to outflow into the far-side vortex. Inflow from the far-side vortex creates a higher-pressure region in the central portion of the fin. At $\phi = +32°$, a suction peak forms near the leading edge at $y' = 1.125$ as the far-side vortex begins to lift off the far-side surface of the fin. This peak is larger at $\phi = +43°$, but has diminished by $\phi = +54°$ because the fin is further from the far-side vortex. The interaction of the far-side vortex with the far-side surface of the fin ends at $\phi = +65°$, and at $\phi = +76°$, the pressure changes little across the far-side surface of the fin.

The ranges of interaction are also seen in the force coefficient curves for each side of the fin, shown in Figure 68(c). As described earlier, the forces on the windward side of the fin are not affected by the vortex system beyond a certain range of azimuthal angles. The forces on the leeward side of the fin exhibit the effects of interaction with the vortex system. Because the far-side vortex dominates the wake at this axial fin location, distinct changes are seen in the forces on the near side of the fin over a small range of negative azimuthal angles. At positive azimuthal angles, changes seen on the far side of the fin are less distinct, but occur over a wider range. The range of interaction for each side of the fin was determined in the way described previously for $\alpha = 30°$. With the fin at station 3 for $\alpha = 45°$ and $Re_d = 6000$, the near side of the fin is influenced by the vortex system over the range $-43° < \phi < +27°$. The far side of the fin is influenced by the vortex system over the range $-32° < \phi < +54°$. Changes in the range of interaction with Reynolds number will be described later.

As for the $\alpha = 30°$ cases, Figure 68(c) shows peaks in the C_{ft} curve at azimuthal angles around $\phi = \pm 151°$. Again, experimental evidence indicates that these peaks are features of the external flow around the fin at these angles. At $\phi = -151°$ the peak is much larger than that at $\phi = +151°$. This is due to the asymmetry in the flowfield.

Figure 68(d) shows the variation of the normal force coefficient on the fin with the fin at the fourth axial station ($(x/d)_f = 9.4$). The forces at this axial location behave similarly to those at the third fin station shown in Figure 68(c). This is because the flowfield changes little at axial locations this far from the nose of the model. In Figure 68(d), the C_{ft} variation is clearly asymmetric about $\phi = 0°$. At $\phi = 0°$, there is a net force on the fin due to the asymmetry in the flowfield. There is a very large, sharp peak at about $\phi = -49°$, which represents the effect of the large, far-side vortex. At azimuthal angles to the near side of the leeward ray (positive ϕ), there are some small bumps in the curve, but no distinct peaks are seen. This indicates that the vortex system has less of an effect on the fin at these azimuthal positions.

Figure 79 shows a sequence of pressure-coefficient contours and the corresponding flow-visualization photographs at seven azimuthal fin positions to the far

side of the leeward ray, for the same conditions as in Figure 68(d). Figures 45 (x/d = 11.1) and 54(d) show this information for $\phi = 0°$. Comparison of each azimuthal fin position in this figure with the same position in Figure 75, where the fin was at axial station 3, shows that the pressure contours are very similar. The slight differences seen are explained by comparing the flow-visualization photographs. At station 4, the far-side vortex is larger, less coherent, and positioned further away from the body. The near-side vortex is far from the body and not within the field of view. Because the far-side vortex is farther from the body, the recirculation region that develops between it and the body is larger than when the fin was at station 3. This accounts for the large low-pressure region seen along the fin-body junction in the near-side pressure contours of Figures 79(a) and (b) ($\phi = -11°$ and -22°, respectively). At $\phi = -32°$ and -43°, Figures 79(c) and (d), respectively, the far-side vortex is less distorted than it was at the same angles for fin station 3, shown in Figures 75(c) and (d). The pressure contours show essentially the same features, however. In Figure 79(e), (f), and (g), where $\phi = -54°$, -65°, and -76°, respectively, the fin no longer interacts with the far-side vortex, and the pressure contours are nearly identical to those at the same azimuthal angles for fin station 3 (Figures 75(e), (f), and (g)). The recirculation region under the far-side vortex in these figures grows as ϕ increases due to the shifting of the windward stagnation line toward the near side, as described earlier.

Figure 80 shows a sequence of pressure contours and flow visualizations at seven azimuthal fin positions to the near side of the leeward ray with the fin at station 4. Once again, the interaction is similar to that seen at fin station 3; however, comparing Figure 80 with Figure 76 reveals more significant differences at these positive azimuthal angles than were seen at the previously described negative azimuthal angles. These differences can be attributed to the slightly different flowfield behavior at the fourth axial fin station. At this station, not only is the far-side vortex larger and farther from the body, but its path is no longer affected by the azimuthal position of the fin, as it was over a small range of positive azimuthal angles at station 3. Also, as described previously, the recirculation region that develops between the separated far-side vortex and the body is larger when the fin is at station 4. This recirculation region, as well as the greater distance of the far-side vortex from the fin, result in the differences seen in the far-side pressure contours in Figure 80

compared to Figure 76. The same features and trends are seen on the far side of the fin in both figures. Differences in the near-side pressure contours at station 4 in Figures 80(a) and (b) (ϕ = +11° and +22°, respectively) from those at station 3 (Figures 76(a) and (b)) are due to the greater distance of the far-side vortex from the body. The effect of the far-side vortex on the near side of the fin at positive azimuthal angles is much less at station 4 than it was at station 3, where the far-side vortex was closer to the body. Beyond ϕ = +22° in Figure 80, the near side of the fin is no longer influenced by the far-side vortex, and the near-side pressure contours are nearly identical to those at the same azimuthal angles in Figure 76.

The spanwise pressure-coefficient distributions at fin station 4 for negative azimuthal angles, shown in Figure 81, and for positive azimuthal angles, shown in Figure 82, also show similar trends to those at station 3, shown in Figures 77 and 78, respectively. While the trends are similar, the differences due to the larger size of the far-side vortex and its greater distance from the body at station 4 are more apparent. In Figure 81, the pressure distributions on the near side of the fin show a suction peak at about y' = 0.375 which grows in magnitude and extent from ϕ = -11° through -32°. This is the large effect of the far-side vortex. At ϕ = -32° and -43°, the pressure near the tip of the fin (higher y') begins to vary in the chordwise direction, increasing as x' increases. At ϕ = -43°, the near-side pressure varies greatly across the fin in the chordwise direction. Beyond this angle, at ϕ = -54° through -76°, the interaction of the far-side vortex with the near side of the fin has obviously ended. The far-side pressure distributions indicate an influence of the far-side vortex through ϕ = -32°, beyond which the pressure distributions represent the external flow. In Figure 82, the influence of the far-side vortex on the near-side of the fin ends between ϕ = +11° and +22°. The influence of the far-side vortex on the far side of the fin is indicated by suction peak at about half-span in the pressure distributions from ϕ = +11° through +32°. At ϕ = +43° and beyond, the effect diminishes and the external flow dominates the pressures distributions. As expected, no influence of the distant, near-side vortex is seen in either of these figures.

The range of azimuthal fin positions over which the far-side vortex interacts with each side of the fin is easily seen in the spanwise pressure distributions of Figures 80 and 81 as well as the C_{fn} and C_{ff} curves shown in Figure 68(d). The near side of the fin is affected by the vortex over the range $-49° < \phi < +16°$, while the far side of the fin interacts with the vortex over the range $-32° < \phi < +54°$. Changes in this range with increasing Reynolds number will be shown later in this chapter.

Once again, the C_{ft} variation with azimuthal fin position far station 4, shown in Figure 68(d) exhibits a smaller pair of peaks at $\phi = \pm 151°$, which result when the separated, external flow on the leeward side of the fin reattaches as the leeward side of the fin changes to a windward orientation.

4.4 Effects of Change in Fin Axial Location

While the differences in the flowfield and the interaction with the fin between the four axial fin locations studied are clearly stated in the preceding section, the major points are summed up briefly in this section. Figure 83(a) shows the variation of C_{ft} with azimuthal angle at the four axial locations of the fin for $\alpha = 45°$ and $Re_d = 6000$ for further comparison. The same information for $Re_d = 20000$ and 34000 are also shown in Figures 83(b) and (c), respectively. The changes at these two Reynolds numbers will be discussed in the following section. At station 1 in Figure 83(a), the variation is symmetric about $\phi = 0°$. At station 2, the variation is irregular over the entire range of ϕ. The variations at stations 3 and 4 are similar and clearly asymmetric. At station 3, the forces at positive azimuthal angles are affected by the vortex system to a lesser degree than the forces at negative azimuthal angles. At station 4, the forces at positive angles no longer show any effect, while a large effect is seen at negative angles. Figure 84 shows the range of interaction with each side of the fin for the four axial locations at each of the three Reynolds numbers studied. Once again, changes with increasing Reynolds number will be discussed later. In Figure 84(a), where $Re_d = 6000$, the ranges are large and symmetric at low $(x/d)_f$ due to the dominant effect of fin position on the structure and position of the vortex system. As $(x/d)_f$ increases, the ranges become increasingly asymmetric due to the

increasing asymmetry in the flowfield. The ranges grow due to the increase in size of the far-side vortex, which dominates the wake the these locations.

4.5 Effects of Increasing Reynolds Number

Figure 85 shows C_{ft} versus azimuthal angle for the three Reynolds numbers studied at each of the four axial fin locations. As seen at $\alpha = 30°$, the magnitudes of the force coefficients increase with increasing Reynolds number in each case, and the increase is greater from $Re_d = 6000$ to 20000 than it is from 20000 to 34000. Figure 85(a) shows the C_{ft} variations with ϕ for fin station 1 ($(x/d)_f = 2.6$). This figure clearly shows that the flowfield, and hence the interaction, remain symmetric as Reynolds number is increased over the range studied. Figure 85(b), where the fin is at station 2, ($(x/d)_f = 4.9$), shows some very interesting results. As described earlier, the C_{ft} variation with ϕ is very irregular at $Re_d = 6000$ due to the large effect of the azimuthal position of the fin on the structure and trajectories of the vortices. This figure shows that as Re_d increases, the C_{ft} variations smooth out and show only a small degree of asymmetry. When the fin is placed at axial station 3 ($(x/d)_f = 7.1$), as shown in Figure 85(c), the C_{ft} variations are very similar at all three Reynolds numbers. At $\phi = 0°$, the magnitude of the force coefficient decreases as Re_d increases from 6000 to 20000, but then slightly increases again at $Re_d = 34000$. This indicates that the degree of asymmetry changes as Re_d increases. Figure 85(d), where the fin is at station 4 ($(x/d)_f = 9.4$), shows similar results. In this figure, at $Re_d = 34000$, the peaks in the C_{ft} variation smooth out.

Figure 86 shows how the range of interaction changes as Re_d increases at each of the four axial fin stations. When the fin is at station 1, shown in Figure 86(a), the range increases and remains symmetric as Re_d increases. The change in range of interaction with increasing Re_d for fin station 2, shown in Figure 86(b), is very interesting. As Re_d increases, the range of interaction, which is symmetric at $Re_d = 6000$, becomes asymmetric. Figure 86(c) shows the change in the range of interaction with increasing Re_d for fin station 3. Here, the far side of the fin interacts over a wider range than the near

side. Also, as Re_d increases, the overall range of interaction increases, and the degree of asymmetry in the range decreases. The trends are similar trends for fin station 4 (Figure 86(d)). It is clear from these four figures that the influence of the fin on the development of the vortices increases as the fin moves toward the nose, and as Re_d decreases.

CHAPTER V
DISCUSSION OF RESULTS

The results presented in Chapter III document the interaction of the fin and a symmetric flowfield. It was shown that the tip vortices in the wake of the missile model at $\alpha = 30°$ developed symmetrically and remained symmetric throughout the interaction with the fin at each of the four axial fin locations and three Reynolds numbers studied. From the flow visualization performed at $Re_d = 6000$, the development of the vortices was shown in detail, and the trajectories of the centers of the vortices were mapped as they traveled downstream. This information shows that the vortices remain very coherent and attached to the body until they reach the fin section. At this point, they become less coherent and begin to separate from the body. Therefore, while the axial position of the fin does not affect the upstream development of the vortices, it does affect the location at which the vortices separate from the body. Similar results were seen by Washburn et al. (1993), who examined the effects of tail location on the vortical flowfield in the wake of a sharp-edged delta wing. In this case, the vortices were already separated from the wing before they reached the tail, however no upstream effects on the development or trajectories of the vortices were seen as the position of the tail was changed. Effects of the tail location were seen on the location of vortex breakdown, the global structure of the flowfield, and the aerodynamic loads of the tail, however. No vortex breakdown was observed in the present experiments. The three-dimensional perspective views shown in Figures 11 through 14 provide excellent means of visualizing the development, structures, and trajectories of the flowfields at the four axial fin location.

With the fin positioned along the leeward ray ($\phi = 0°$), the surface pressure contour plots and corresponding spanwise pressure distrib ions revealed a characteristic signature of the vortex as is passed over the fin surface. This signature consists of a suction peak which decreases in magnitude and increases in spanwise extent in the chordwise direction. This is shown in Figure 16, which represents the spanwise pressure distribution on the near side of the fin for $\alpha = 30°$, $Re_d = 6000$, and $(x/d)_f = 7.1$. Outboard

of this suction peak, there is a rapid increase is pressure caused by the inflow of fluid from the vortex toward the fin surface. This pressure distribution compares well qualitatively to the data presented by Bodstein et. al. (1993), who studied the interaction of a streamwise vortex with a long plate. Even though the present fin is much smaller in chordwise extent than the plate in the aforementioned study, similar trends are seen. Their data near the leading edge of the plate show a similar asymmetric spanwise distribution. At locations further downstream on the plate, the asymmetry in the pressure distribution decreases, a trend that is also shown in Figure 16.

As the azimuthal position of the fin is changed, the structures and trajectories of the vortices at the fin section are affected. The effects of the vortices on the each side of the fin also change. Because the flowfield is symmetric, the effects of the interaction at azimuthal angles to one side of the leeward ray are the same as at azimuthal angles to the other side of the leeward ray. This is clearly illustrated by comparing the pressure data on the near-side surface of the fin at azimuthal angles to one side with the pressure data on the far-side surface of the fin at azimuthal angles to the other side and vice versa.

While this study is mainly concerned with the effects of the vortex system on the fin, the effects of the fin position on the vortex system is also of interest. The effect of axial fin location on the development of the vortex system has already been discussed for $\phi = 0°$, but nothing has been said about the existence of any upstream effects of the azimuthal position of the fin on the vortex system. At this angle of attack, it appears from the flow visualization that there is no upstream influence of the azimuthal position of the fin on the structures or trajectories of the vortices. This is clear in the vortex trajectory plots of Figures 27 through 30, but it is not so clear in the flow-visualization photographs. This is because slight differences in the positions of the smoke wires to either side of the upstream stagnation line can result in vortices that are symmetric, but appear slightly different. These differences are apparent in some of the flow-visualization photographs in Figures 31 through 34, but the differences are not consistent and therefore are not believed to be actual features of the flow.

The effects of the vortex interaction with the fin are best shown by examining the normal forces on the fin. The total normal-force coefficients were computed, as described

earlier, directly from the surface-pressure data. The expected behavior of the force variations with changing azimuthal fin position were discussed at the beginning of Section 3.3.1 and will not be repeated here. Potential flow calculations with no separation, as well as theoretical computations with flow separation, were performed by Mendenhall and Perkins (1989) for a similar forebody with fin arrangement. They also performed experiments which they used to validate their computational model. Comparing the force-coefficient variations obtained in the present study with the results they presented, similar features are seen. However, their data show a small reversal in the direction of the force coefficient in the region $\phi = \pm 30°$ that is not seen in the present data. The reasons for this difference are not clear, however it may be due to different experimental conditions and fin geometry. The fin used by Mendenhall and Perkins had a rectangular planform, a span equal to the body radius, and was placed 10.4 diameters from the missile nose. In the present experiment, a clipped-delta planform with a tapered leading edge was used. The span was four times the body radius, and the fin was not positioned further than 9.4 diameters from the missile nose. The fin used by Mendenhall and Perkins was smaller in size relative to the vortices, which may account for the different behavior of the force coefficients at azimuthal positions near the leeward ray.

A feature of the normal force coefficient variations not seen by Mendenhall and Perkins is the small pair of peaks around $\phi = \pm 151°$, which are seen at each fin location in Figure 35. As described earlier, these are not due to the interaction of the fin with the vortex system. They occur at azimuthal angles well outside the observed ranges of interaction. The surface-pressure distributions at angles around $\phi = \pm 151°$ show large changes. These are shown in Figure 36 with the fin at station 3. The pressure on the leeward side of the fin at azimuthal positions prior to $\phi = \pm 151°$ had been decreasing as ϕ increased and the flow was separated on that side of the fin. At $\phi = \pm 151°$ the pressure reaches its lowest level on the leeward side of the fin, and at azimuthal angles beyond this, it appears that the leading edge of the leeward side of the fin comes around to a windward orientation. The flow which was separated on the leeward side of the fin reattaches, causing a sudden change on the fin surface pressures and hence the normal forces.

Peaks in the normal-force coefficient variations can be seen which represent the influence of the vortex system. Between these peaks, the fin interacts with the vortex system in the following manner. As the fin rolls away from the leeward ray, and thus away from the center of the vortex system, it is exposed to varying degrees of interaction until it passes out of the vortex system altogether. The fin in turn, has an effect on the structure and path of the vortex located on the side of the body to which the fin is moved. As the fin is moved away from the leeward ray, it crosses the path of the vortex on the side to which it is moved. Once it has passed through the vortex, the vortex system creates a region of low pressure on the leeward side of the fin. When the fin is moved toward the far side, this low pressure on the near side of the fin creates a larger positive normal force on the fin, which causes the peak in the force curve shown in Figure 35. Likewise, when the fin moves toward the near side, the low-pressure region on the far side creates a larger, negative normal force on the fin, which is seen in Figure 35 as a negative peak. The azimuthal angles at which these peaks occur indicate the range of the interaction. The ranges of interaction are symmetric about the leeward ray for each case at this angle of attack. As the fin is placed axially further from the nose, the ranges increase due to the increase in size of the vortices as they travel downstream. These ranges are seen in the variations of the normal-force coefficient components for each side of the fin as well. The C_{fn} and C_{ff} variations show that the force variations for the surface away from the vortex system are relatively smooth and sinusoidal, while the variations for the surface exposed to the vortex system show the deviations seen in the total force.

Only three Reynolds numbers based on model diameter were studied in this project. As the Reynolds number is increases, the magnitudes of the force coefficients increase. The increase is greater from Re_d = 6000 to 20000 than it is from 20000 to 34000. The increase in Reynolds number over this range does not appear to affect the nature of the flowfield at this angle of attack.

In Chapter IV, the interaction between the fin and an asymmetric flowfield was documented. At $\alpha = 45°$, the vortex system differs significantly at each of the four axial fin locations studied. Essentially, at each axial station, the fin was exposed to a different flowfield configuration. These differences arise due to effects of both the axial and

azimuthal positions of the fin. The flow visualizations documenting the development of the flowfield at each axial fin station, and the trajectories of the vortices with the fin at $\phi = 0°$, show the effects of the axial fin location. At station 1 (Figure 47), no asymmetry develops in the vortex system. At station 2 (Figure 46), the asymmetry is apparent, but both vortices are close to the body. At station 3 (Figure 44), a large degree of asymmetry is seen. The far-side vortex is very large and close to the body, while the near-side vortex has separated from the body and is smaller in size. The flowfield at station 4 (Figure 45) is similar to that at station 3, however, the far-side vortex is now separated from the body and the near-side vortex is much further away. The side views of the vortex center trajectories (Figure 48) show that at stations 3 and 4, the flowfields are essentially the same. As the fin is positioned closer to the nose, however, the flowfield changes. The axial location of fin has significant upstream effects on the development of the flowfield at locations close to the nose at this angle of attack. The top views of the same trajectories (Figure 49) for stations 2, 3, and 4, show that as the near-side vortex separates from the body, the far side vortex center moves toward the near side of the model. Similar trends were seen by Ward and Katz (1987) in their flow visualization study of the vortex structures around a forebody of similar geometry, but without a fin. They show that on a longer body, this behavior leads to the formation of additional wake vortices similar to the primary pair. The structure and development of the vortex system for each axial fin location is easier to visualize by studying the three-dimensional perspective views shown in Figures 50 through 53. The size and shape of the vortices as they interact with the fin are clearly shown in these figures.

Just as the axial location of the fin affects the development of the vortex system, the azimuthal position of the fin also has significant upstream effects. The vortex trajectories in Figures 56 through 59 indicate that there is little if any upstream effect of the azimuthal fin position on the paths of the vortices, although the path of the far-side vortex, which remains attached to the body the longest, is changed significantly at the fin section. The flow-visualization sequences shown in Figures 60 through 63, however, show upstream effects of the azimuthal fin position on the structures of the vortices at the first two fin stations. In the first case, for fin station 1, the vortex on the side of the body to

which the fin is placed is greatly affected at all x/d locations shown. For fin station 2, the effect is not as pronounced, and is only seen immediately upstream of the fin's leading edge. The flow-visualization sequences at the last two fin stations, shown in Figures 64 through 67, show no upstream influence of the azimuthal fin position.

The normal-force coefficient variations with azimuthal fin position once again demonstrate the effects of the vortex system on the fin, and they emphasize the flowfield differences between the four axial fin locations. The force-coefficient variations for α = 45° and Re_d = 6000 are shown in Figure 68. When the fin is placed at station 1 ($(x/d)_f$ = 2.6), it is very close to the region where the vortices form. As shown before, the vortices are small, attached to the body, and develop symmetrically before they reach the fin. With the fin at ϕ = 0°, the vortices are symmetric as they pass over the fin. As the azimuthal angle of the fin is changed, the fin has a devastating effect on the vortex on the side of the body to which the fin is moved. The vortex is severely distorted and is slow to re-form once the fin has passed. The interaction between the fin and the vortex system is the same as it moves to either side of the leeward ray. This is clearly seen in the variation of the force coefficients at station 1 in Figure 68(a). The behavior is the same at positive and negative azimuthal angles. The range of interaction appears to be very large, due to the effect of fin position on the trajectories of both vortices, resulting from a movement of the windward stagnation line. The axial location of the fin causes the vortex system to develop symmetrically, and the azimuthal position of the fin affects the structure and trajectories of the vortices, creating an interaction that is symmetric about the leeward ray. Even though the interaction is symmetric, it differs from the interactions seen at α = 30°. The peaks associated with the vortex interaction are much broader and occur at larger azimuthal angles to either side of the leeward ray. This is because the trajectories of the vortices are affected by the azimuthal position of the fin to a greater degree at α = 45° than at α = 30°. At α = 45°, when the fin is at an azimuthal angle, it exposes a larger projected frontal area to the mean flow. Therefore, it provides a larger obstruction to the flow around the body on the side to which it is positioned. This has a greater effect on the windward stagnation line, and creates a larger low-pressure region on the leeward side of the model. This allows the vortex on the opposite side of the body from the fin to move easily into this

low-pressure region. Because the trajectory of this vortex changes, it remains closer to the surface of the fin over a wider range of azimuthal fin positions. All this results in a range of interaction that is larger than those seen at $\alpha = 30°$. The two smaller peaks at $\phi = \pm 162°$ are caused by the same phenomenon as the ones seen at $\phi = \pm 151°$ in each case for $\alpha = 30°$. They are located at higher azimuthal angles because of the extended range of interaction.

Drastic changes in the flowfield result when the axial location of the fin is moved toward the nose. At station 2 ($(x/d)_f = 4.9$), only a moderate degree of asymmetry is present in the wake. Both vortices are very close to the body, and their paths and structures change greatly with the azimuthal position of the fin, as does the degree of interaction between the fin and each vortex. Flow visualization shows that as the fin is moved toward the far side of the leeward ray, the path and structure of the far-side vortex are affected and the near-side vortex remains unchanged. As the fin is moved toward the near side, the path and structure of the near-side vortex are affected; however, the far-side vortex is affected as well. The trajectory of the center of the far-side vortex follows the movement of the fin toward the near side, and the size of the vortex increases. Therefore, as the azimuthal position of the fin changes over a certain range on the near side of the leeward ray, the position of the far-side vortex relative to the surface of the fin does not change. At each azimuthal position of the fin, the distances between the fin and each vortex are different, resulting in different degrees of interaction as the position of the fin changes. The variation of force coefficient at this location, shown in Figure 68(b) is very irregular. Surface pressure contours show that the pressure on the leeward side of the fin is affected by the vortex system over a much larger range of azimuthal angles, due to the effect of the fin on the trajectories of the vortices. This range is even larger than that seen at station 1. This is due to the asymmetry in the flowfield at this axial location. Because the flowfield is asymmetric, it is more susceptible to the influence of the azimuthal fin position. The flow visualization in Figure 71 shows that as the fin is placed at azimuthal angles to the near side, it obstructs the flow around the near side of the body, again causing the windward stagnation line to shift toward the far side. This feeds more fluid into the far-side vortex causing it to grow. Since the near-side vortex is weaker and has

separated from the body, there is nothing to inhibit the movement of the far-side vortex into the low-pressure region on the leeward side of the fin as ϕ increases. This greatly extends the range of interaction to the near side of the leeward ray. The flow visualization in Figure 73 shows that as the fin is placed at azimuthal angles to the far side, it greatly affects the structure of the far-side vortex. Because the windward stagnation line is now shifted toward the near side, a recirculation of fluid appears on the near side and grows as ϕ increases. Because the far-side vortex is distorted by the fin and the near-side vortex is weak and separated from the body, this recirculation eventually dominates the flowfield and the leeside of the body and moves into the low-pressure region created on the leeward side of the fin. This greatly extends the range of interaction to the far side of the leeward ray. Because the flowfield is asymmetric, it is surprising to notice that the pressure contours and spanwise distributions appear very similar at equal azimuthal angles to either side of the leeward ray. Careful examination, however, reveals that while the pressure data exhibit symmetric trends and features, the azimuthal angles at which these features are present differ slightly from one side to the other, and the magnitudes of the pressures are slightly different as well.

For the fin at station 3 ($(x/d)_f = 7.1$), there is already a large degree of asymmetry in the flowfield by the time the vortex system reaches the fin. The near-side vortex is separated from the body, but is still close enough to the fin tip over a small range of azimuthal angles to interact with the fin. This interaction, while not very evident in the pressure contours, is seen in the flow-visualization photographs. The far-side vortex is very large, dominates the wake on the leeward side of the body, and greatly affects the pressure on the fin surfaces. When the fin is placed in its path, the structure of the far-side vortex is affected. Also, the path of the far-side vortex shifts slightly toward the fin when the fin is at higher azimuthal angles. The asymmetry in the flowfield is clearly seen by comparing Figures 75(a)-(e) with 76(a)-(e). The fin is affected by the vortex system over a wider range when it moves toward the near side of the leeward ray. As the fin moves toward the far side of the leeward ray, it obstructs the path of the far side vortex, limiting its interaction with the fin. A comparison of Figures 75(f) and (g) with 76(f) and (g) shows that the effect of the flowfield is fairly symmetric outside the range of vortex interaction.

The pressure distribution on the far side at ϕ = -76° is very similar to that on the near side at ϕ = +76°, and vice-versa. This interaction between the fin and the very asymmetric flowfield results in a range of interaction that is also asymmetric about the leeward ray. Because the far-side vortex dominates the interaction, the near side of the fin is effected over a smaller range of azimuthal angles than the far side. However, since the far-side vortex trajectory is effected at a few positive azimuthal angles, the range of interaction extends further to the near side of the leeward ray than to the far side.

When the fin is moved to a higher x/d, the overall flowfield does not change. Since the fin is in a different region of the flow, however, the interaction is slightly different. When the fin is at station 4 ($(x/d)_f$ = 9.4), the near-side vortex is even further away from the body and very weak. It no longer has any interaction with the fin. The far-side vortex is much larger, is separated from the body, and dominates the wake. Its path is no longer affected by the azimuthal position of the fin, but its structure is slightly changed at low azimuthal angles. Figure 68(d) shows the variation of the force coefficient on the fin with azimuthal angle at this fin location for Re_d = 6000. Overall, the behavior is similar to that at station 3. However, there is a larger effect of the vortex system on the forces at negative azimuthal angles, and there is no distinct effect of the vortex system on the forces at positive azimuthal angles. Because the far-side vortex, which dominates the wake at axial fin station 4, is larger and farther from the body and its path is not affected by the azimuthal position of the fin, the range of azimuthal angles over which it interacts with the vortex system is different than the range at axial station 3. The overall range increases slightly due to the increase in size of the far-side vortex. However, since the far-side vortex is further away from the body than it was at station 3, the range of angles over which the near side of the fin is effected is slightly smaller.

Increasing Reynolds number has a more significant effect at α = 45° than is did at α = 30°. Once again, as Re_d increased, the magnitudes of the normal force coefficients on the fin increased, and the increase was more prominent from Re_d = 6000 to 20000 than from 20000 to 34000. The flowfields with the fin at axial stations 1, 3, and 4 were not affected by the increase in Reynolds number over the range studied. At station 1, the

flowfield remained symmetric, and the range of interaction increased slightly. At stations 3 and 4, the flowfield remained asymmetric, and the ranges of interaction also slightly increased. At station 2, however, the influence of the vortex system on the fin changes significantly when Re_d is increased from 6000 to 20000. The flowfield remains asymmetric, but it appears that the degree of asymmetry increases as Reynolds number increases. This is seen in the ranges of interaction shown in Figure 86(b). At $Re_d = 20000$ and 34000, the fin is affected by the vortex system over a much smaller range of azimuthal angles, and the range is now asymmetric about the leeward ray. This behavior is similar to that at stations 3 and 4, where a greater degree of asymmetry exists. It is evident that at the higher Reynolds numbers studied, the trajectories of the vortices are influenced less at station 2, resulting in behavior similar to that seen at stations 3 and 4.

CHAPTER VI

CONCLUSIONS AND RECOMMENDATIONS, PART A

6.1 Conclusions

Experiments were conducted to examine the interaction between the tip vortices in the wake of a missile with a single control surface. A model of a typical missile geometry and a generic fin section were designed and constructed. The model was modular in design with four interchangeable body sections. This allowed the fin section to be placed in four different axial regions of the flowfield. A positioning system was designed and constructed which allowed the model to be positioned in the central portion of the wind tunnel test section at the desired pitch, yaw, and roll angles.

The results of these experiments effectively document important details of this interaction for two very different flowfields. At an angle of attack of 30°, the flowfield was found to be symmetric. At an angle of attack of 45°, the flowfield was found to be asymmetric for all but the first axial fin location studied. The experiments performed included a detailed flow-visualization study and mean surface-pressure measurements on the fin.

The laser-sheet smoke-wire technique for visualizing the flowfield in cross-sectional planes proved to be very effective for documenting the development of the flowfield as well as the structure of the flowfield throughout the interaction. The formation and growth of the tip vortices, the trajectories of these vortices, and the structures of these vortices at the fin section during the interaction were documented, at the two angles of attack studied, for the four axial locations of the fin section. At $\alpha = 30°$, the vortices developed symmetrically and remained symmetric throughout the interaction with the fin at all four axial fin locations. At the fin section, the structures and trajectories of the vortices were effected at different azimuthal fin positions. No upstream influence of the axial or azimuthal fin positions was seen. At $\alpha = 45°$, the flowfield at the fin section was significantly different at each axial fin location. At the location closest to the nose, $(x/d)_f = 2.6$, the flowfield developed symmetrically and remained symmetric throughout

the interaction. At the second axial location, $(x/d)_f$ = 4.9, the vortices developed asymmetrically, and were both very close to the body. At the third location, $(x/d)_f$ = 7.1, a greater degree of asymmetry was found in the flowfield. The far-side vortex remained attached to the body longer, and grew much larger than the near-side vortex. The flowfield at the fourth axial location ($(x/d)_f$ = 9.4) was similar to that at the third location, however at this location, the far-side vortex was separated from the body. At this angle of attack, there was an influence of the axial fin position on the flowfield. Also, at the two axial fin locations closest to the nose, an upstream influence of the azimuthal fin position on the structures of the vortices was observed.

The surface-pressure measurements, taken over a wide range of azimuthal fin positions for each angle of attack, axial fin location, and Reynolds number, helped greatly in interpreting the flow-visualization results. The signature of the vortex interaction with the surface was seen, and the changes in pressure with changing azimuthal fin position were documented. Information on the size and position of the vortices, taken from the flow visualization, was correlated with the surface-pressure data to determine the vortex effects on the pressure distributions. For the cases where the flowfield was symmetric, the influence of the vortices on the pressure distributions were the same at equal azimuthal fin positions to either side of the leeward ray. For the cases where the flowfield was asymmetric, this was not the case.

The pressure data were integrated across the surface of the fin to determine the normal forces on the fin at different azimuthal positions. The results showed differences from potential flow calculations. These differences appeared as peaks in the variations of the normal-force coefficient with azimuthal angle. Detailed examination of the pressure data at azimuthal angles where the peaks occurred, helped to determine if they were effects of the interaction.

Information provided by the individual normal force components on each side of the fin, along with careful examination of the trends shown in the pressure distributions as the azimuthal angle of the fin is increased, allowed the ranges of azimuthal fin positions over which the fin interacts with the vortex system to be determined. At α = 30°, the

ranges were symmetric about the leeward ray for all cases. The ranges were seen to increase as the fin was placed further axially from the nose, and as Reynolds number was increased. At $\alpha = 45°$, the range of interaction was large and symmetric at the first axial fin station, and it increased slightly as Reynolds number increased. At the second fin station, the range was very large and symmetric at the lowest Reynolds number, but it became smaller and asymmetric as the Reynolds number was increased. At the third and fourth fin stations, the range of interaction was asymmetric about the leeward ray, and increased in size as the axial location of the fin was increased and as Reynolds number was increased.

Overall, this study provides a detailed examination of the interaction between a generic fin with the pair of vortices in the leeside wake of a missile model. It has provided information on the effect of the interaction on the fin, as well as information of the effect of the fin position on the vortex system. The flow visualization, coupled with pressure and force data has enabled a greater understanding of the vortex-induced effects on the loading of the fin, the range of interaction, and the effects of axial fin position and Reynolds number.

The results of this study can be very useful in missile design projects. Knowledge of the nature of the flowfield around the fin at different axial and azimuthal positions can be used to determine optimal fin placement on the missile. The effectiveness of the fin as a control surface can be estimated from the force data presented for different axial and azimuthal fin positions. These results can be extended to multi-fin configurations if the fins are placed so that they do not alter the upstream development of the flowfield and we assume the presence of additional fins does not change the characteristics of the interaction, which were described for a single fin in this study.

6.2 Recommendations

While this study provided a better overall understanding of some of the important mechanisms involved in the interaction between a control surface and the vortices in the wake of a missile at angle of attack, further studies are suggested to gain a deeper understanding of the problem:

- While not apparent at the lower angle of attack ($\alpha = 30°$), effects of the axial placement of the fin were seen at the higher angle of attack ($\alpha = 45°$). These effects are very important to consider in the design of missile control surfaces. Only one generic geometry was studied in the present work, so the effect of control surface size and shape could not be discussed. Future work should be performed with fins of different size and planform shape. This would provide a better understanding of the influence of fin construction and placement on the development of the flowfield.

- A more detailed flow-visualization study at more axial locations at the fin section would help to better understand the changes the vortices undergo due to contact with the fin.

- Only three Reynolds number were studied over a small range. The results obtained in the present work show some effects of increasing Reynolds number on the flowfield, especially for the asymmetric case. The reasons for these effects are not clear, however, and therefore, a study of the interaction at more Reynolds numbers over a larger range would significantly contribute to a better understanding of the Reynolds number effects.

- A logical extension of this work would be to examine the interaction of the tip vortices with multiple fin configurations. Since actual missiles incorporate three- and four-fin arrangements, a study such as this would be very helpful in missile design.

- It would be interesting to compare the pressure data obtained in the present work with a simple, theoretical model. Such a comparison would help single out the effects of the vortex system and further interpret the pressure results.

- The present work dealt with the interaction between tip vortices and a control surface for a steady configuration. Extension of this work to a missile configuration undergoing unsteady, pitching behavior would be useful in developing an understanding of the unsteady interactions that take place on maneuvering missiles.

PART B

CHAPTER VII

SURFACE-PRESSURE MEASUREMENTS

Preliminaries

Initial experiments at a Reynolds number of 6000 revealed that the Setra transducer was not sensitive enough to detect the pressure differences. It was also observed that small drifts in the transducer zero offset during the measurement were enough to cause relatively significant errors in the measurements. To overcome this problem, the Setra transducer was replaced by a Validyne transducer with an adequate resolution for measurements at this Reynolds number. Tests showed this replacement to be satisfactory.

The approach of rolling the body and maintaining the tip and aft body section fixed in order to record the pressure data at different azimuthal angles proved to be successful. The pressure measurements along the main ray port and a complementary port at Reynolds numbers 6000 and 34000 shown in Figure 87, are in excellent agreement, indicating that both measurements were consistent, and that rolling the body to make the measurements did not change the flow field.

7.1 Flow Visualization

The flow visualizations provided a qualitative description of the flow over a steady missile model. As is well known, the three main flow states, in terms of the leeside vortices are symmetric, asymmetric, and unsteady. As shown in Figure 88, at Reynolds number 6000 and α=20° the flow field on both sides of the missile is symmetric; the size and location of each tip vortex is about the same. These vortices originate from the tip, wrap around the body, and leave the model over the aft body section. On the other hand, an asymmetric flow field would have tip vortices that wrap around the leeward side and peel off at different x/d locations. Comparing the flow fields on the near and far sides of the model as shown in Figure 89, for a Reynolds number 6000 and α=45°, the near side vortex leaves the body at a location closer to the tip than one at the far side. Lastly, Figure 90, which was recorded at Reynolds number 6000 and α=60°, shows that the tip vortices

separate from the model near the tip, and that additional body vortices were shed parallel to the body, indicative of a periodic unsteadiness in the leeside.

7.2 Pressure Distribution and Regions of Flow Field

In addition to flow visualization records, the three flow regimes could be described from the measured pressure distributions. The pressure distribution around the body was obtained for angles of attack ranging from 0° to 85°, over x/d from 1.5 to 11.5, and for Reynolds numbers from 6000 to 34000.

The pressure distribution at α=0° and Reynolds number 6000 is shown in Figure 91(a) and 91(b). At this position, the pressure distribution is constant for all azimuthal angles. Figure 91(c) aids in a description of the flow development as it passes around the model. The pressure drops initially with distance away from the nose, reaching a minimum value at x/d about 2. It then starts to increase for a small stretch, and then becomes fairly constant over the rest of the model axis. The cylindrical portion of the model starts at x/d=2.6.

Figures 92 and 93 indicate the pressure distributions at α=15° and α=30° respectively, at Reynolds number 6000. The distribution over both near and far sides of the model is essentially the same at both angles. This symmetry is maintained up to x/d=11.5.

When the angle of attack is increased to 37°, asymmetry is detected over the second half of the model, for x/d>6.6. Here the pressure on the near side is higher than that on the far side. Nonetheless, Figure 94(a) shows that the flow field is still symmetric for x/d<6.2. When the angle is increased further, the x/d location where asymmetry starts to develop moves toward the tip. In Figures 95(a), asymmetry is seen at the first half of the model, for x/d<6.2 at α=45°.

Finally, a symmetric flow field was re-established as the model is pitched up beyond 60°. Pressure distributions at α=70° and α=85°, shown in Figures 96 and 97 respectively, identify this flow feature. At α=70°, asymmetry is present at the initial x/d positions, even though the pressure difference between the near and far sides is somewhat difficult to distinguish. The second part of the model, however, shows that the flow field is

very symmetric. At α=85°, the flow field is entirely symmetric and separated over the leeward side, with fairly constant surface pressures on the leeside. The entire leeward side experiences this flow separation with the result that the pressure distributions for both the first and second parts of the body have a similar shape.

7.3 Local Force Distribution

The pressure data acquired at different angles of attack and Reynolds numbers could be integrated to calculate local force coefficients for the side, normal, and resultant forces. The side force acting out of plane on the model indicates the strength of asymmetry due to the vortices which originate from the tip region of the model. The normal force acting in the model plane usually has a positive value due to a larger pressure on the windward side than that on the leeward side. The resultant force and its direction could be evaluated from the side and normal forces. At Reynolds number 6000 the coefficients were calculated from the available data. The local force coefficients at Reynolds number 34000 is discussed at Section 7.5.

At α=0° the definition of the local force coefficient was modified by taking $\sin^2\alpha$ to be unity in the denominator. Figure 98 shows that all the local force coefficients are close to zero, indicating that the flow is symmetric over the model. A similar result is obtained for the side force coefficients at α=15° and α=30°, as shown in Figures 99 and 100, respectively. The resultant force line is practically coincident with the normal force line since the magnitude of the side force is very small. As a result, the circumferential location, ϕ, where the resultant force acts is constant at about 180° for all x/d's.

At α=37°, as shown in Figure 101, the side force is quite constant and small for x/d<5 and begins to decrease toward the back of the model. Beyond x/d of about 7, the side force makes a discernible contribution to the resultant force. The normal force is slightly higher in the nose region because the surface curvature results in a higher effective angle of attack. As the magnitude of the side force increases, the resultant swings around from 180° to the far side. At x/d=7, it acts at about 200° and reaches a value of 210° at x/d=10 before swinging back.

At α=45°, the flow field asymmetry manifests itself clearly in the force distributions, as shown in Figure 102. The side force coefficient, which is nearly zero at x/d=1.5, begins to decrease and reaches a maximum negative value at x/d about 5.5. It then starts to increase, crosses zero at x/d about 8.0, and attains a maximum positive value at x/d about 9. It then decreases once again. The resultant force behavior at this angle of attack is dominated by the side force, since the normal force is more or less constant along x/d. The azimuthal location where the resultant force acts varies in the range from 150° to 230°. Initially, the resultant force acts at about 180°, reaches 230°, where the side force is maximum negative, and then decreases to 150° at which angle the side force is at a positive maximum.

As the angle of attack is increased to 70° and 85°, the flow becomes symmetric, as indicated by the local force coefficient distributions in Figures 103 and 104, respectively. At these two angles of attack, the magnitude of the side force is once again small, and the resultant force is dominated by the normal force. At α=85°, the magnitude of the normal force coefficient is about 0.5. This coefficient may be expected to approach a value of about 0.2 which is the drag coefficient of cylinder in a cross flow. At both angles, the resultant force is quite constant along x/d, and acts at about ϕ=180°.

7.4 Effects of Change in Angles of Attack

To examine the effect of angle of attack on the flow field in more detail, pressure measurements were made at x/d=1.5 with a finer change in α over the range from 20° to 69°. Figure 105(a) records symmetry in the leeward pressure distribution up to α=40°. Asymmetry is then seen to set in, with a larger decrease in pressure on the far side, relative to the near side. As the angle of attack is increased from 49° to 57°, a clear pattern of asymmetry is observed, as shown in Figure 105(b). The pressure distribution on the near side collapses onto one line, indicating an unchanged flow state, while the far side pressure continues to decrease with increase in α. Between 59° to 63°, the tendency toward asymmetry abruptly stops (Figure 105(c)). The mean pressure exhibits large azimuthal variations as seen at 61°, before symmetry is reestablished in the pressure distribution. At

63° the azimuthal variations have decreased and the distribution is almost symmetric. For α greater than 65°, the distribution is almost unchanged with α and symmetric, as displayed in Figure 105(d).

The fluctuations recorded at α=61° were examined more closely by averaging the pressure signal over different acquisition times ranging from four to ten seconds. Figure 106 displays the result. The mean pressure variations are independent of the averaging times, suggesting that the flow indeed undergoes a drastic change in state. In addition to documenting the effects of changing the angle of attack on the pressure distributions, experiments were carried out to examine the influence of Reynolds numbers.

7.5 Effects of Change in Reynolds Numbers

Measurements similar to those described above were made at two additional Reynolds numbers, 20000 and 34000. At Reynolds number 20000, the onset of asymmetry is observed at an angle of attack of 45°, as shown in Figure 107(a). After asymmetry has set in, the near-side pressure distributions collapse onto one line, as seen previously at Reynolds number 6000. The pressure over the far side decreases as the angle is increased, and the magnitude of the suction peaks is considerably larger. With increase in α (Figure 107(b)), the behavior is also similar; large azimuthal variations in pressure set in at α=63°. A return to a symmetry occurs beyond α=65° (Figure 107(c)). The C_p magnitudes are somewhat larger than those at Reynolds number 6000.

The same behavior was observed at Reynolds number 34000. The results are displayed in Figure 108. Onset of symmetry was found at α=45° and the azimuthal variation in mean pressure at α=66°. No measurements were recorded beyond α=66° since the flow was expected to return to symmetry as shown at the previously selected Reynolds numbers. The suction pressure levels were larger than those at Re 20000 for the corresponding angle of attack.

The pressure distributions at α=45° for three Reynolds numbers are compared in Figure 109. From a comparison of the minimum suction peak, indicated by straight lines, it is evident that asymmetry has developed at this particular x/d location and angle of attack

for all three Reynolds numbers. It is also seen that the magnitude of the suction peak increases with Reynolds number.

At Reynolds number 34000 and α=45°, the same pattern of force coefficient distributions was observed (Figure 110) as for Reynolds number 6000. Comparison of this figure with Figure 102 shows that the x/d locations where maximum and minimum values of C_y occur are about the same. At these Reynolds numbers, the minimum side force and maximum ϕ are located at x/d about 5.7, while the maximum side force and minimum ϕ are at x/d nearly 9.5. The flow fields at this angle of attack and these two different Reynolds numbers are almost similar.

CHAPTER VIII

DISCUSSION OF SURFACE-PRESSURE RESULTS

The procedure of rolling the body in order to measure the pressure at different azimuthal angles does not create any noticeable disturbance in the flow field. As shown in Figure 87, the measurements along the main ray and the complementary ports fall on one line, indicating that the measurements are repeatable and consistent. Several advantages could be gained from this approach. One could measure the pressure at any desired azimuthal angle (within the constraint of the smallest increment available in the roll-motor positioning system). This allowed detailed measurements over a region, a feature that is not possible with pressure ports at fixed locations on a model. Also, concurrent measurements using the complementary ports could be used to indicate if vortex-flipping occurred during the measurement, in which case the pressures measured would differ along the two rays.

Initially, when the model is at zero angle of attack, the flow about the model is symmetric and the pressure data at different ϕ's collapse on one line as shown in Figure 91(c). The plot is useful to describe flow field changes along the body with increase in x/d. The pressure coefficient at the tip, x/d=0, should be unity because this is a stagnation point. As the flow passes over the nose, the velocity increases, causing the pressure to drop to a minimum value. A part of this decreasing pressure distribution is captured in the measurement from x/d=1.5 to x/d=2.1, where the minimum pressure value is obtained. Between this location and about x/d=4, the velocity decreases, resulting in an increase in the pressure distribution. After that, as the model geometry remains unchanged from x/d=2.6, the pressure is nearly constant, with a slight increase toward the end of the model, at about x/d=11.5. This measurement provides proof that the model was aligned properly at zero yaw and pitch relative to the flow. Since the pressure distributions along rays symmetrically placed about the 180° ray are very closely matched, it is expected that the side force coefficient would be close to zero. Figure 98 confirms this expectation.

The flow visualization and pressure measurements confirmed that three main flow states occur in the vortical flow over a missile configuration, associated with symmetric,

asymmetric, and unsteady vortices respectively, in the separated leeside flow. Flow visualization at Reynolds number 6000 and α=20°, shown in Figure 88, indicates that the tip vortices wrap around the model on the leeward side and remain attached to the surface up to the aft end of body. The visualizations could be correlated to the pressure measurements at α=15° and α=30°, where the flow field is symmetric, as shown in Figures 92 and 93. The pressure at ϕ=0° (or 360°) is the highest because this is the stagnation line. Figure 92 shows mixed effects of the curvature of the model at the nose region and the tip vortices location on the pressure distribution. The curvature effect, is seen in Figure 91, where the pressure at the nose decreases and then increases along the body. The pressure distribution along ϕ=90° in Figure 92 exhibits this contribution. On the other hand, Figure 93 at α=30° indicates that the suction level is higher at a smaller x/d than that at large x/d, since the tip vortex cores are closer to the surface of the model. A brief explanation of the pressure distribution behind a tangent ogive body was given by Zilliac et al. (1990). The local side force coefficients at these two angles of attack are small, indicating that the flow is symmetric.

The same explanation of symmetrical vortical flow applies to the pressure distributions up to x/d=6.6 at α=37°, as shown in Figure 94(a). However, as seen in Figure 94(b), asymmetry sets in between x/d=6.6 and x/d=11.5, and the pressure distributions over the near and far sides on leeward side are not equal to one another. When the tip vortex peels off from the surface, leaving the body on one side, the pressure over this location increases, because the tip vortex core which is a low-pressure region is replaced by a body-bound vortex. Consequently, a negative side force starts to build up and the line of action of the resultant force moves away from 180°, as shown in Figure 21.

The flow visualization and pressure distributions for angle of attack of 45° are shown in Figure 89 and Figure 95, respectively. The x/d location where the tip vortices leave the surface moves closer toward the tip, to a point between 1.5<x/d<6.2. Toward the aft end of the model, the pressure distributions tend first to become symmetric and then become asymmetric but in the opposite direction. The side force distribution shown in Figure 102(a) clearly shows this behavior. Reding and Ericsson (1984) conjectured that

this switching is due to "relaminarization" in boundary layer. However, to date there is no confirmation to this.

With further increase in the angle of attack beyond 60°, the tip vortices peel away from the body at a location closer to the tip. The flow field behind the body is now mainly dominated by vortex-shedding generated by the cross flow. Flow visualization at α=60°, as shown in Figure 90, indicates this parallel shedding. Time-averaged pressure data at α =70° and α=85° could not confirm this; fluctuating pressure data are needed. It is expected that the spectra of the surface-pressure fluctuations or the velocity of the near wake behind the body would display the shedding frequency. The spectra of pressure fluctuations has been examined by Degani and Zilliac (1990), while Ramberg (1983) has looked at the near wake. Flow visualization and pressure measurements only indicate that the flow is separated on the leeward side. At this high angle of attack, the measurements show that the mean pressure distribution is symmetric. Consequently, the side force distributions calculated from the mean pressure have a small value, also indicating that the flow is symmetric.

By varying the angle of attack from 20° to 69° at three different Reynolds numbers from 6000 to 34000 and acquiring pressure data at the x/d=1.5 location, a general pattern of symmetry, asymmetry, unsteadiness, and symmetry is seen. First, the pressure distribution is symmetric and decreasing. As the angle of attack is increased from α=20° to 45°, the pressure over the leeward side decreases and asymmetry sets in. When the angle of attack is increased, the velocity of the tip vortices increases, causing the pressure to decrease at the leeward side. Several researchers (Lamont, (1982) and Zilliac et al., (1990)) have pointed out that asymmetry at α=45° and above is caused by a microasymmetry in the configuration at the nose tip. Once asymmetry sets in, the pressure distribution over the near side collapses into one line. This can be explained by the fact that the tip vortex leaves the body at a location x/d<1.5. Thus, an increase in the angle of attack beyond 45° does not change the pressure distribution. On the other hand, the tip vortex on the far side remains attached to the body and leaves the surface at a location x/d>1.5. This location approaches the tip as the angle of attack is increased.

As the angle of attack is increased beyond 60°, the pressure distribution on the leeward side changes from asymmetric to unsteady. The separation locations of the tip vortices are close to the tip and flip from one side to another, causing the pressure over the aft region to fluctuate. With a further increase in the angle of attack, the vortex flipping is still present but moves closer to the tip. Therefore, the unsteady mean pressure variations are still detected, but they are smaller in magnitude than those at the lower angles of attack. Finally, increasing the angle of attack causes the tip vortices to peel off from the surface at a location even closer to the tip. As a result, the port at x/d=1.5 could not detect the pressure caused by the tip vortices but sensed one which is distributed quite similar to that in two-dimensional cross flow over a cylinder.

Comparing the changes in the flow field as the angle of attack and Reynolds numbers are varied, two distinct characteristics could be identified. First, the location where asymmetry sets in is at about α=45°. Although the onset of asymmetry might occur at a position a few degrees before 45°, the measurements at this angle could serve as the starting point to observe the asymmetry. The second characteristic is the angle of attack at which spatial variation of the mean pressure is seen. Even though the angles of attack at which the mean pressure fluctuates are not identical for the three different Reynolds numbers, they are well above 60°, which may be considered as the angle of attack for the beginning of the unsteady flow regime. In addition to the position of asymmetry and fluctuating mean pressure, the local force coefficients and direction of C_r at α=45° for both Reynolds number 6000 and 34000 are almost identical. The same pattern of flow is seen at the selected Reynolds numbers because the flow is separated in the laminar region, as described by Lamont (1982). According to him, the Reynolds number must be increased to 0.2×10^6 in order to observe the transitional separation in the boundary region.

The above observations and explanations are based on data at a particular x/d location close to the nose. Similar measurements at other x/d locations should be carried out to confirm this behavior.

CHAPTER IX

CONCLUSIONS AND RECOMMENDATIONS, PART B

A tangent ogive missile model was designed, built, and tested as part of an investigation of vortical flow over missile configurations. The experimental setup involved the design and development of the model, positioning system, electrical interface, and a motion control code to position the model at the center of the test section with a desired attitude. While the nose and fin sections of the model were kept stationary, maintaining the same model configuration throughout the experiment, the body was rolled about its axis to acquire the pressure data at different azimuthal angles. The flow field was unaffected by this rolling motion. This was shown by a comparison of the pressure measurement along the main ray and the complementary ports. The measurement was also used to justify the acceptable magnitude of a transducer zero voltage drift during the experiment.

From the results presented and discussed in the previous chapters the following conclusions can be drawn. First, the pressure distribution over the model can be used to describe some aspects of the vortical flow over the missile configuration at different angles of attack. Flow symmetry exists in the range from α=0° to α=30° followed by an asymmetric regime up to 60°. An unsteady flow region is present from α=60° to α=90°. The flow visualization records also confirm the presence of these. Secondly, the development of asymmetric vortical flow begins at the end of the body and moves toward the nose as angle of attack is increased from zero to 60°. A few degrees beyond this angle of attack, tip vortices flip from one side to another resulting in the unsteady mean pressure distributions. Third, the onset of asymmetry at a particular x/d location and angle of attack, as seen in the azimuthal variation of pressure is not influenced by the Reynolds numbers, over the range of these parameters selected in this experiment. The flow field at selected Reynolds numbers, as shown by local force coefficients, is identical presumably because vortical separation under these conditions is still laminar. Finally, local distributions of the normal, side, and resultant force coefficients could be used as an

additional tool to describe the flow field, especially useful in identifying the presence of coning motion.

The following additional measurements would provide a deeper understanding of this complex flow field:

- shear stress measurements around the model surface to document the skin friction at the wall as it interacts with the tip and bound body vortices at different flow conditions. This measurement could help in locating the region of high or low intensity of vortical interaction.

- pressure distributions along the main ray of the model at different angles of attack and Reynolds numbers to pinpoint the x/d location when asymmetry sets in. Selecting two φ locations symmetrically placed on the near and far sides should be sufficient to determine that x/d location. This procedure should be carried out with finer increments of α.

- measurements of pressure and shear stress at the fin section to quantify the flow field around this aft body region.

- change the nose configuration from a tangent ogive to a sharp or blunt cone to observe the effect of nose geometry on the flow field.

APPENDIX

Scientific personnel participating in project

1. Dr. Mukund Acharya, Principal Investigator
2. Mr. Maskan Md. Hassan, Graduate Research Assistant. (awarded MMAE degree, December 1992)
3. Mr. John W. Kiedaisch, Graduate Research Assistant (awarded MS degree, May 1994)

Publications

1. Kiedaisch, J. W., and Acharya, M., "Interaction of Missile Tip Vortices with a Control Surface," AIAA Paper 94-0527, 32nd Aerospace Sciences Meeting, Reno January 1994.

Four additional manuscripts will be prepared for publication during summer 1994. Copies of these will be forwarded to ARO as soon as they are available.

FIGURES

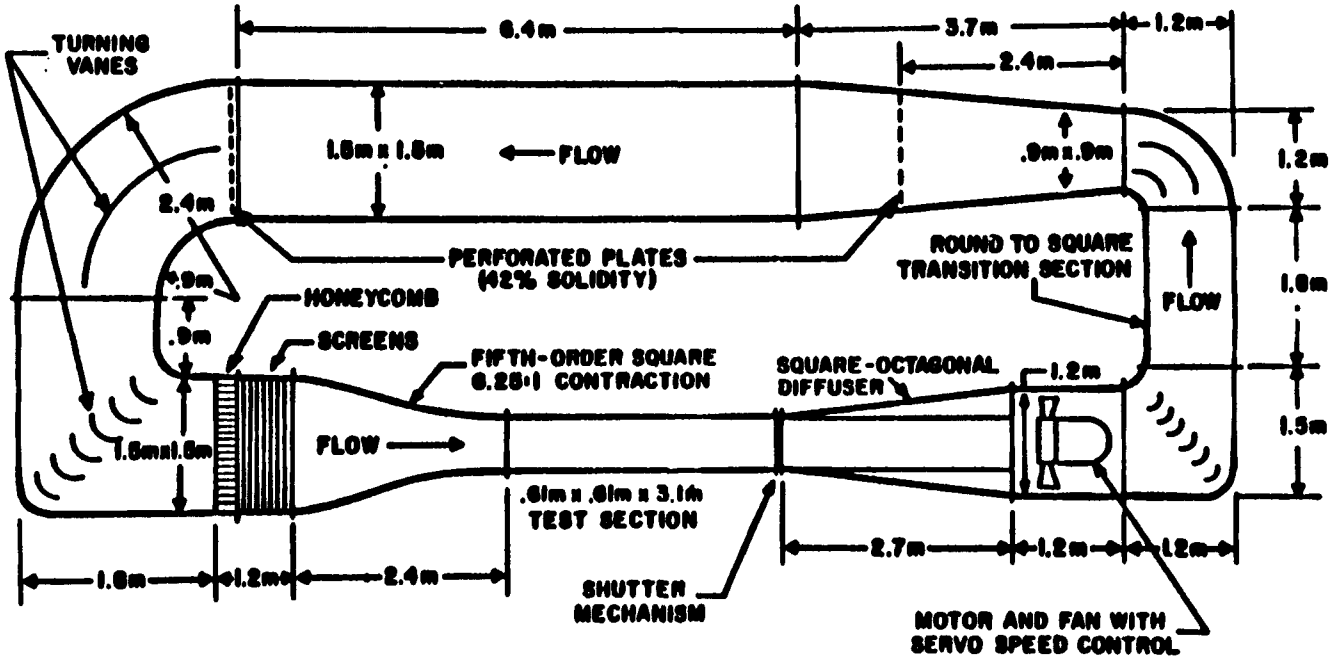

Figure 1. Schematic of the Andrew A Fejer Unsteady Wind Tunnel.

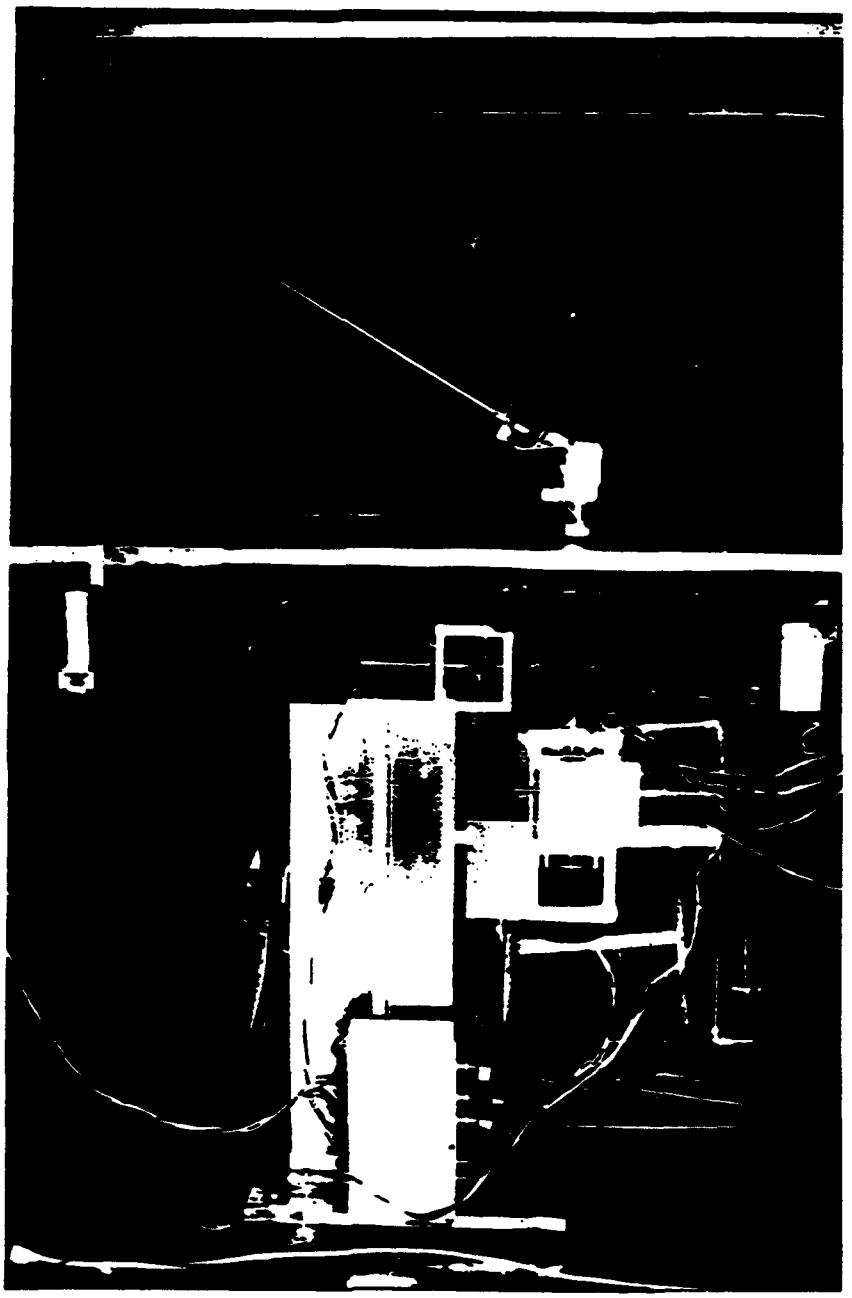

Figure 2. Model and Positioning System Installed in the Wind Tunnel.

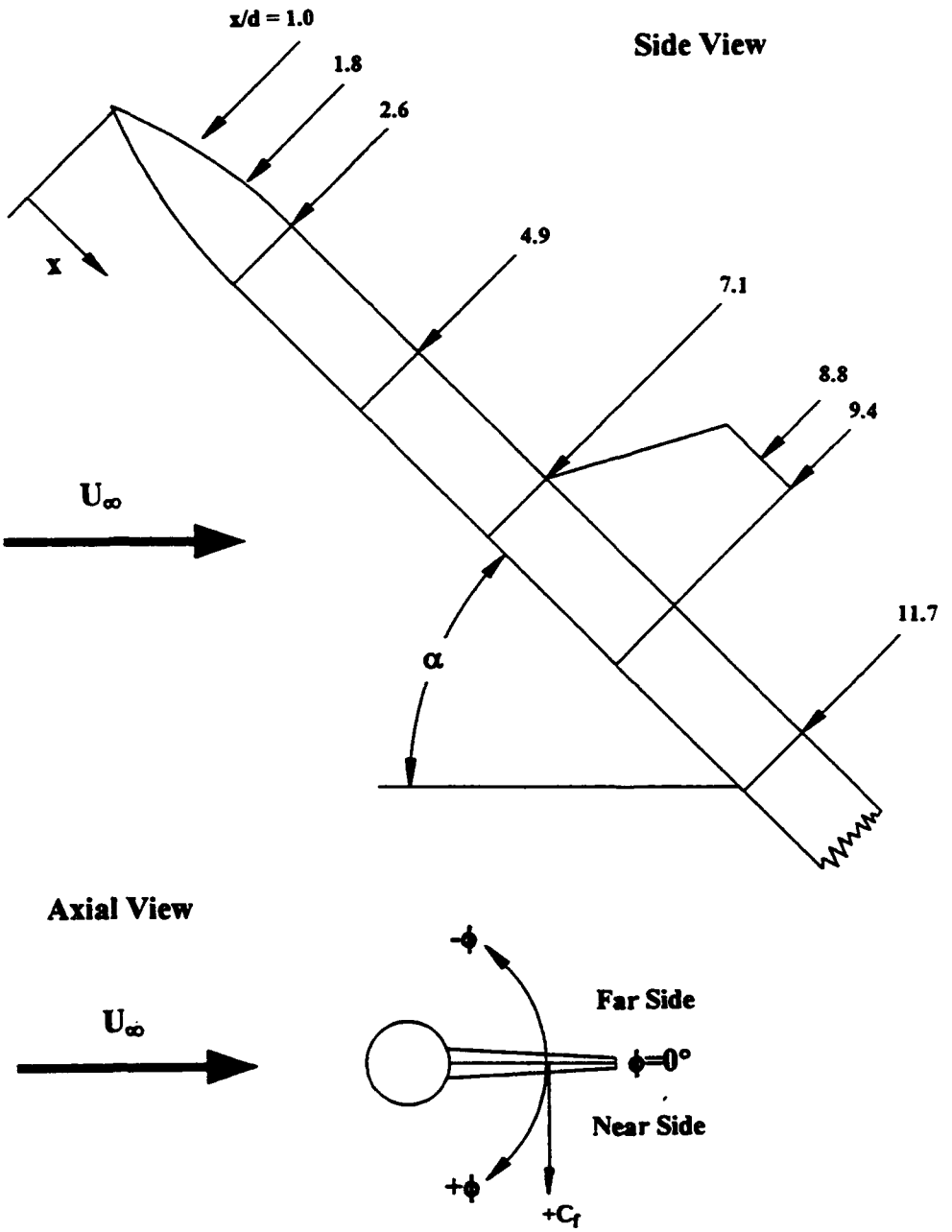

Figure 3(a). Model Schematic and Coordinate System.

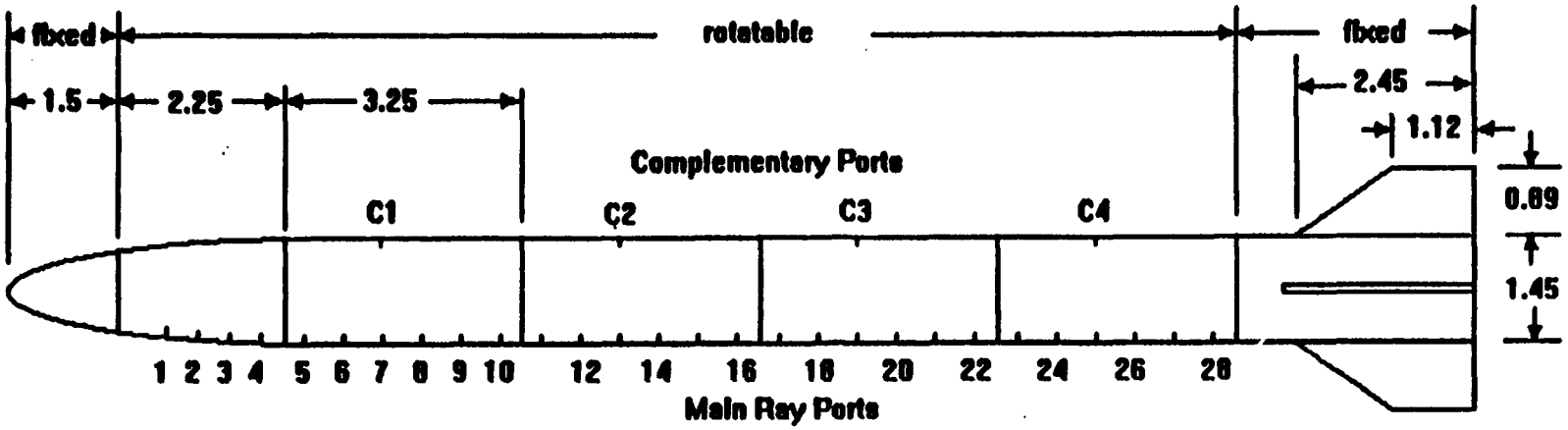

Port	1	2	3	4	5	6	7	8	9	10	11	12	13	14	15	16	17	18	19	20	21	22	23	24	25	26	27	28
x/d	1.5	1.8	2.1	2.4	2.8	3.2	3.6	3.9	4.3	4.7	5.1	5.4	5.8	6.2	6.6	6.9	7.3	7.7	8.1	8.4	8.8	9.2	9.6	10.0	10.3	10.7	11.1	11.5
Complementary							C1						C2						C3						C4			

Notes: a) Dimension in Inches, Drawn to Scale 1 : 1.86
b) Body and Aftbody Sections are 3.25 Inches Long
c) Radius of Ogive is 9.43 Inches

Figure 3b. Schematic of the Location of the Pressure Ports and Corresponding x/d

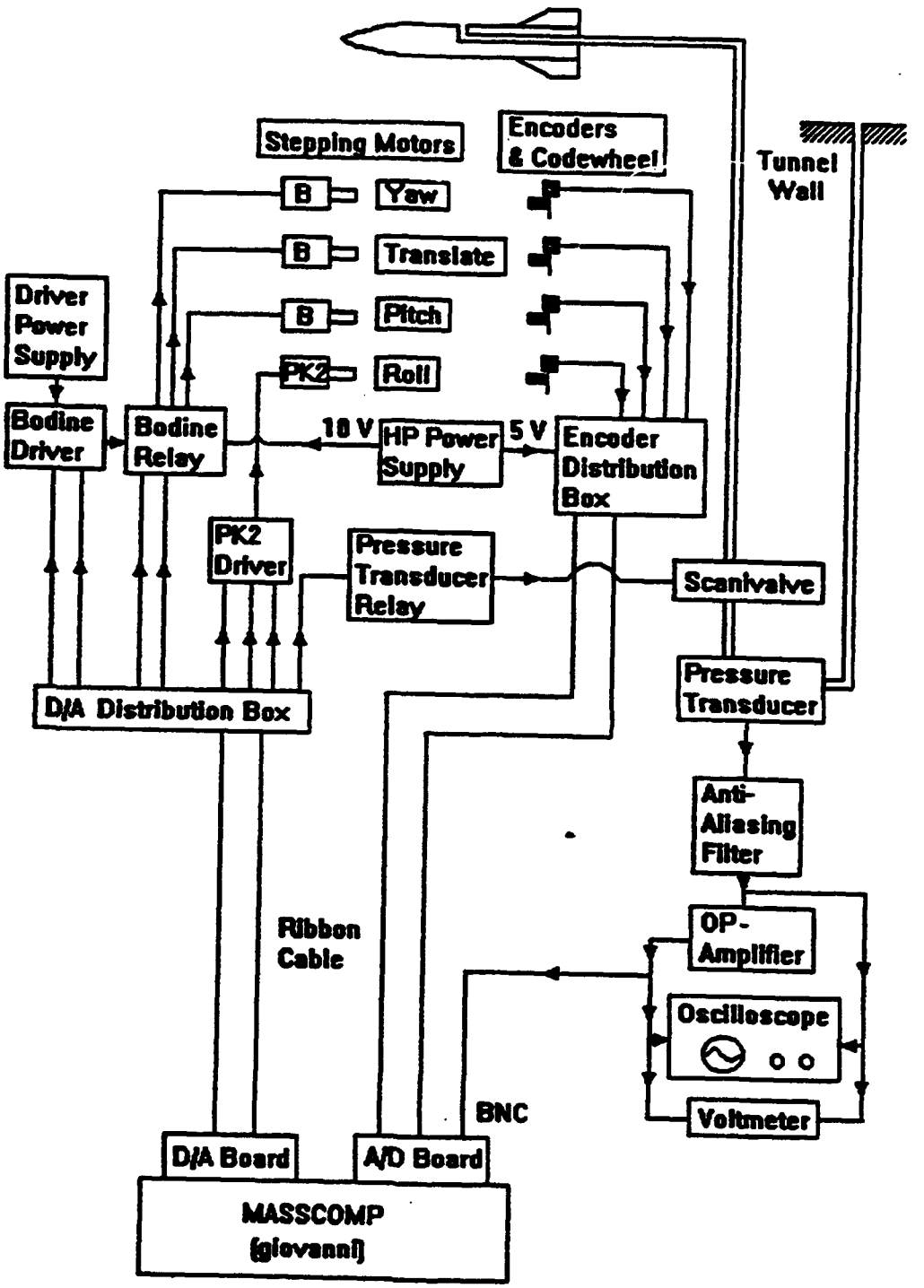

Figure 3 c. Schematic of the Electrical Interface between the Computer, Model, and Positioning System; and Pressure Setup

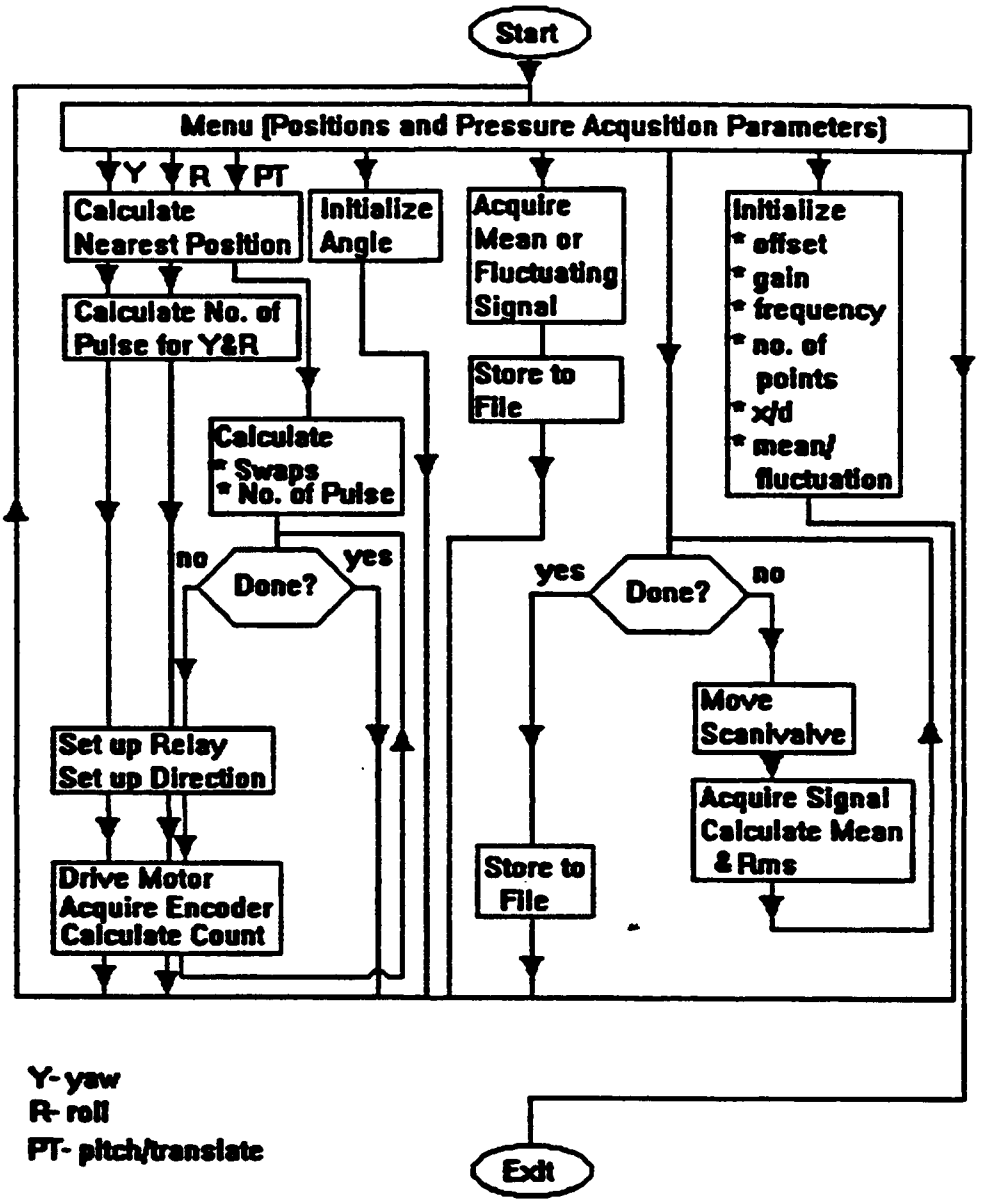

Figure 3 d. Block Diagram of Motion Control and Pressure Acquisition Code

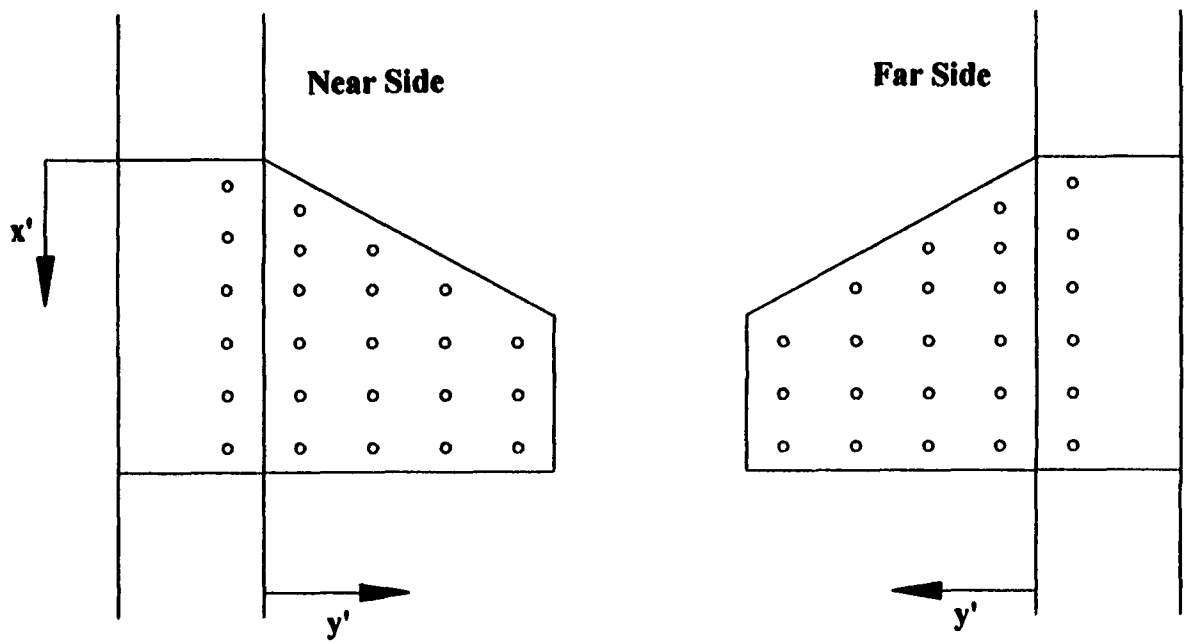

Figure 4. Pressure Port Locations on Fin Section.

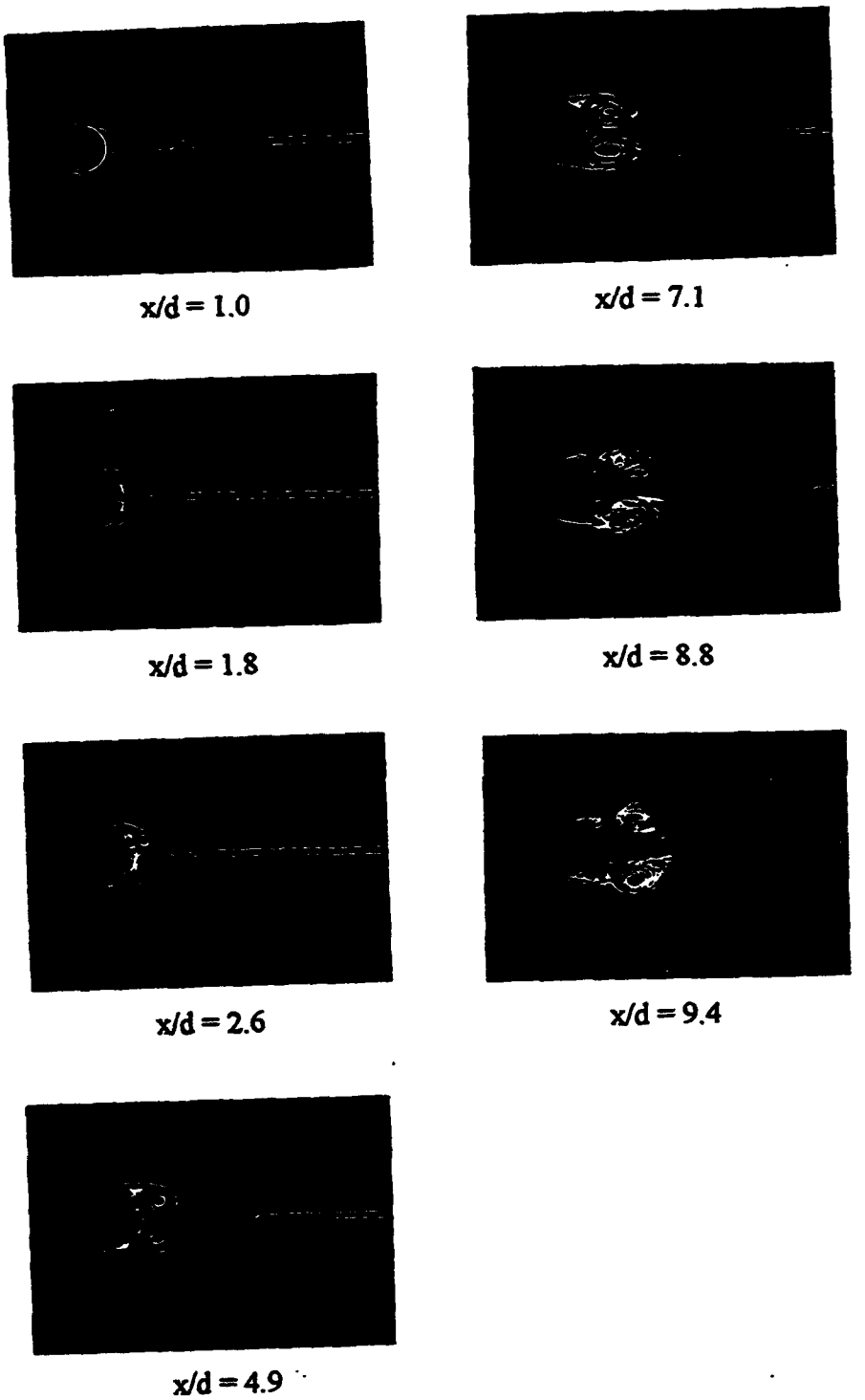

Figure 5. Cross-Sectional Flow Visualization Showing Flowfield Development ($\alpha = 30°$, $\phi = 0°$, $Re_d = 6000$, $(x/d)_f = 7.1$).

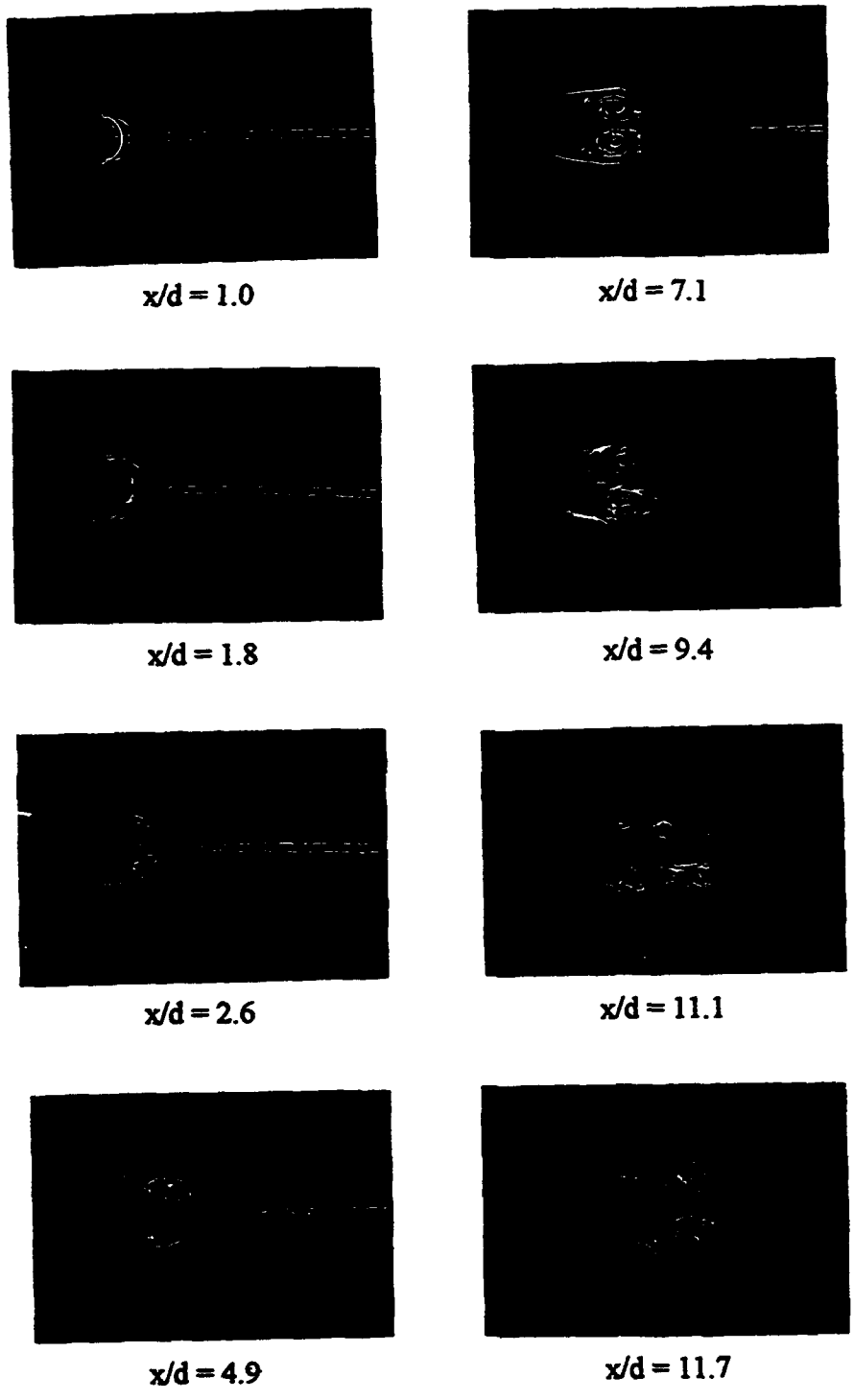

Figure 6. Cross-Sectional Flow Visualization Showing Flowfield Development ($\alpha = 30°$, $\phi = 0°$, $Re_d = 6000$, $(x/d)_f = 9.4$).

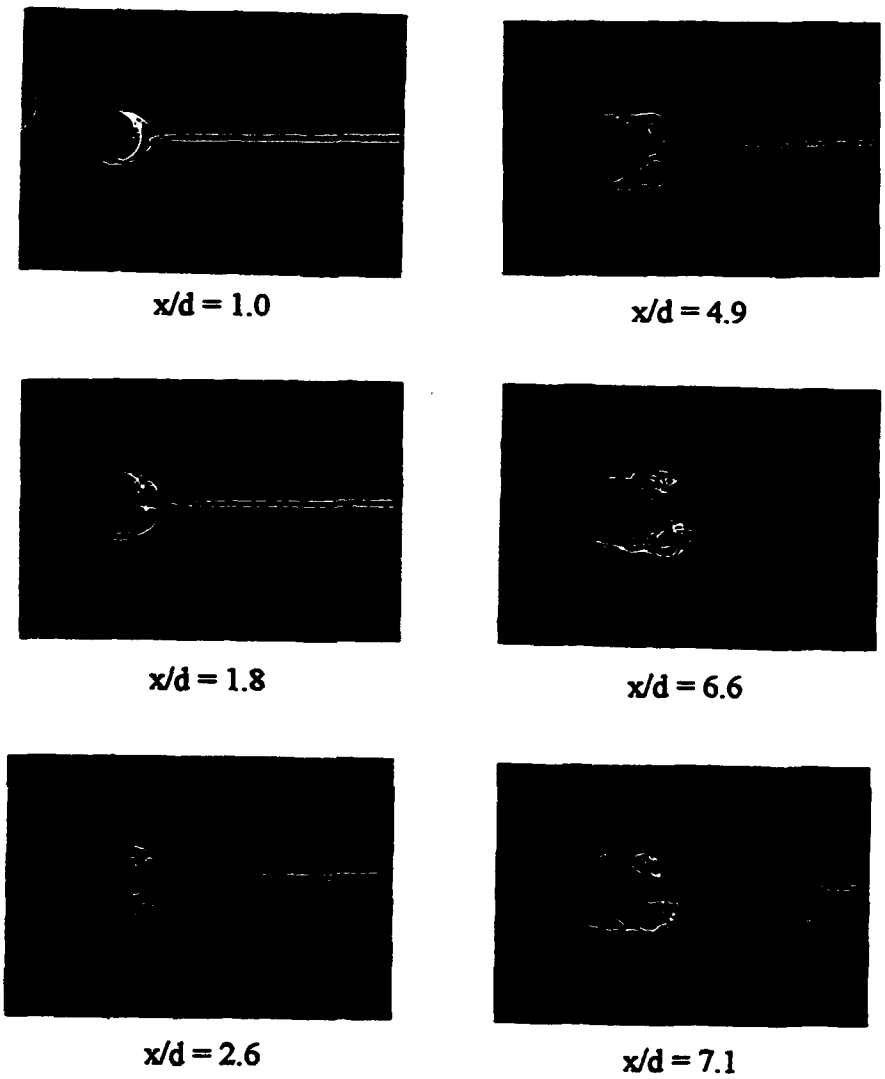

Figure 7. Cross-Sectional Flow Visualization Showing Flowfield Development ($\alpha = 30°$, $\phi = 0°$, $Re_d = 6000$, $(x/d)_f = 4.9$).

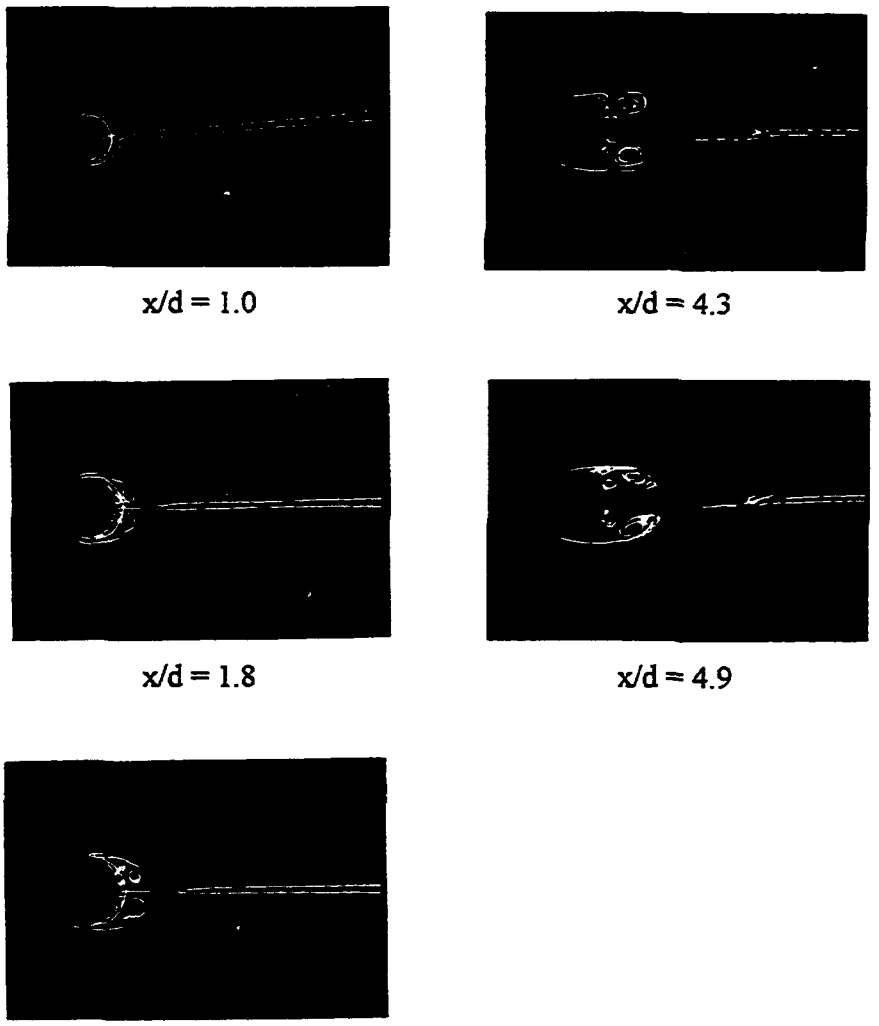

Figure 8. Cross-Sectional Flow Visualization Showing Flowfield Development ($\alpha = 30°$, $\phi = 0°$, $Re_d = 6000$, $(x/d)_f = 2.6$).

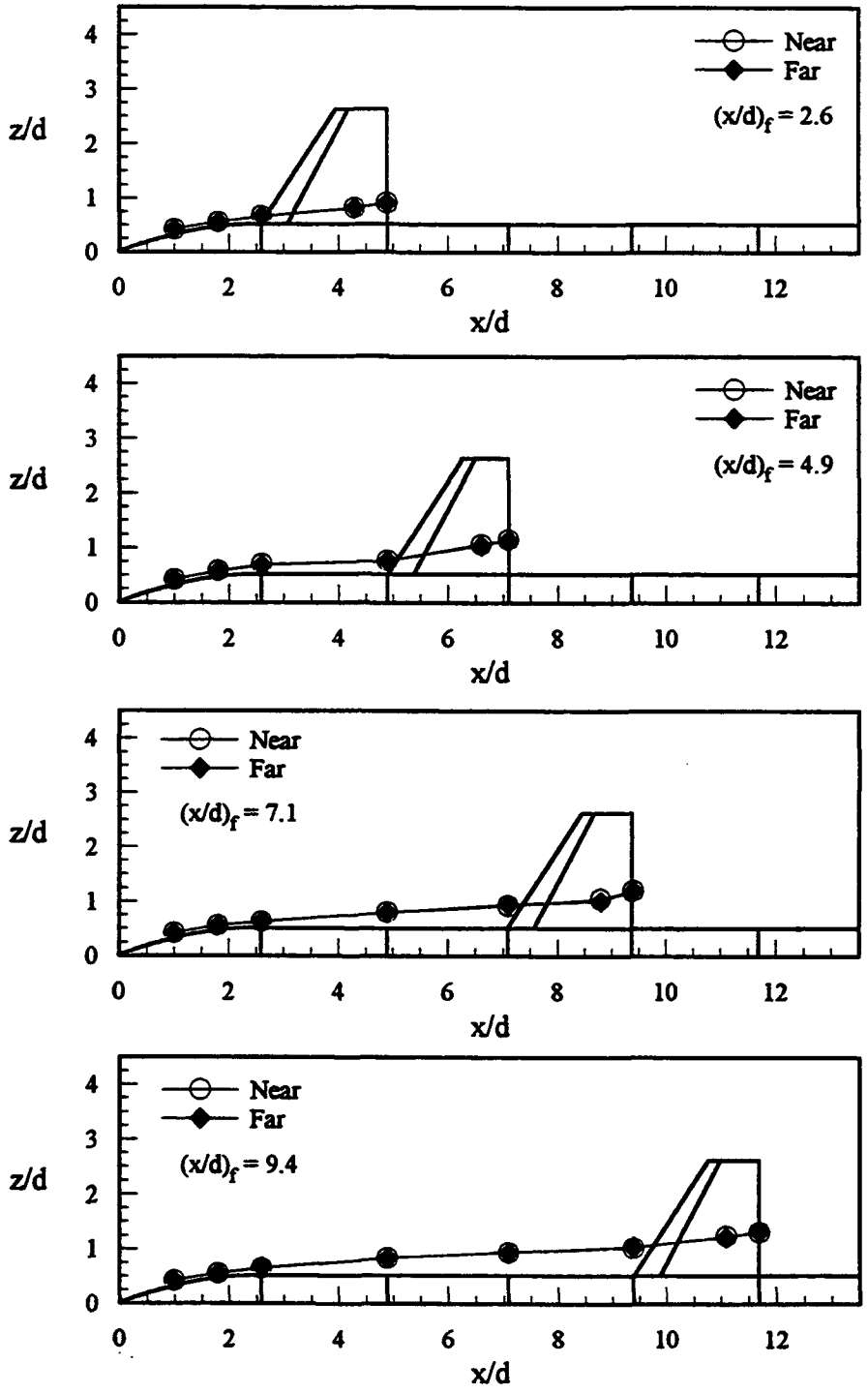

Figure 9. Vortex Center Trajectories, Side View ($\alpha = 30°$, $\phi = 0°$, $Re_d = 6000$).

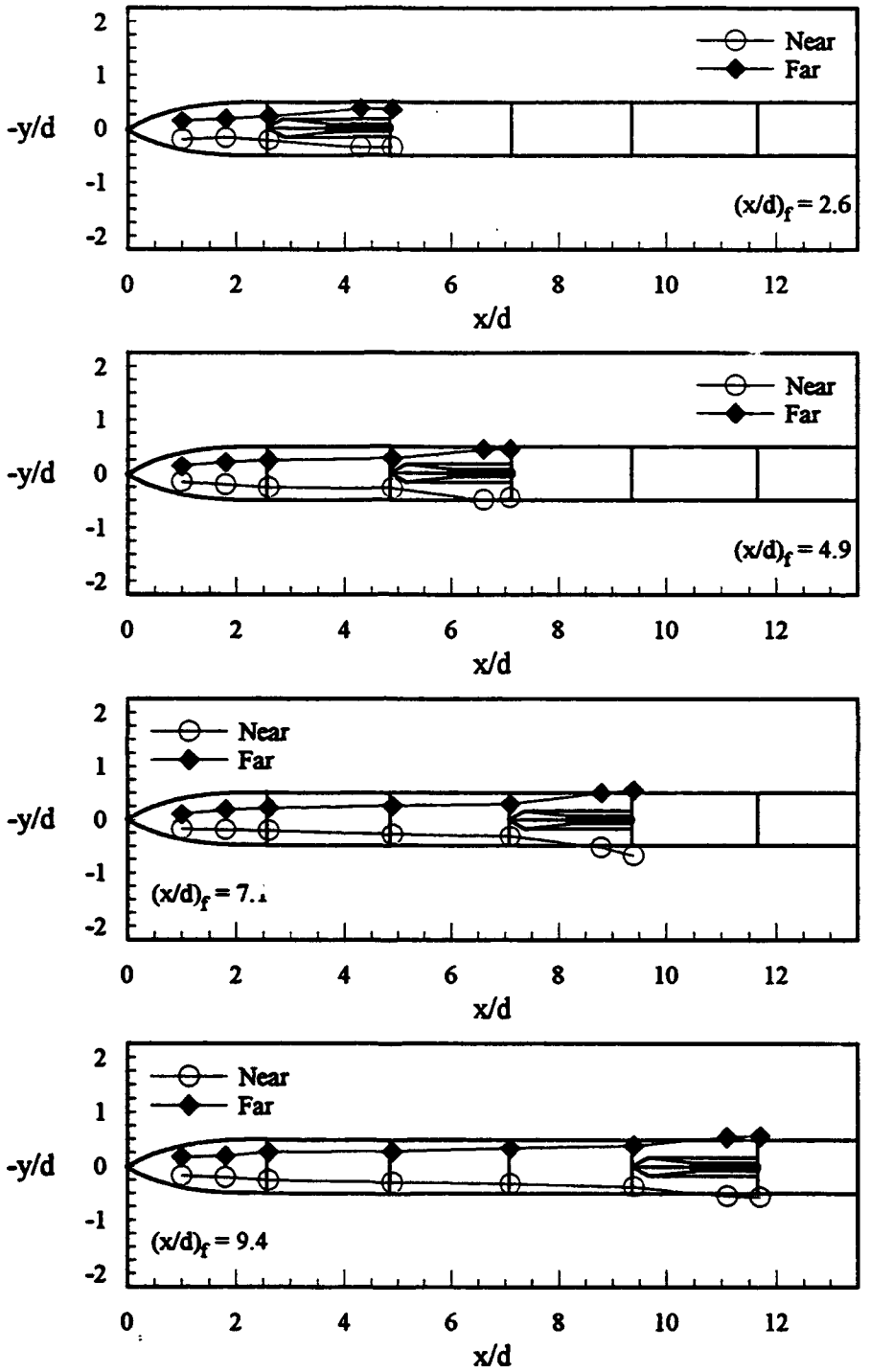

Figure 10. Vortex Center Trajectories, Top View ($\alpha = 30°$, $\phi = 0°$, $Re_d = 6000$).

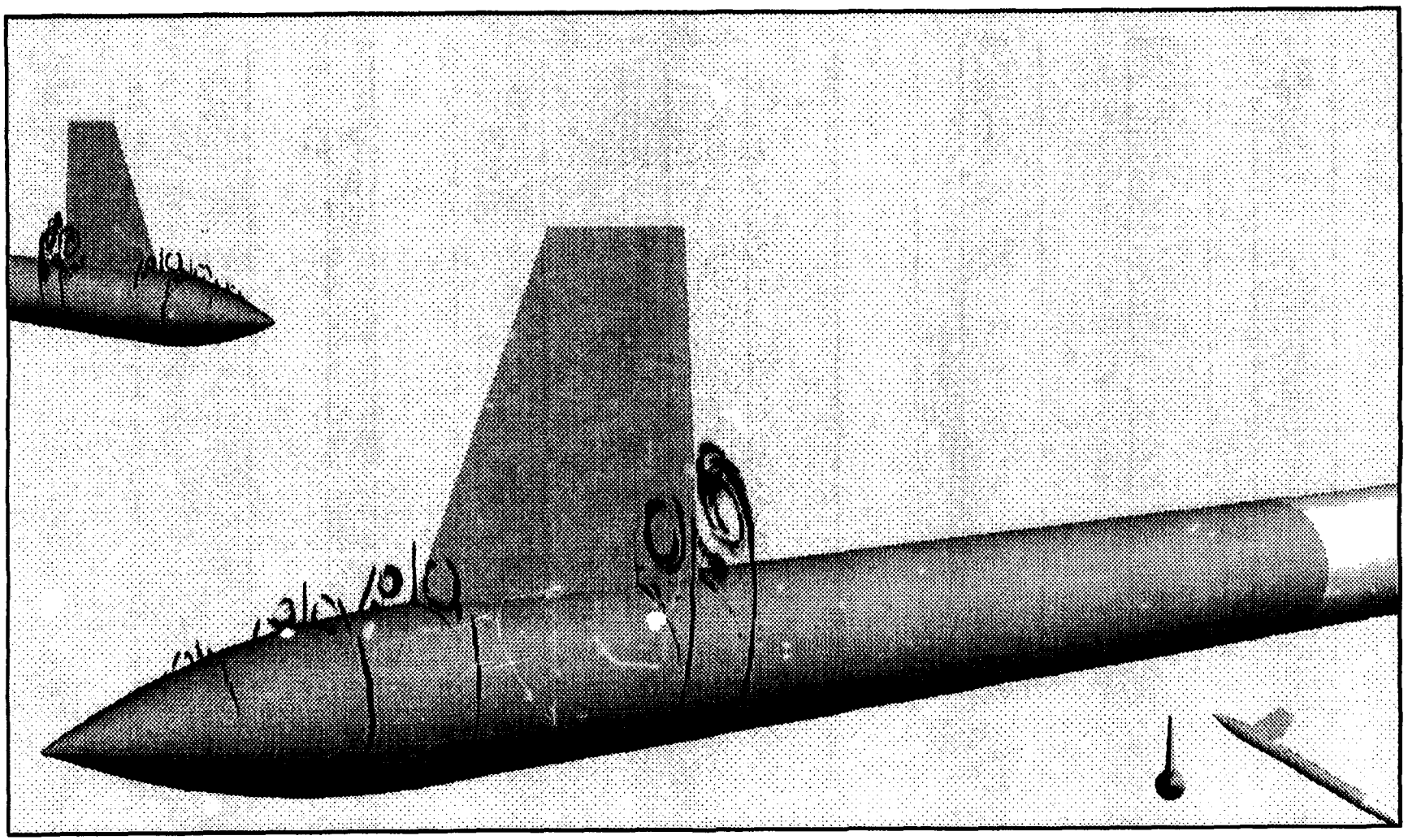

Figure 11. Three-Dimensional Perspective View of Flowfield ($\alpha = 30°$, $\phi = 0°$, $Re_d = 6000$, $(x/d)_f = 2.6$).

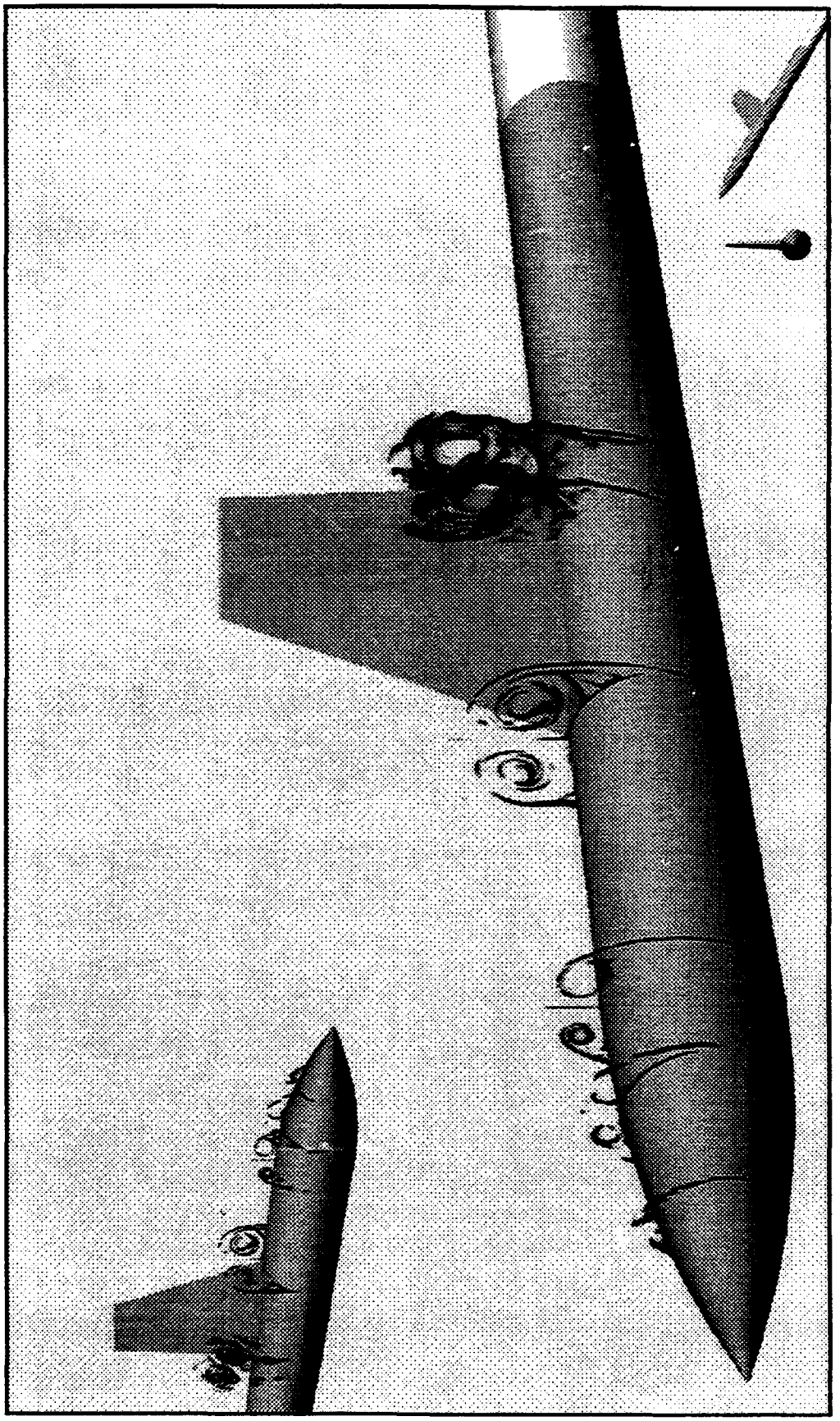

Figure 12. Three-Dimensional Perspective View of Flowfield ($\alpha = 30°$, $\phi = 0°$, $Re_d = 6000$, $(x/d)_f = 4.9$).

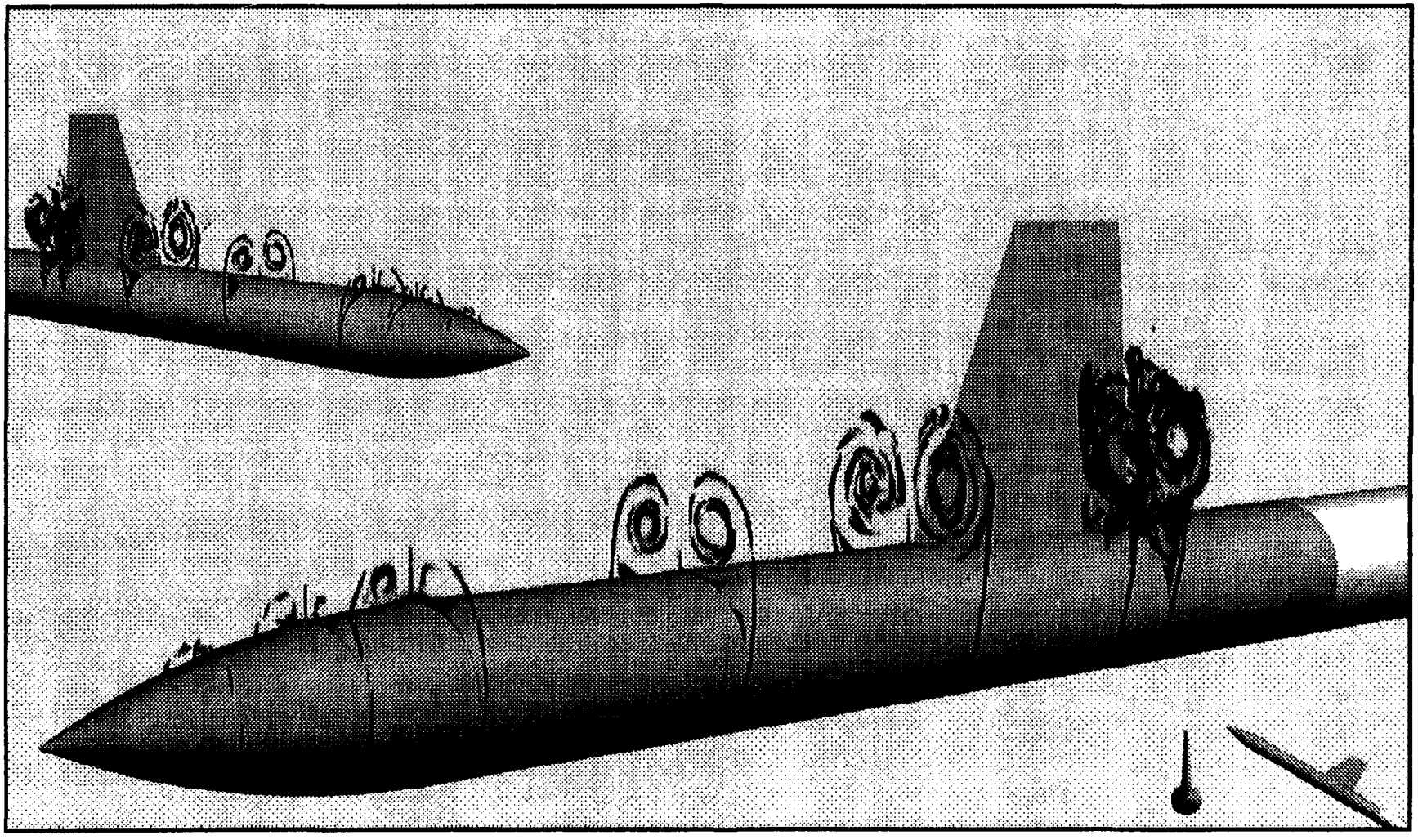

Figure 13. Three-Dimensional Perspective View of Flowfield ($\alpha = 30°$, $\phi = 0°$, $Re_d = 6000$, $(x/d)_f = 7.1$).

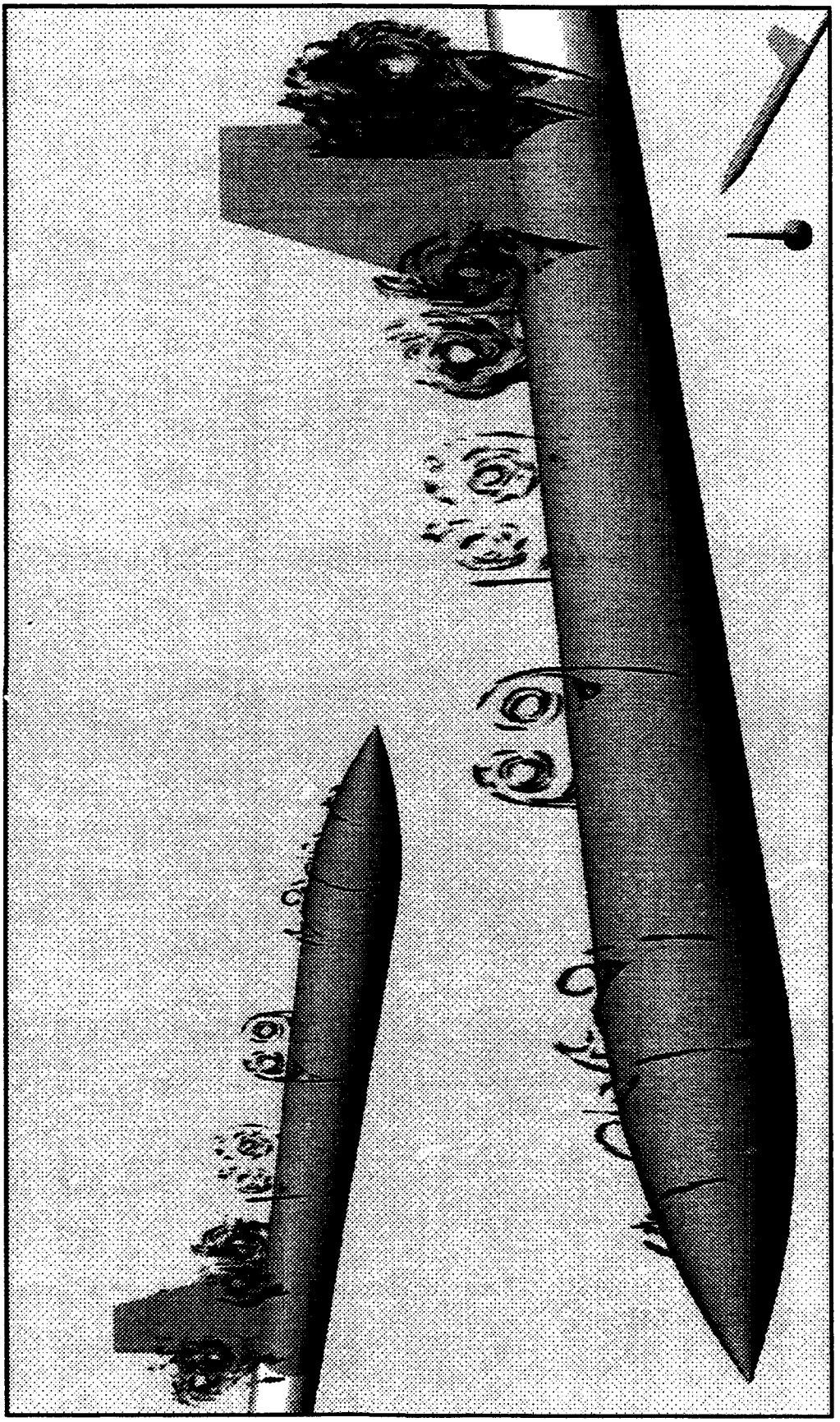

Figure 14. Three-Dimensional Perspective View of Flowfield ($\alpha = 30°$, $\phi = 0°$, $Re_d = 6000$, $(x/d)_f = 9.4$).

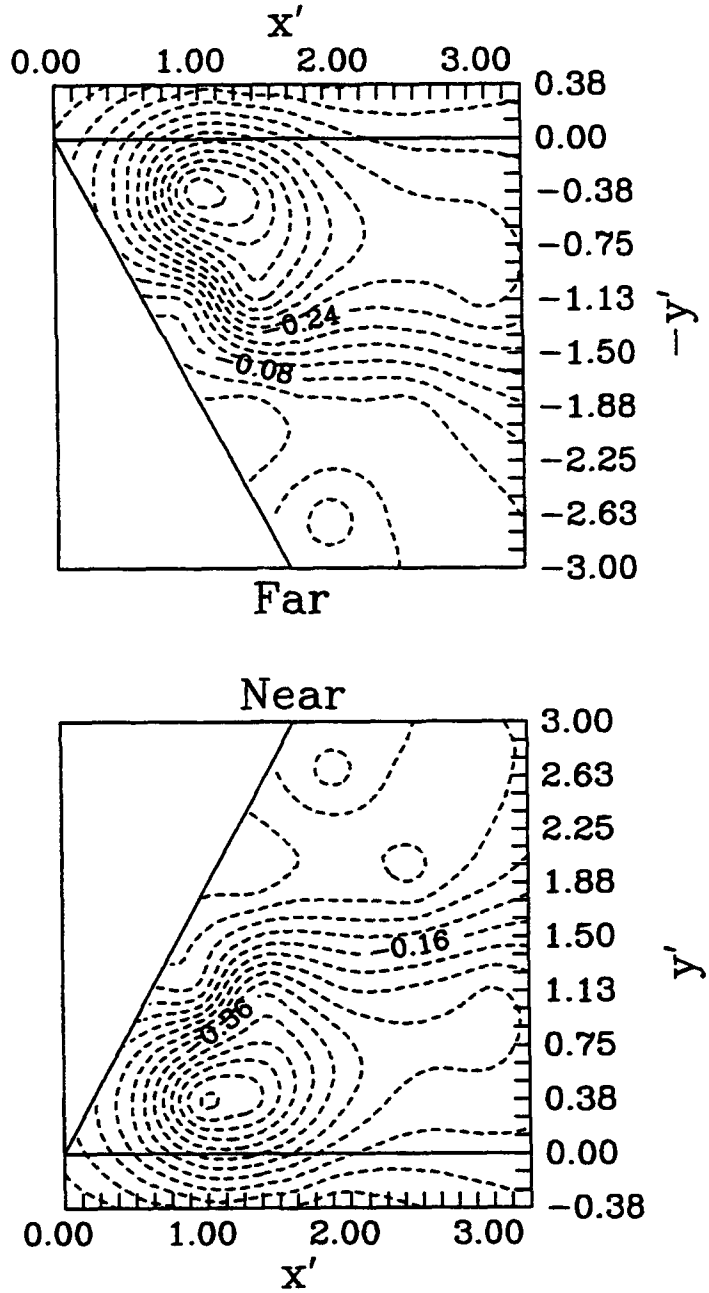

Figure 15. Coefficient of Pressure Contours on Fin ($\alpha = 30°$, $\phi = 0°$, $Re_d = 6000$, $(x/d)_f = 7.1$).

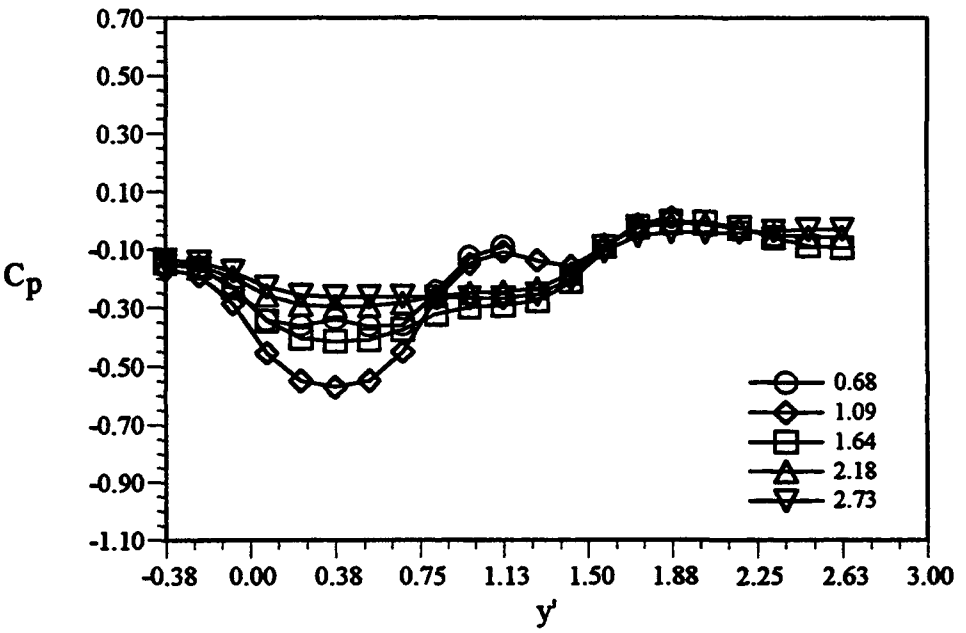

Figure 16. Spanwise Pressure Distributions on Near Side of Fin ($\alpha = 30°$, $\phi = 0°$, $Re_d = 6000$, $(x/d)_f = 7.1$).

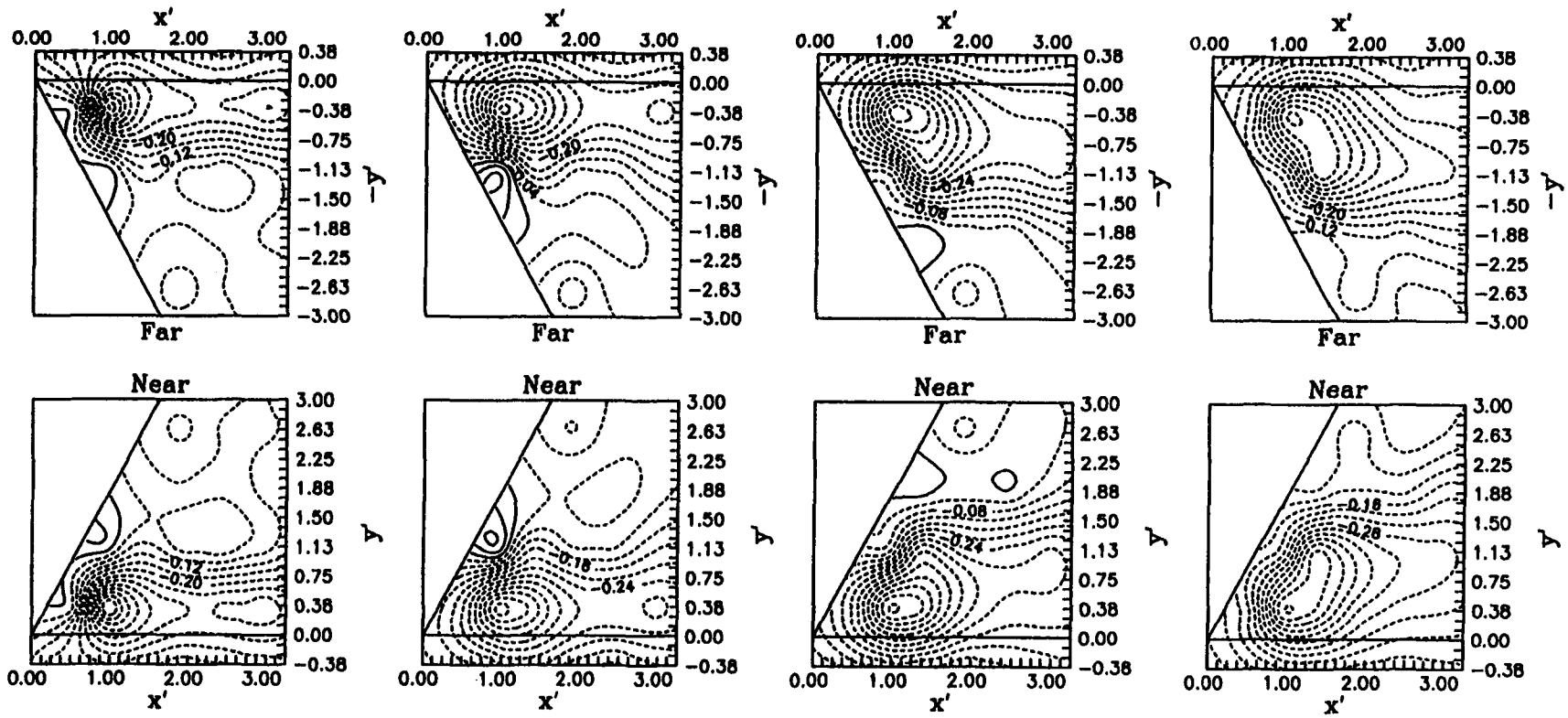

(a) $(x/d)_f = 2.6$ (b) $(x/d)_f = 4.9$ (c) $(x/d)_f = 7.1$ (d) $(x/d)_f = 9.4$

Figure 17. Coefficient of Pressure Contours on Fin ($\alpha = 30°$, $\phi = 0°$, $Re_d = 6000$).

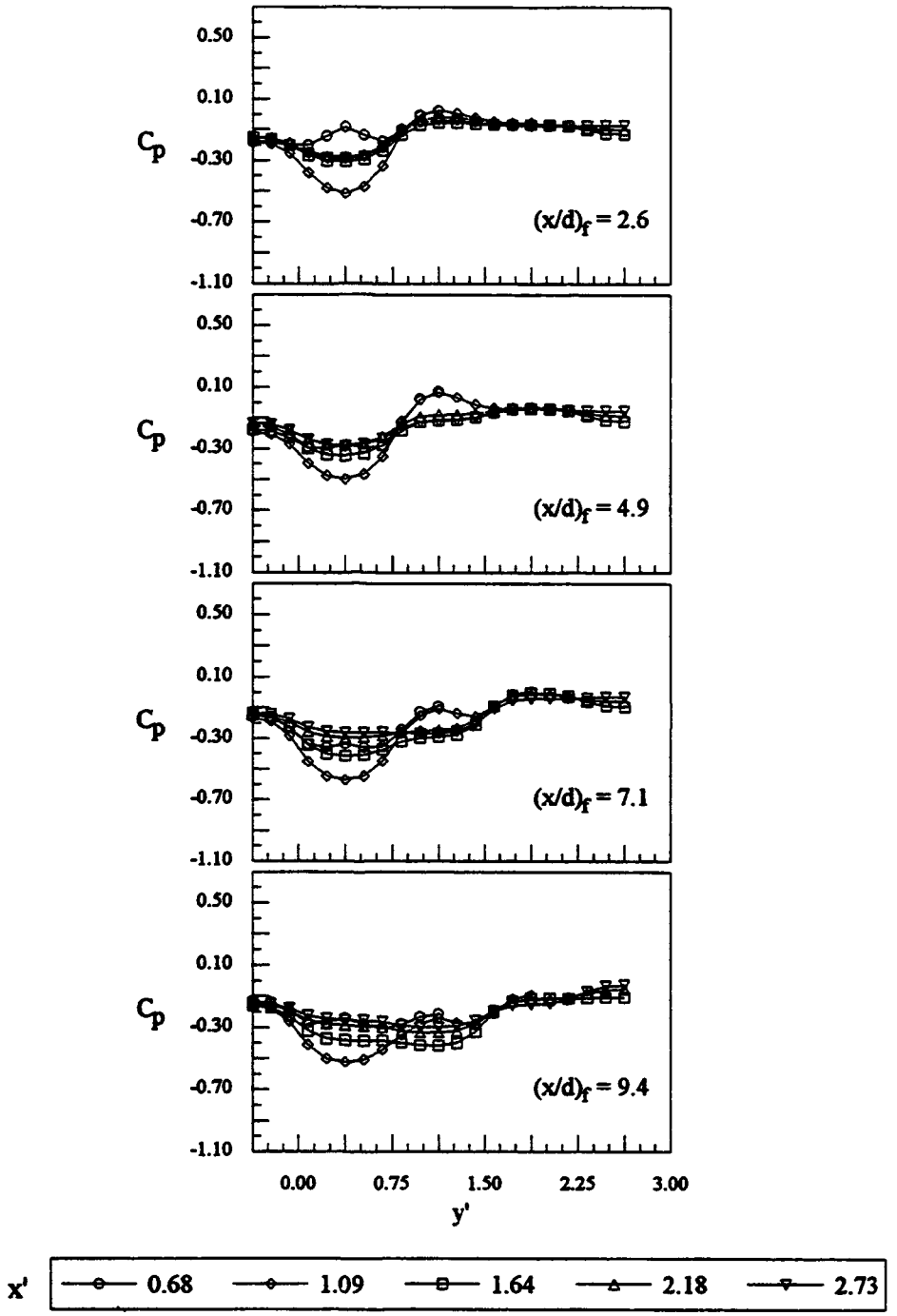

Figure 18. Spanwise Pressure Distributions on Near Side of Fin ($\alpha = 30°$, $\phi = 0°$, $Re_d = 6000$).

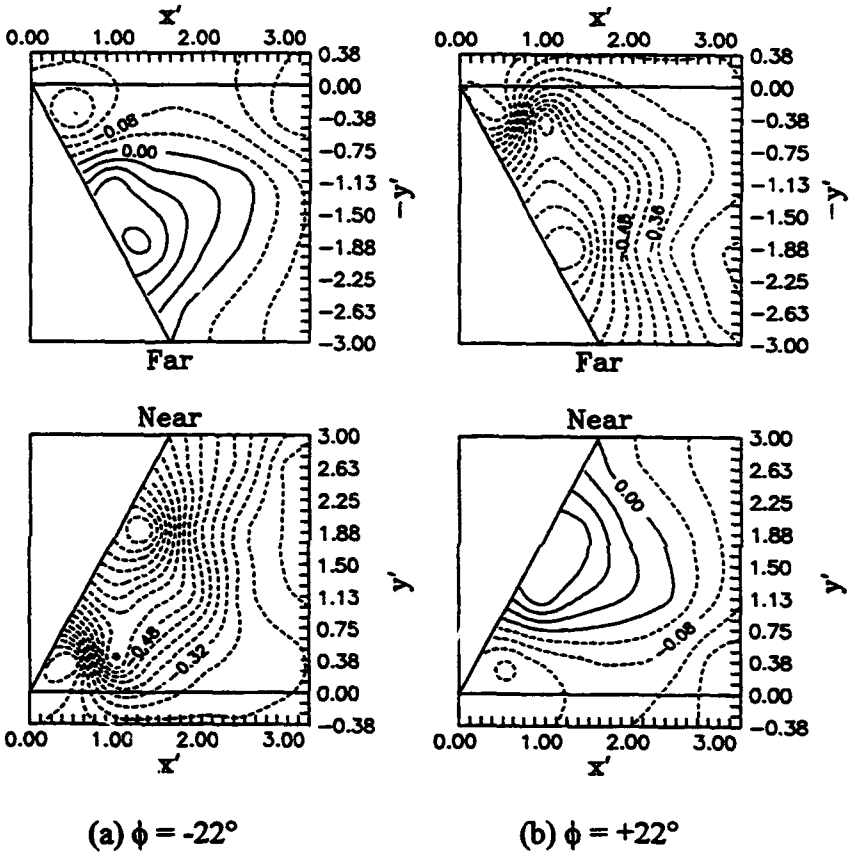

Figure 19. Coefficient of Pressure Contours on Fin ($\alpha = 30°$, $Re_d = 6000$, $(x/d)_f = 7.1$).

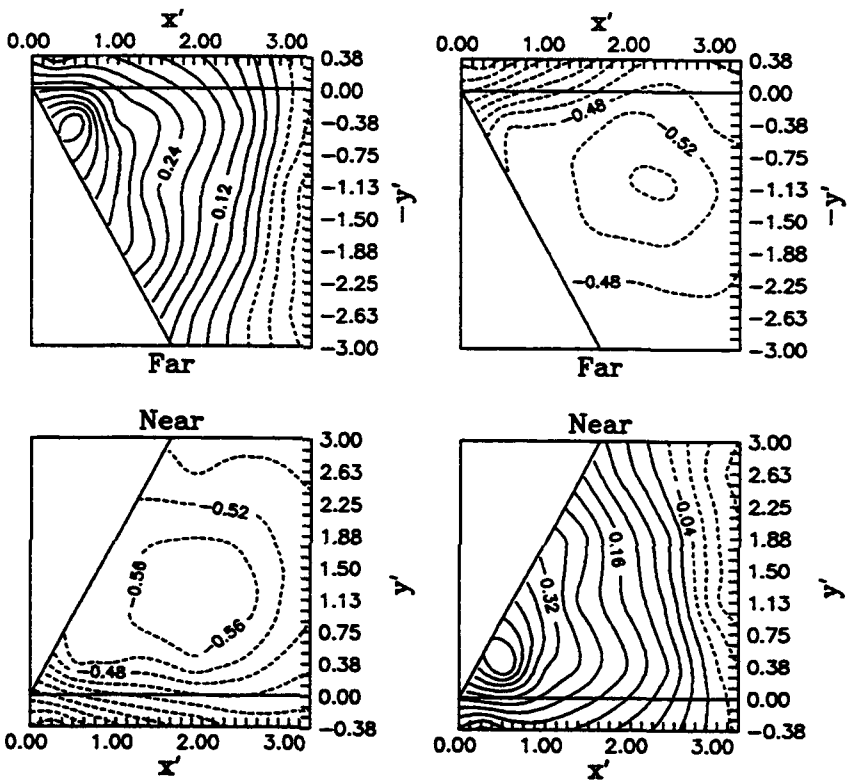

Figure 20. Coefficient of Pressure Contours on Fin ($\alpha = 30°$, $Re_d = 6000$, $(x/d)_f = 7.1$).

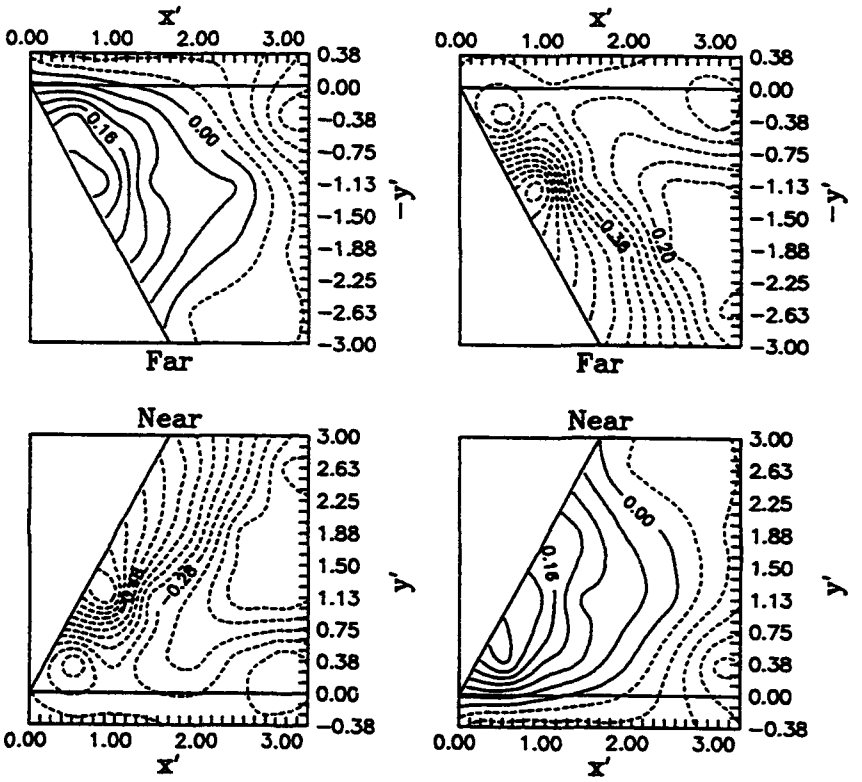

Figure 21. Coefficient of Pressure Contours on Fin ($\alpha = 30°$, $Re_d = 6000$, $(x/d)_f = 2.6$).

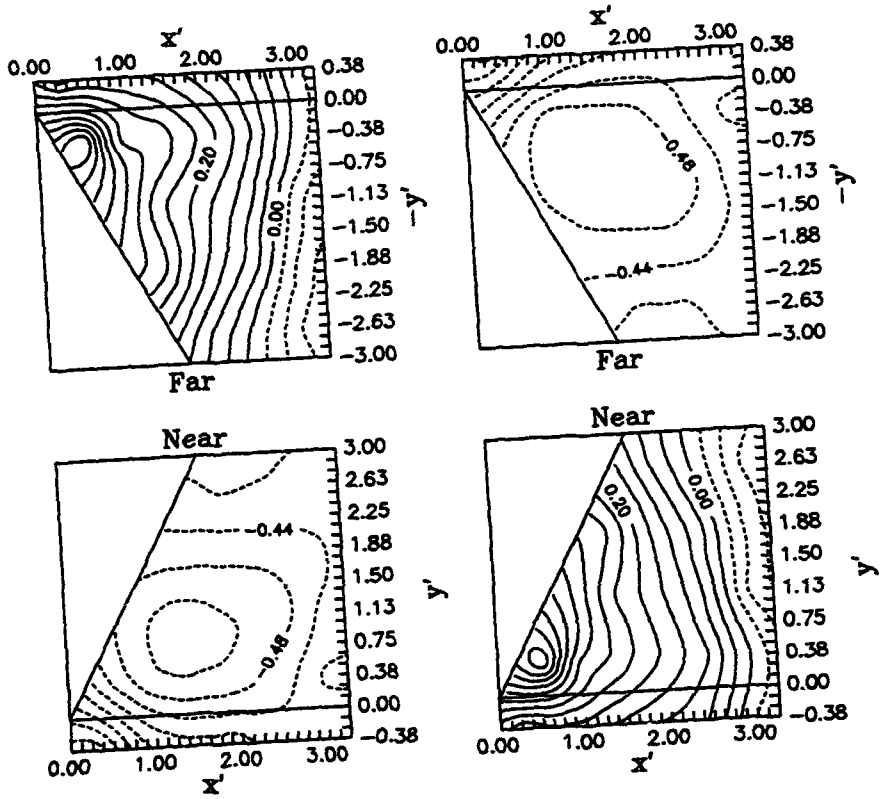

(a) $\phi = -54°$ (b) $\phi = +54°$

Figure 22. Coefficient of Pressure Contours on Fin ($\alpha = 30°$, $Re_d = 6000$, $(x/d)_f = 2.6$).

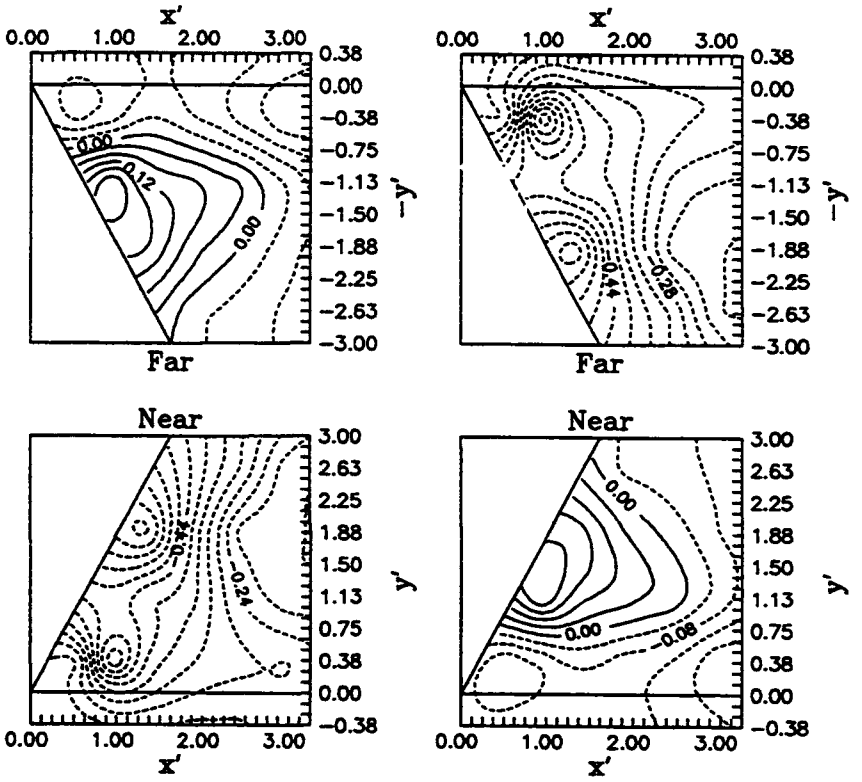

(a) $\phi = -22°$ (b) $\phi = +22°$

Figure 23. Coefficient of Pressure Contours on Fin ($\alpha = 30°$, $Re_d = 6000$, $(x/d)_f = 4.9$).

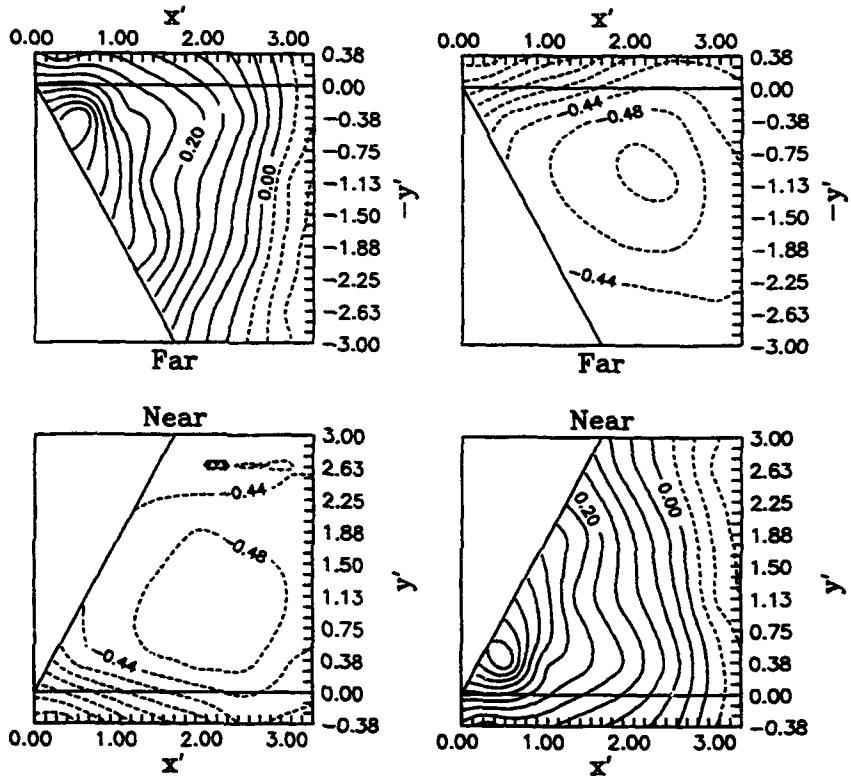

(a) $\phi = -54°$ (b) $\phi = +54°$

Figure 24. Coefficient of Pressure Contours on Fin ($\alpha = 30°$, $Re_d = 6000$, $(x/d)_f = 4.9$).

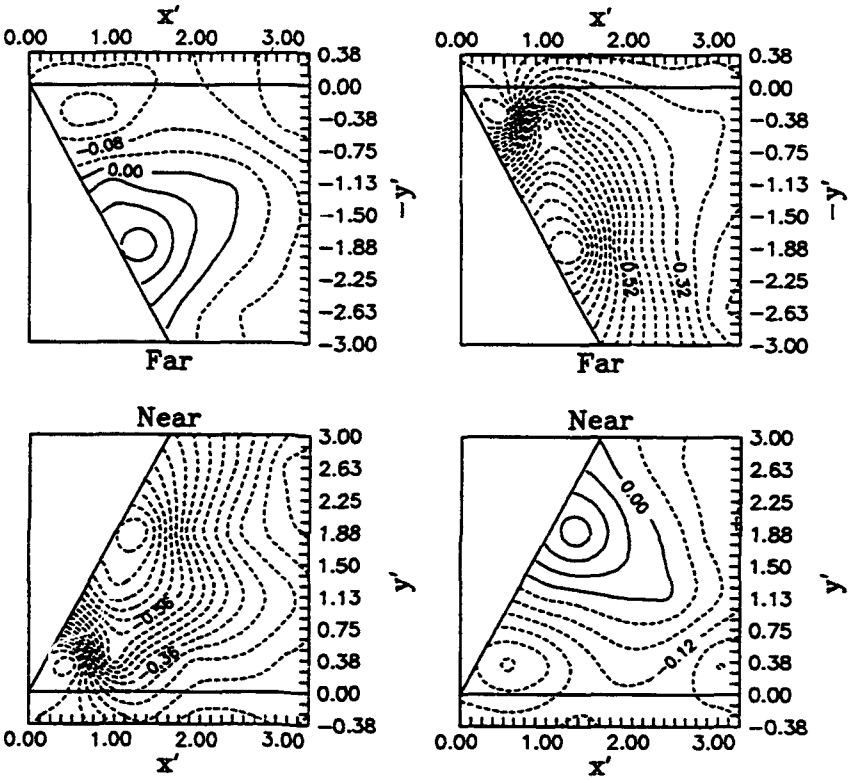

(a) $\phi = -22°$ (b) $\phi = +22°$

Figure 25. Coefficient of Pressure Contours on Fin ($\alpha = 30°$, $Re_d = 6000$, $(x/d)_f = 9.4$).

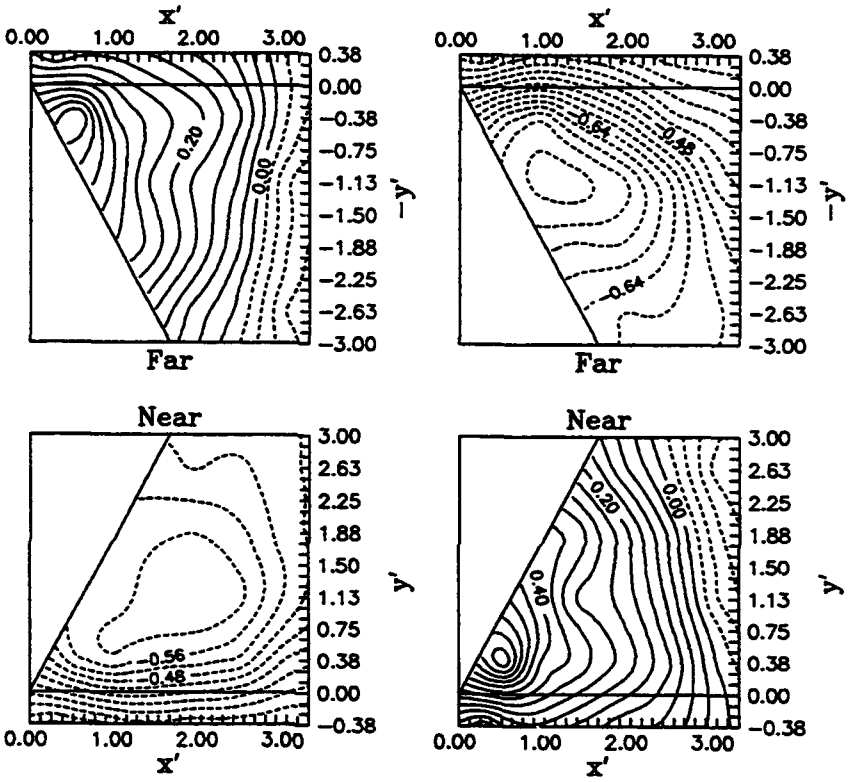

(a) $\phi = -54°$ (b) $\phi = +54°$

Figure 26. Coefficient of Pressure Contours on Fin ($\alpha = 30°$, $Re_d = 6000$, $(x/d)_f = 9.4$).

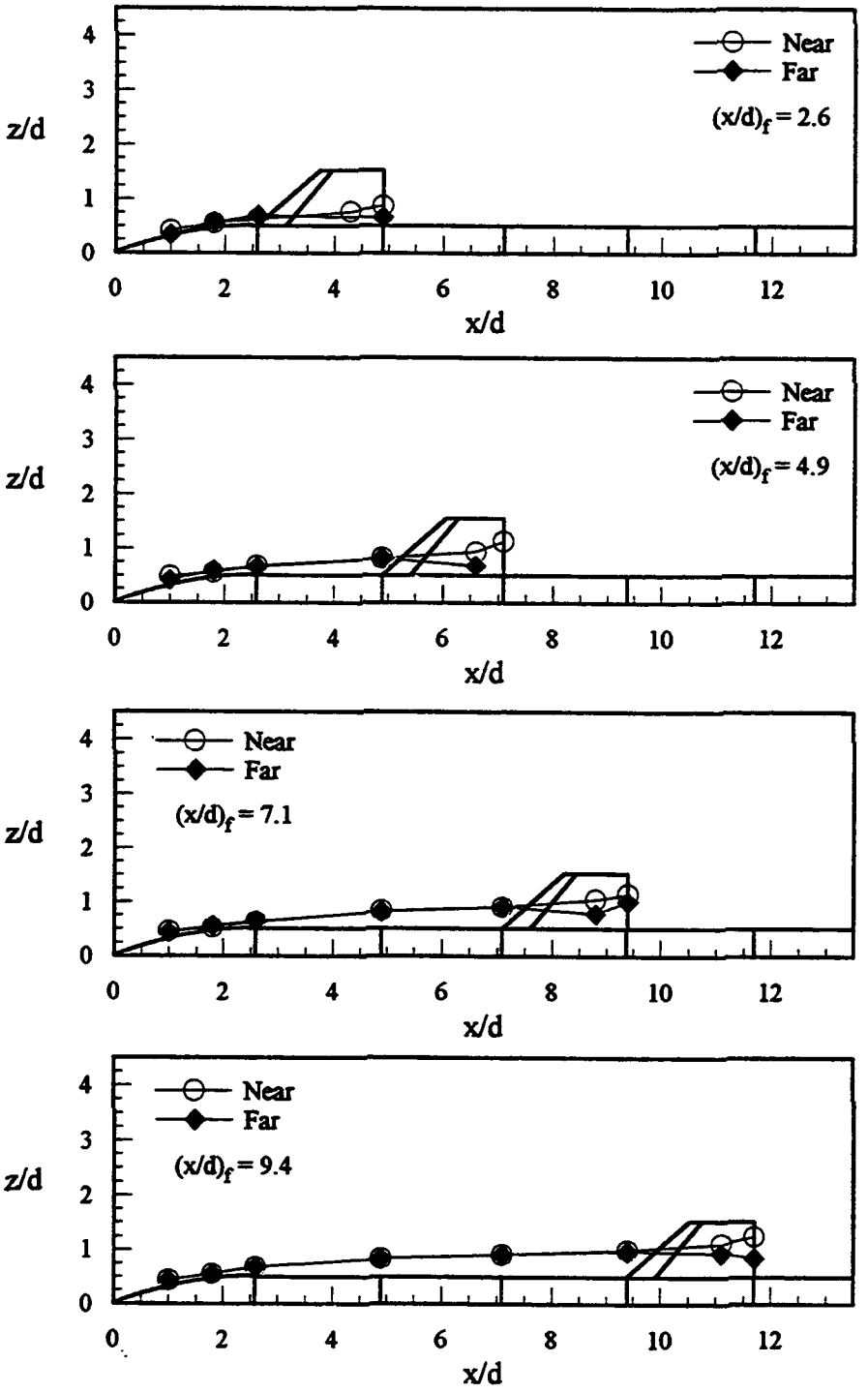

Figure 27. Vortex Center Trajectories, Side View ($\alpha = 30°$, $\phi = -54°$, $Re_d = 6000$).

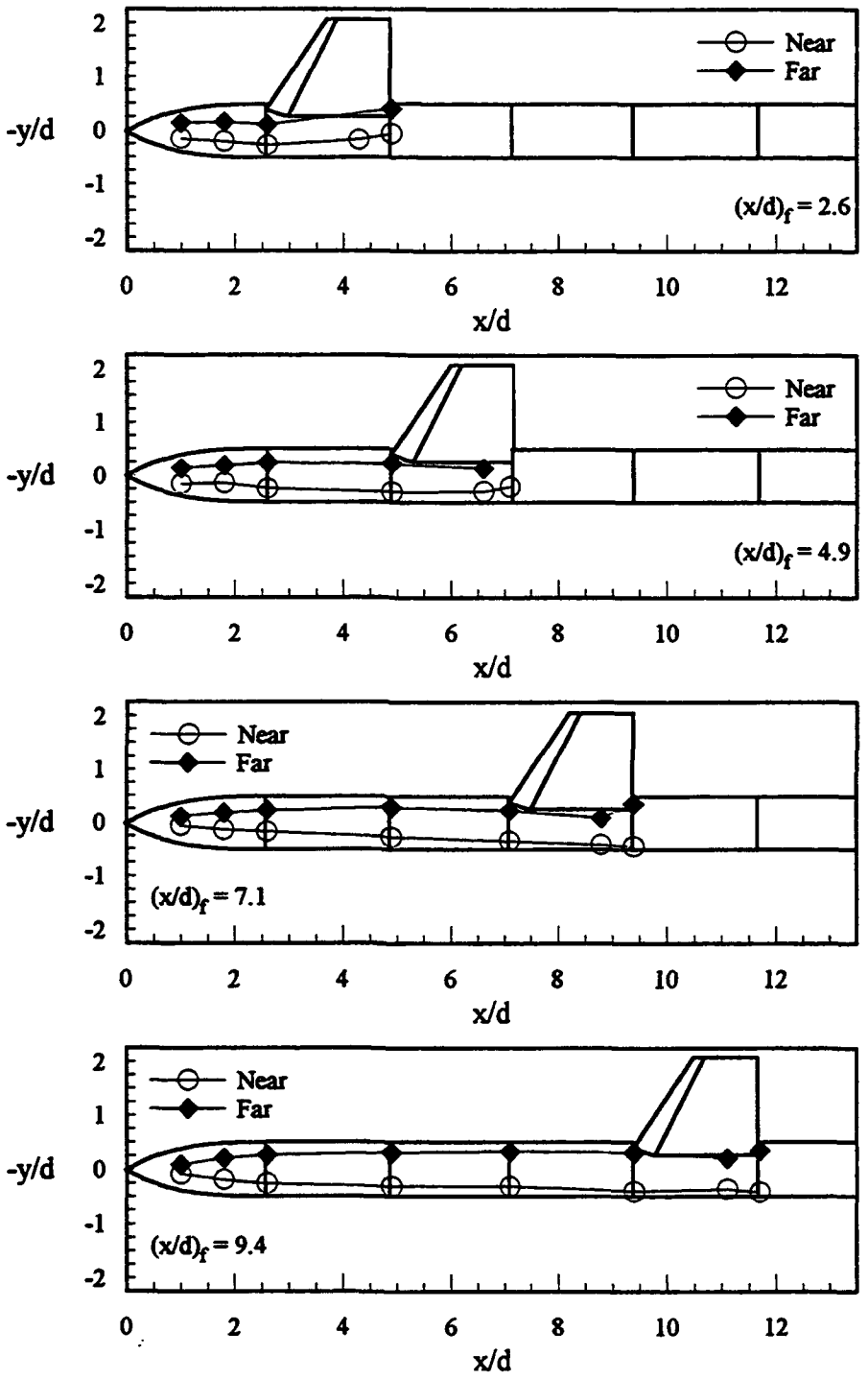

Figure 28. Vortex Center Trajectories, Top View ($\alpha = 30°$, $\phi = -54°$, $Re_d = 6000$).

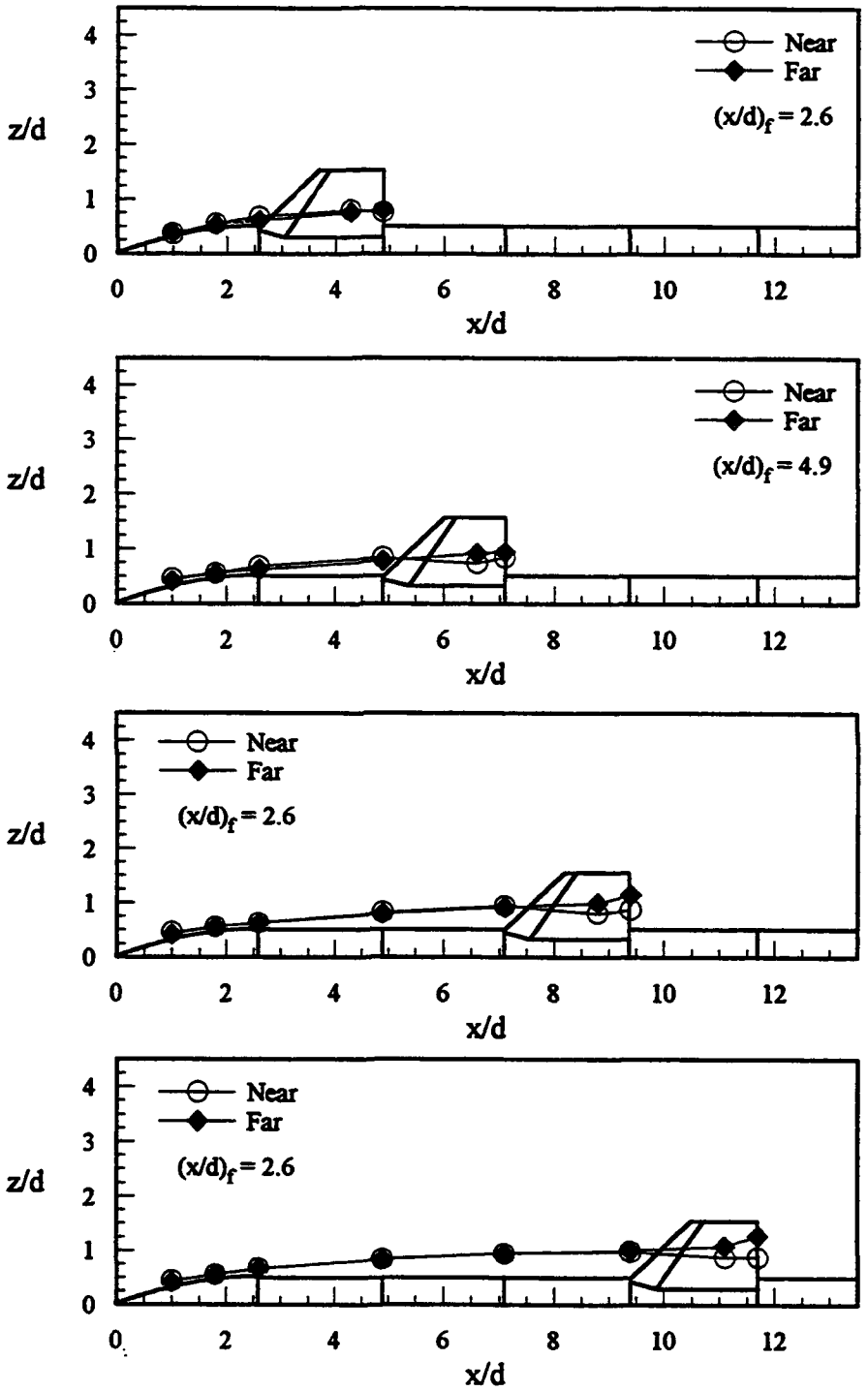

Figure 29. Vortex Center Trajectories, Side View ($\alpha = 30°$, $\phi = +54°$, $Re_d = 6000$).

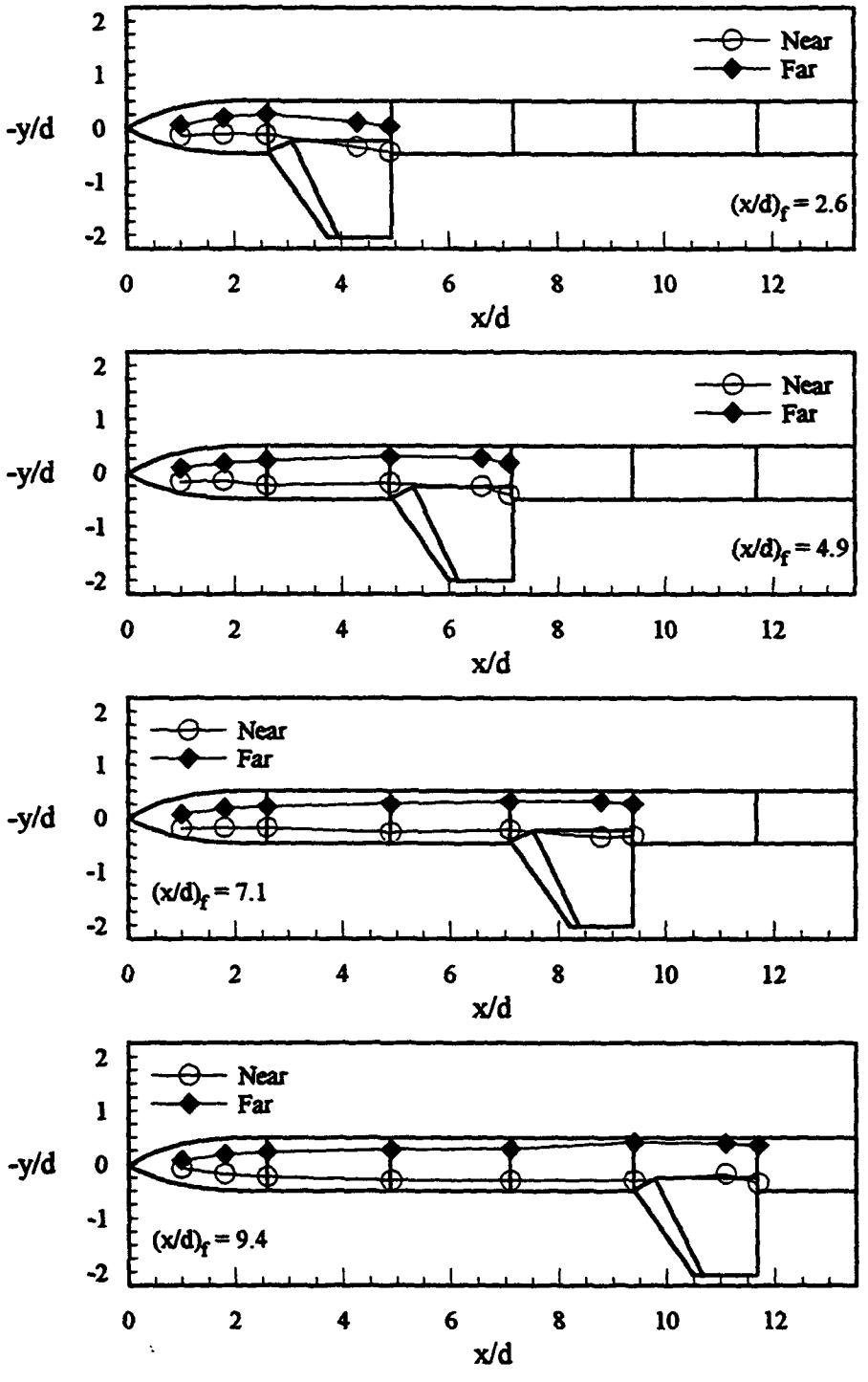

Figure 30. Vortex Center Trajectories, Top View ($\alpha = 30°$, $\phi = +54°$, $Re_d = 6000$).

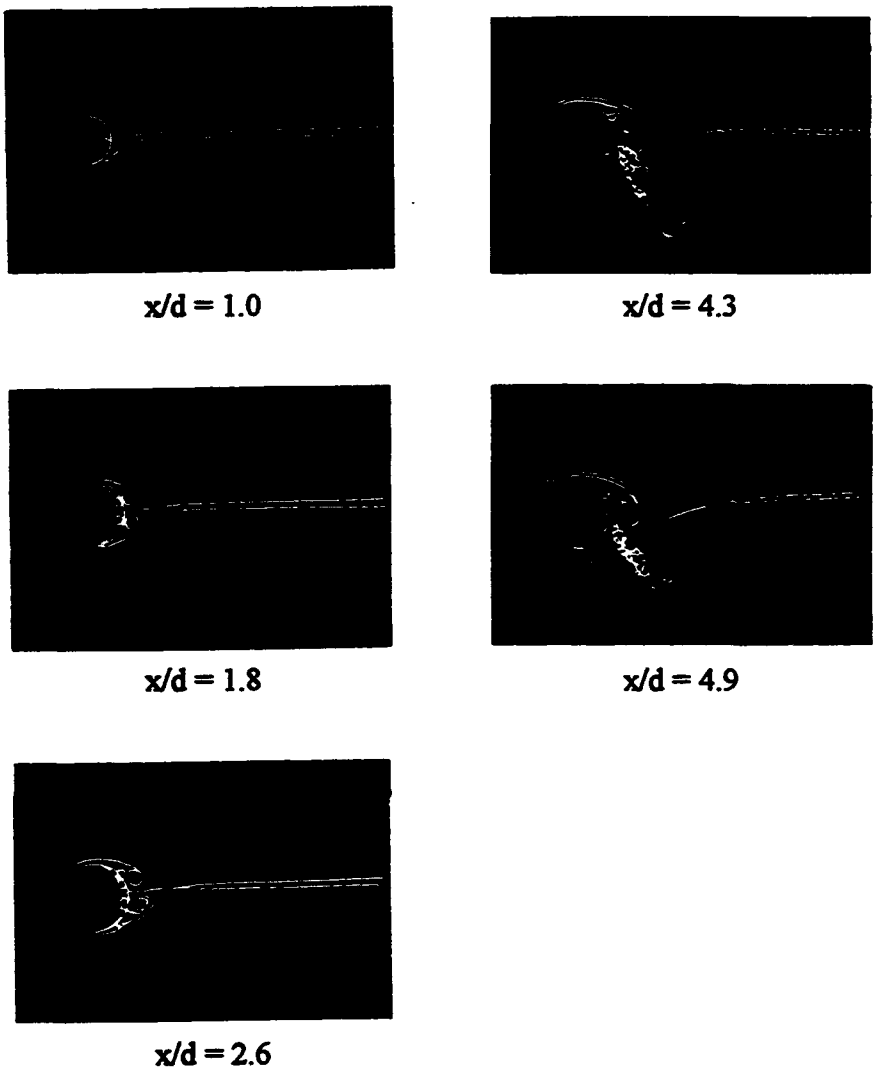

Figure 31. Cross-Sectional Flow Visualization Showing Flowfield Development ($\alpha = 30°$, $\phi = +54°$, $Re_d = 6000$, $(x/d)_f = 2.6$).

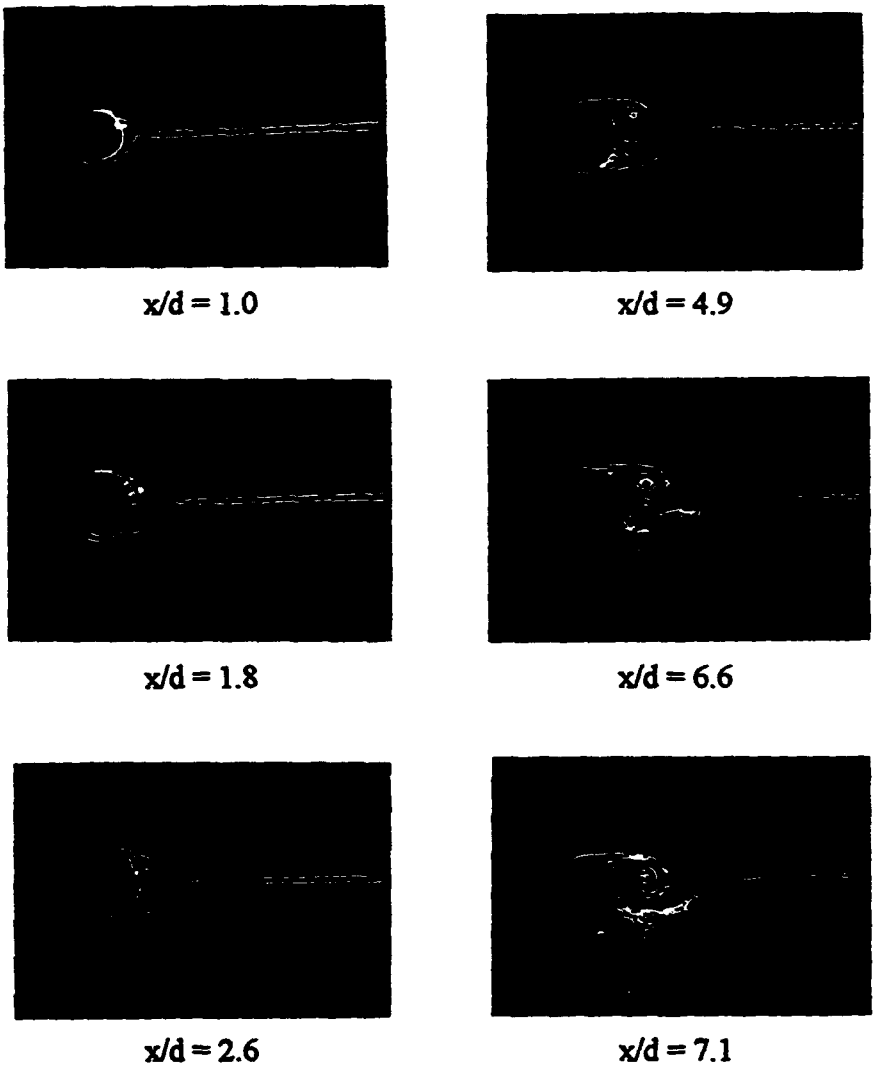

Figure 32. Cross-Sectional Flow Visualization Showing Flowfield Development ($\alpha = 30°$, $\phi = +54°$, $Re_d = 6000$, $(x/d)_f = 4.9$).

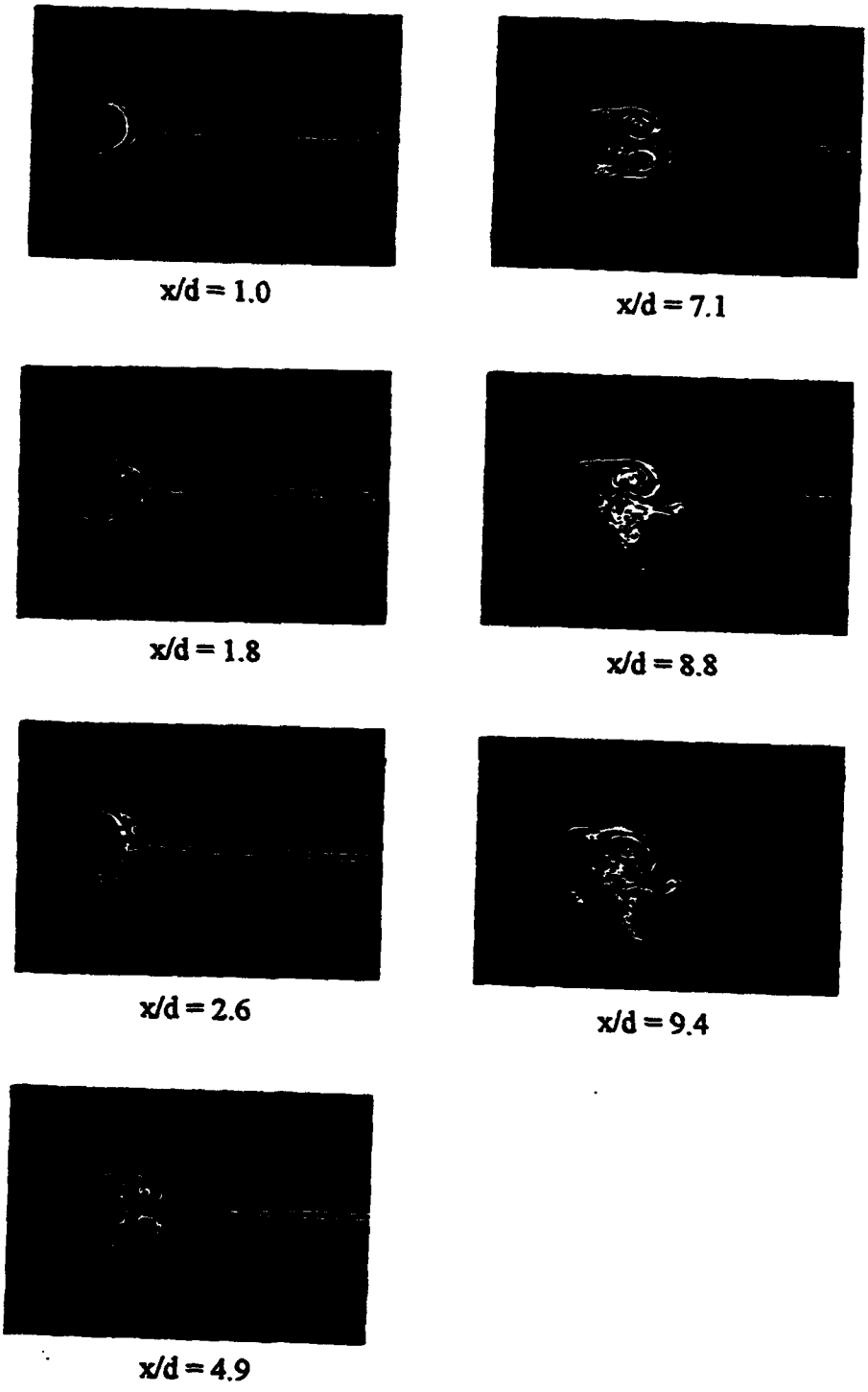

Figure 33. Cross-Sectional Flow Visualization Showing Flowfield Development ($\alpha = 30°$, $\phi = +54°$, $Re_d = 6000$, $(x/d)_f = 7.1$).

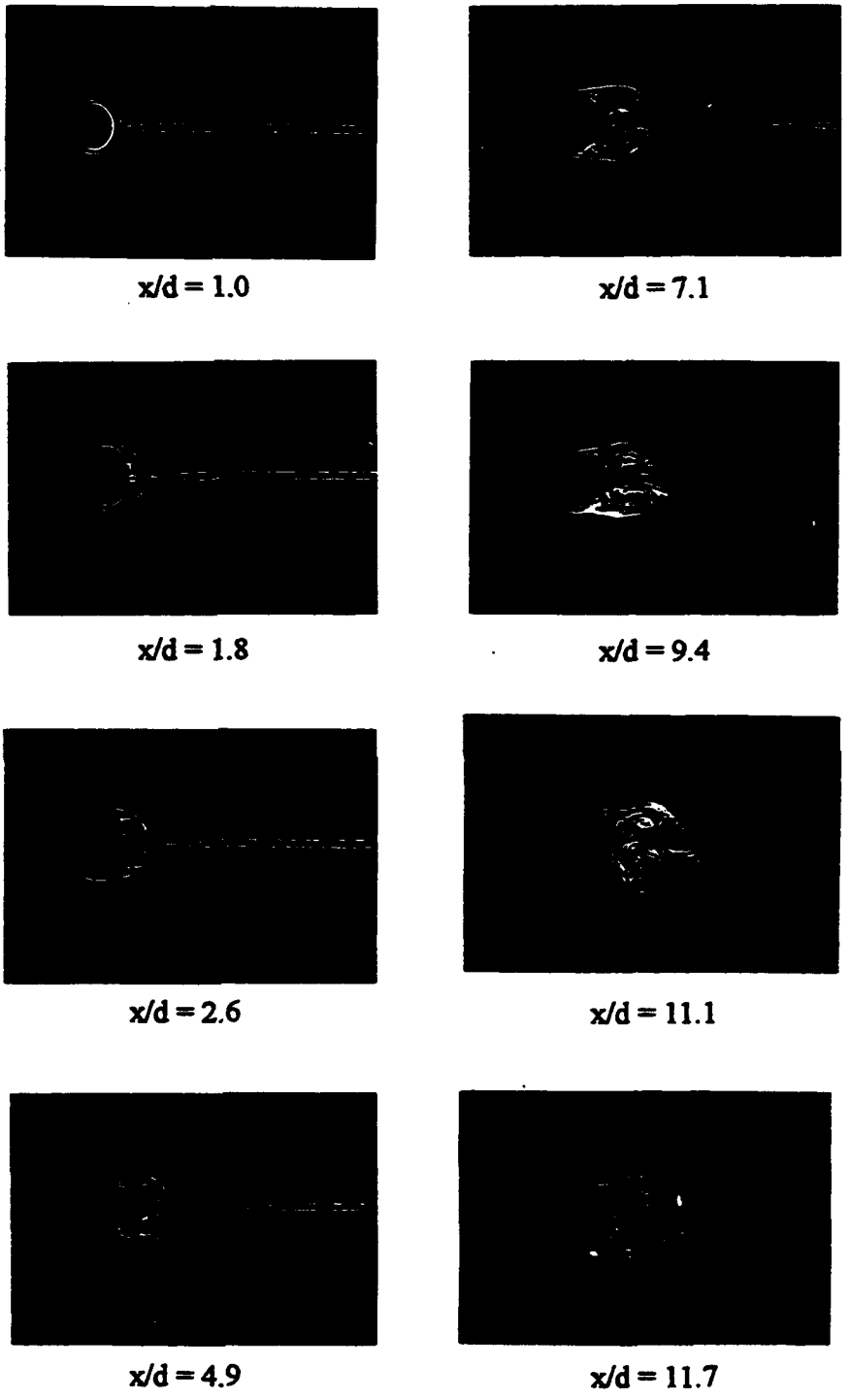

Figure 34. Cross-Sectional Flow Visualization Showing Flowfield Development ($\alpha = 30°$, $\phi = +54°$, $Re_d = 6000$, $(x/d)_f = 9.4$).

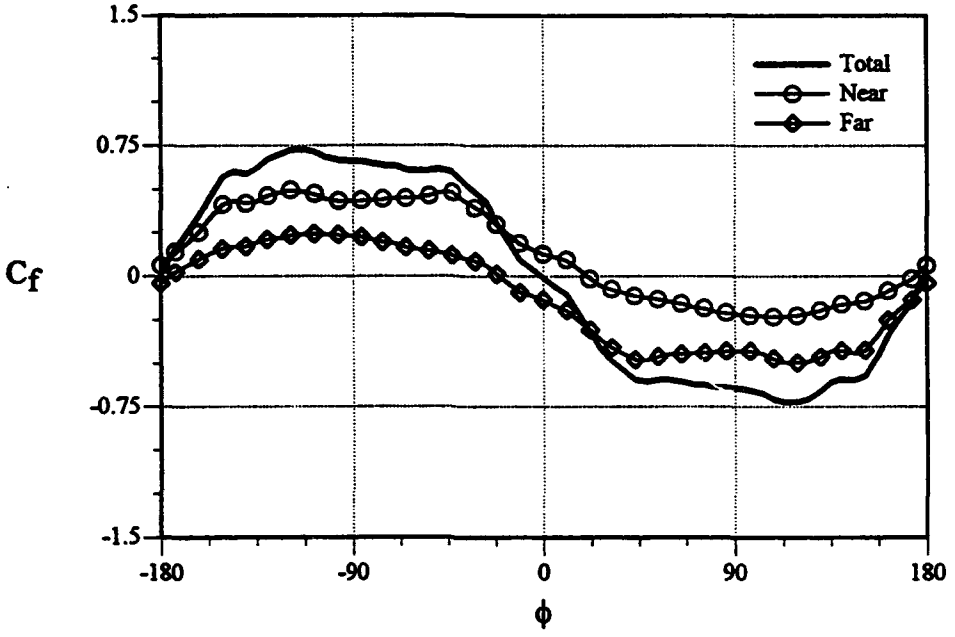

(a) $(x/d)_f = 2.6$

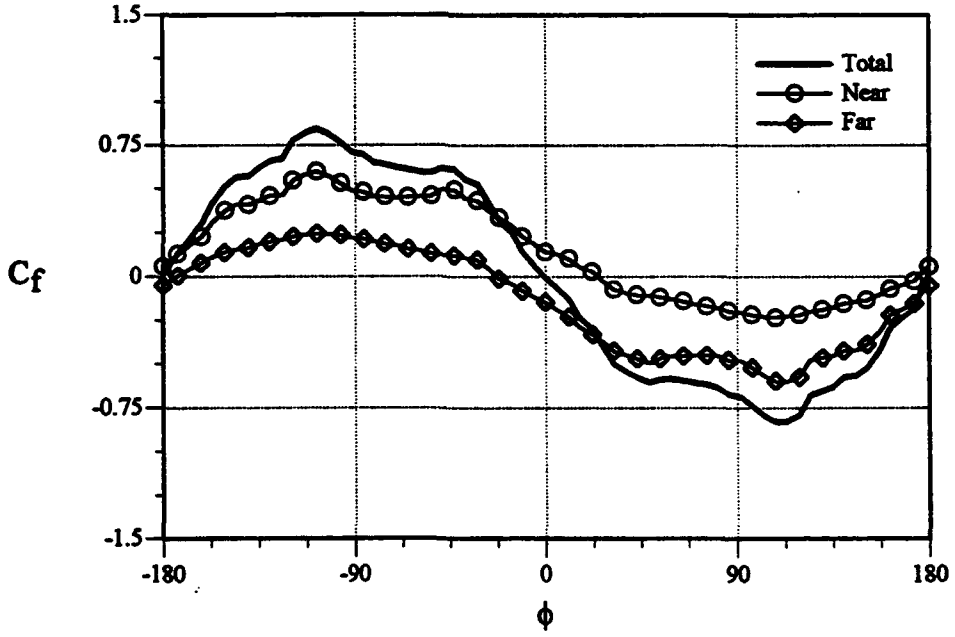

(b) $(x/d)_f = 4.9$

Figure 35. Variation of Normal Force Coefficient on Fin with ϕ ($\alpha = 30°$, $Re_d = 6000$).

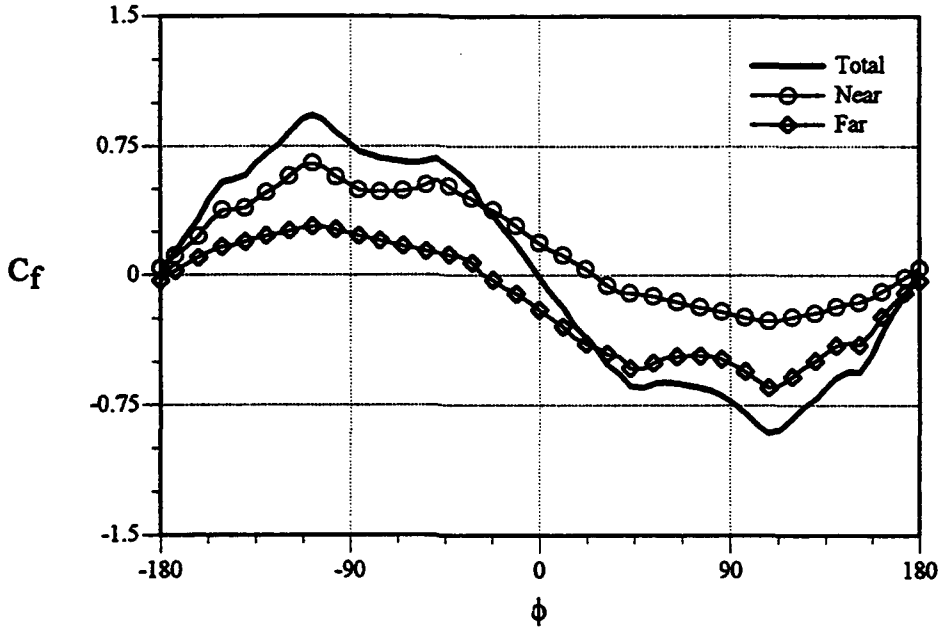

(c) $(x/d)_f = 7.1$

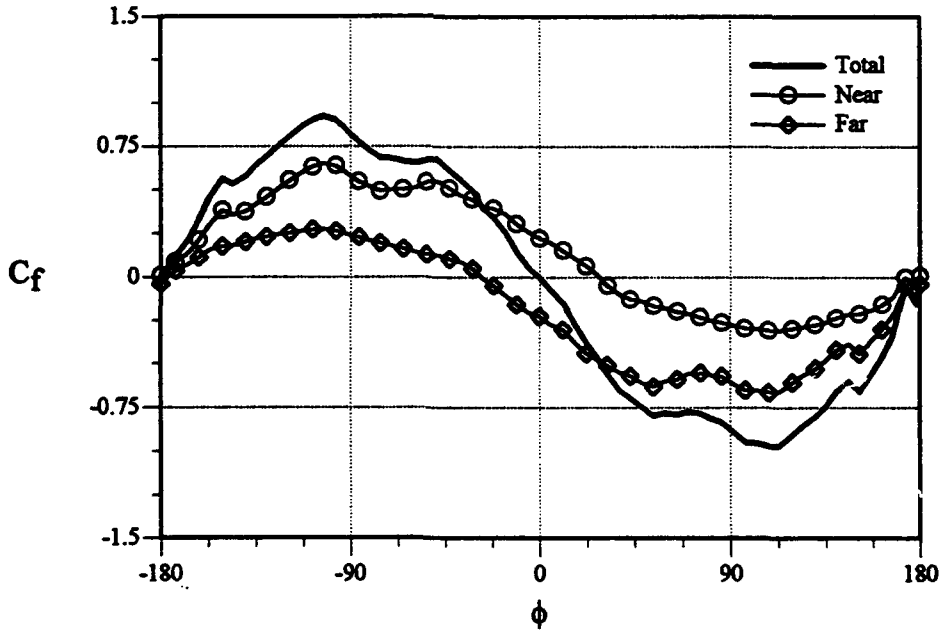

(d) $(x/d)_f = 9.4$

Figure 35. (Concluded)

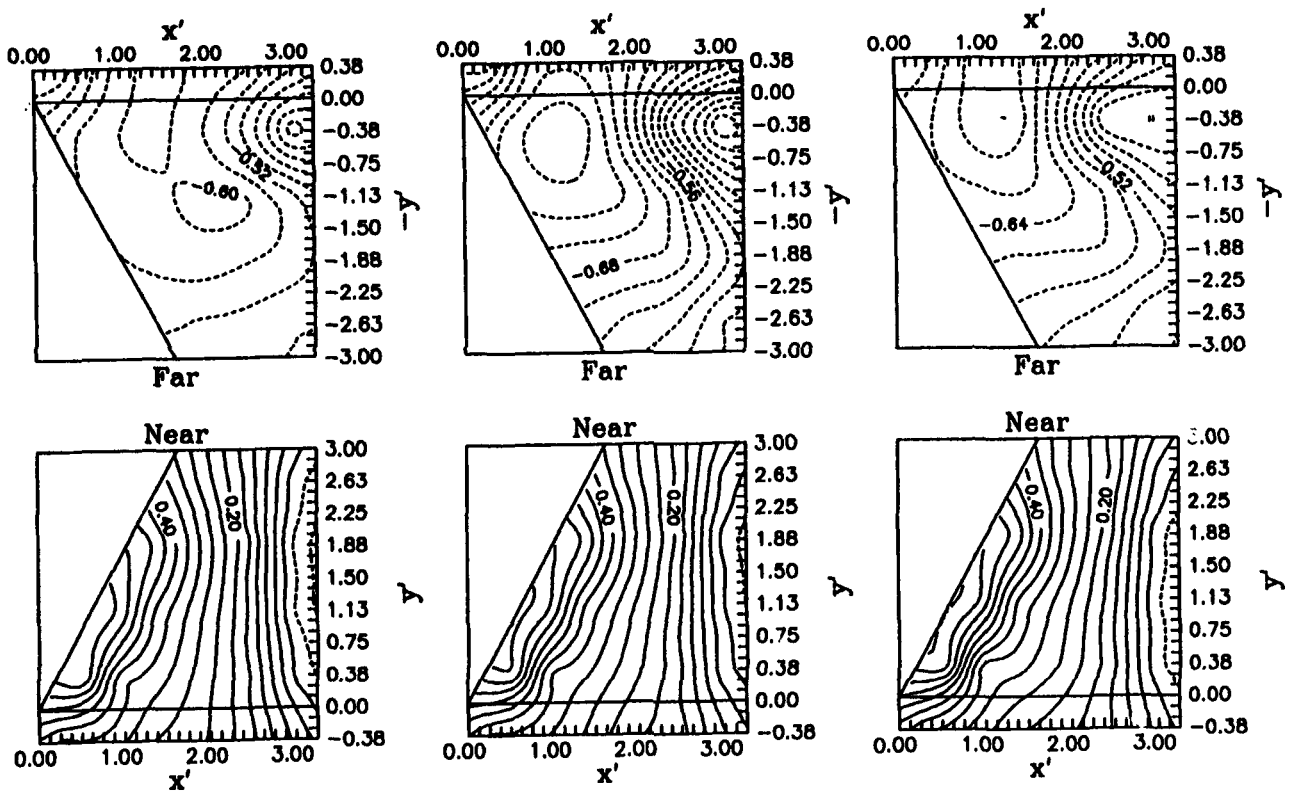

(a) $\phi = +97°$ (b) $\phi = +108°$ (c) $\phi = +119°$

Figure 36. Coefficient of Pressure Contours on Fin ($\alpha = 30°$, $Re_d = 6000$, $(x/d)_f = 7.1$).

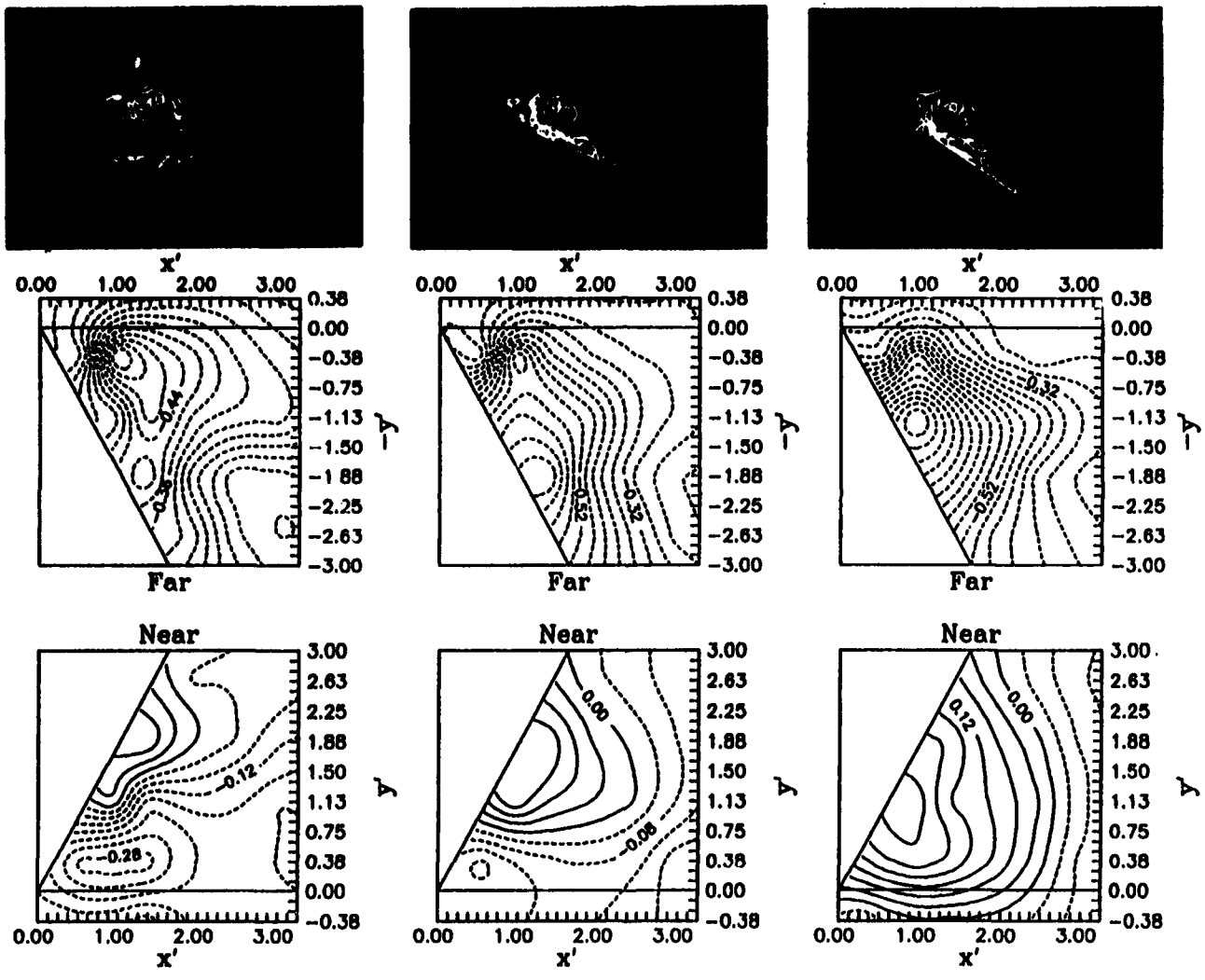

(a) $\phi = +11°$ (b) $\phi = +22°$ (c) $\phi = +32°$

Figure 37. Coefficient of Pressure Contours with Cross-Sectional Flow Visualization ($\alpha = 30°$, $Re_d = 6000$, $(x/d)_f = 7.1$).

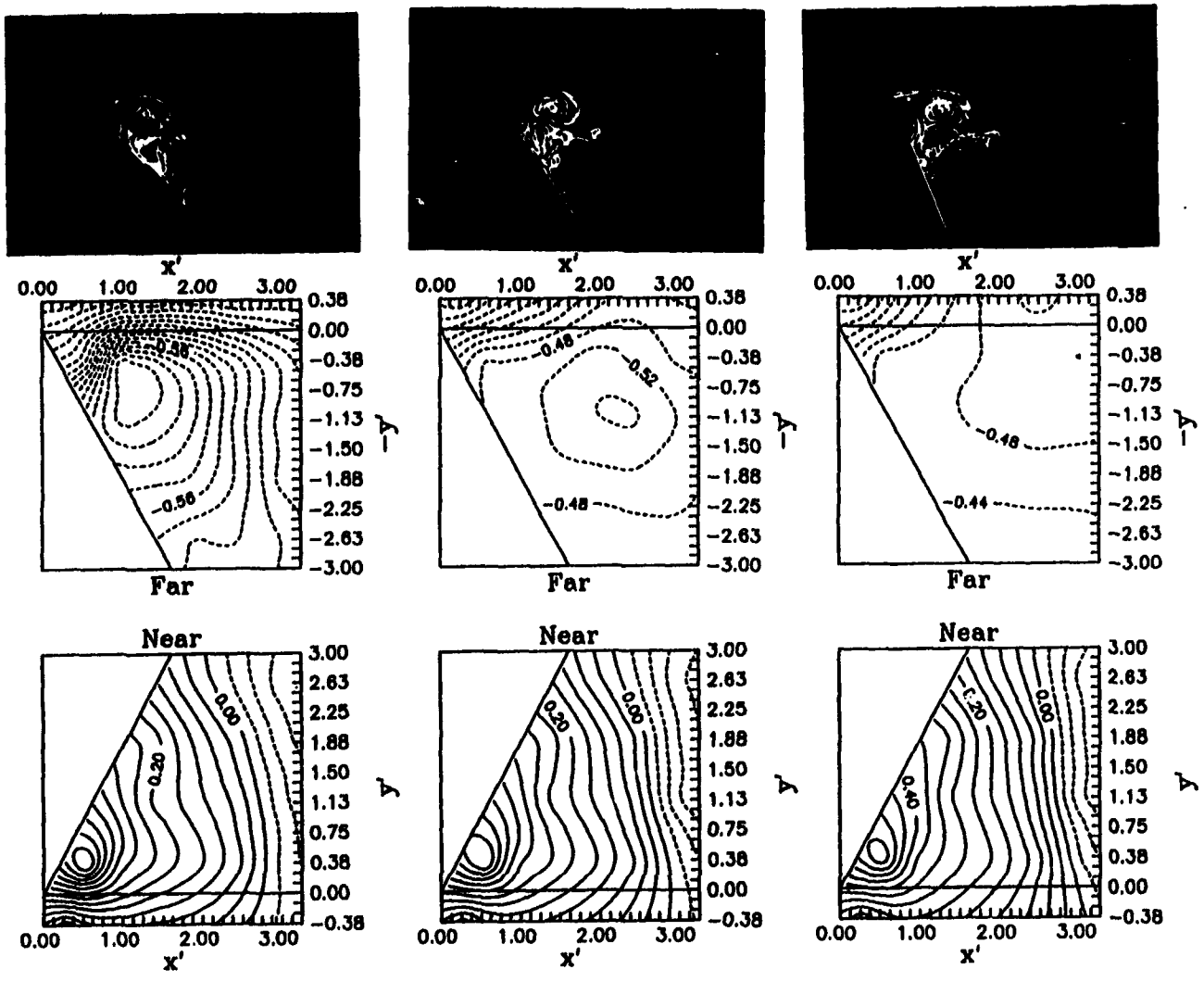

(a) $\phi = +11°$ (b) $\phi = +22°$ (c) $\phi = +32°$

Figure 37. (Concluded)

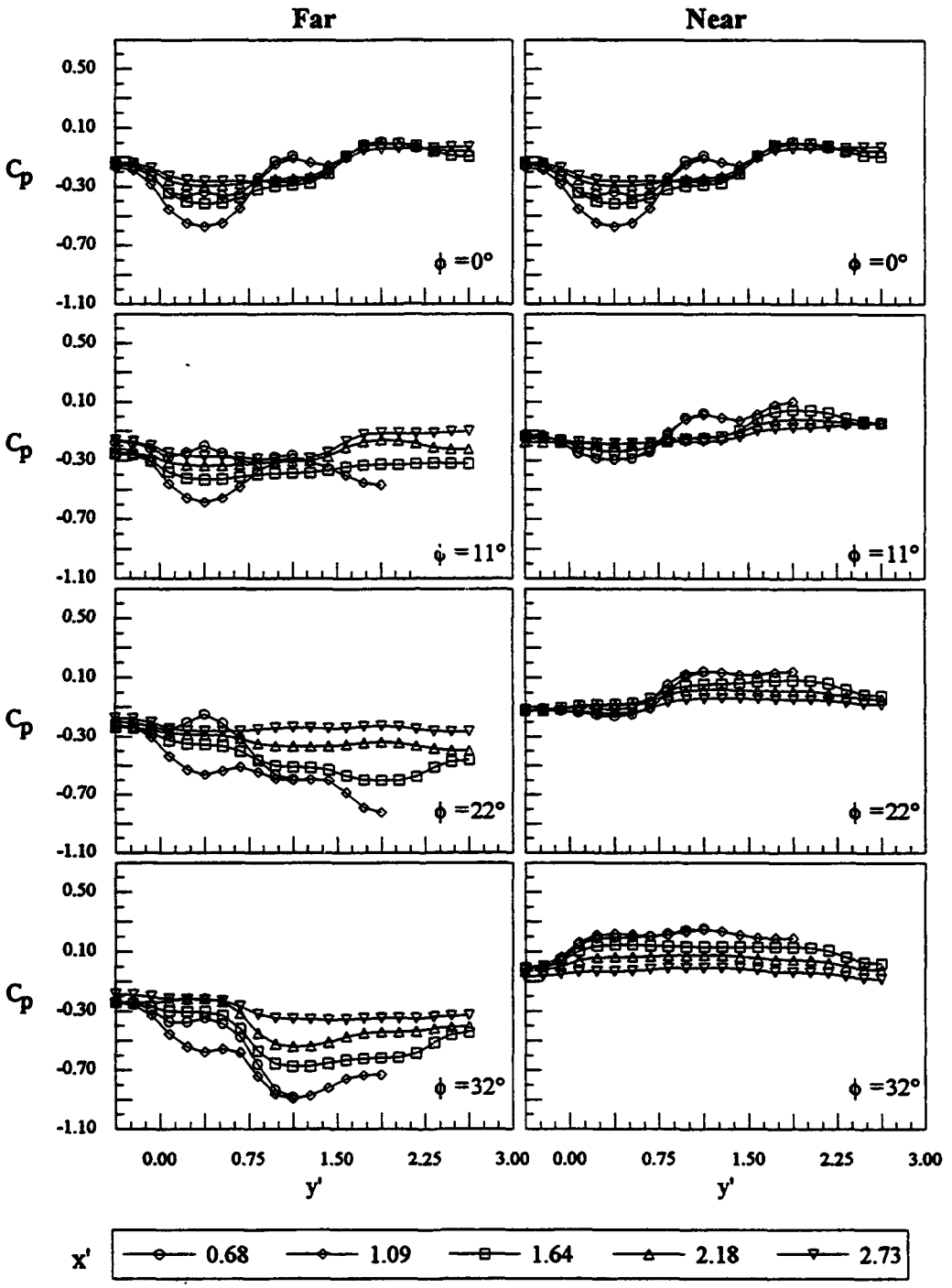

Figure 38. Spanwise Pressure Distributions on Fin ($\alpha = 30°$, $Re_d = 6000$, $(x/d)_f = 7.1$).

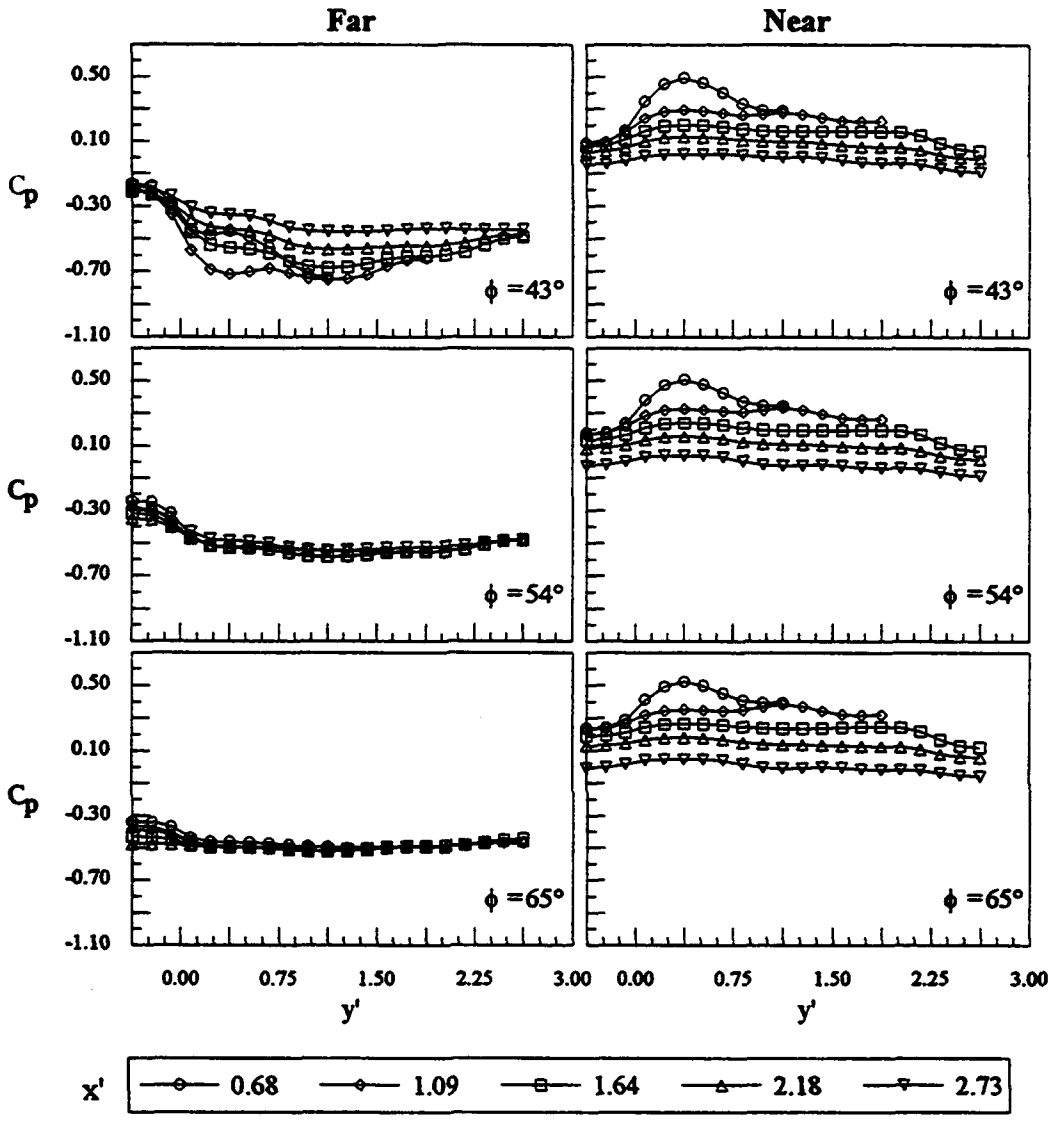

Figure 38. (Concluded)

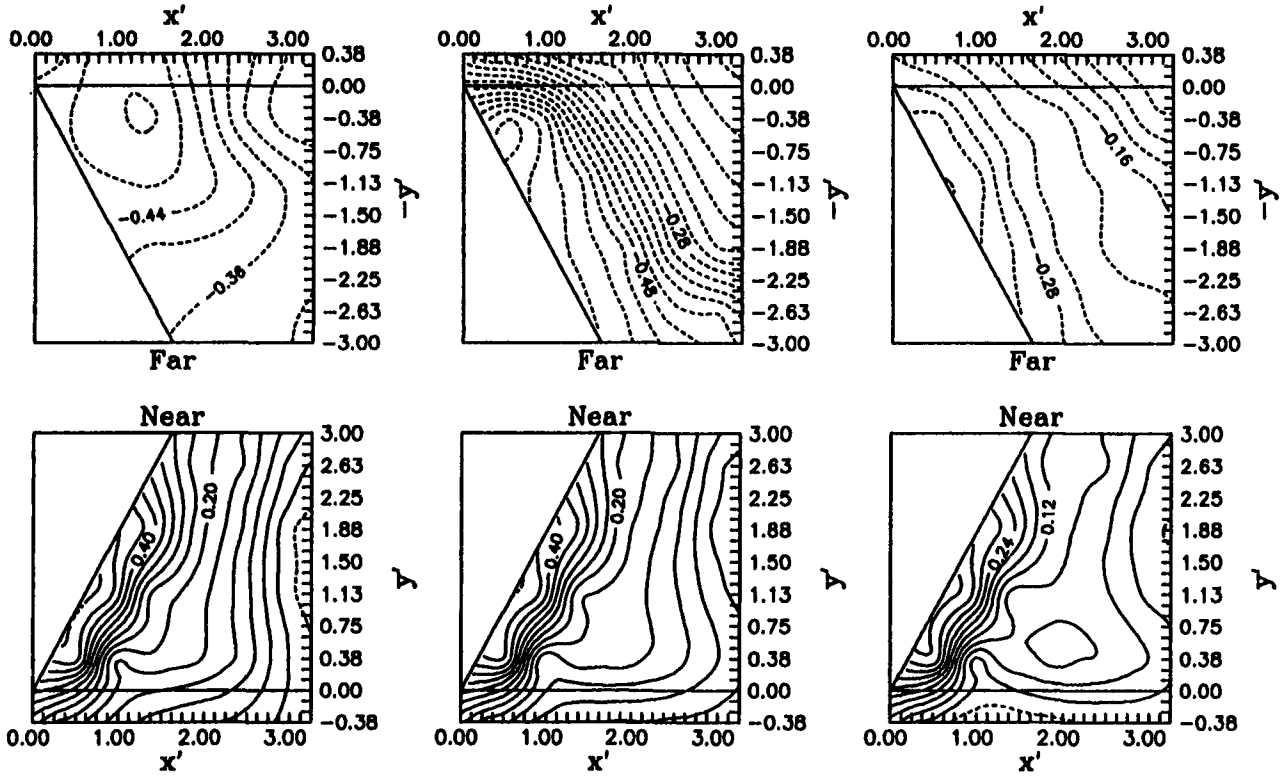

(a) $\phi = +140°$ (b) $\phi = +151°$ (c) $\phi = +162°$

Figure 39. Coefficient of Pressure Contours on Fin ($\alpha = 30°$, $Re_d = 6000$, $(x/d)_f = 7.1$).

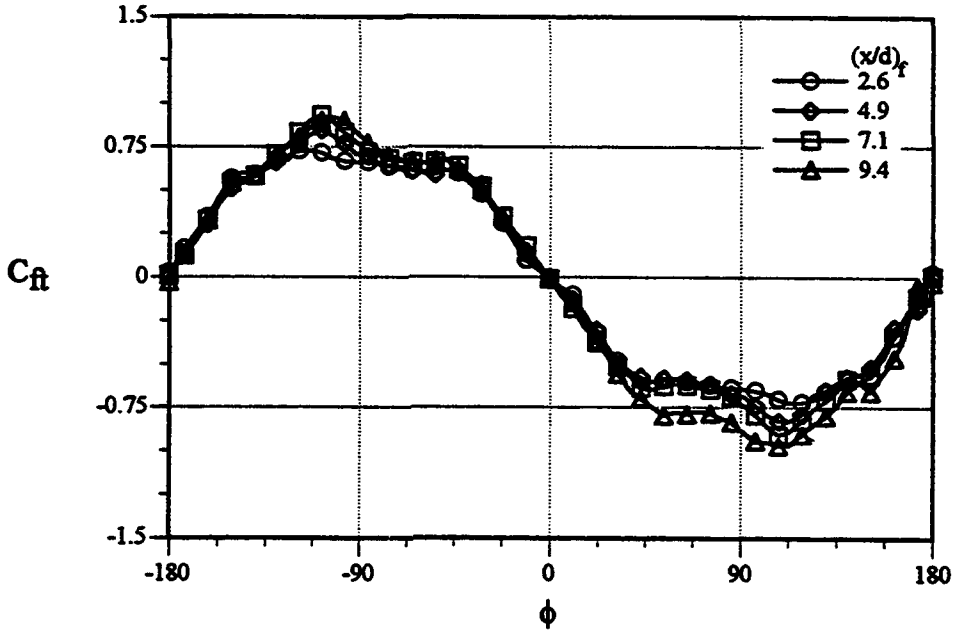

(a) $Re_d = 6000$

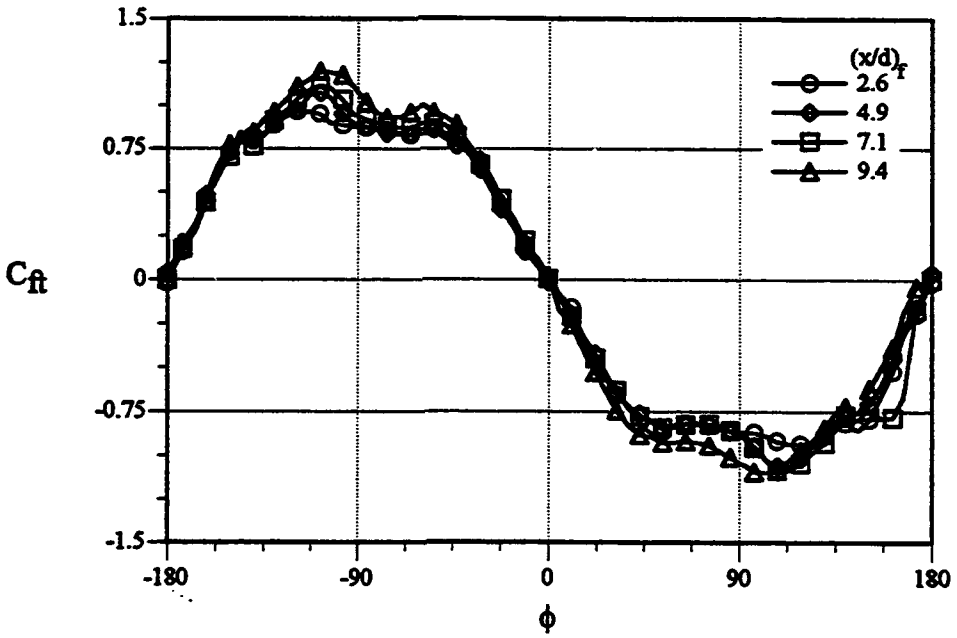

(b) $Re_d = 20000$

Figure 40. Normal Force Coefficient Variations with ϕ for Different $(x/d)_f$ ($\alpha = 30°$).

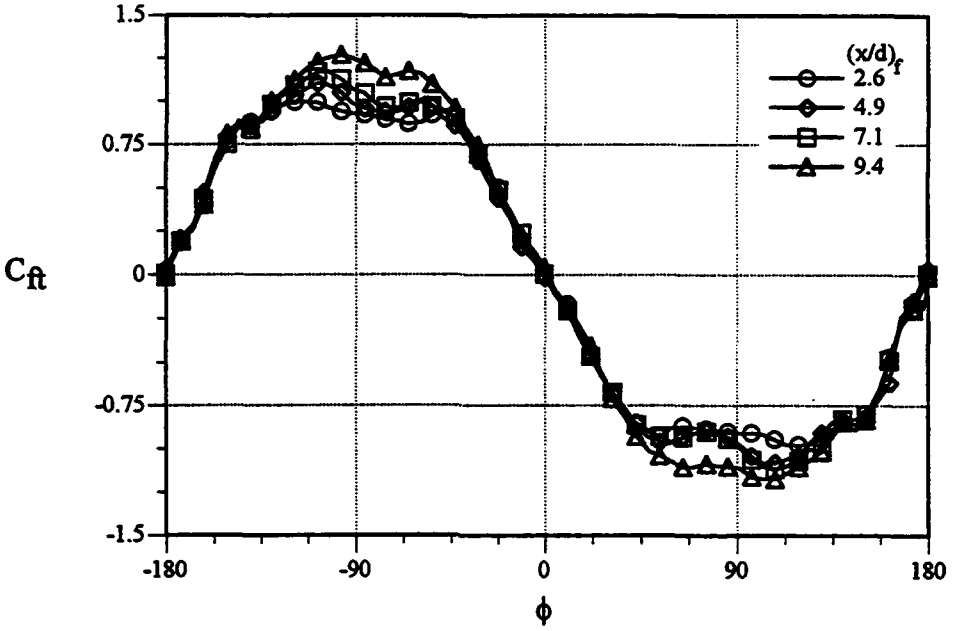

(c) $Re_d = 34000$

Figure 40. (Concluded)

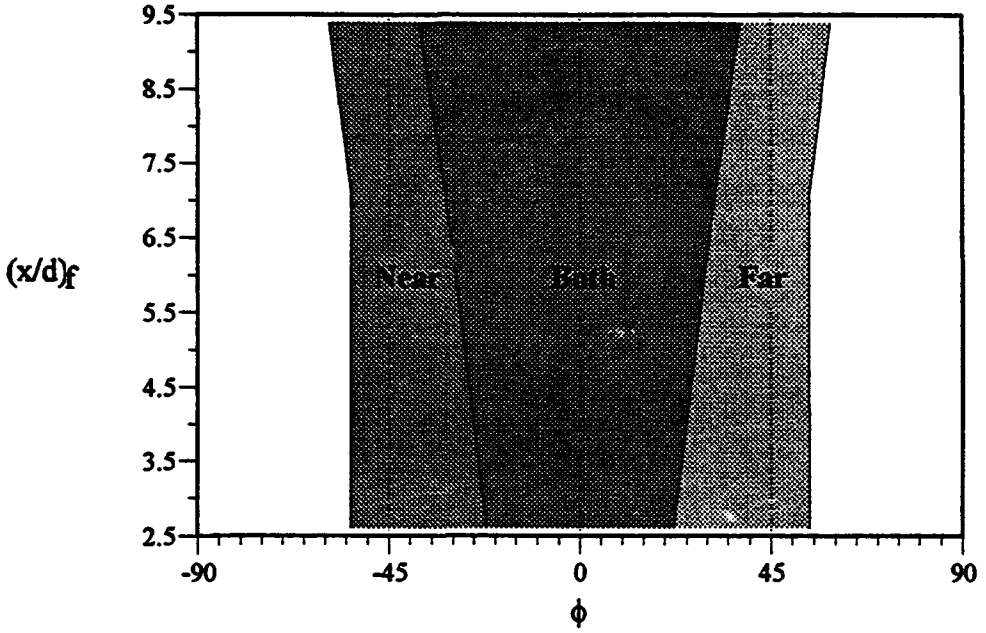

(a) $Re_d = 6000$

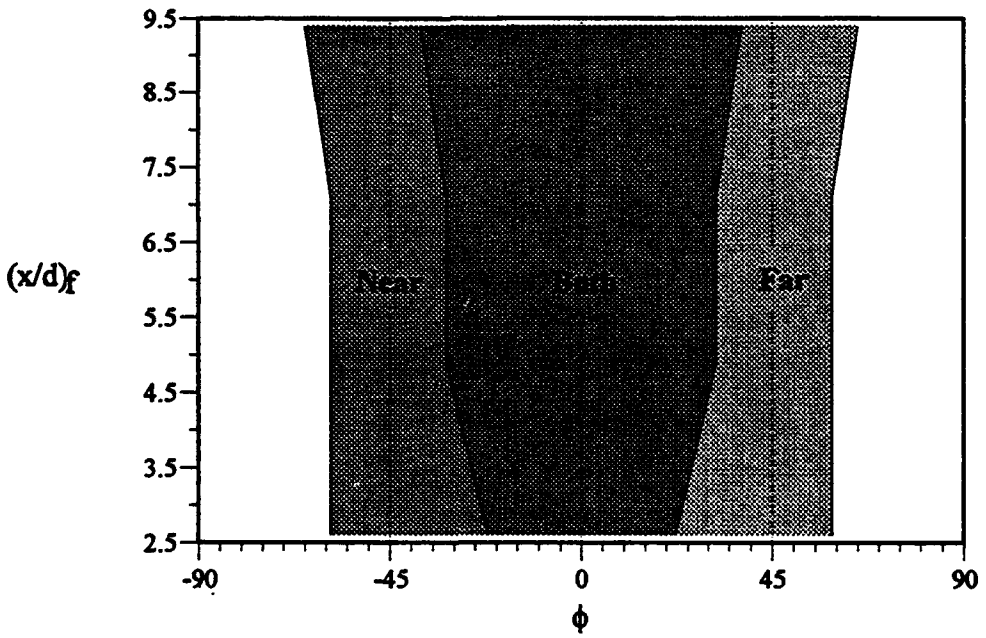

(b) $Re_d = 20000$

Figure 41. Range of Vortex Interaction with Fin for Different $(x/d)_f$ ($\alpha = 30°$).

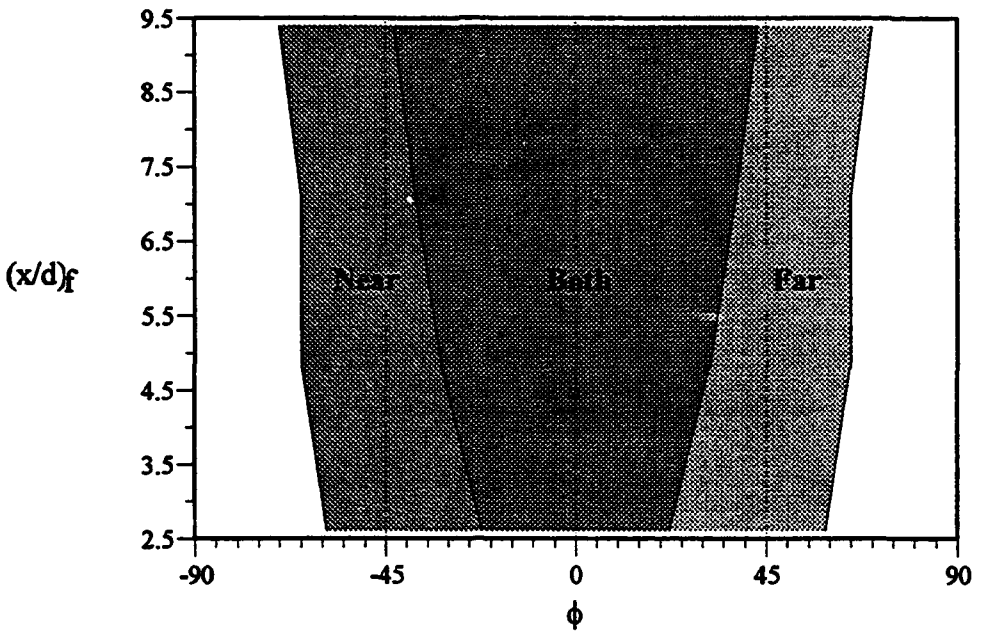

(c) $Re_d = 34000$

Figure 41. (Concluded)

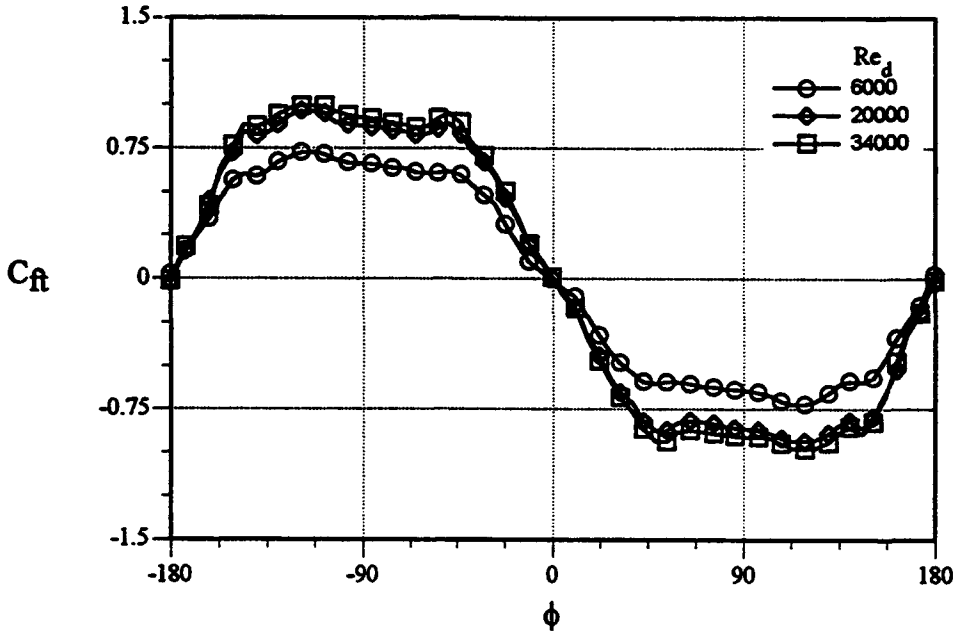

(a) $(x/d)_f = 2.6$

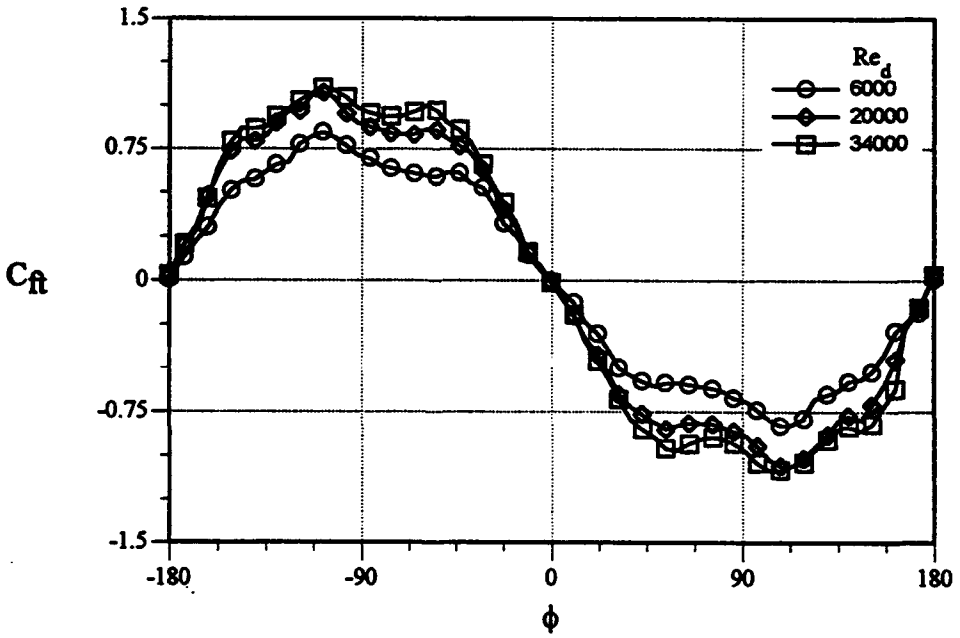

(b) $(x/d)_f = 4.9$

Figure 42. Normal Force Coefficient Variations with ϕ for Different Re_d ($\alpha = 30°$).

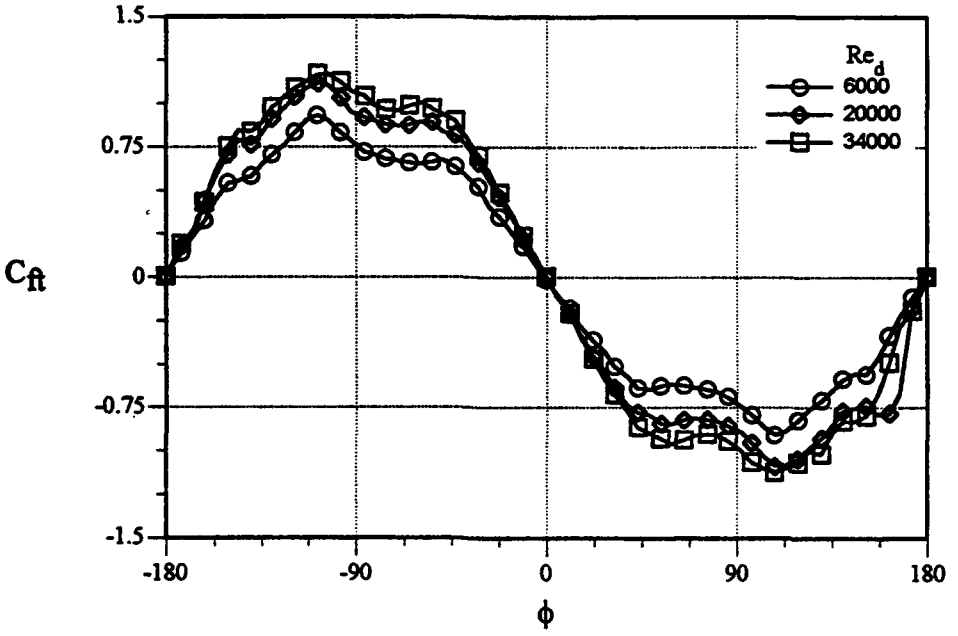

(c) $(x/d)_f = 7.1$

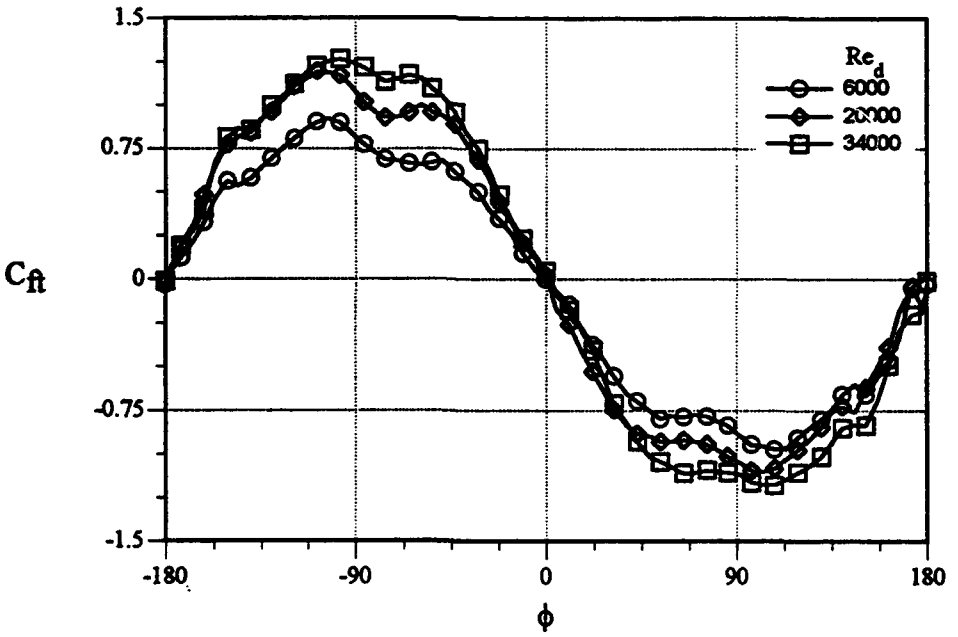

(d) $(x/d)_f = 9.4$

Figure 42. (Concluded)

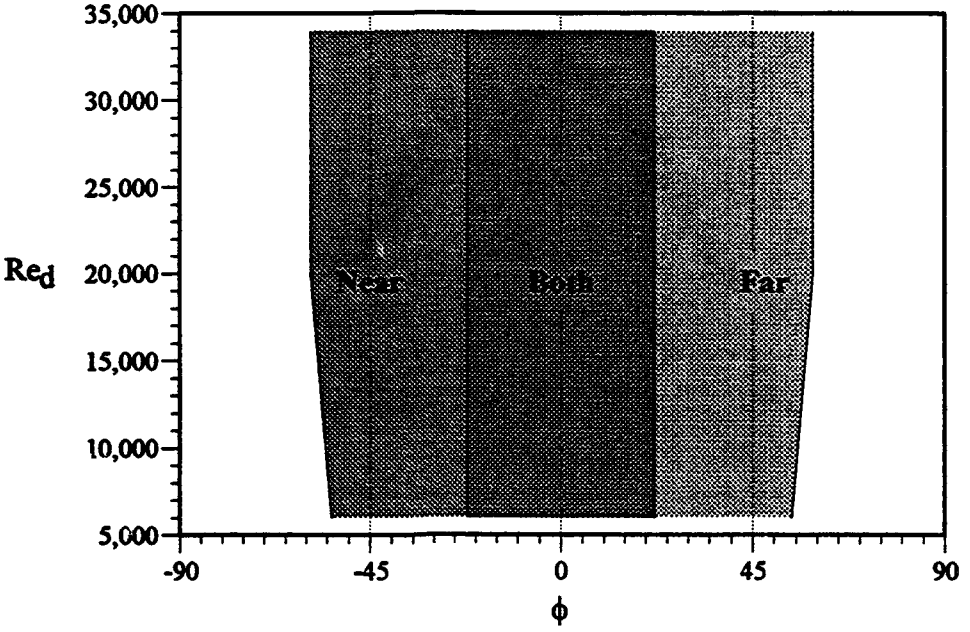

(a) $(x/d)_f = 2.6$

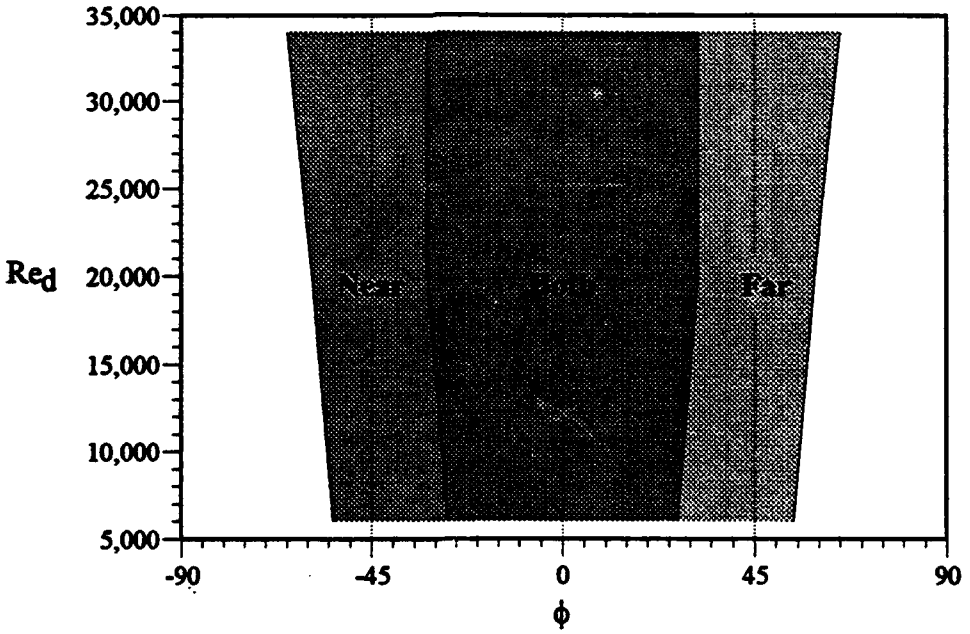

(b) $(x/d)_f = 4.9$

Figure 43. Range of Vortex Interaction with Fin for Different Re_d ($\alpha = 30°$).

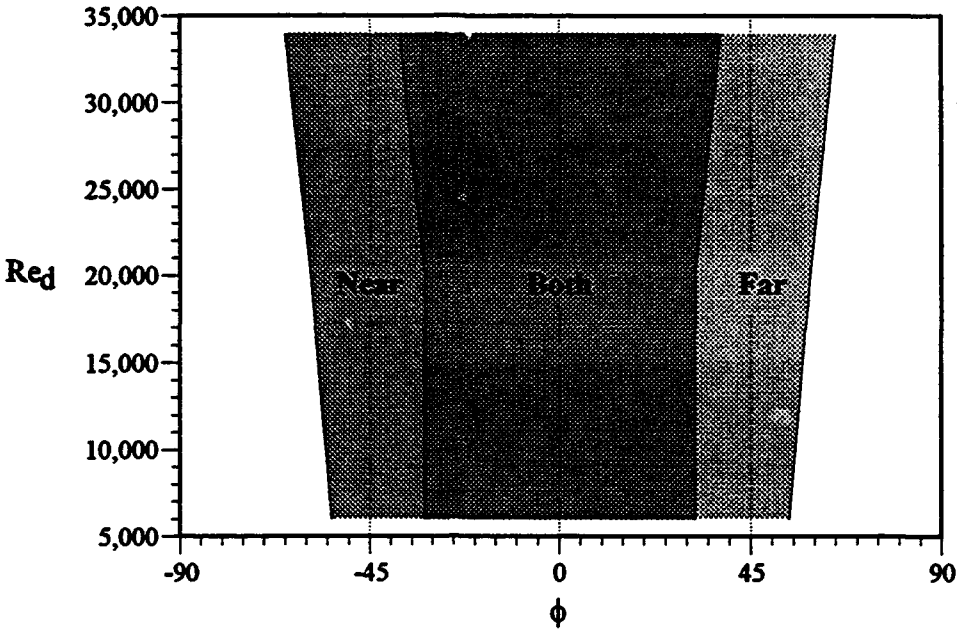

(c) $(x/d)_f = 7.1$

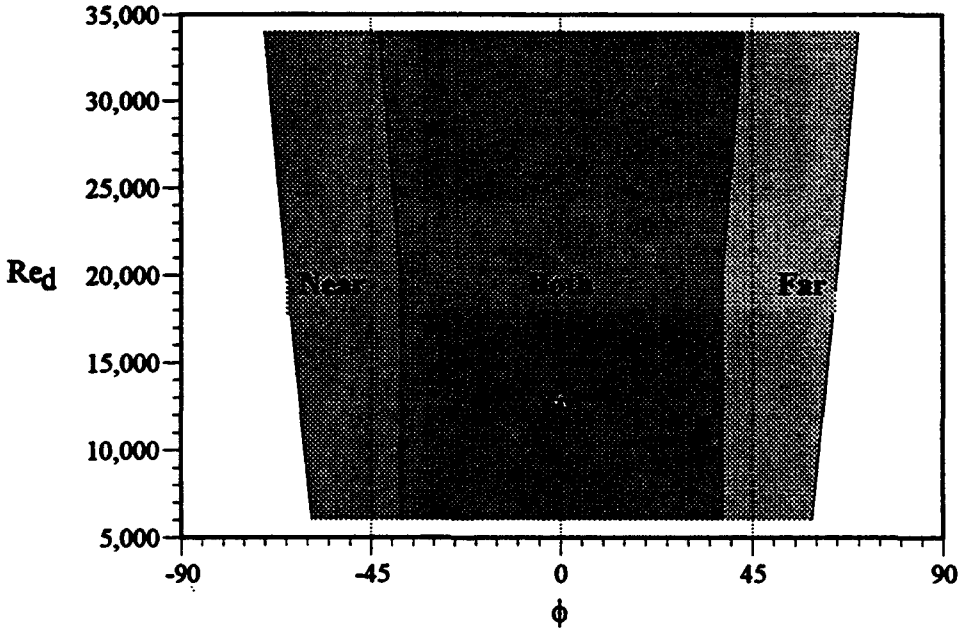

(d) $(x/d)_f = 9.4$

Figure 43. (Concluded)

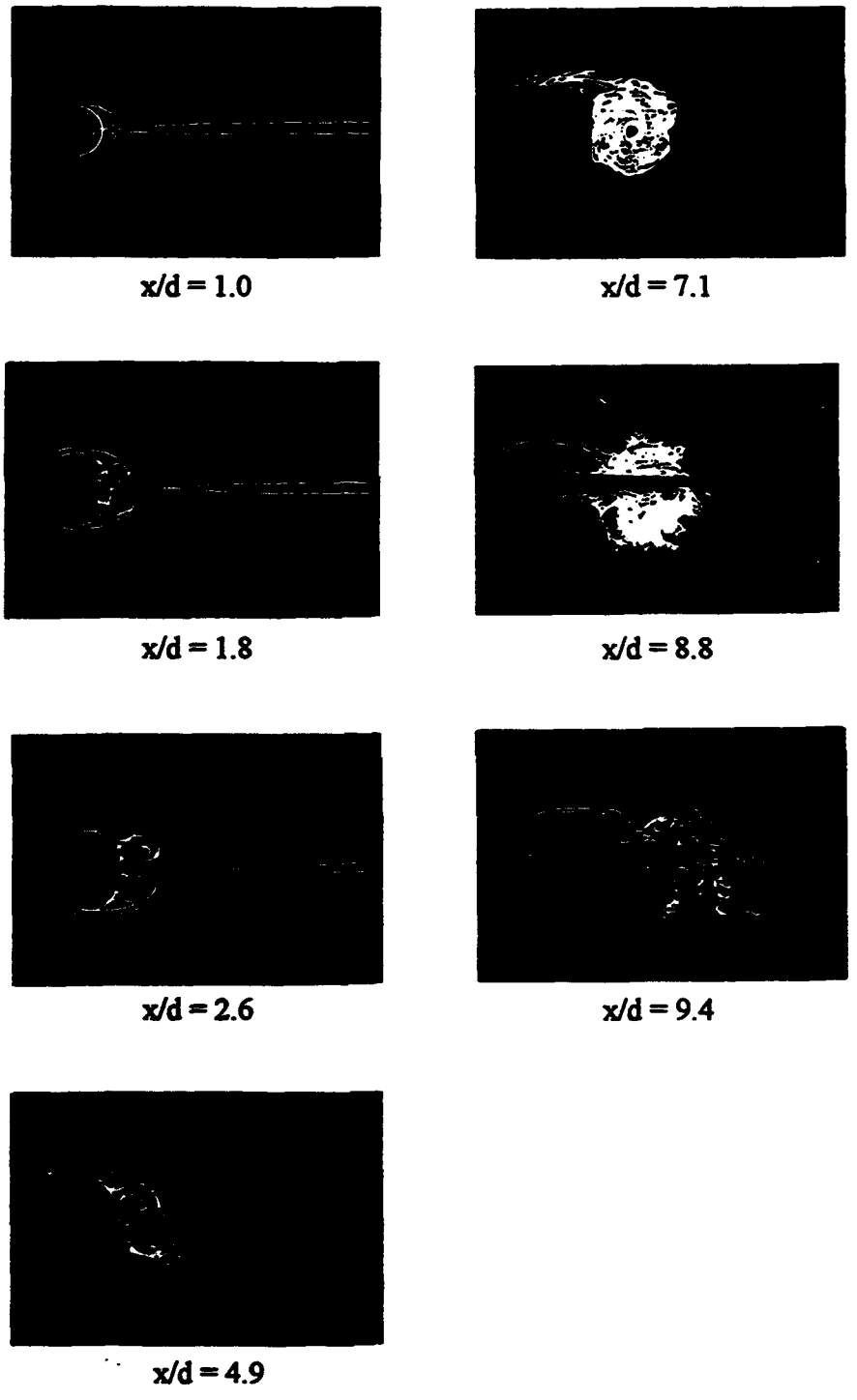

Figure 44. Cross-Sectional Flow Visualization Showing Flowfield Development ($\alpha = 45°$, $\phi = 0°$, $Re_d = 6000$, $(x/d)_f = 7.1$).

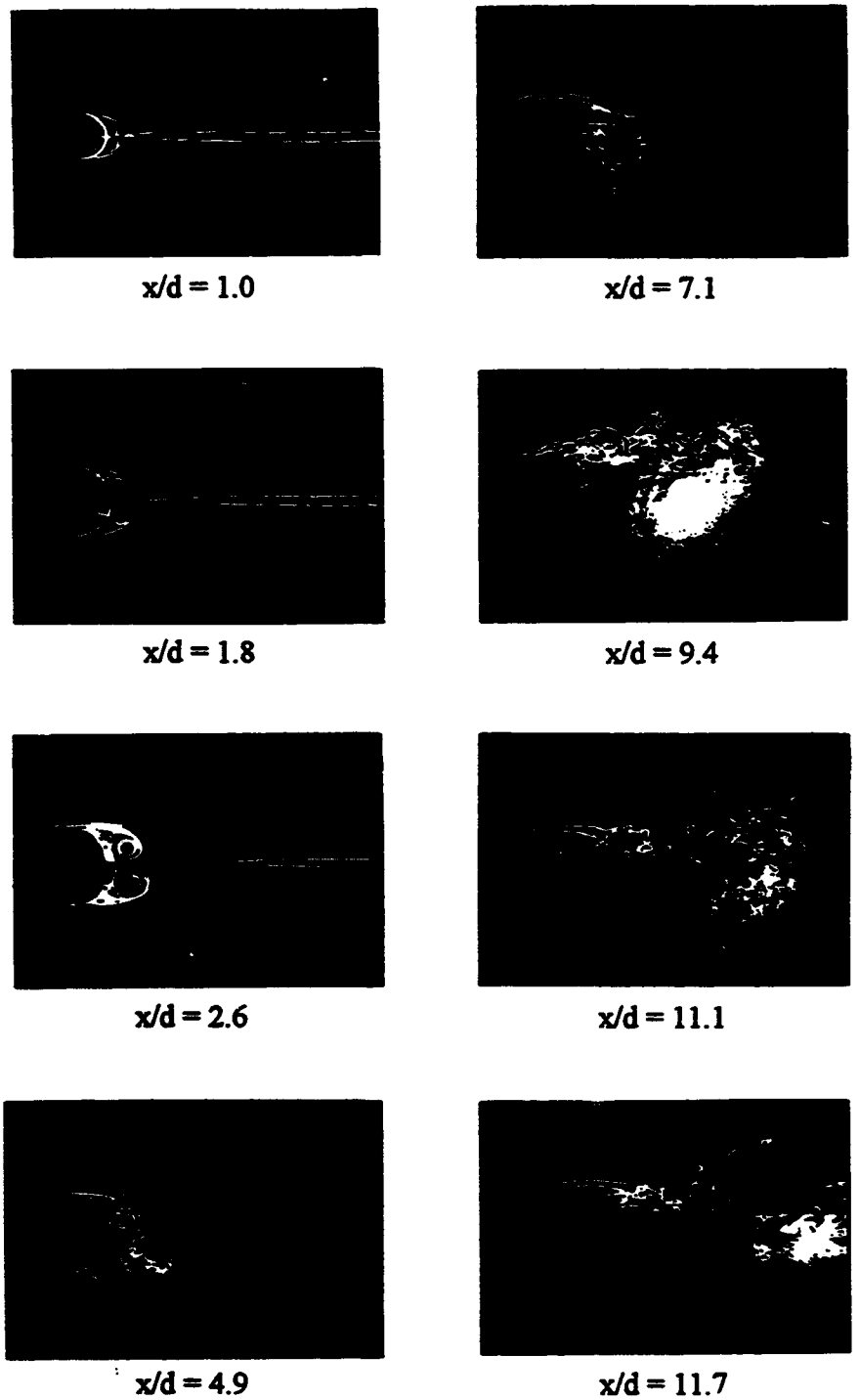

Figure 45. Cross-Sectional Flow Visualization Showing Flowfield Development ($\alpha = 45°$, $\phi = 0°$, $Re_d = 6000$, $(x/d)_f = 9.4$).

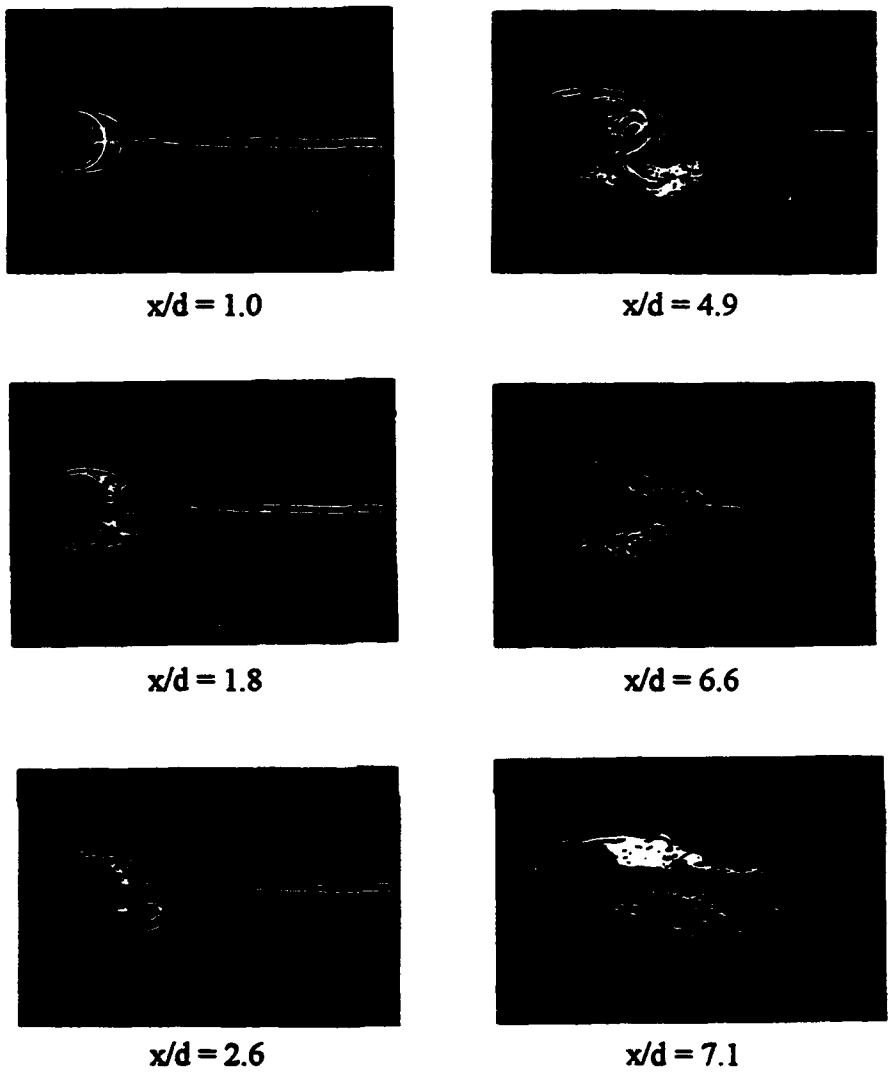

Figure 46. Cross-Sectional Flow Visualization Showing Flowfield Development ($\alpha = 45°$, $\phi = 0°$, $Re_d = 6000$, $(x/d)_f = 4.9$).

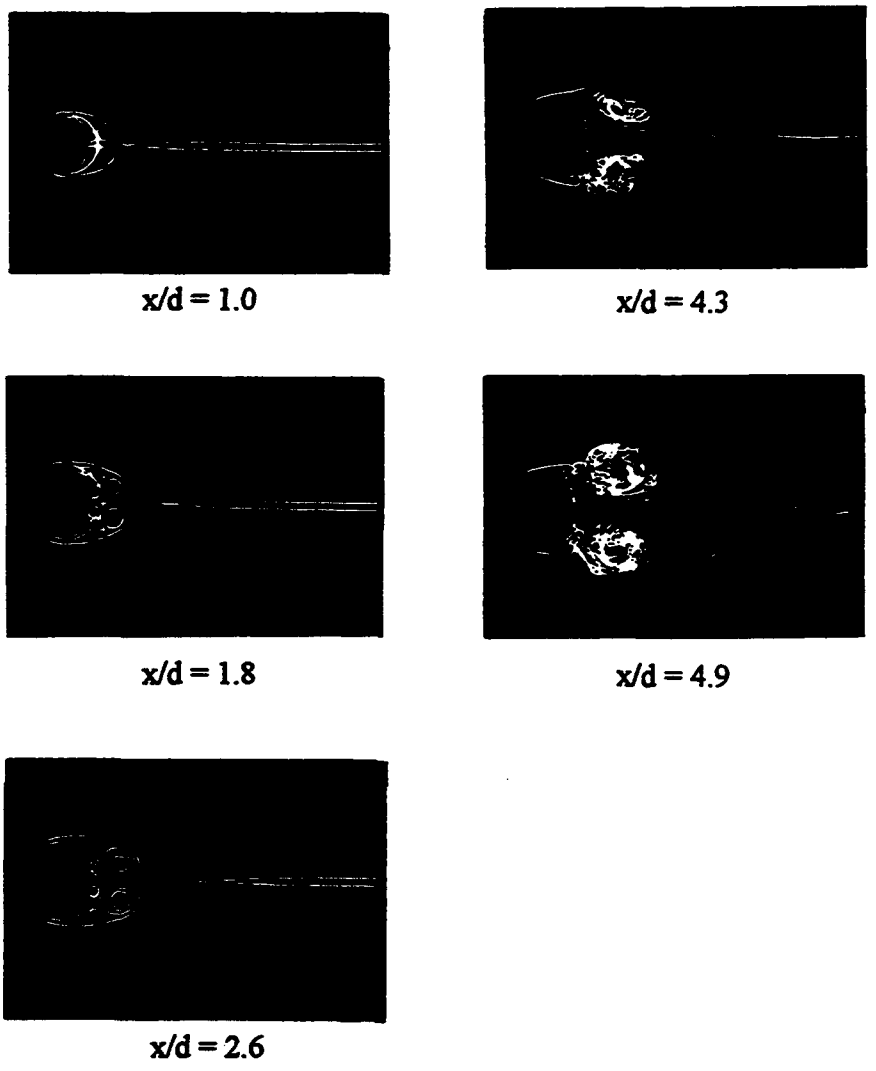

Figure 47. Cross-Sectional Flow Visualization Showing Flowfield Development ($\alpha = 45°$, $\phi = 0°$, $Re_d = 6000$, $(x/d)_f = 2.6$).

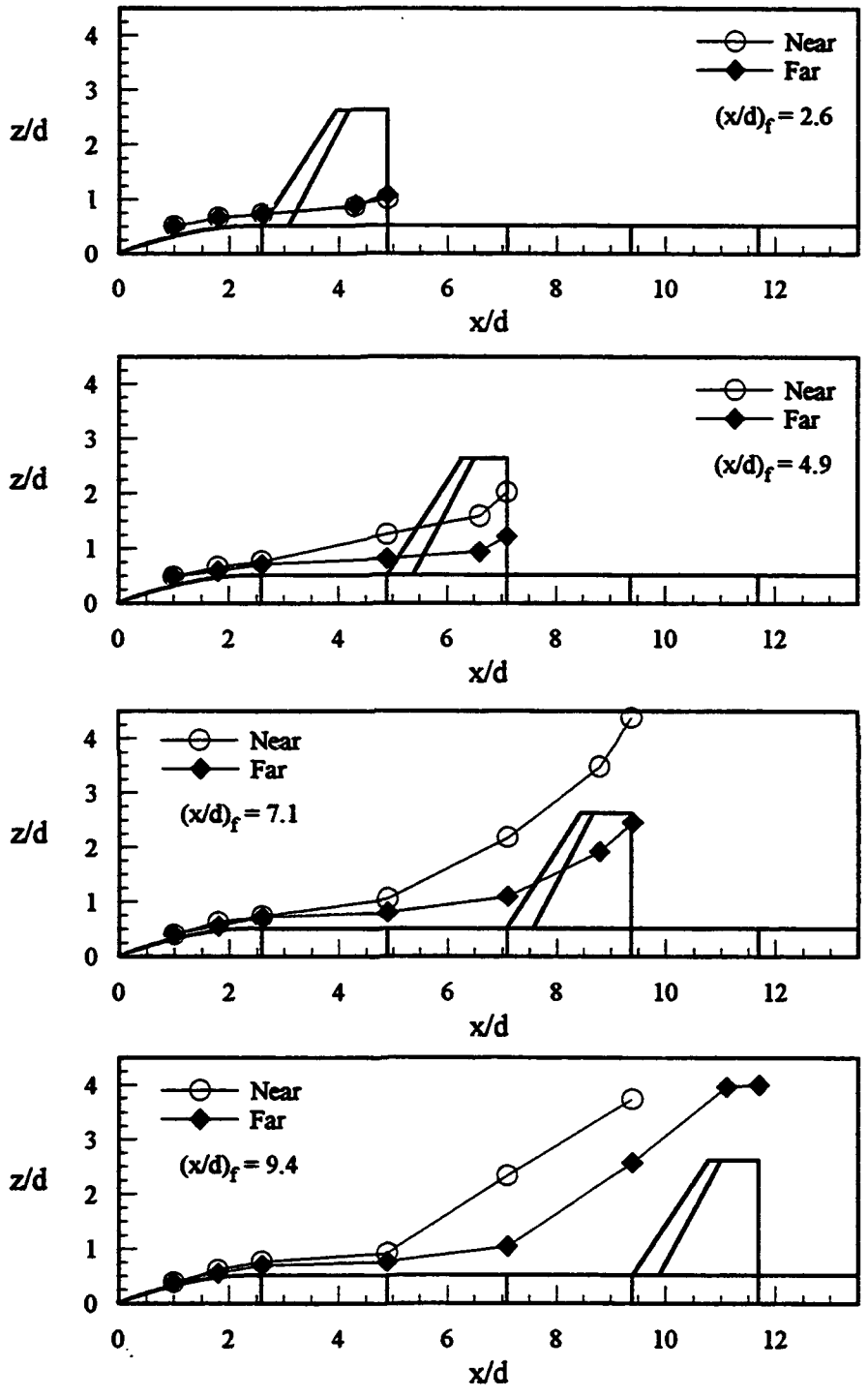

Figure 48. Vortex Center Trajectories, Side View ($\alpha = 45°$, $\phi = 0°$, $Re_d = 6000$).

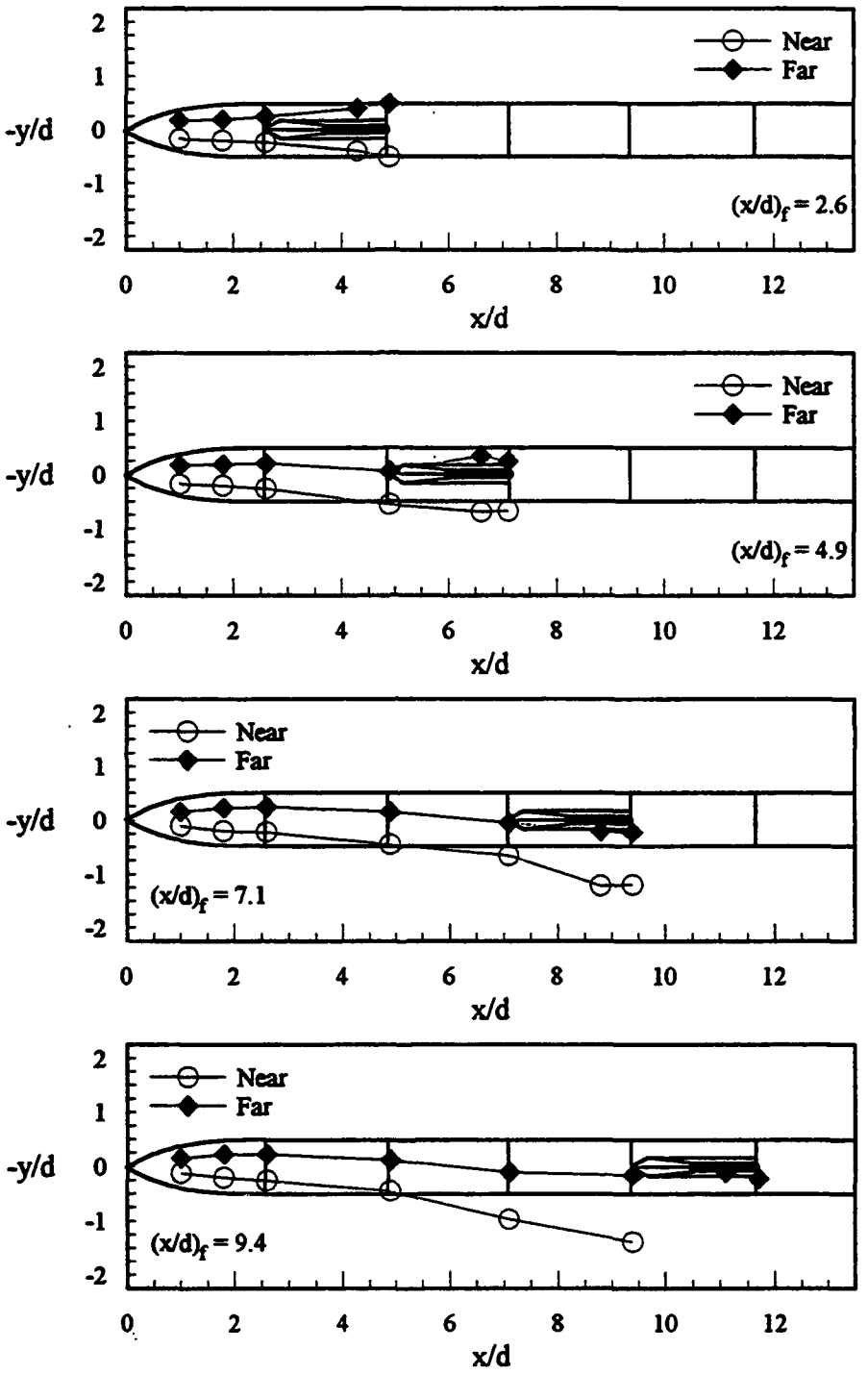

Figure 49. Vortex Center Trajectories, Top View ($\alpha = 45°$, $\phi = 0°$, $Re_d = 6000$).

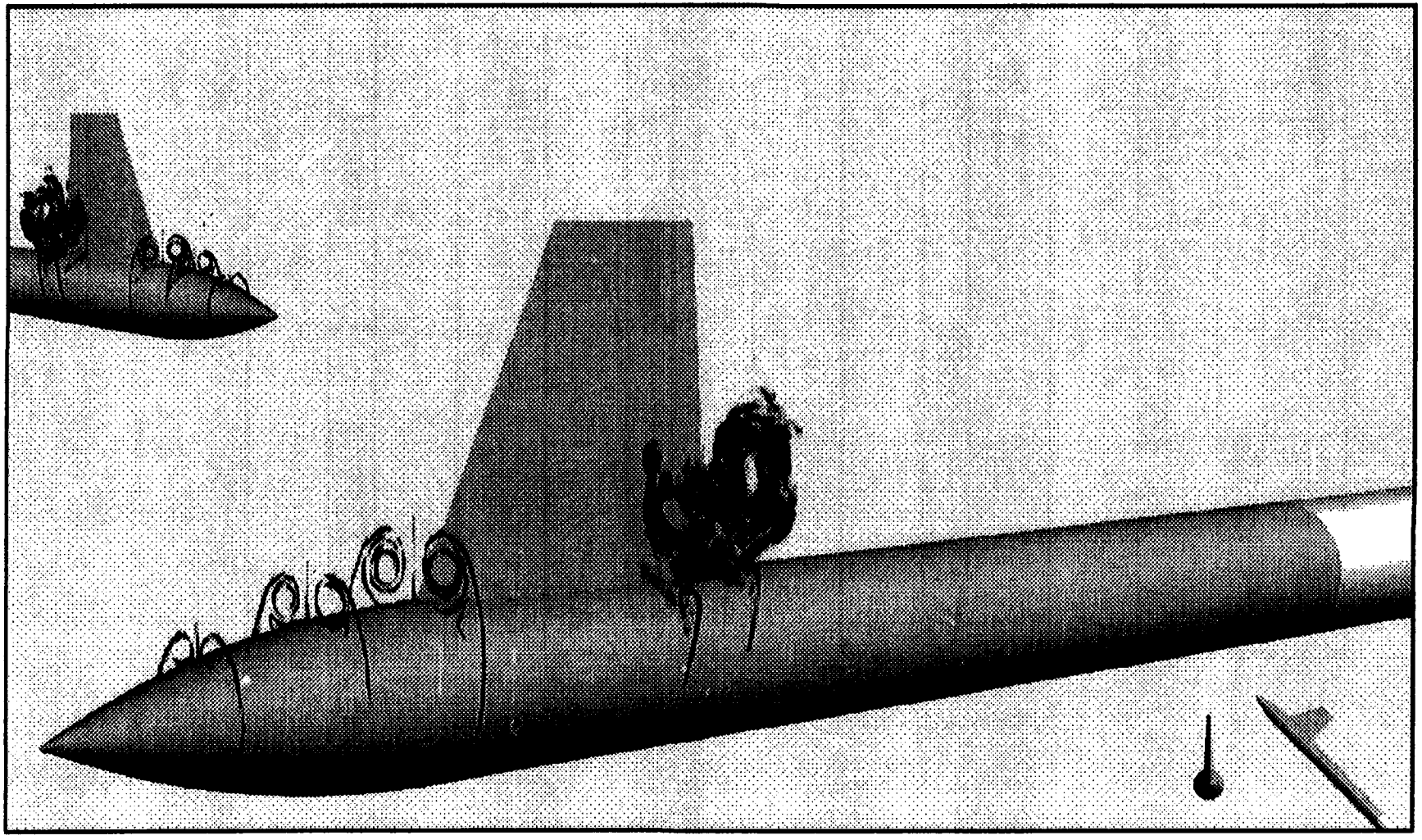

Figure 50. Three-Dimensional Perspective View of Flowfield ($\alpha = 45°$, $\phi = 0°$, $Re_d = 6000$, $(x/d)_f = 2.6$).

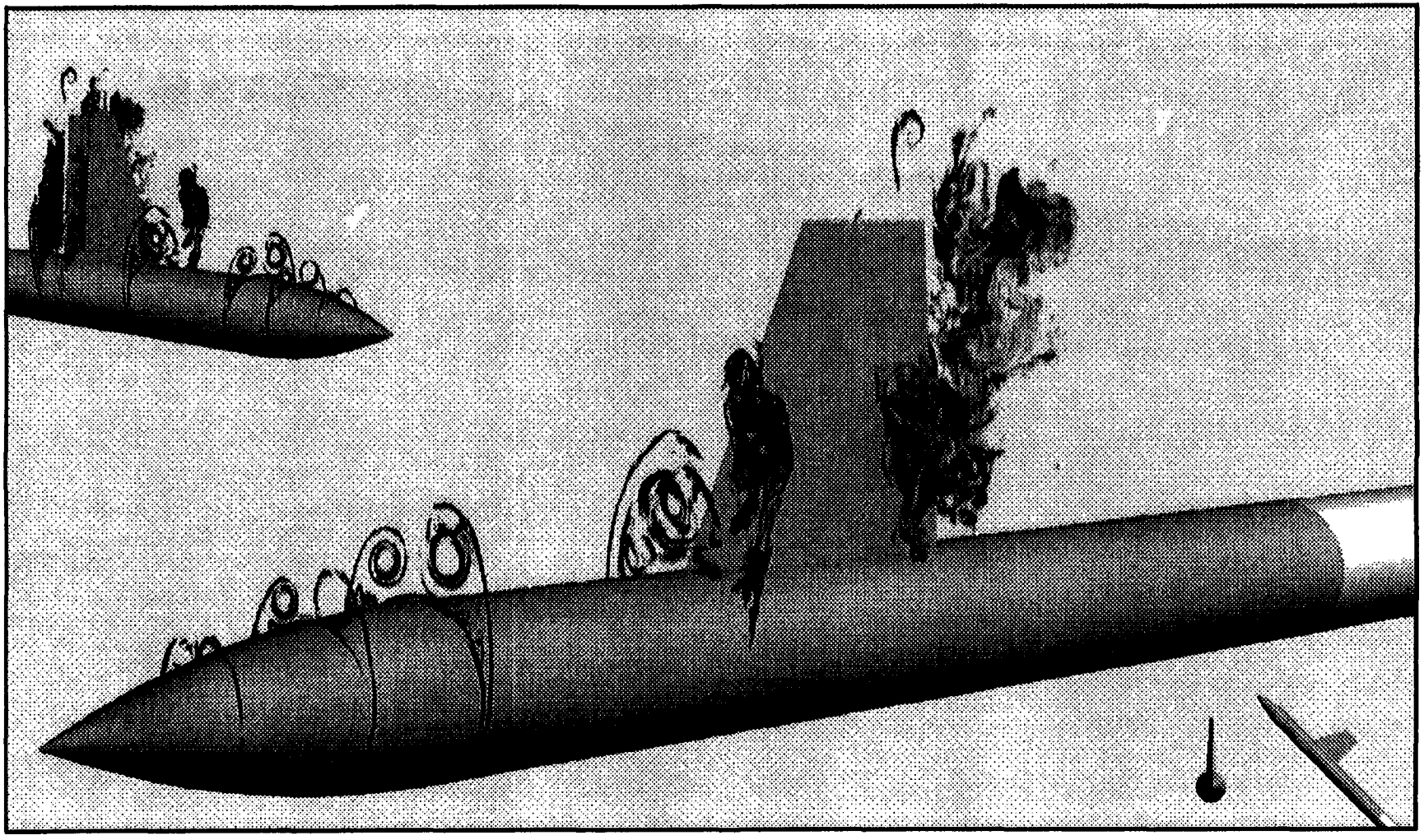

Figure 51. Three-Dimensional Perspective View of Flowfield ($\alpha = 45°$, $\phi = 0°$, $Re_d = 6000$, $(x/d)_f = 4.9$).

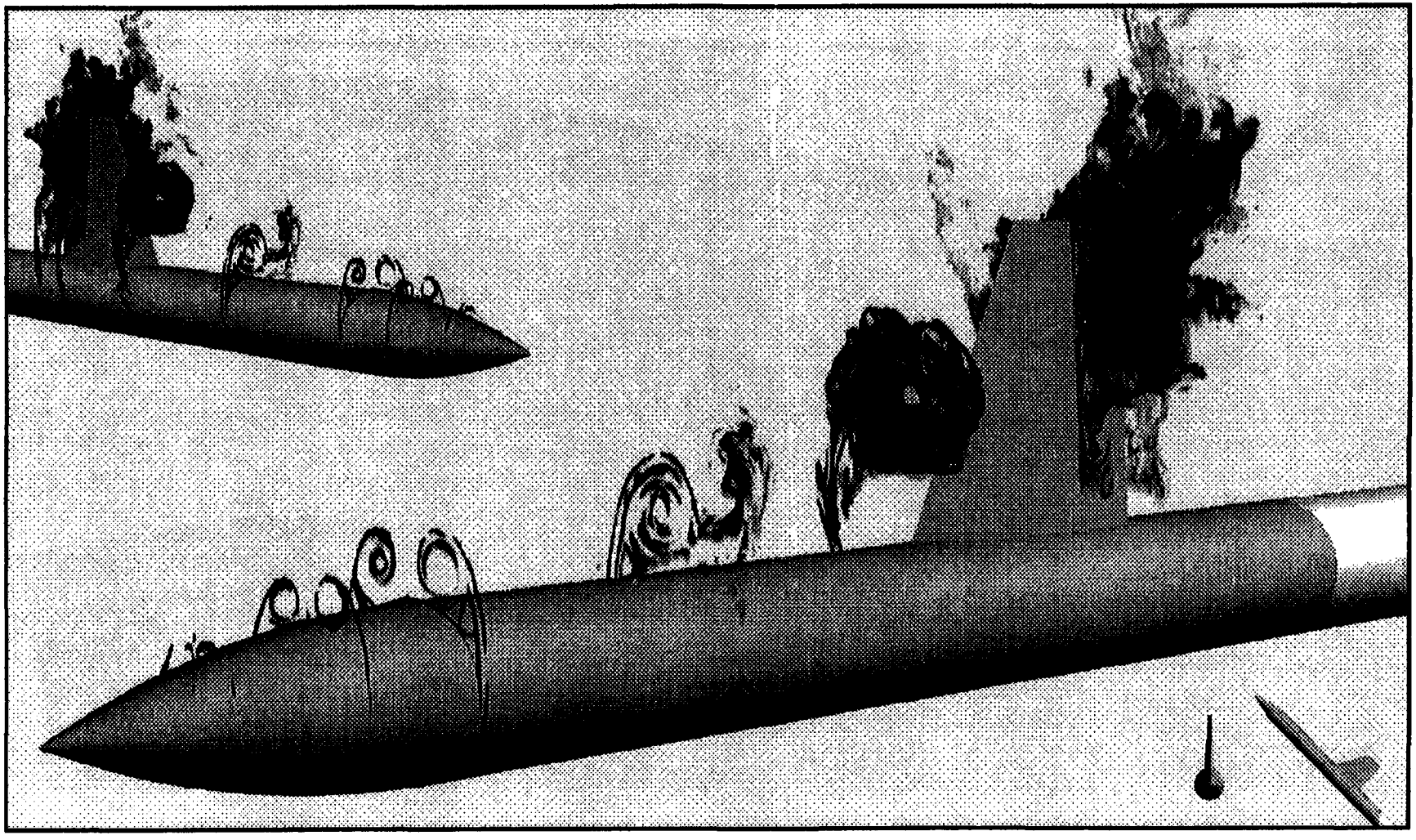

Figure 52. Three-Dimensional Perspective View of Flowfield ($\alpha = 45°$, $\phi = 0°$, $Re_d = 6000$, $(x/d)_f = 7.1$).

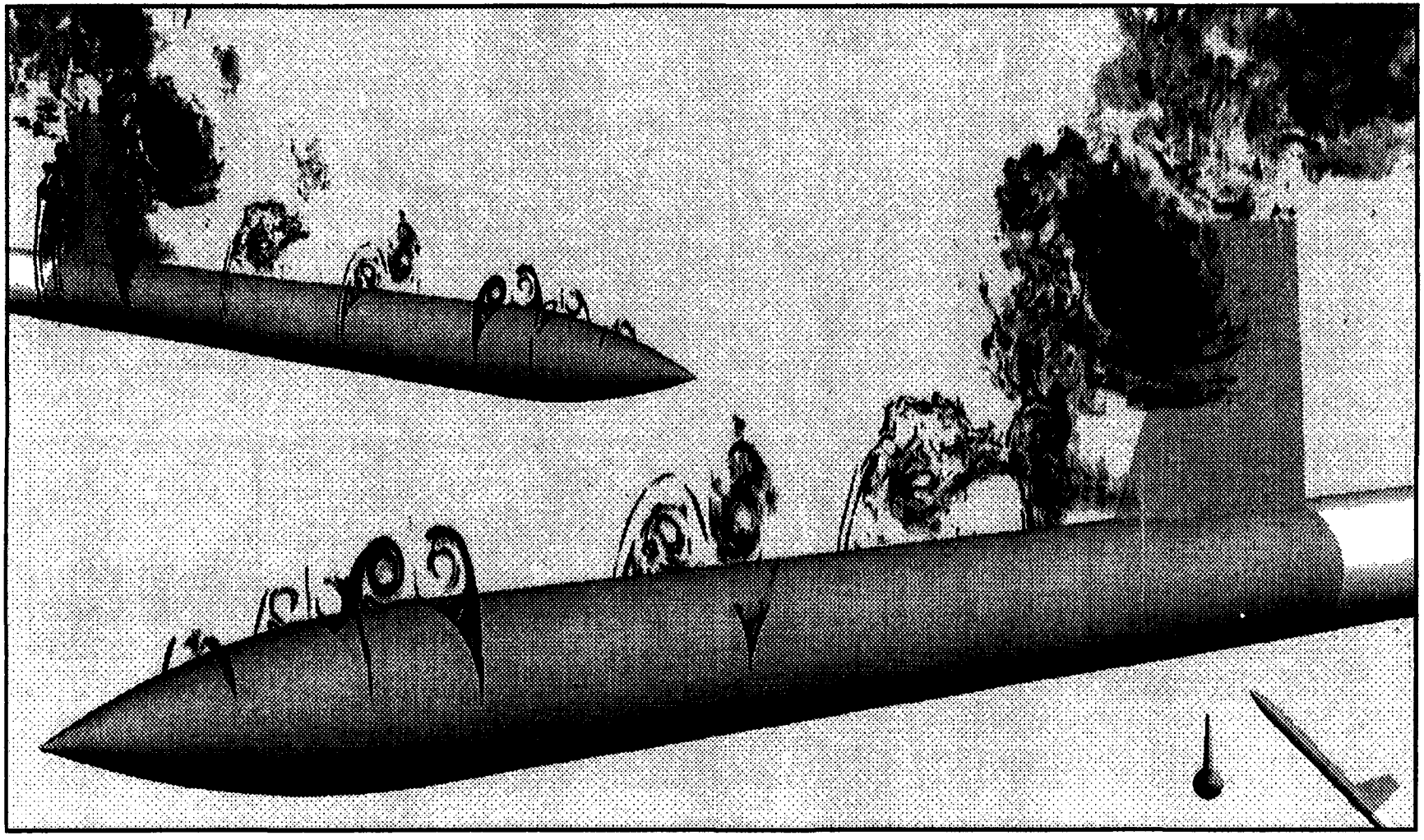

Figure 53. Three-Dimensional Perspective View of Flowfield ($\alpha = 45°$, $\phi = 0°$, $Re_d = 6000$, $(x/d)_f = 9.4$).

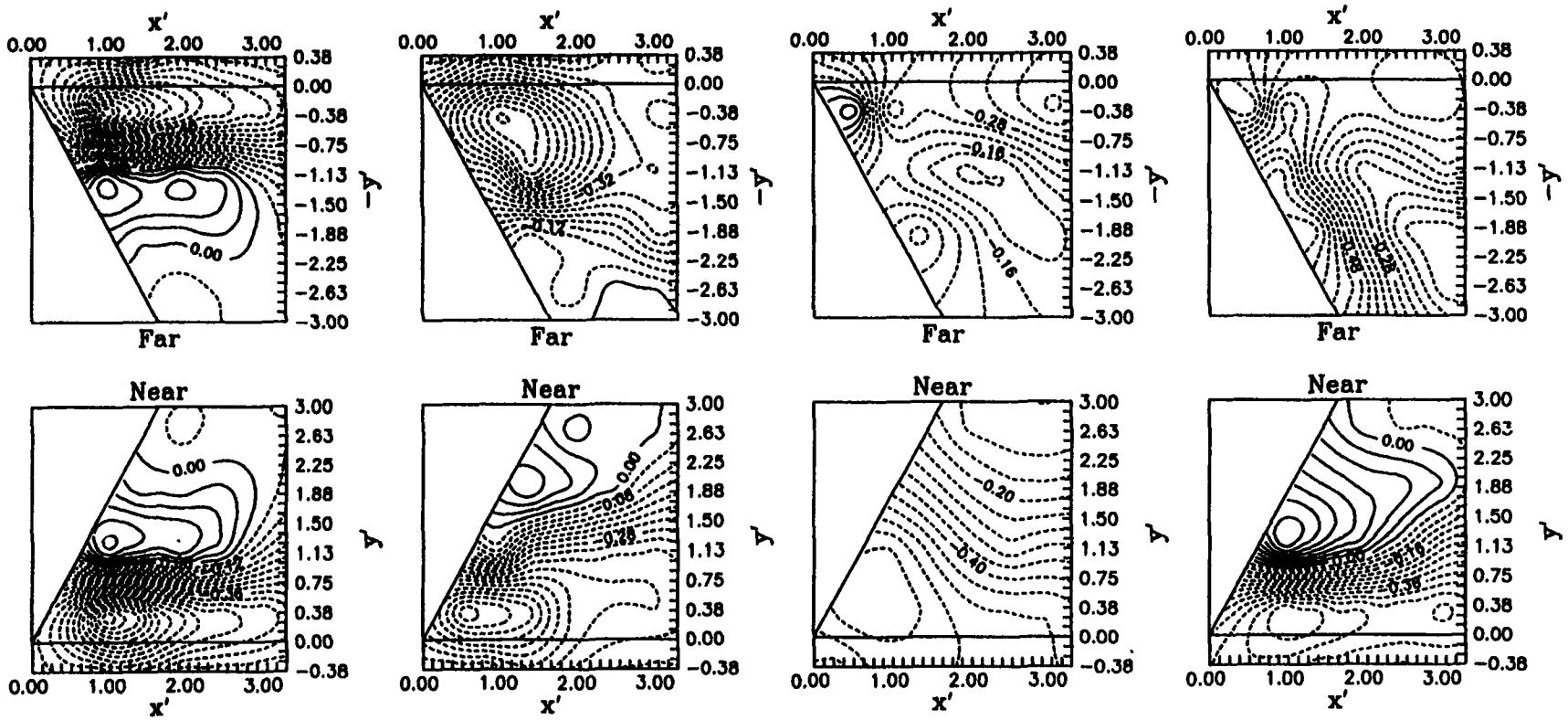

(a) $(x/d)_f = 2.6$ (b) $(x/d)_f = 4.9$ (c) $(x/d)_f = 7.1$ (d) $(x/d)_f = 9.4$

Figure 54. Coefficient of Pressure Contours on Fin ($\alpha = 45°$, $\phi = 0°$, $Re_d = 6000$).

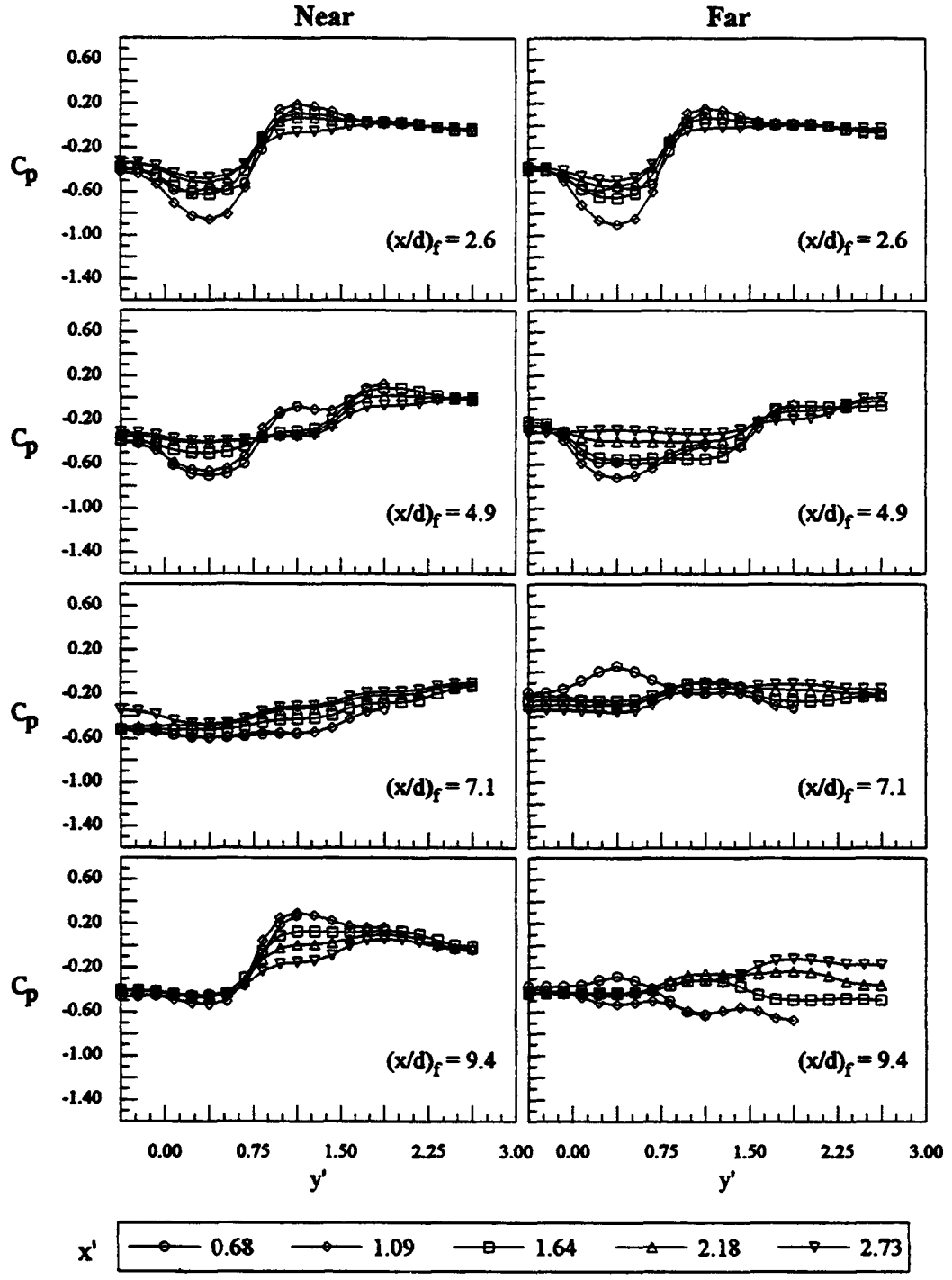

Figure 55. Spanwise Pressure Distributions on Fin ($\alpha = 45°$, $\phi = 0°$, $Re_d = 6000$).

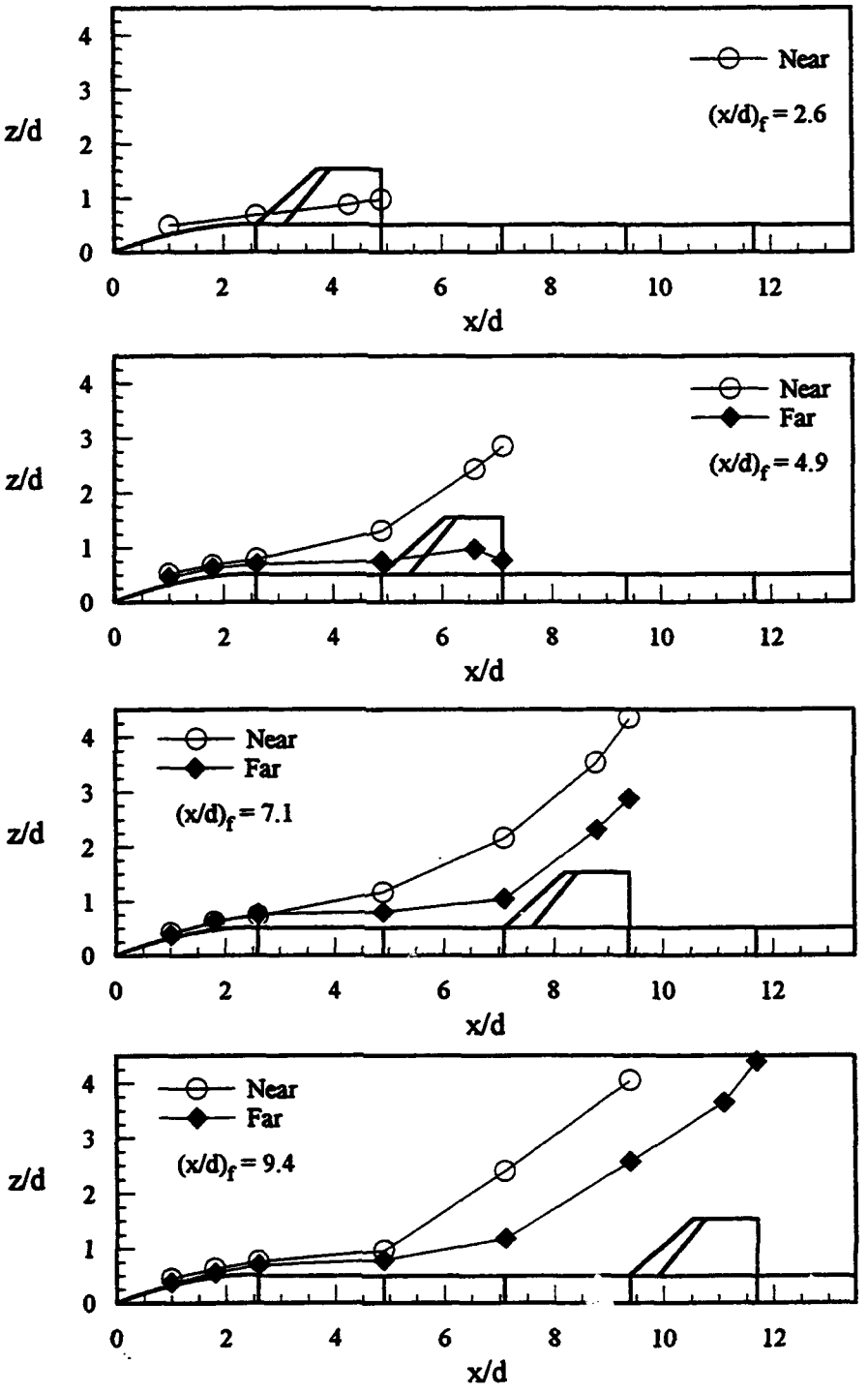

Figure 56. Vortex Center Trajectories, Side View ($\alpha = 45°$, $\phi = -54°$, $Re_d = 6000$).

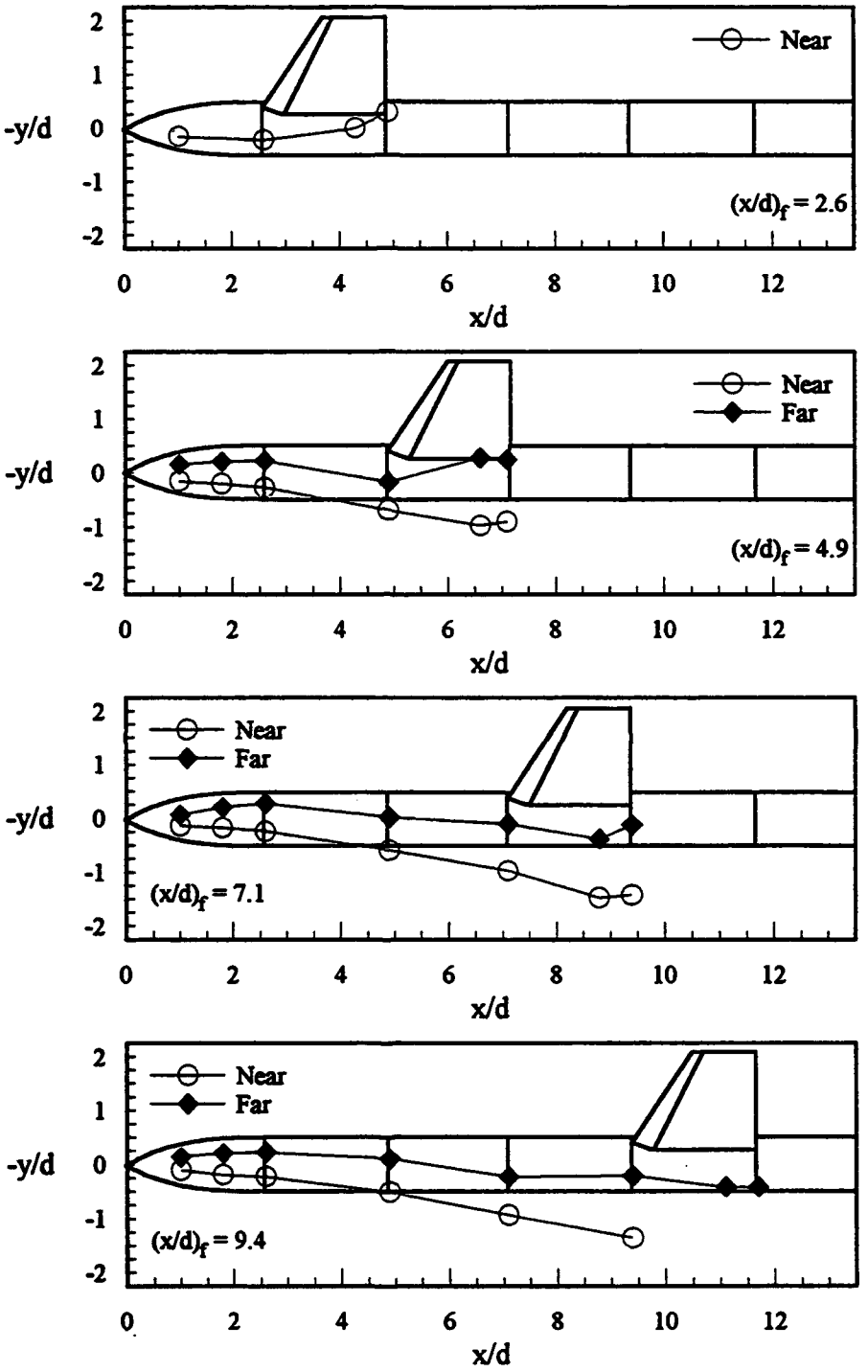

Figure 57. Vortex Center Trajectories, Top View ($\alpha = 45°$, $\phi = -54°$, $Re_d = 6000$).

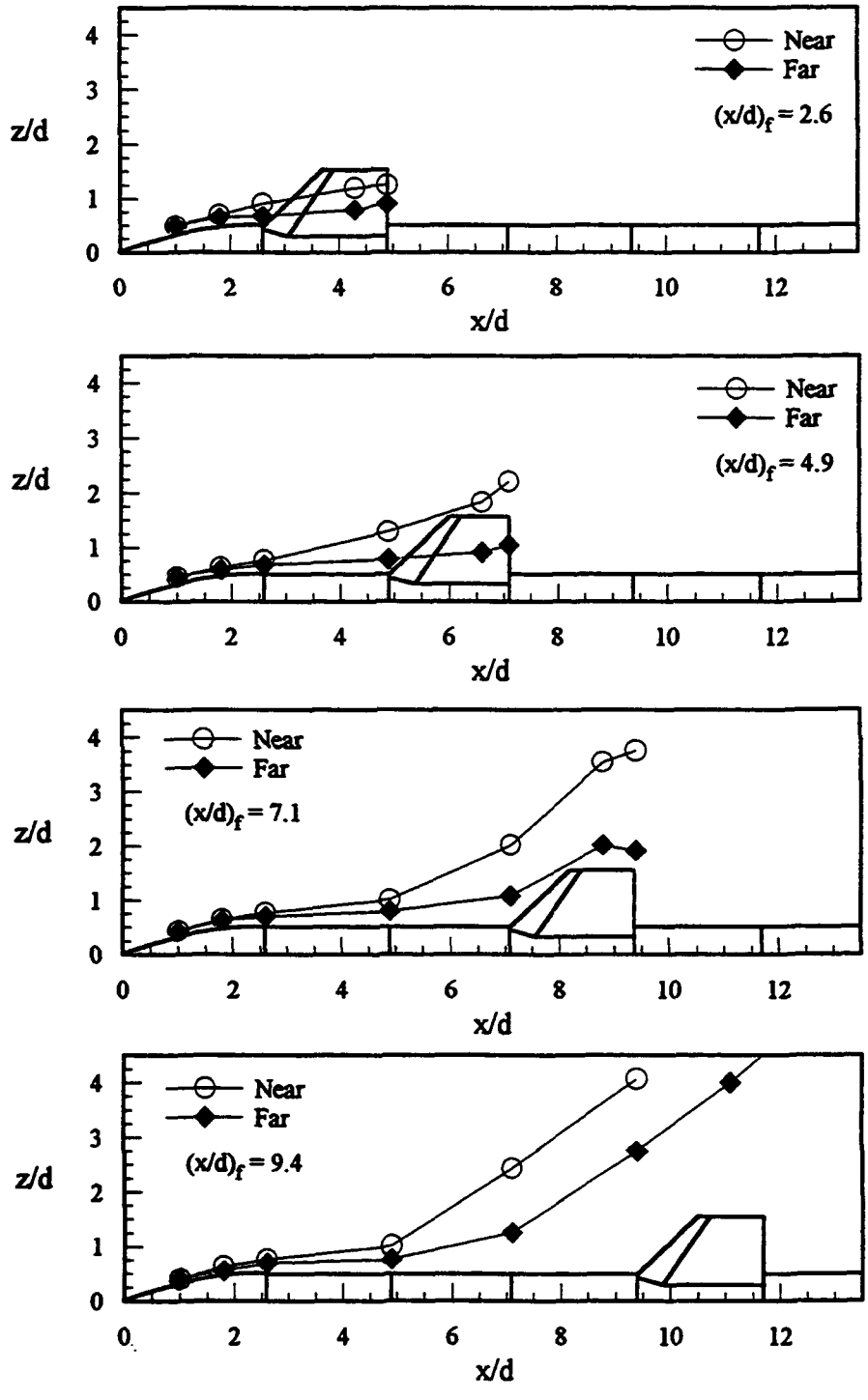

Figure 58. Vortex Center Trajectories, Side View ($\alpha = 45°$, $\phi = +54°$, $Re_d = 6000$).

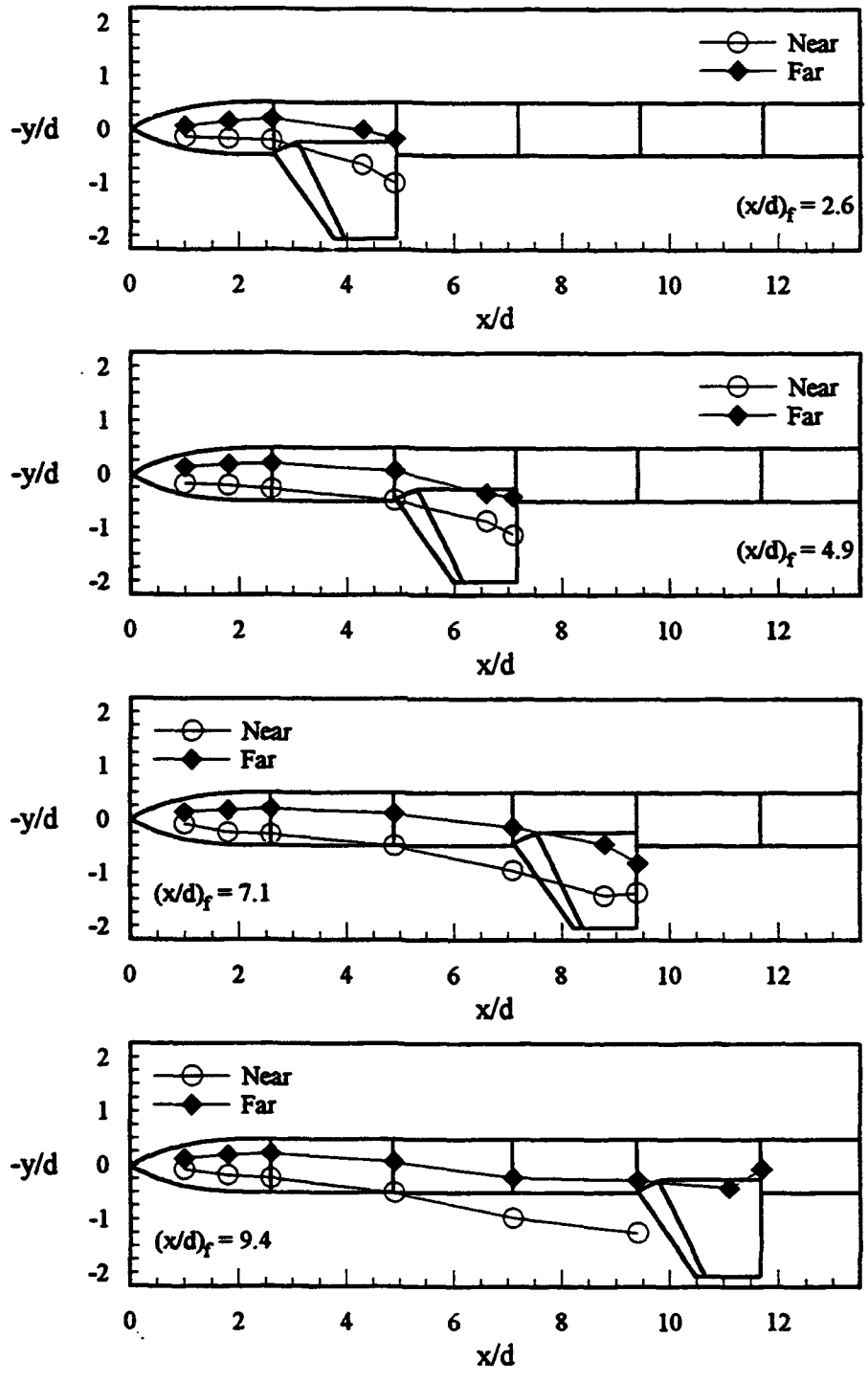

Figure 59. Vortex Center Trajectories, Top View ($\alpha = 45°$, $\phi = +54°$, $Re_d = 6000$).

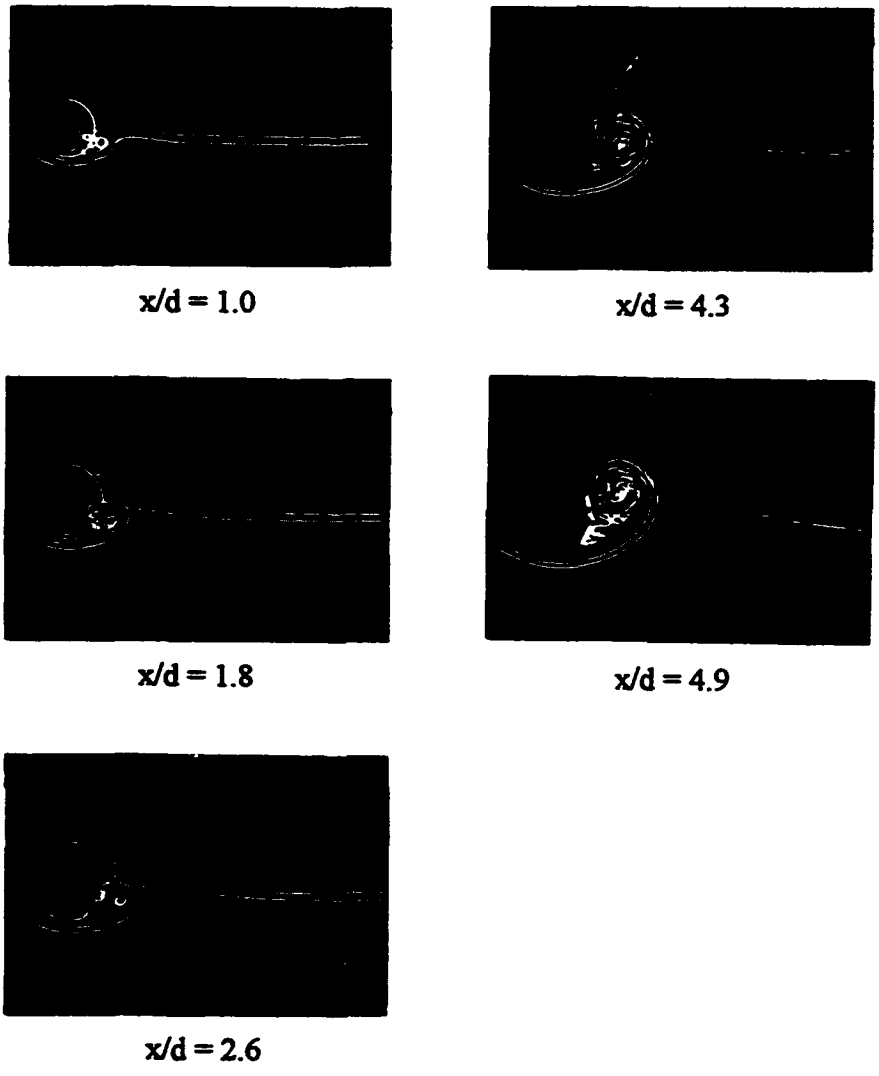

Figure 60. Cross-Sectional Flow Visualization Showing Flowfield Development ($\alpha = 45°$, $\phi = -54°$, $Re_d = 6000$, $(x/d)_f = 2.6$).

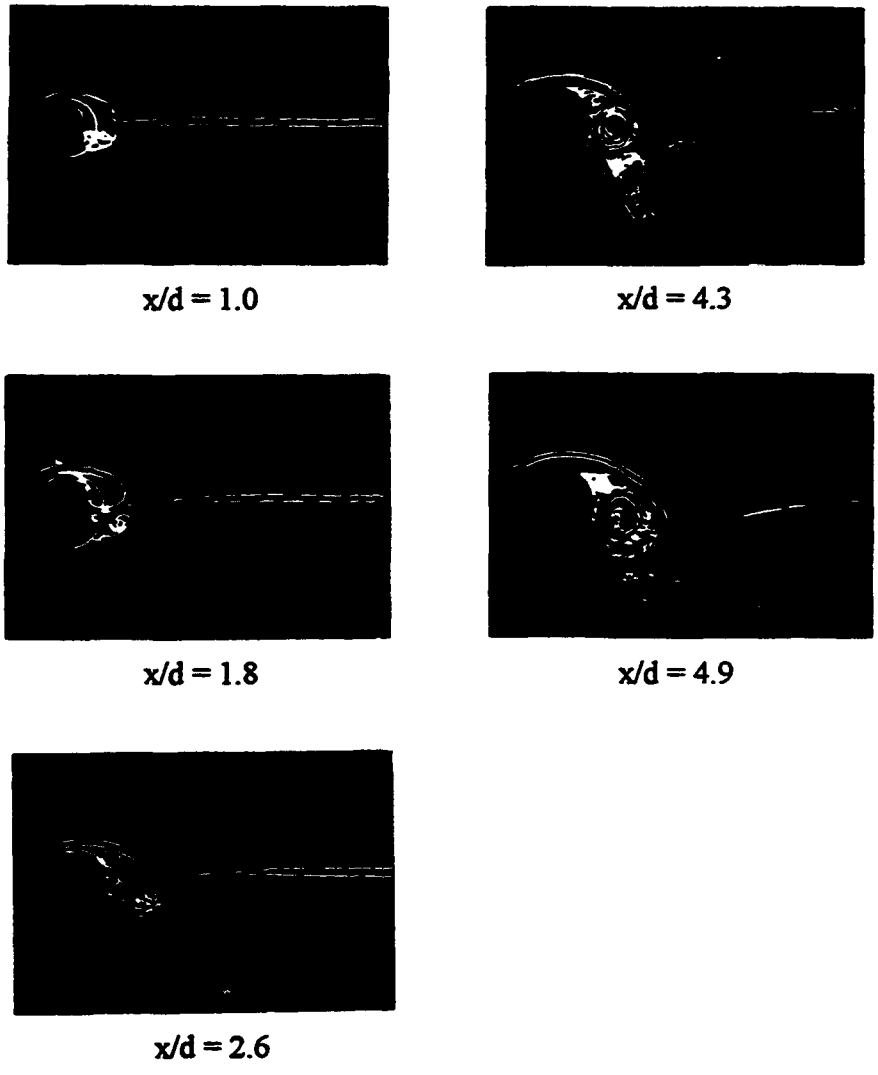

Figure 61. Cross-Sectional Flow Visualization Showing Flowfield Development ($\alpha = 45°$, $\phi = +54°$, $Re_d = 6000$, $(x/d)_f = 2.6$).

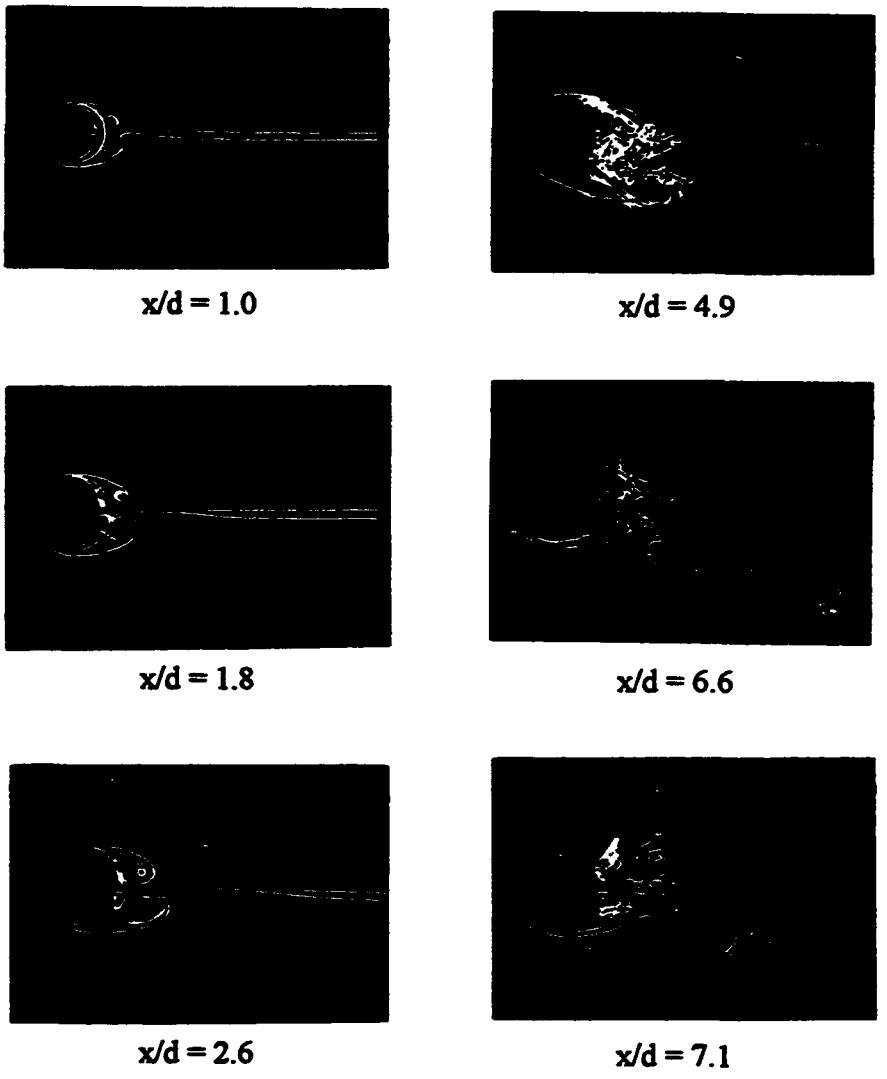

Figure 62. Cross-Sectional Flow Visualization Showing Flowfield Development ($\alpha = 45°$, $\phi = -54°$, $Re_d = 6000$, $(x/d)_f = 4.9$).

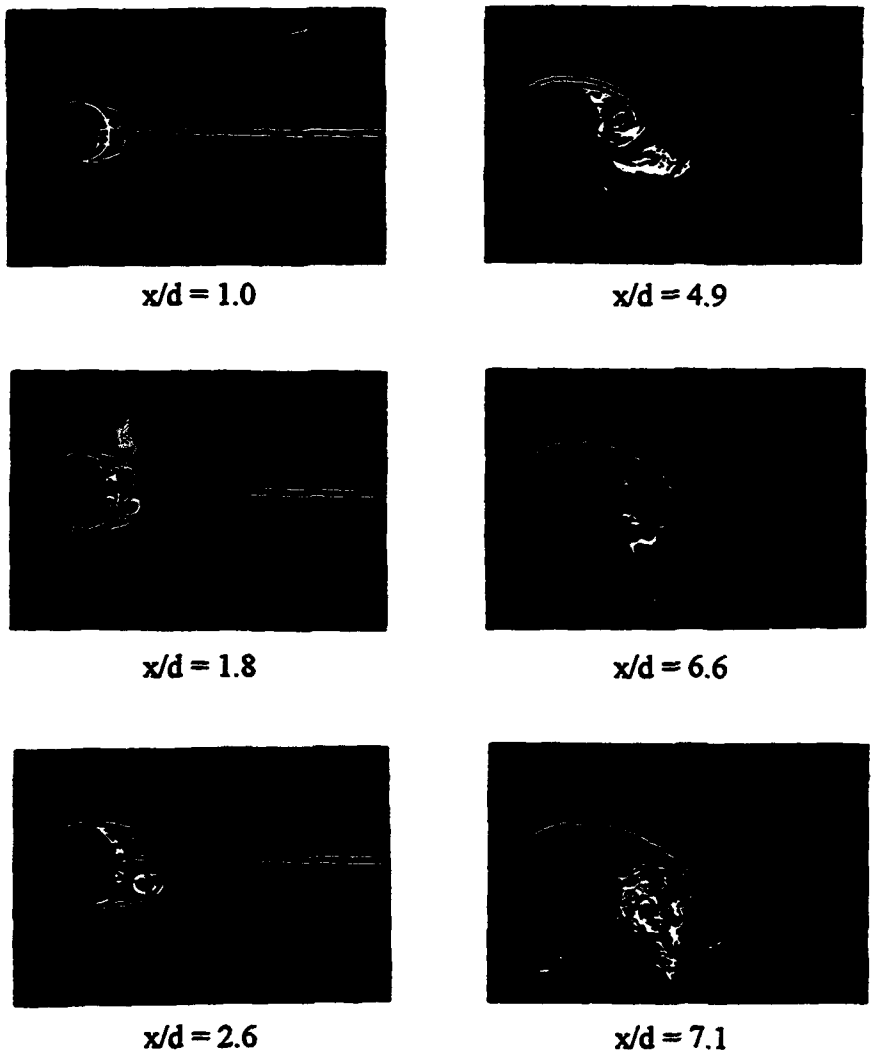

Figure 63. Cross-Sectional Flow Visualization Showing Flowfield Development ($\alpha = 45°$, $\phi = +54°$, $Re_d = 6000$, $(x/d)_f = 4.9$).

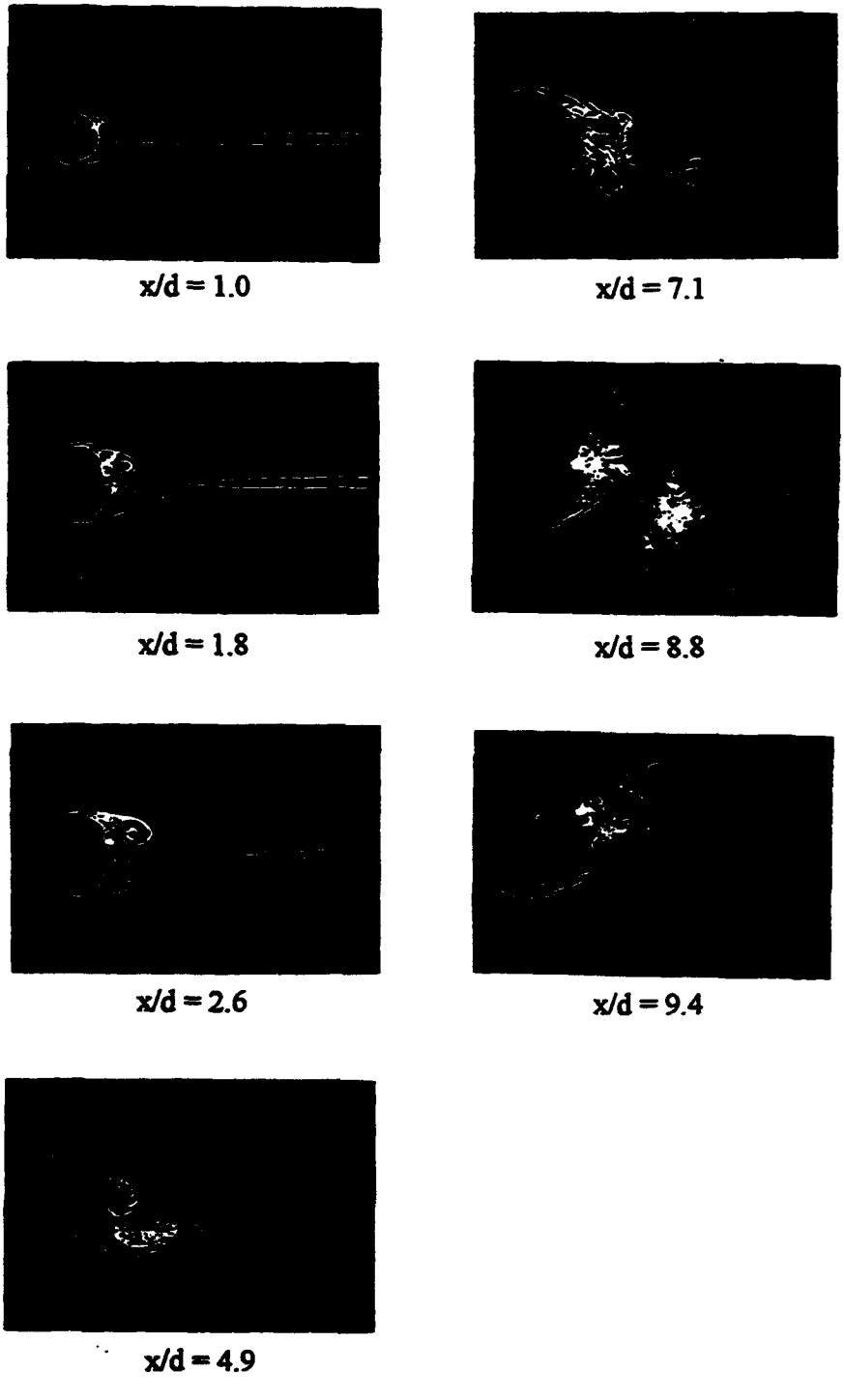

Figure 64. Cross-Sectional Flow Visualization Showing Flowfield Development ($\alpha = 45°$, $\phi = -54°$, $Re_d = 6000$, $(x/d)_f = 7.1$).

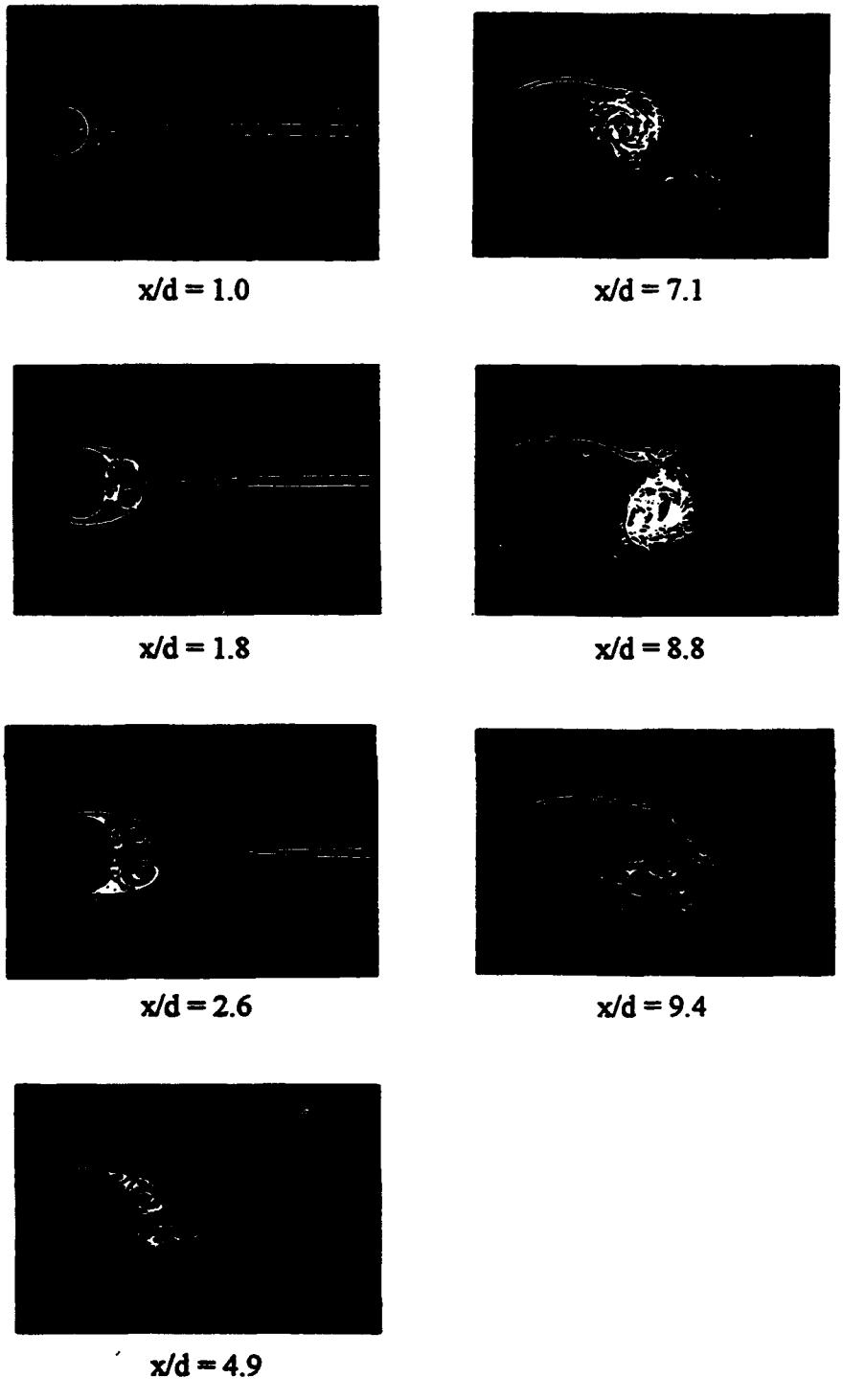

Figure 65. Cross-Sectional Flow Visualization Showing Flowfield Development ($\alpha = 45°$, $\phi = +54°$, $Re_d = 6000$, $(x/d)_f = 7.1$).

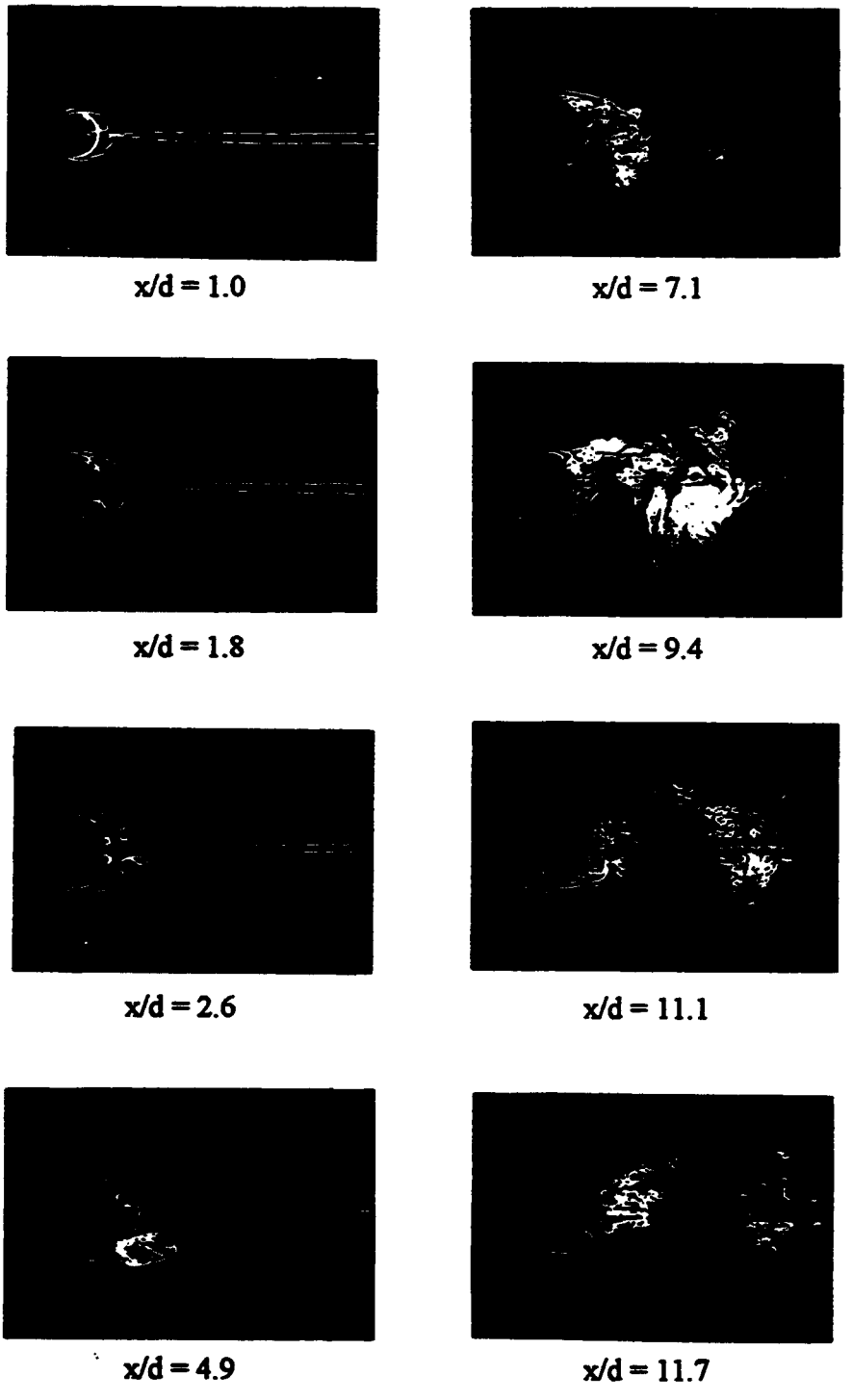

Figure 66. Cross-Sectional Flow Visualization Showing Flowfield Development ($\alpha = 45°$, $\phi = -54°$, $Re_d = 6000$, $(x/d)_f = 9.4$).

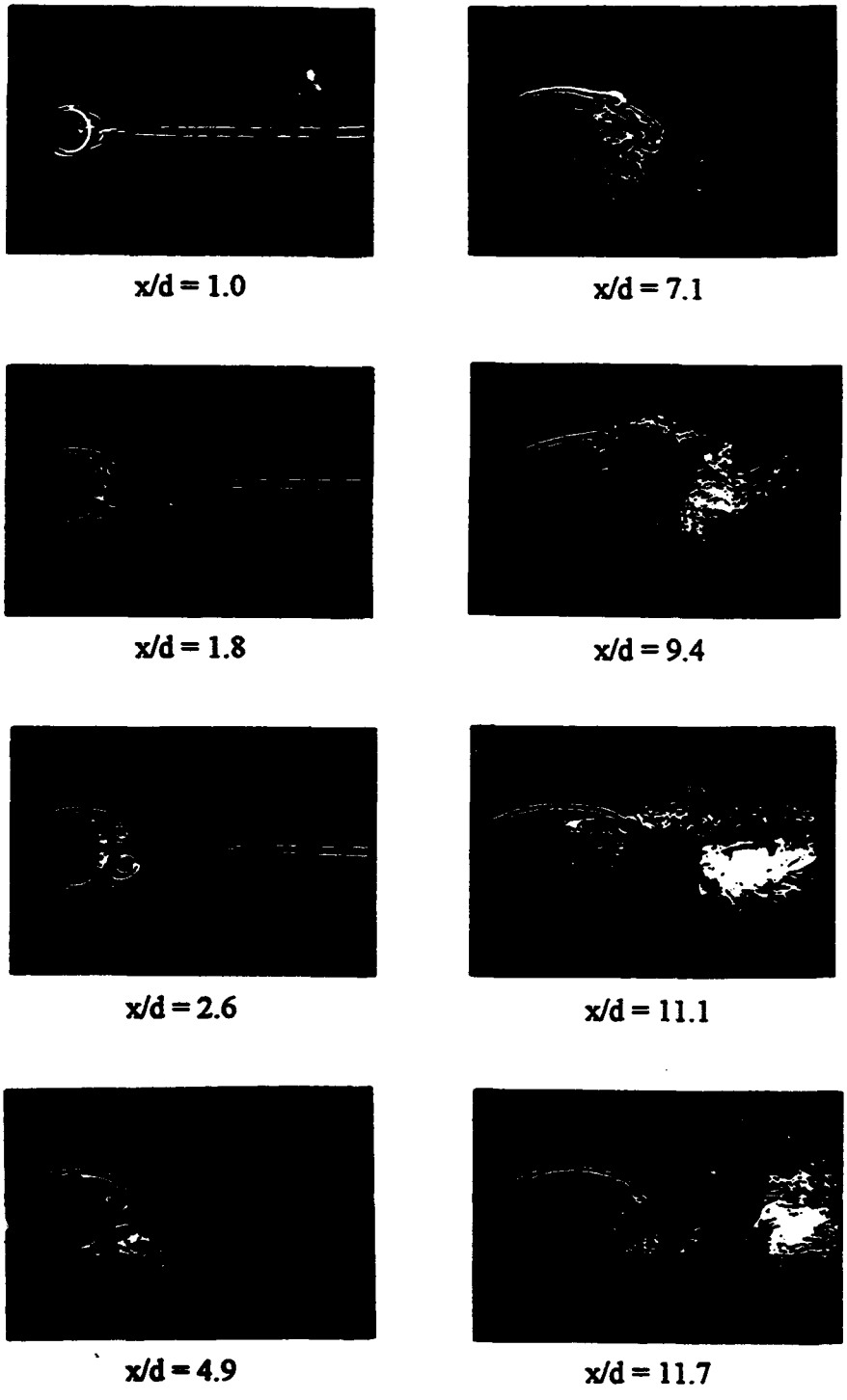

Figure 67. Cross-Sectional Flow Visualization Showing Flowfield Development ($\alpha = 45°$, $\phi = +54°$, $Re_d = 6000$, $(x/d)_f = 9.4$).

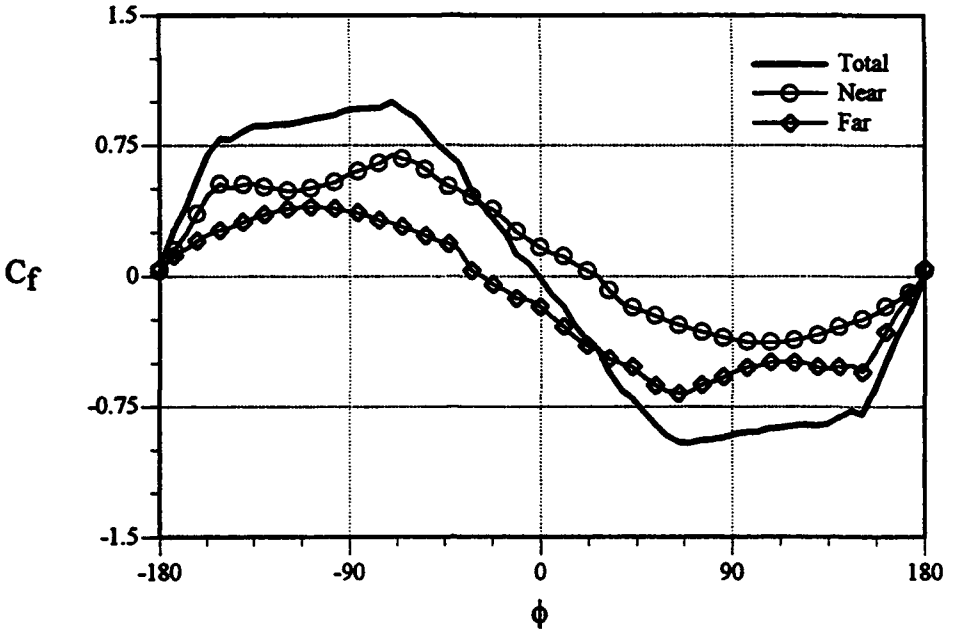

(a) $(x/d)_f = 2.6$

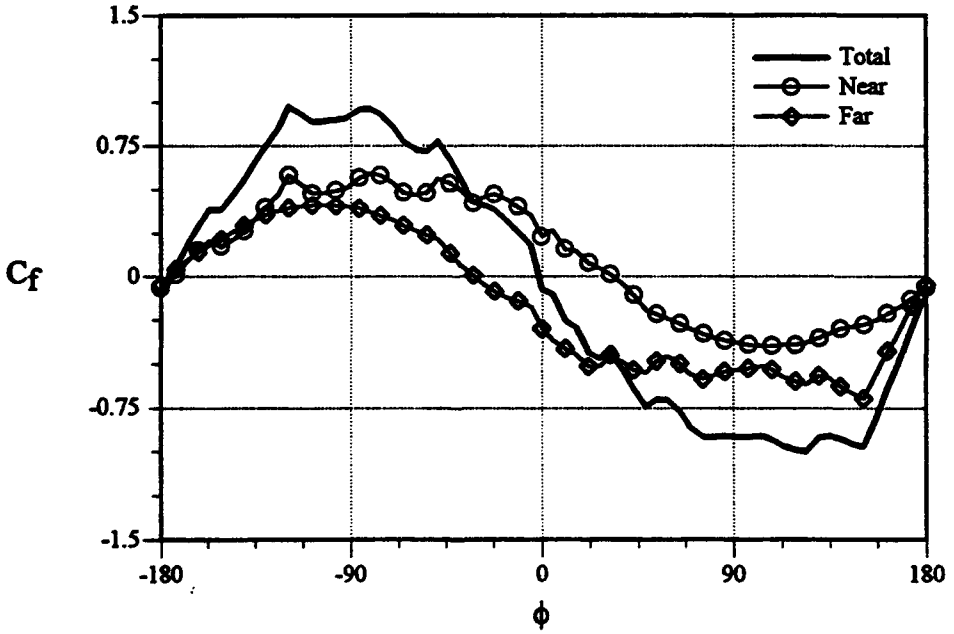

(b) $(x/d)_f = 4.9$

Figure 68. Variation of Normal Force Coefficient on Fin with ϕ ($\alpha = 45°$, $Re_d = 6000$).

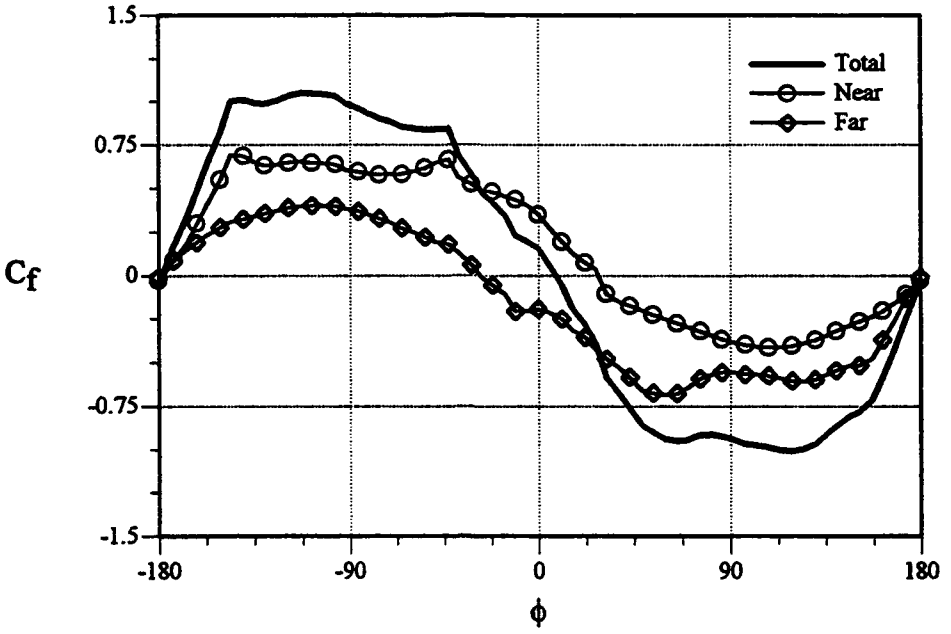

(c) $(x/d)_f = 7.1$

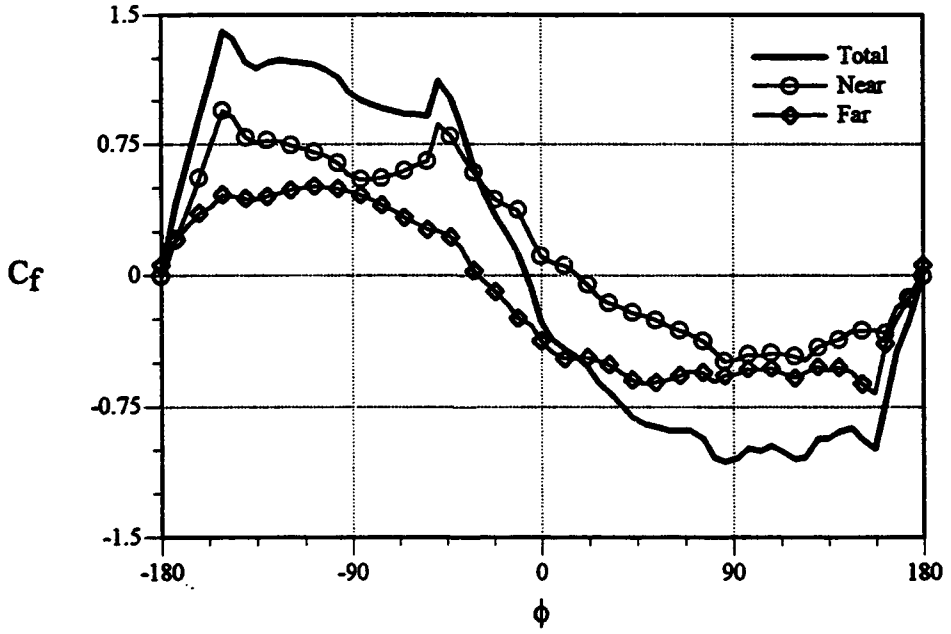

(d) $(x/d)_f = 9.4$

Figure 68. (Concluded)

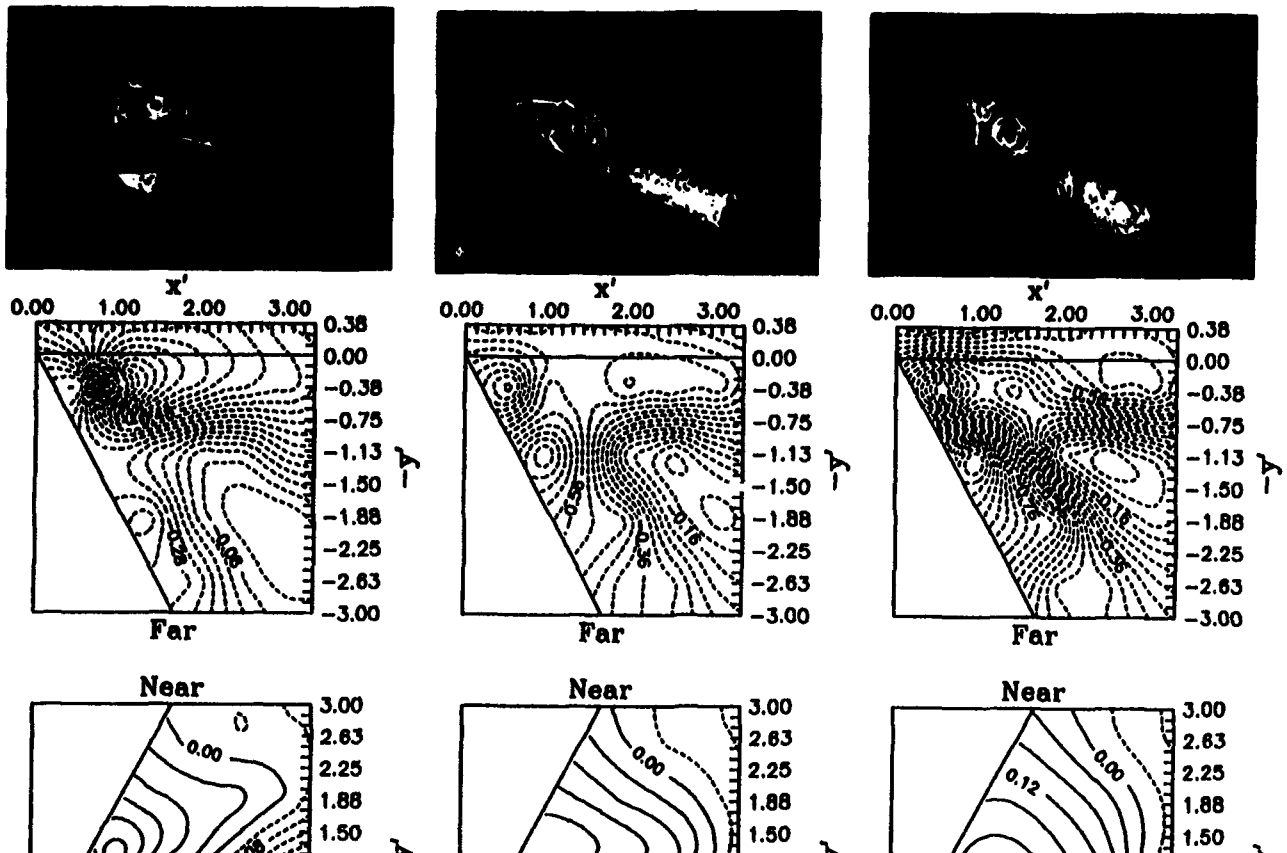

(a) $\phi = +11°$ (b) $\phi = +22°$ (c) $\phi = +32°$

Figure 69. Coefficient of Pressure Contours with Cross-Sectional Flow Visualization ($\alpha = 45°$, $Re_d = 6000$, $(x/d)_f = 2.6$).

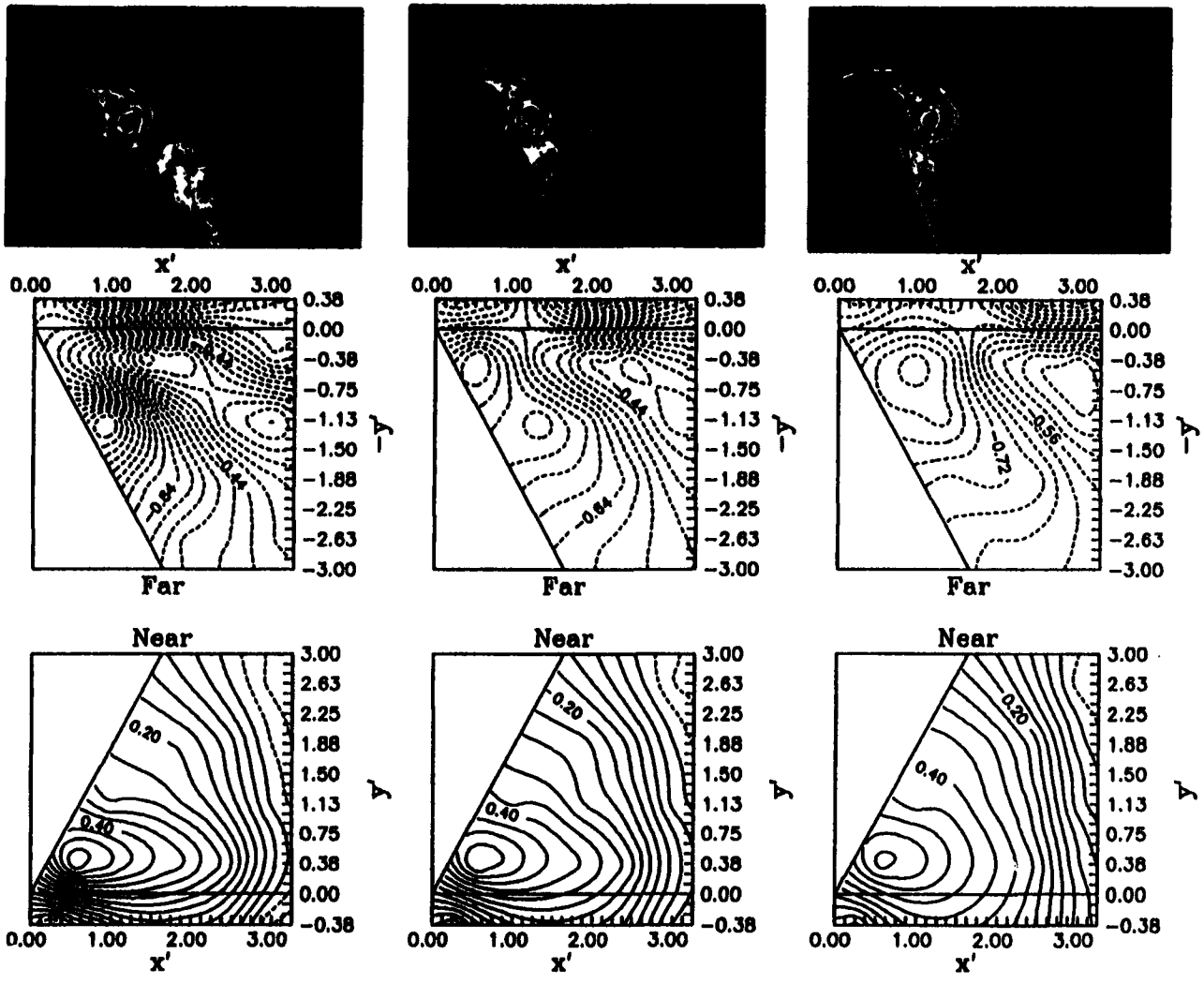

(a) $\phi = +43°$ (b) $\phi = +54°$ (c) $\phi = +65°$

Figure 69. (Continued).

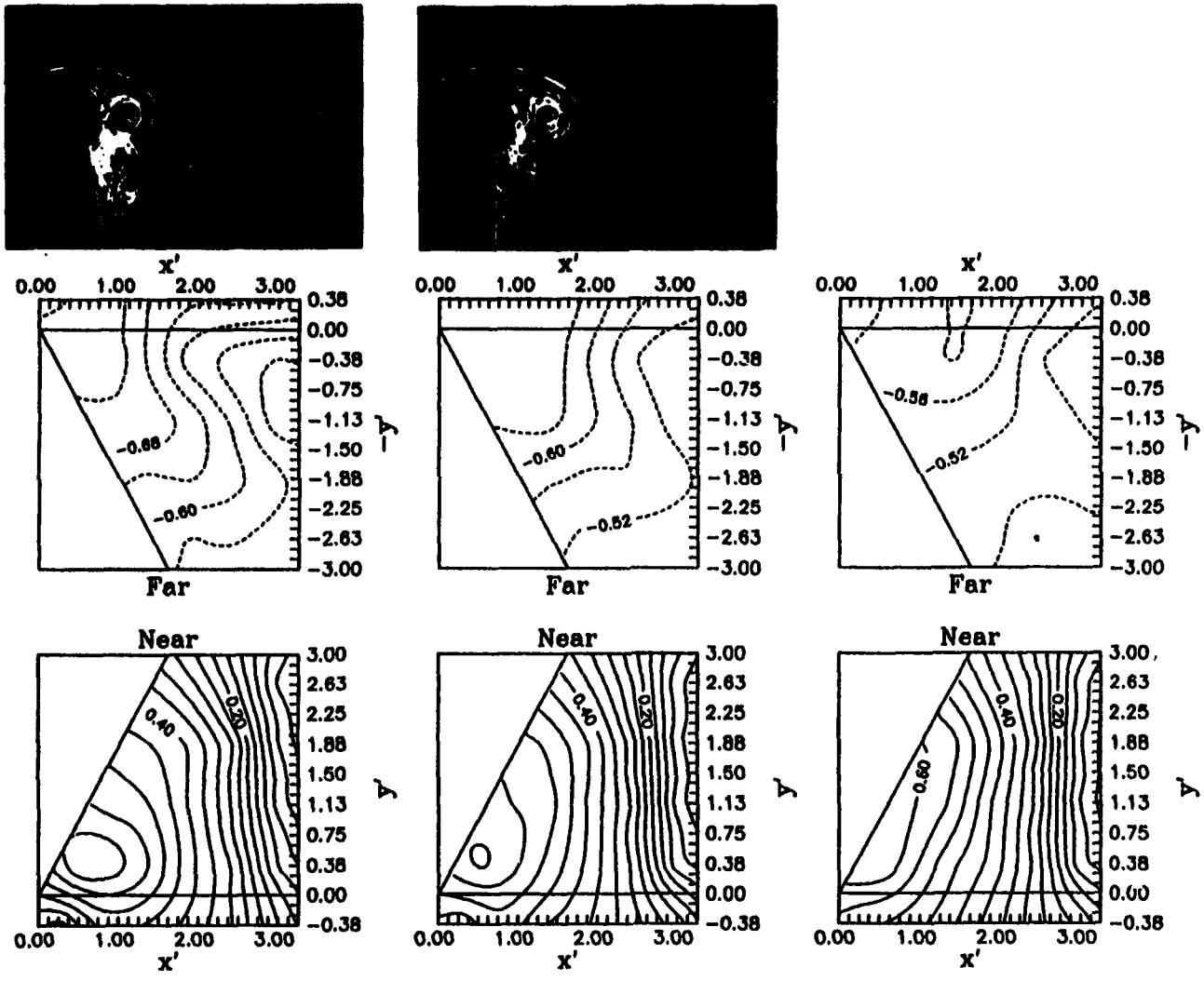

(a) $\phi = +76°$ (b) $\phi = +86°$ (c) $\phi = +97°$

Figure 69. (Concluded).

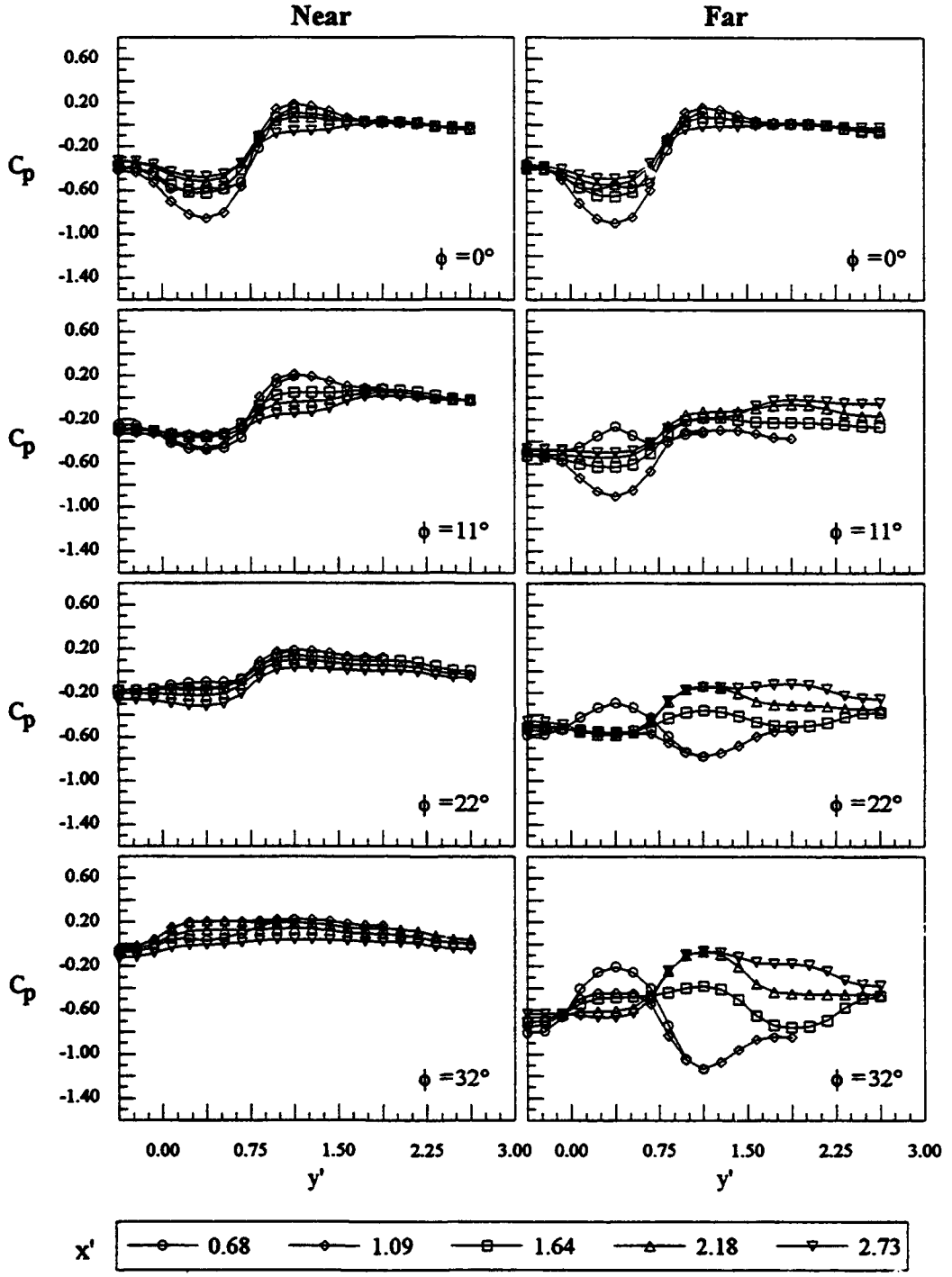

Figure 70. Spanwise Pressure Distributions on Fin ($\alpha = 45°$, $Re_d = 6000$, $(x/d)_f = 2.6$).

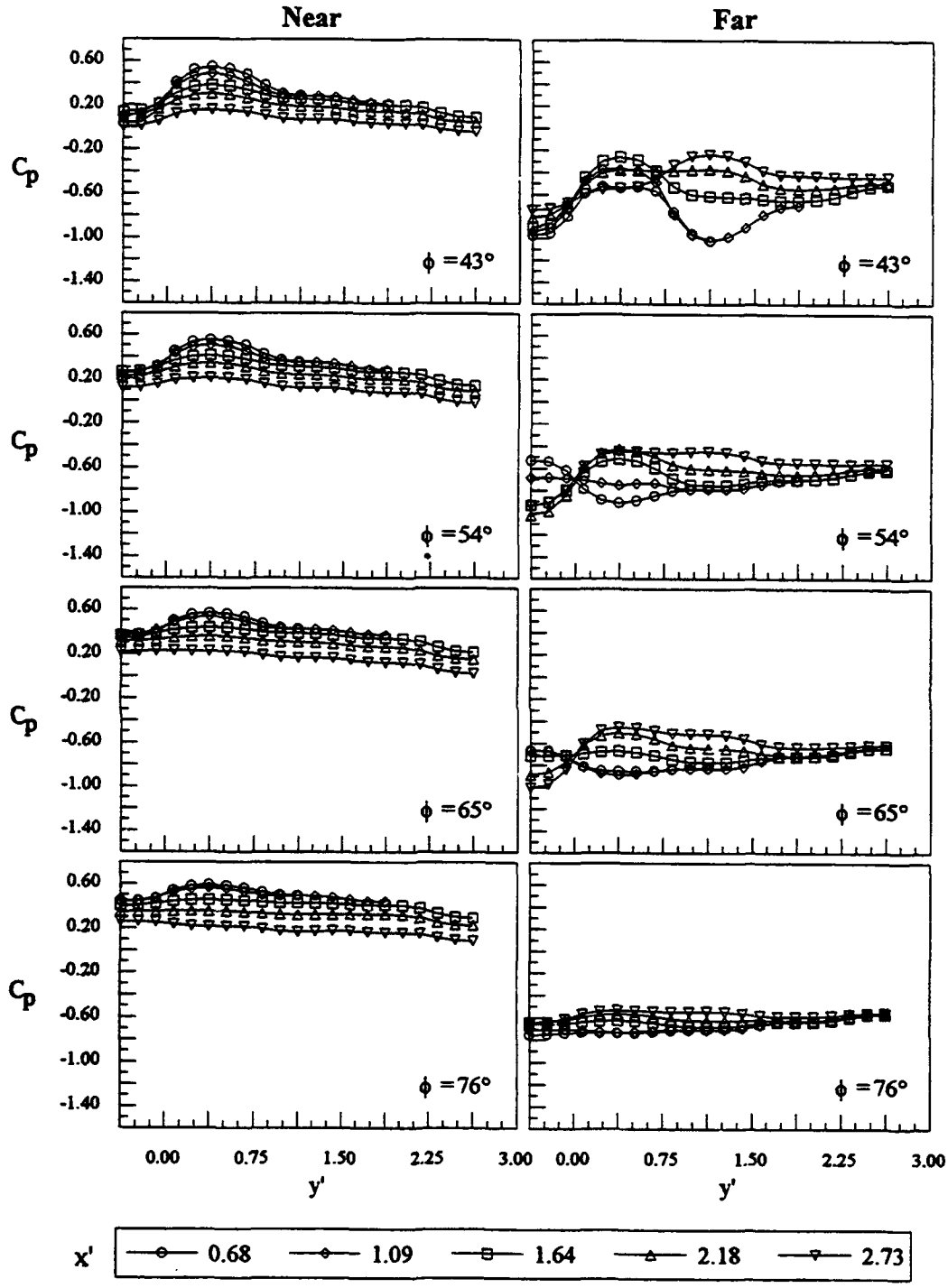

Figure 70. (Continued)

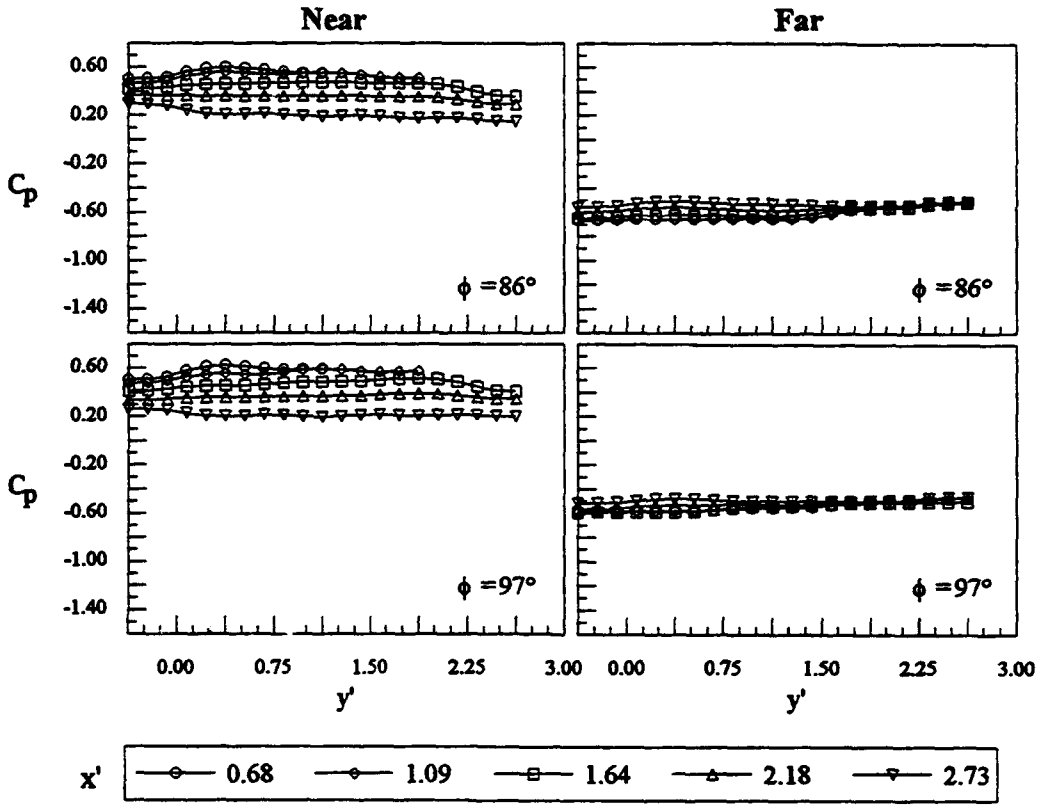

Figure 70. (Concluded)

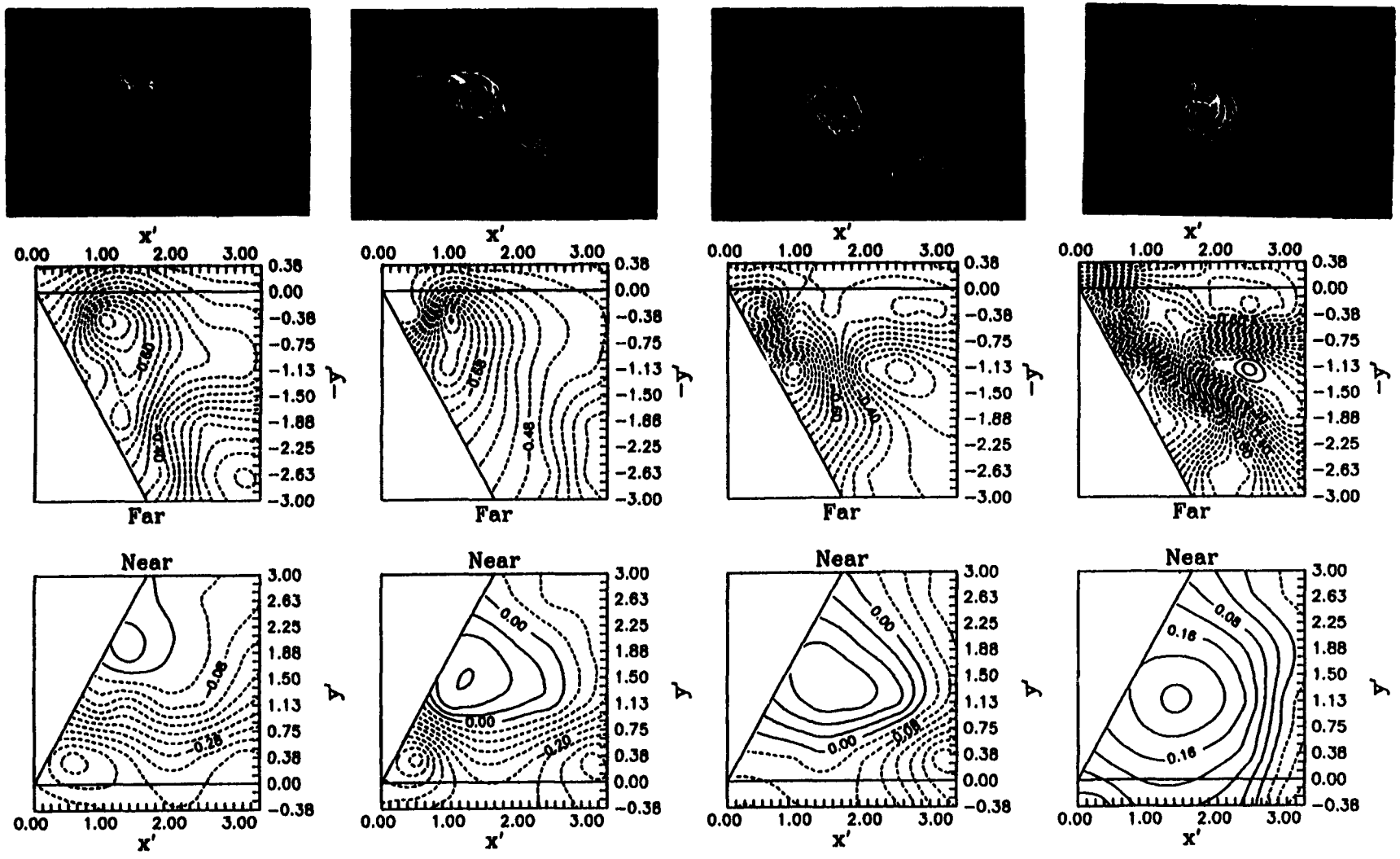

(a) $\phi = +11°$ (b) $\phi = +22°$ (c) $\phi = +32°$ (d) $\phi = +43°$

Figure 71. Coefficient of Pressure Contours with Cross-Sectional Flow Visualization ($\alpha = 45°$, $Re_d = 6000$, $(x/d)_f = 4.9$).

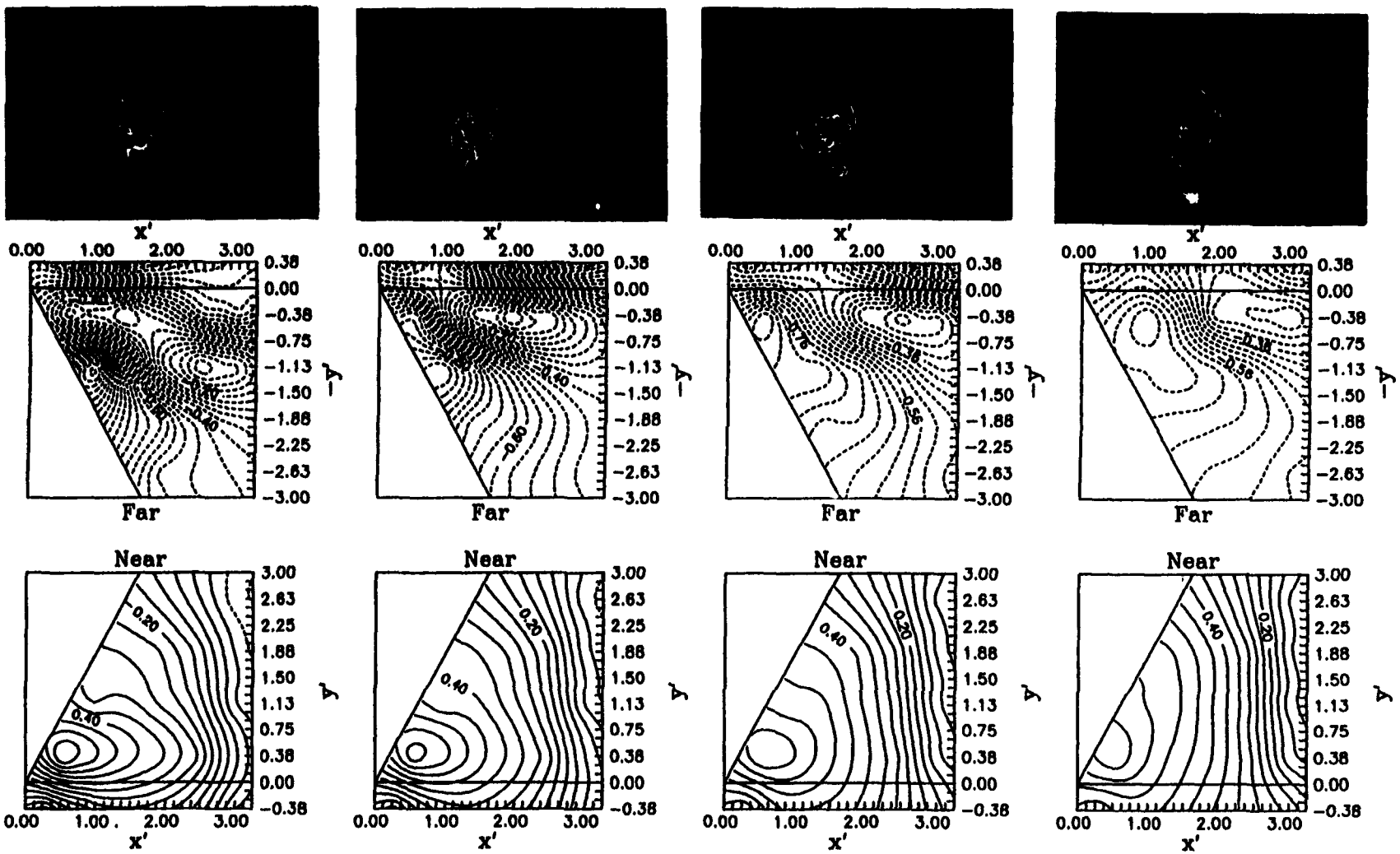

(a) $\phi = +54°$ (b) $\phi = +65°$ (c) $\phi = +76°$ (d) $\phi = +86°$

Figure 71. (Continued).

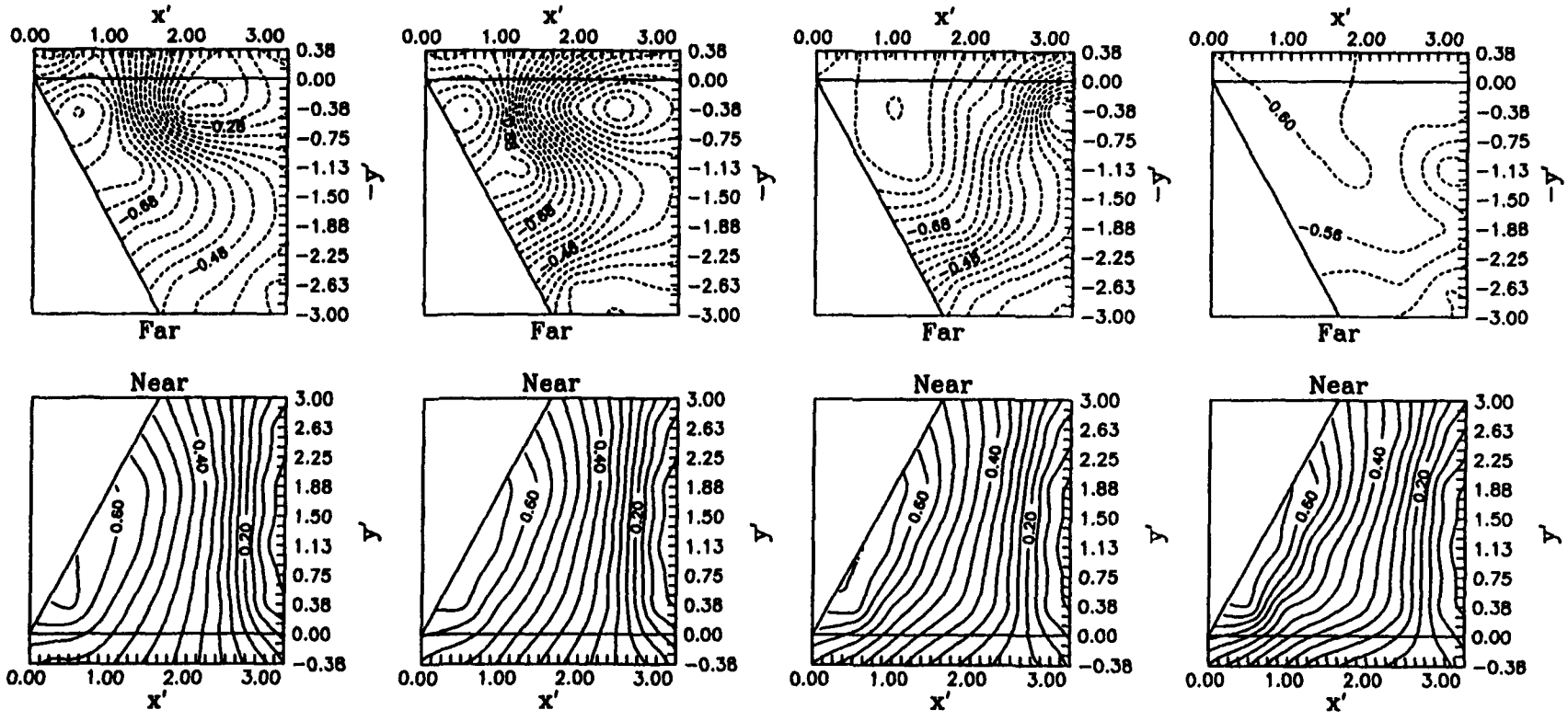

(a) $\phi = +97°$ (b) $\phi = +108°$ (c) $\phi = +119°$ (d) $\phi = +130°$

Figure 71. (Concluded).

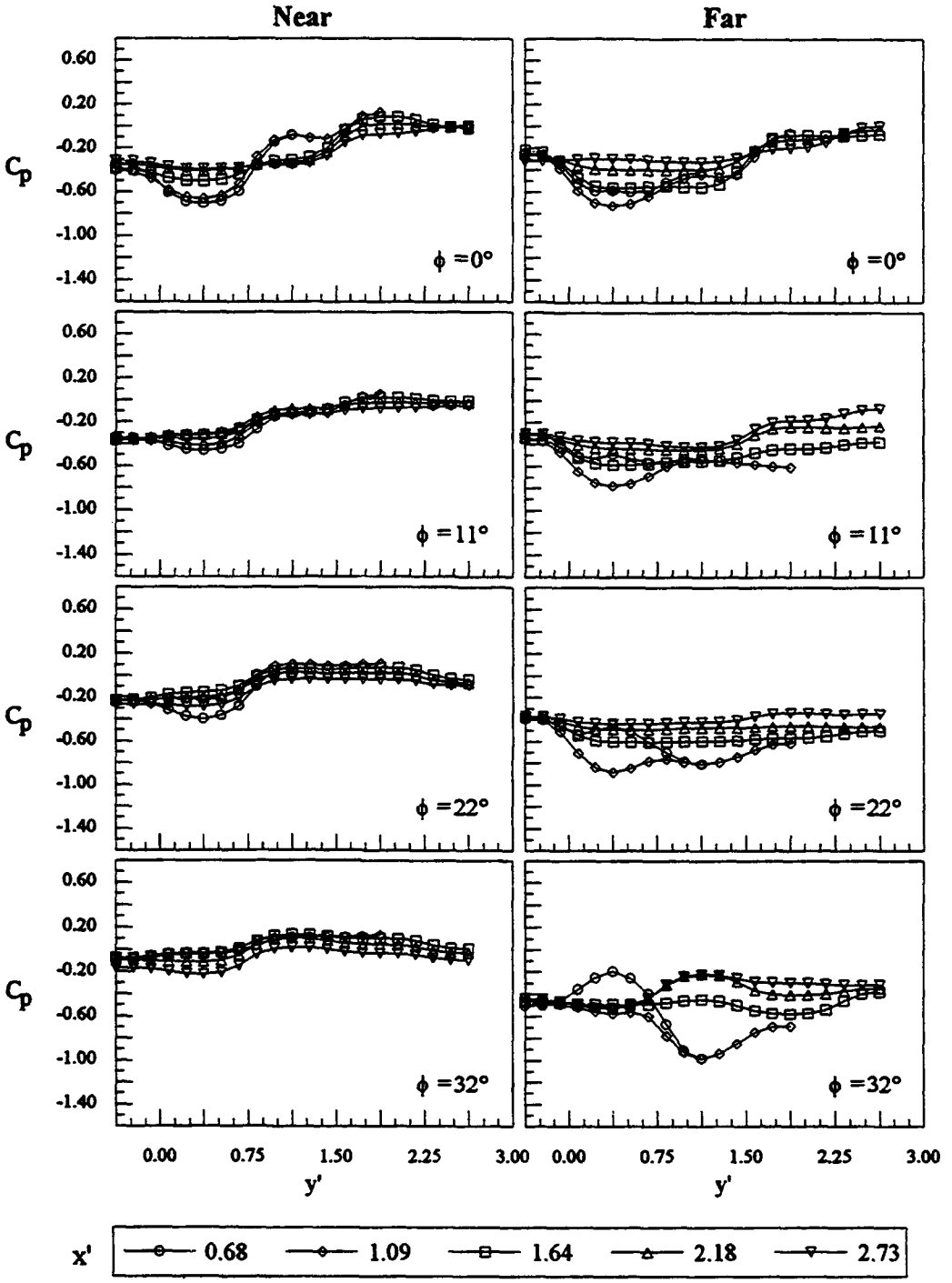

Figure 72. Spanwise Pressure Distributions on Fin ($\alpha = 45°$, $Re_d = 6000$, $(x/d)_f = 4.9$).

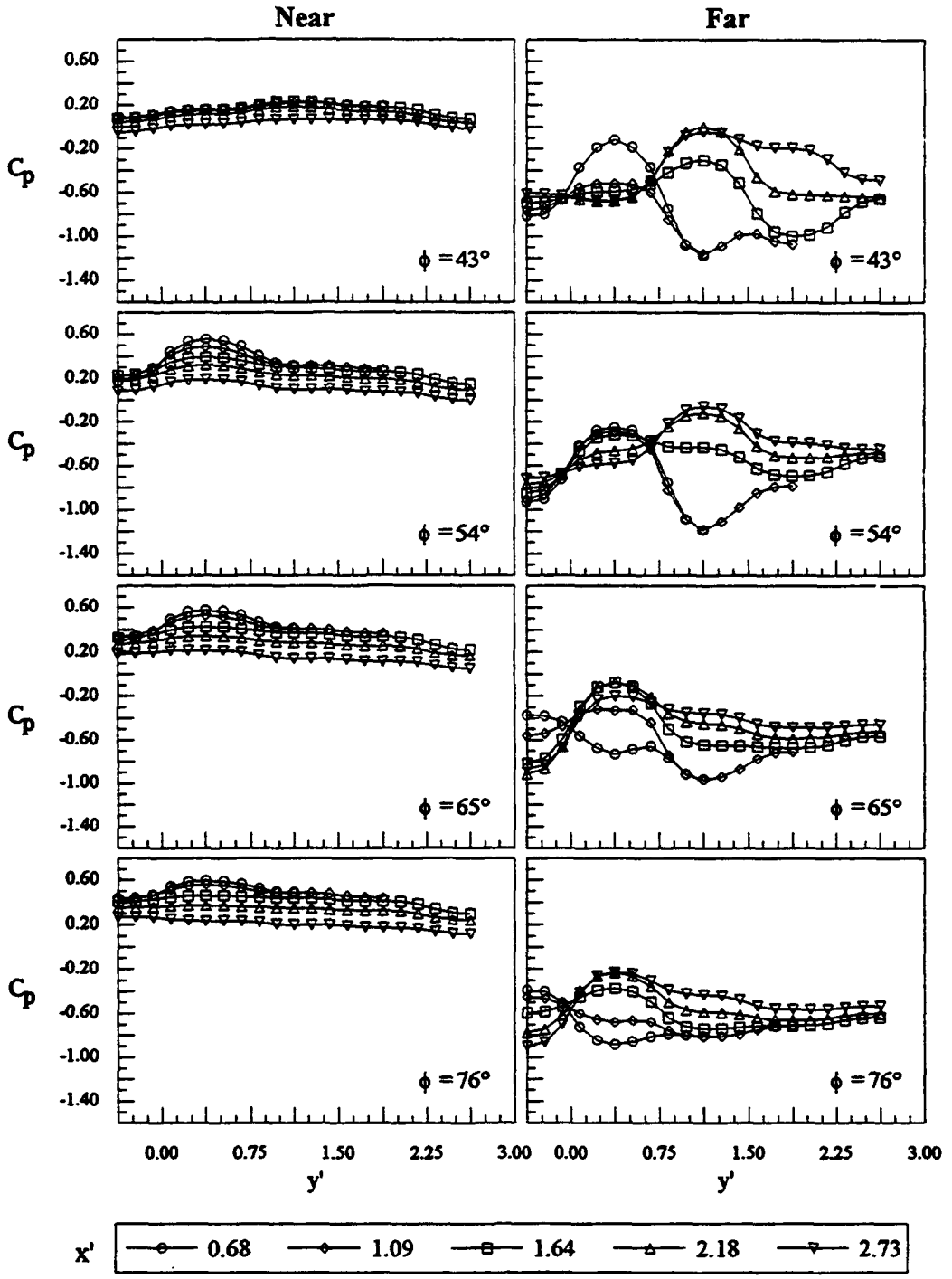

Figure 72. (Continued)

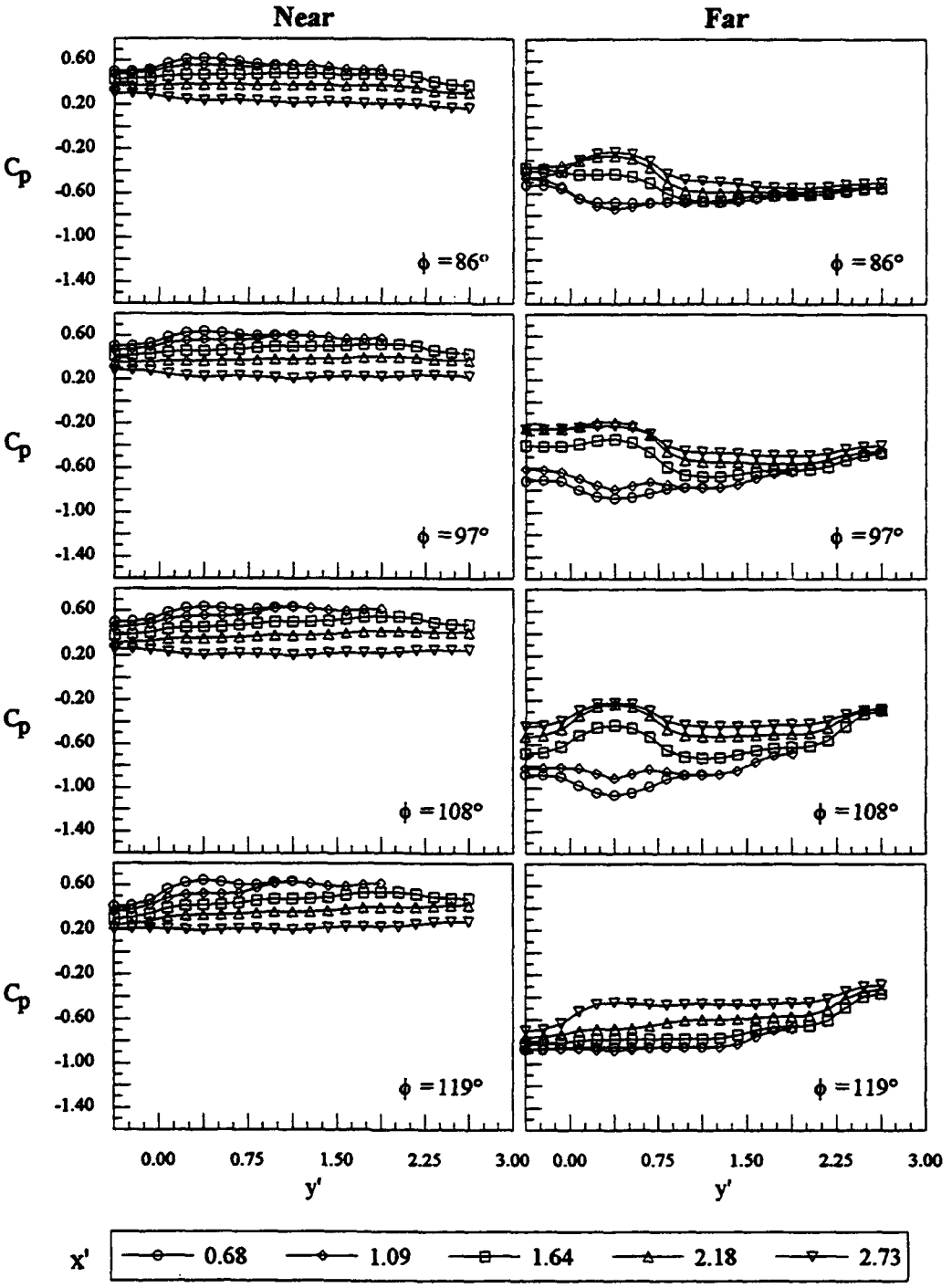

Figure 72. (Continued)

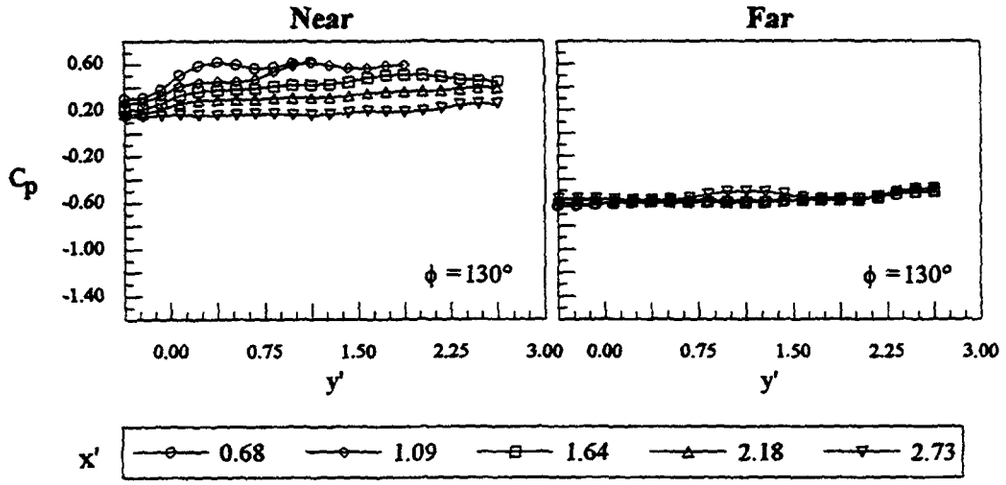

Figure 72. (Concluded)

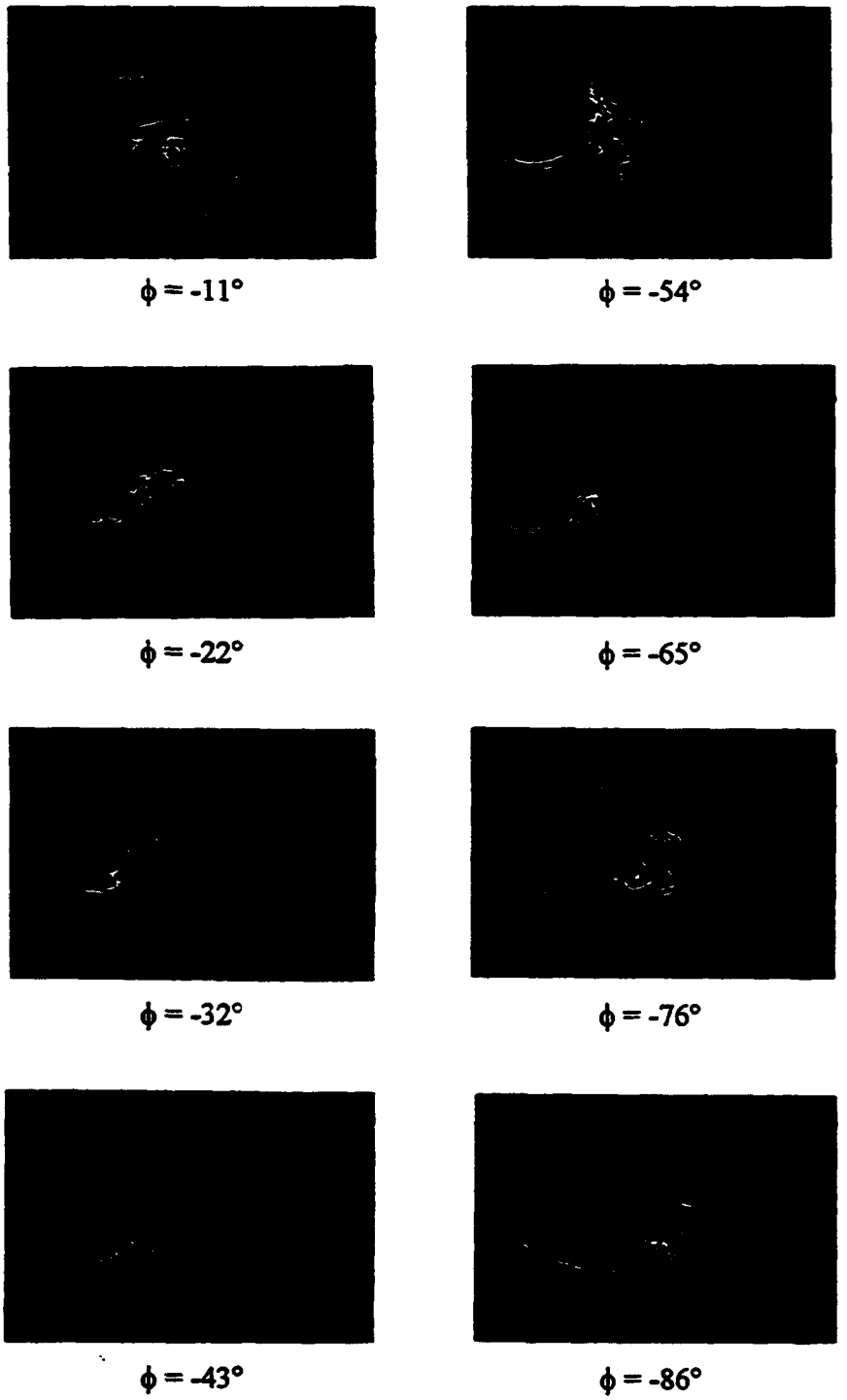

Figure 73. Cross-Sectional Flow Visualization ($\alpha = 45°$, $Re_d = 6000$, $(x/d)_f = 4.9$).

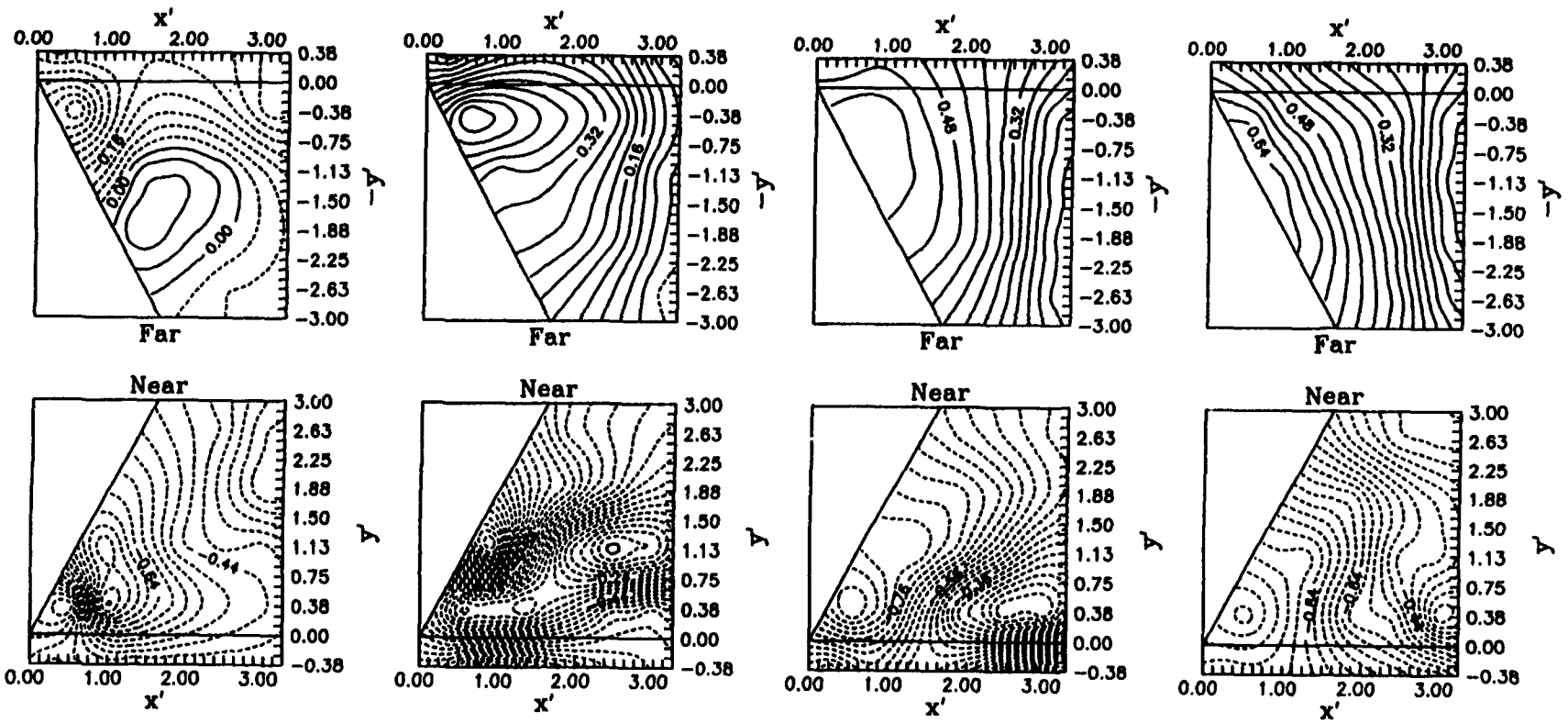

Figure 74. Coefficient of Pressure Contours on Fin ($\alpha = 45°$, $Re_d = 6000$, $(x/d)_f = 4.9$).

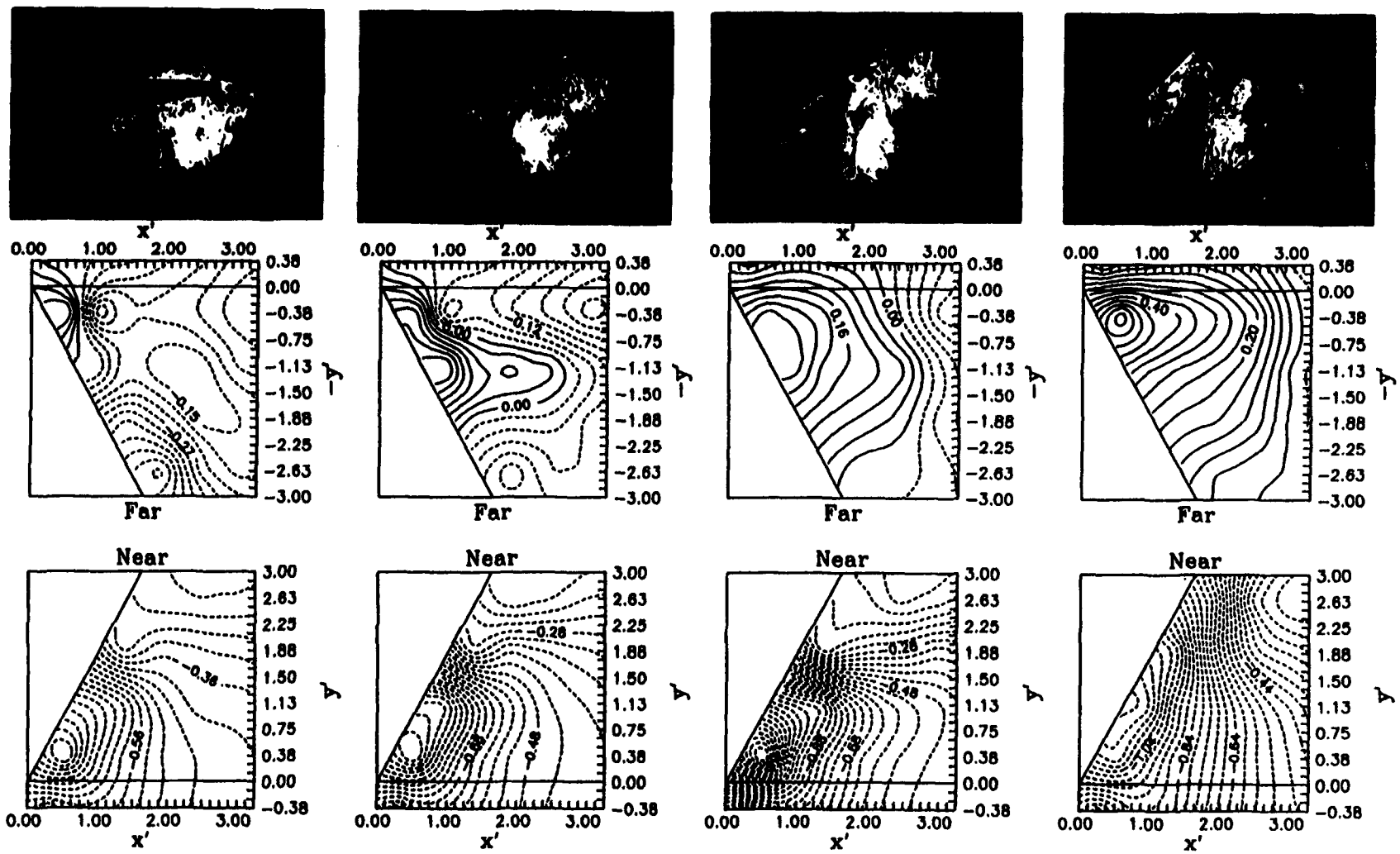

(a) $\phi = -11°$ (b) $\phi = -22°$ (c) $\phi = -32°$ (d) $\phi = -43°$

Figure 75. Coefficient of Pressure Contours with Cross-Sectional Flow Visualization ($\alpha = 45°$, $Re_d = 6000$, $(x/d)_f = 7.1$, negative ϕ).

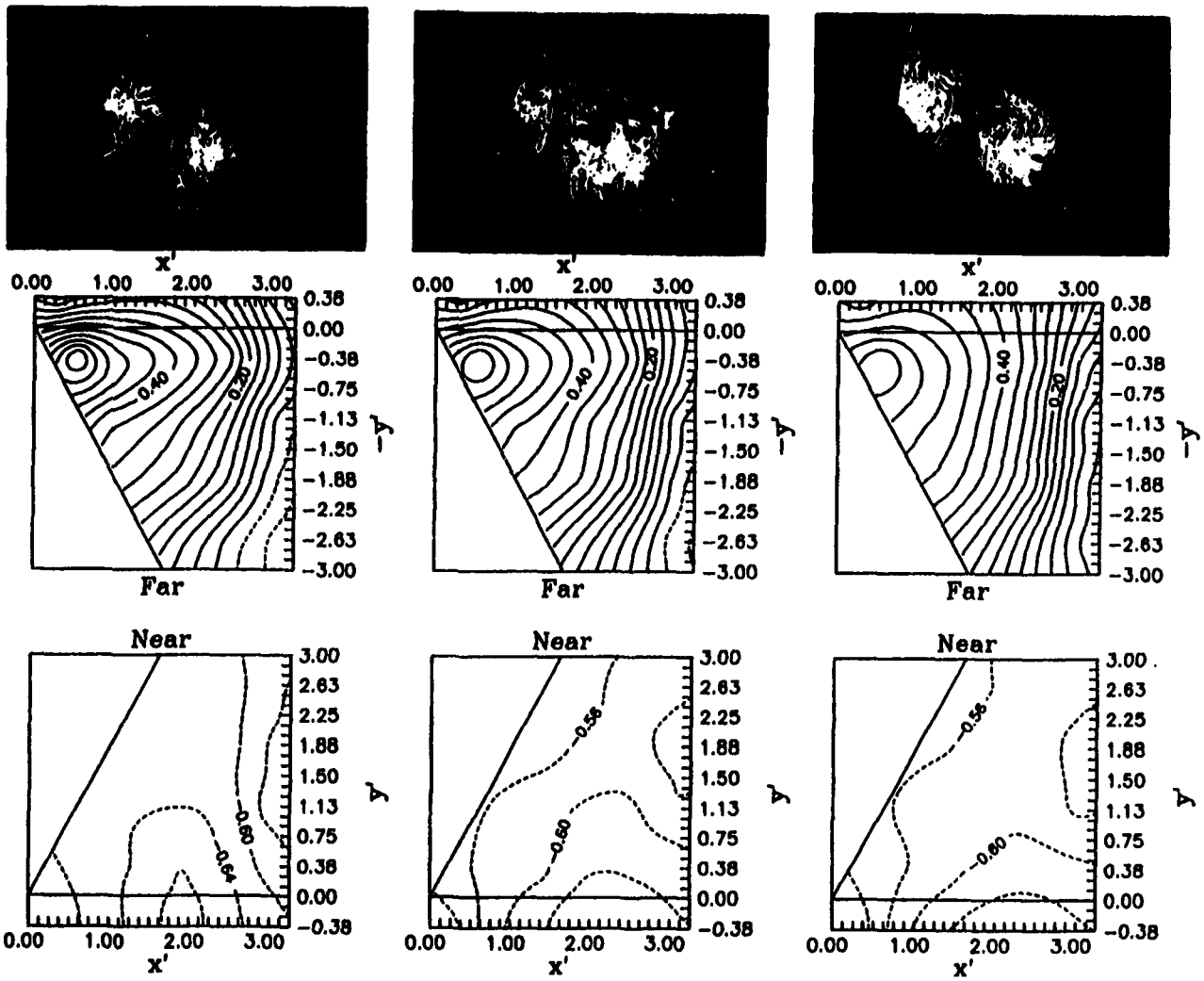

(a) ϕ = -54° (b) ϕ = -65° (c) ϕ = -76°

Figure 75. (Concluded).

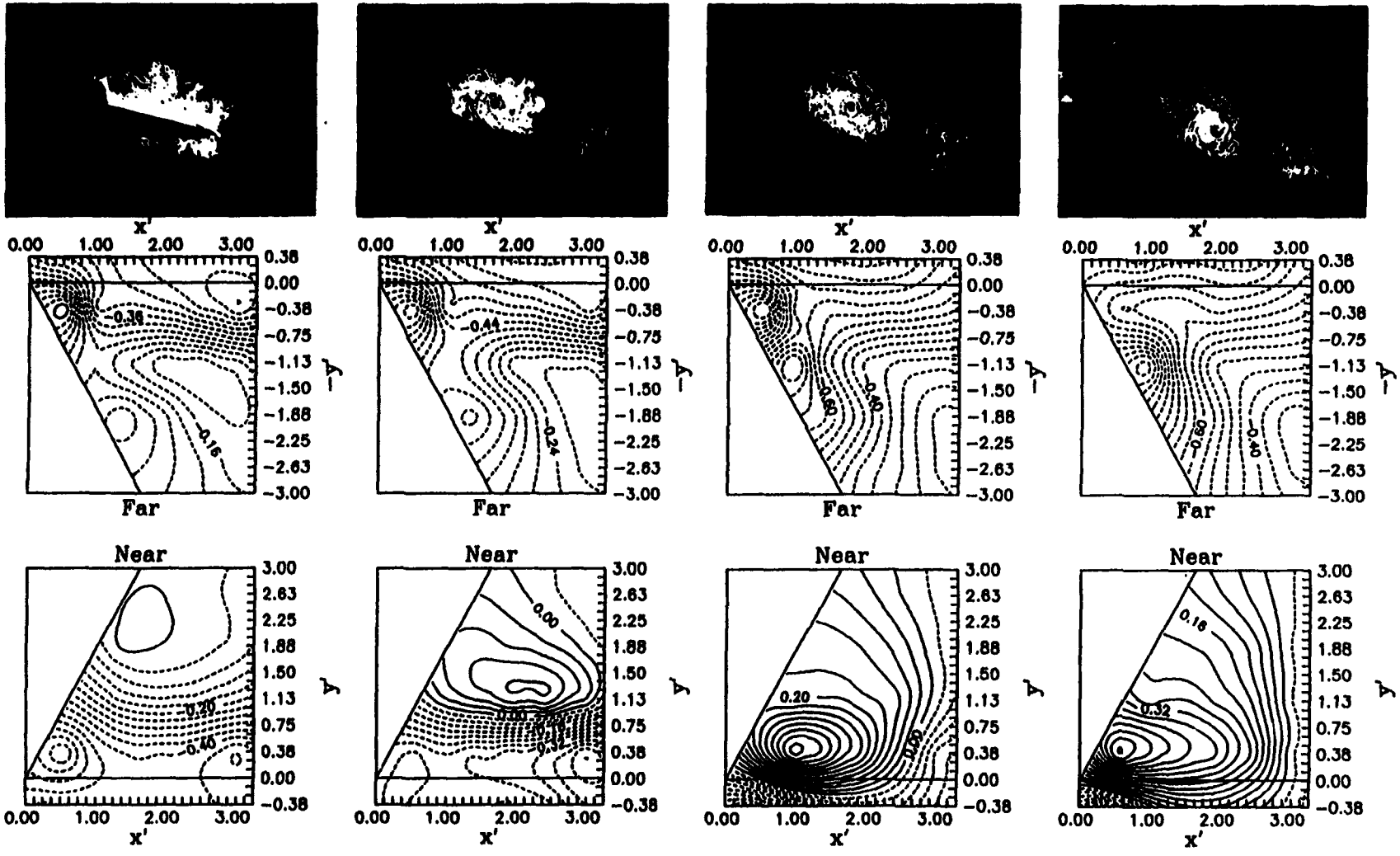

(a) $\phi = +11°$ (b) $\phi = +22°$ (c) $\phi = +32°$ (d) $\phi = +43°$

Figure 76. Coefficient of Pressure Contours with Cross-Sectional Flow Visualization ($\alpha = 45°$, $Re_d = 6000$, $(x/d)_f = 7.1$, positive ϕ).

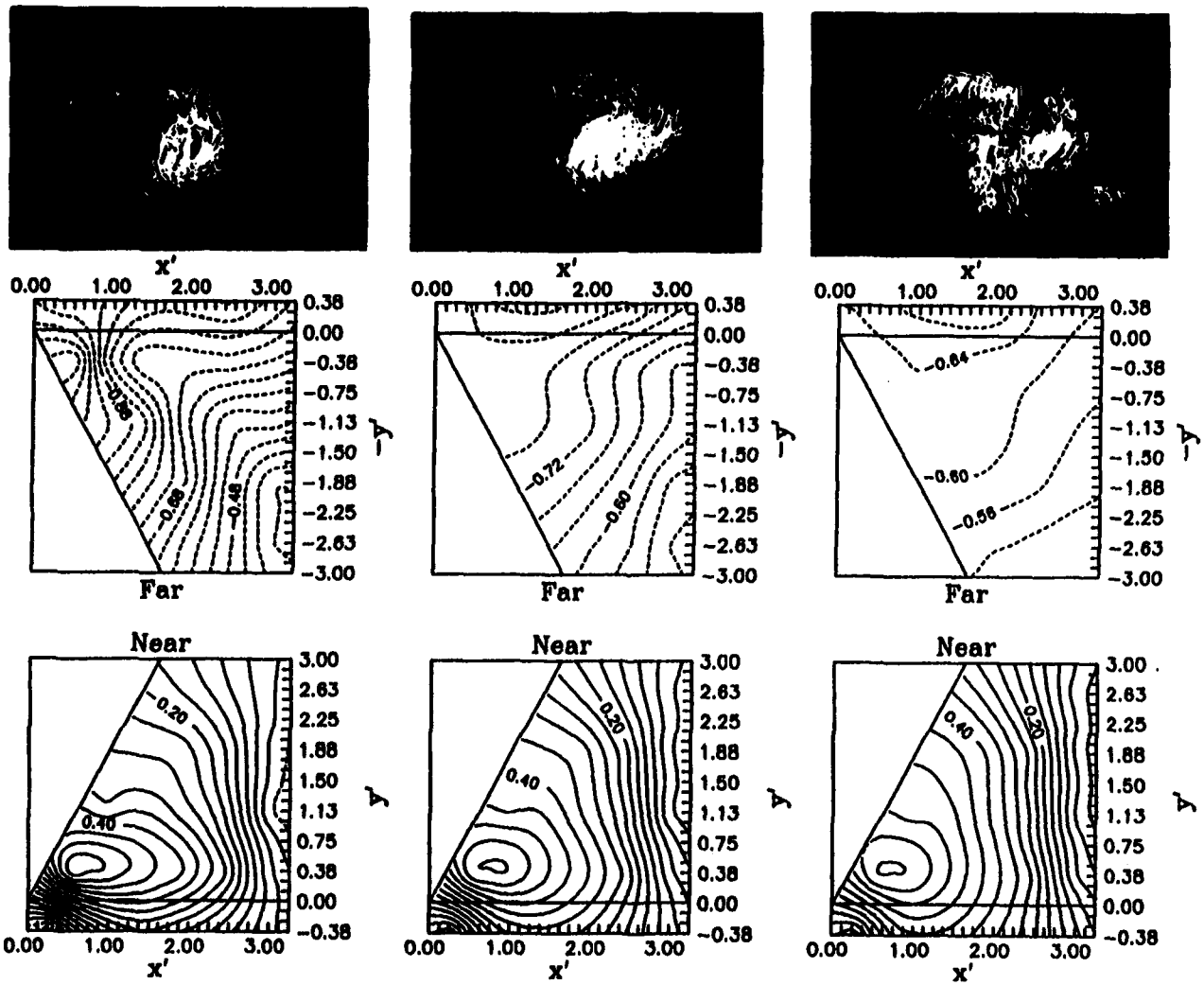

(a) $\phi = +54°$ (b) $\phi = +65°$ (c) $\phi = +76°$

Figure 76. (Concluded).

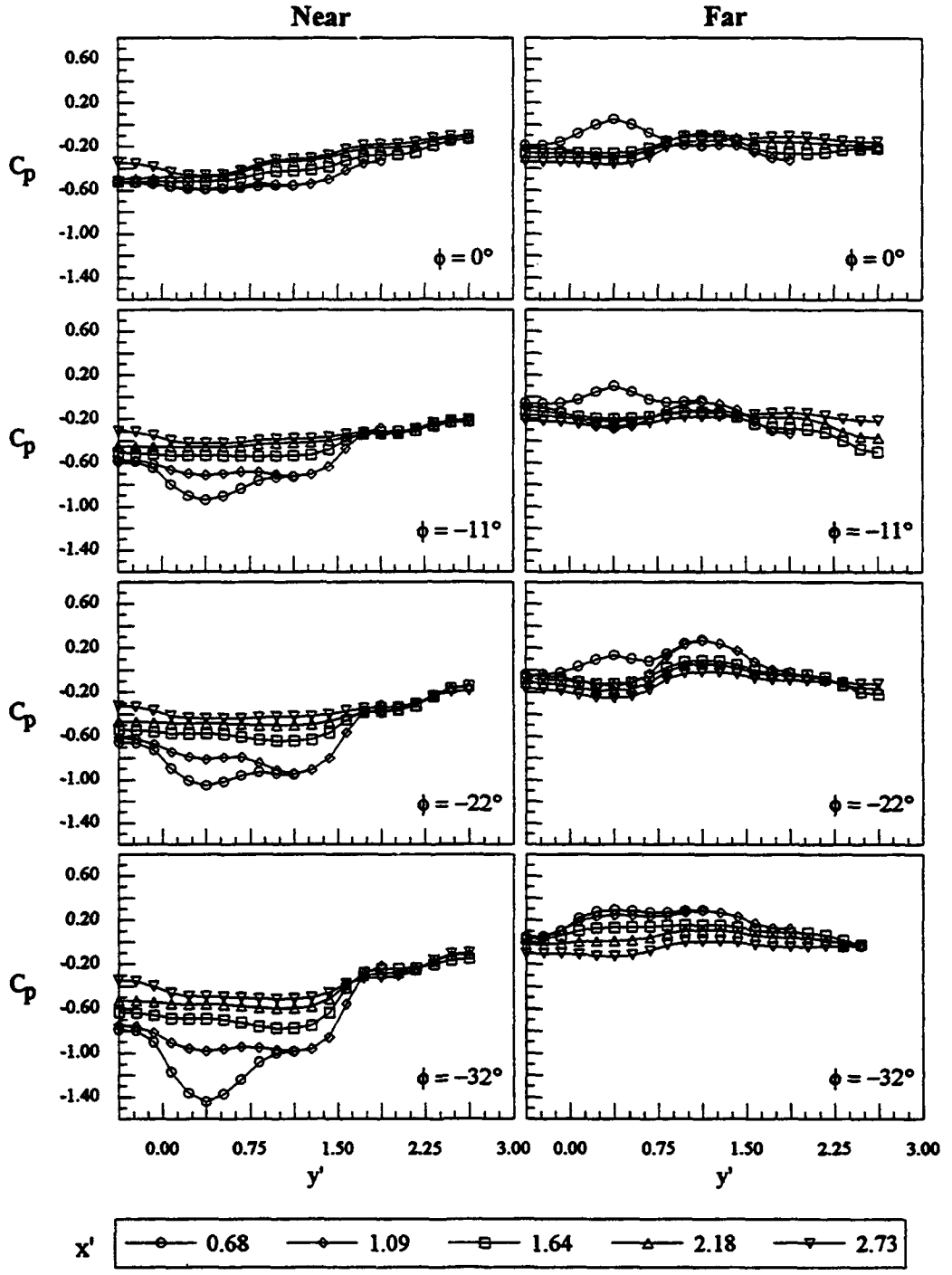

Figure 77. Spanwise Pressure Distributions on Fin ($\alpha = 45°$, $Re_d = 6000$, $(x/d)_f = 7.1$, negative ϕ).

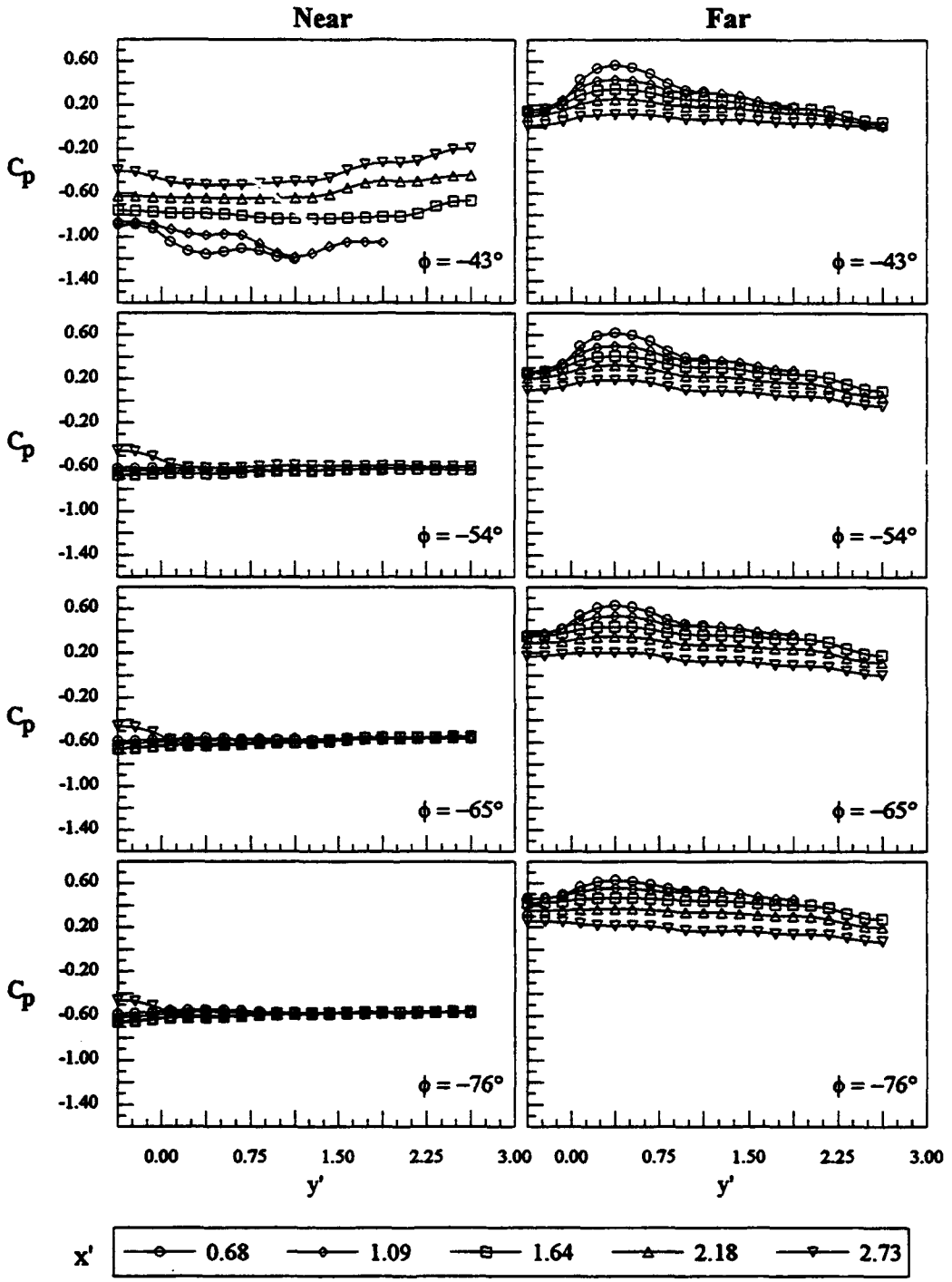

Figure 77. (Concluded)

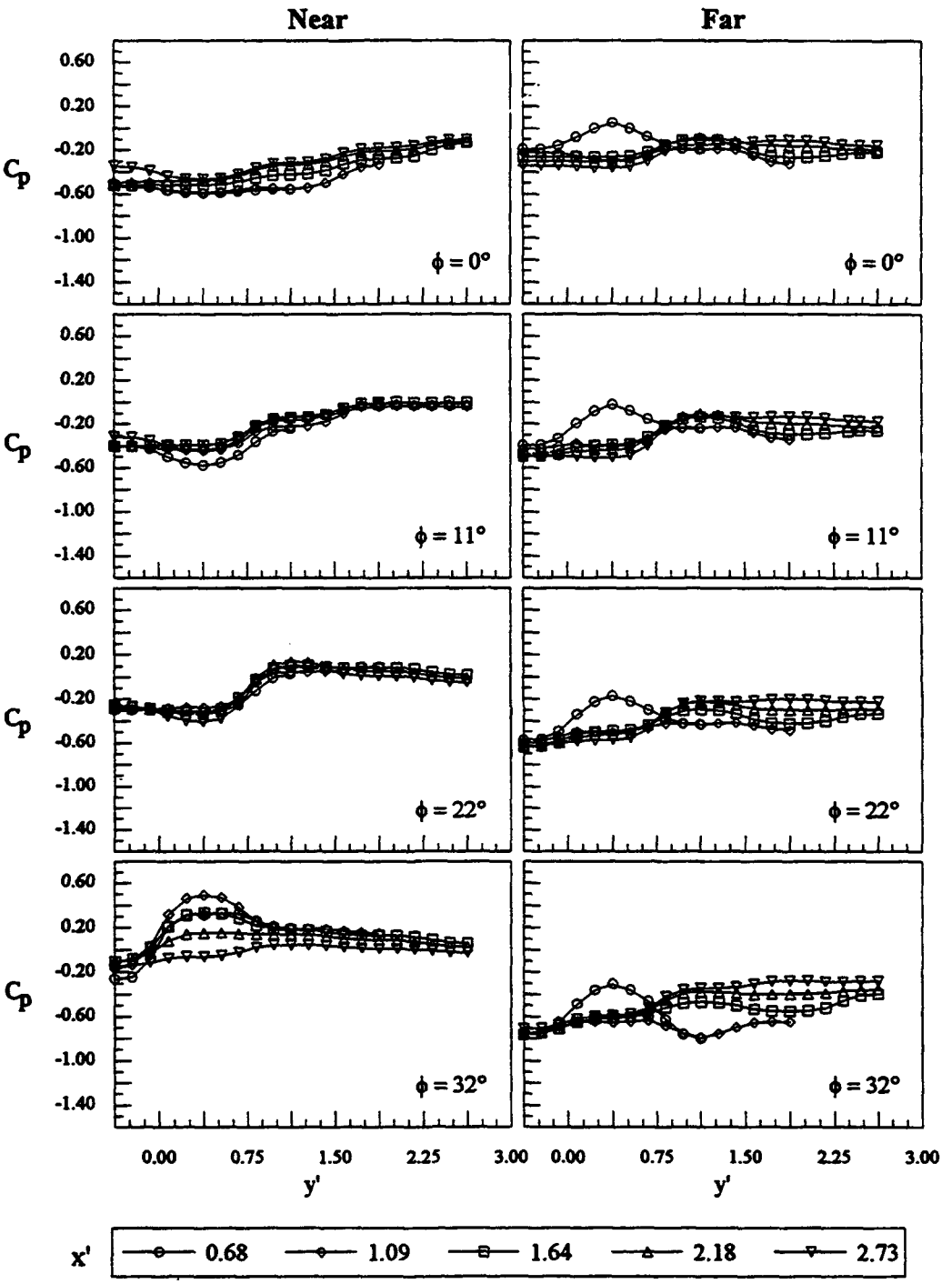

Figure 78. Spanwise Pressure Distributions on Fin ($\alpha = 45°$, $Re_d = 6000$, $(x/d)_f = 7.1$, positive ϕ).

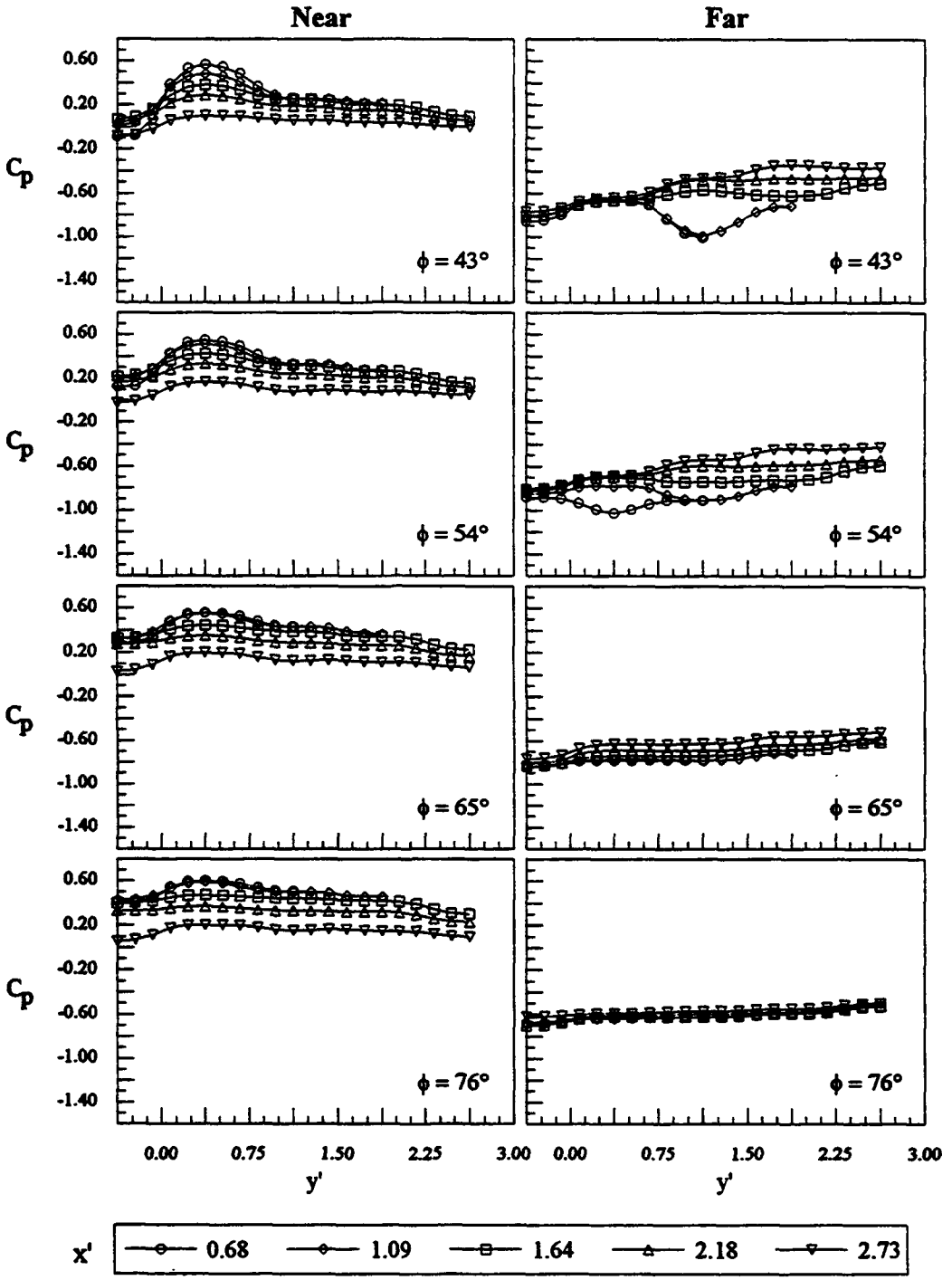

Figure 78. (Concluded)

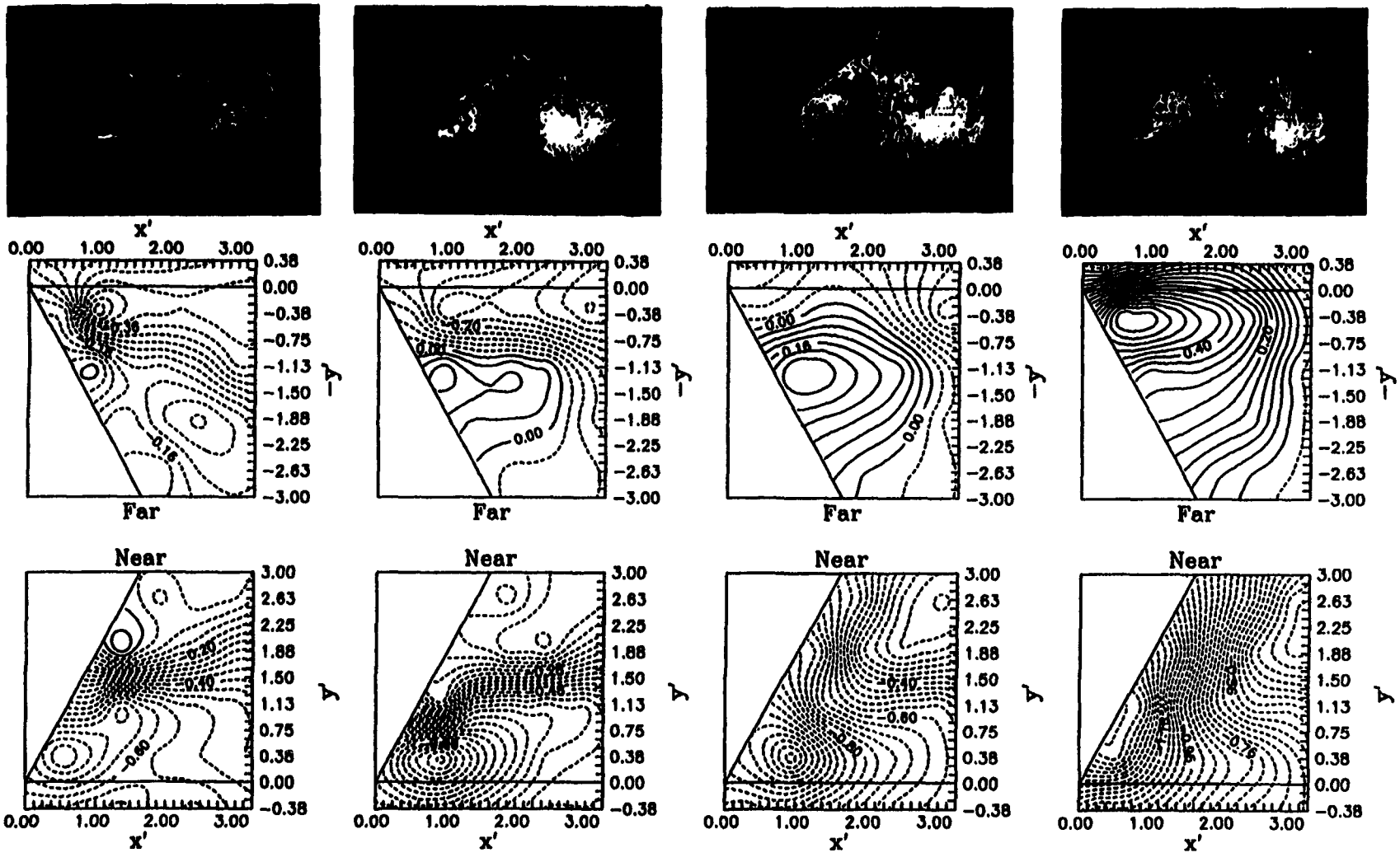

(a) ϕ = -11° (b) ϕ = -22° (c) ϕ = -32° (d) ϕ = -43°

Figure 79. Coefficient of Pressure Contours with Cross-Sectional Flow Visualization (α = 45°, Re_d = 6000, $(x/d)_f$ = 9.4, negative ϕ).

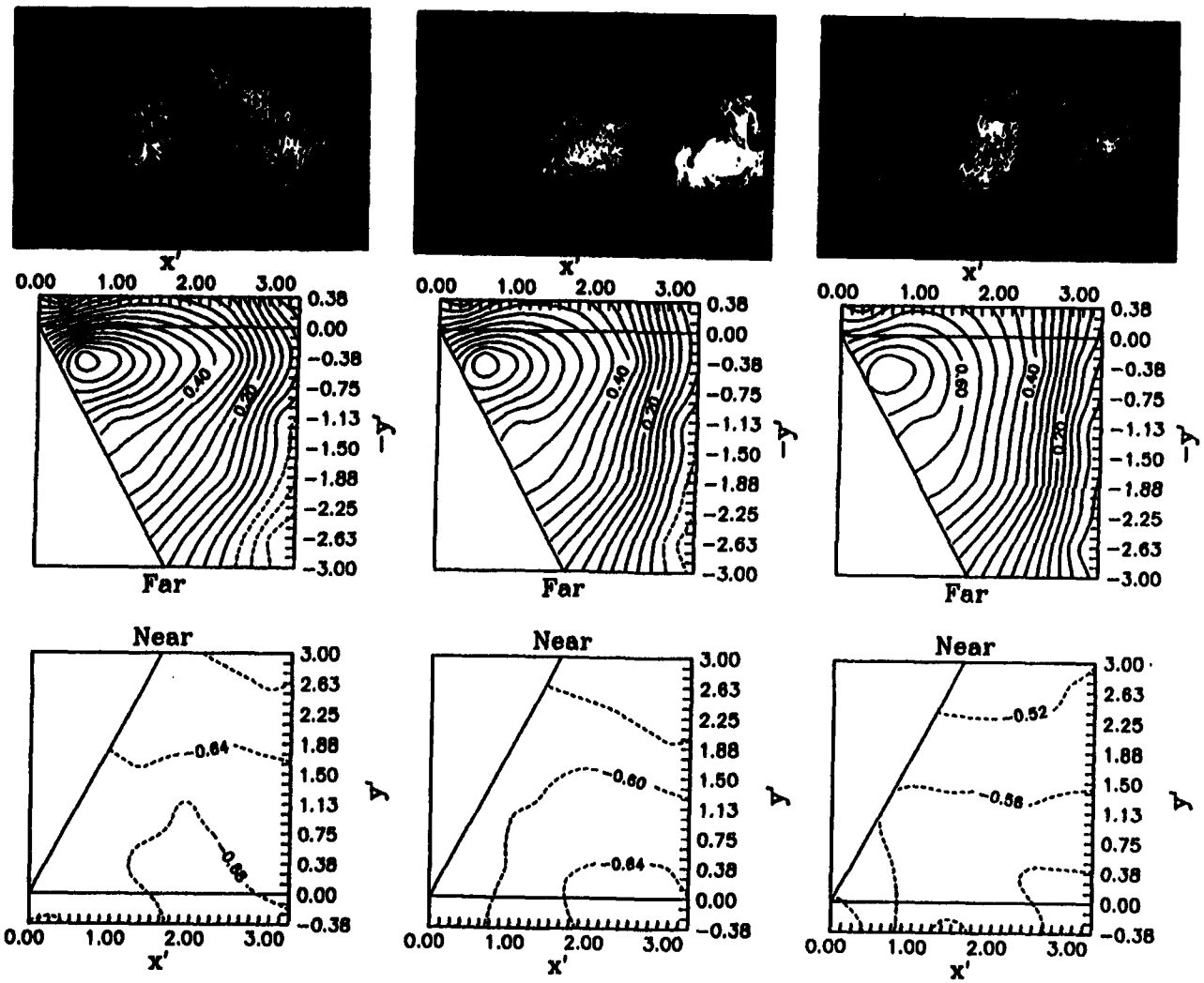

(a) $\phi = -54°$ (b) $\phi = -65°$ (c) $\phi = -76°$

Figure 79. (Concluded).

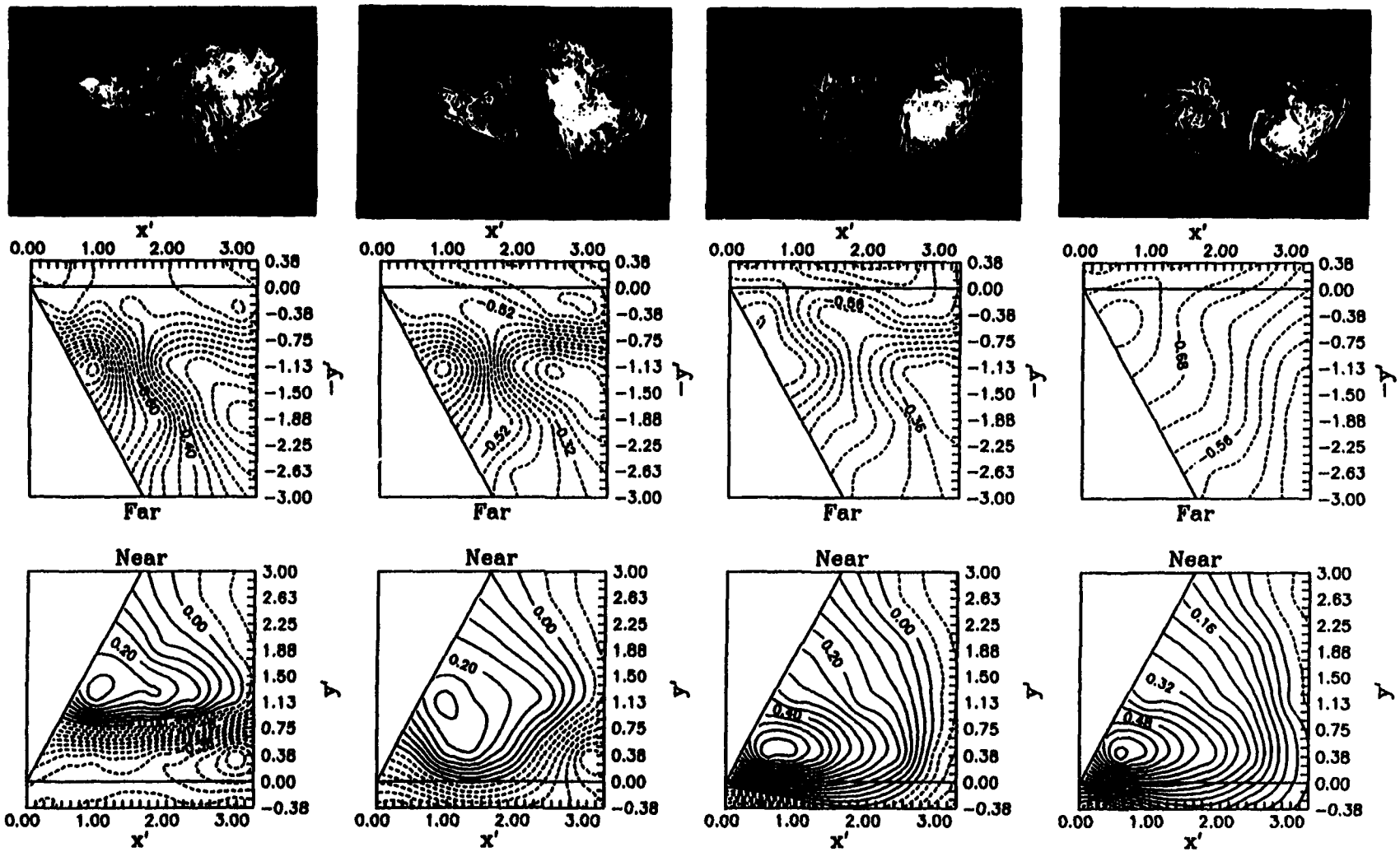

(a) $\phi = +11°$ (b) $\phi = +22°$ (c) $\phi = +32°$ (d) $\phi = +43°$

Figure 80. Coefficient of Pressure Contours with Cross-Sectional Flow Visualization ($\alpha = 45°$, $Re_d = 6000$, $(x/d)_f = 9.4$, positive ϕ).

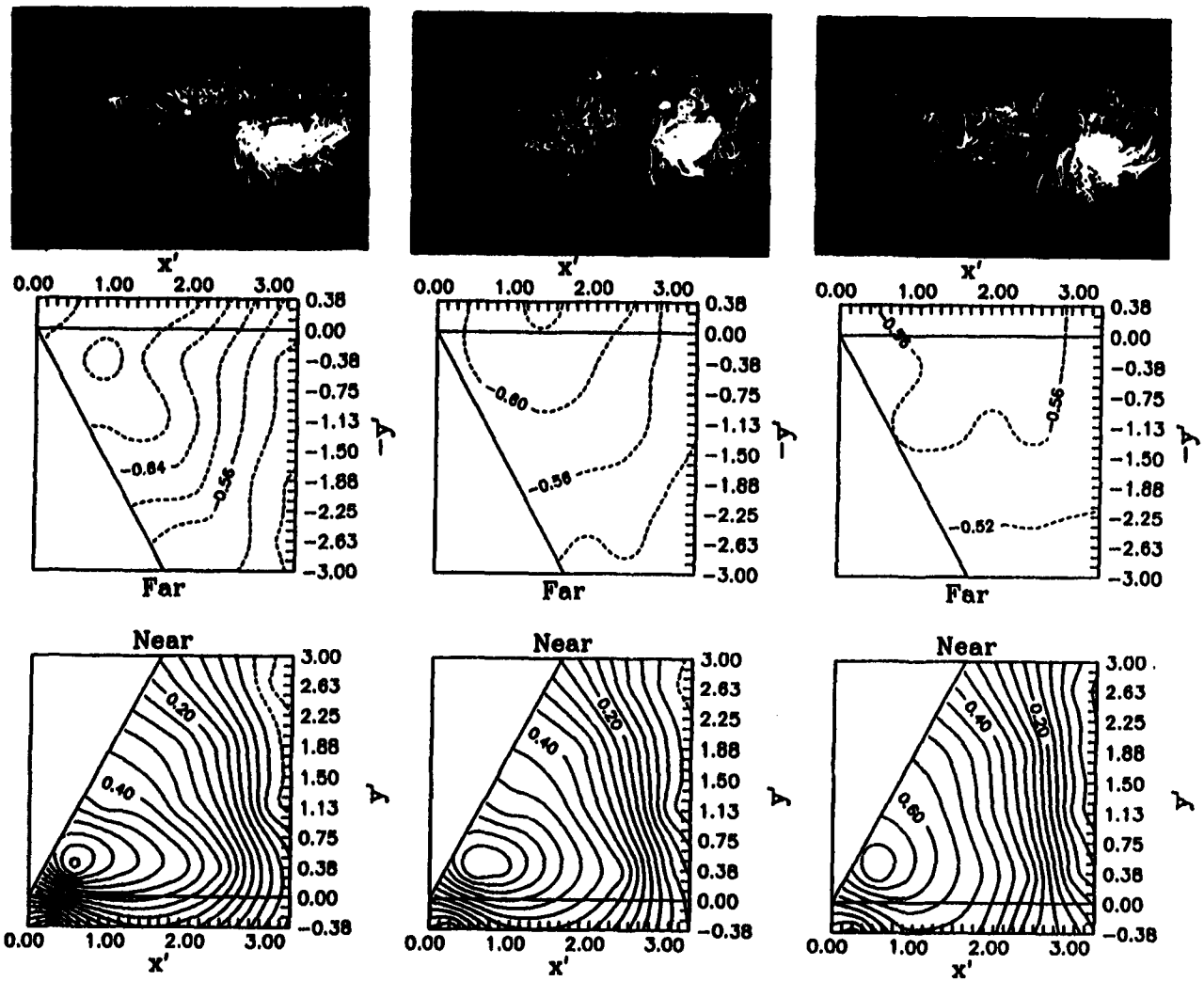

(a) $\phi = +54°$ (b) $\phi = +65°$ (c) $\phi = +76°$

Figure 80. (Concluded).

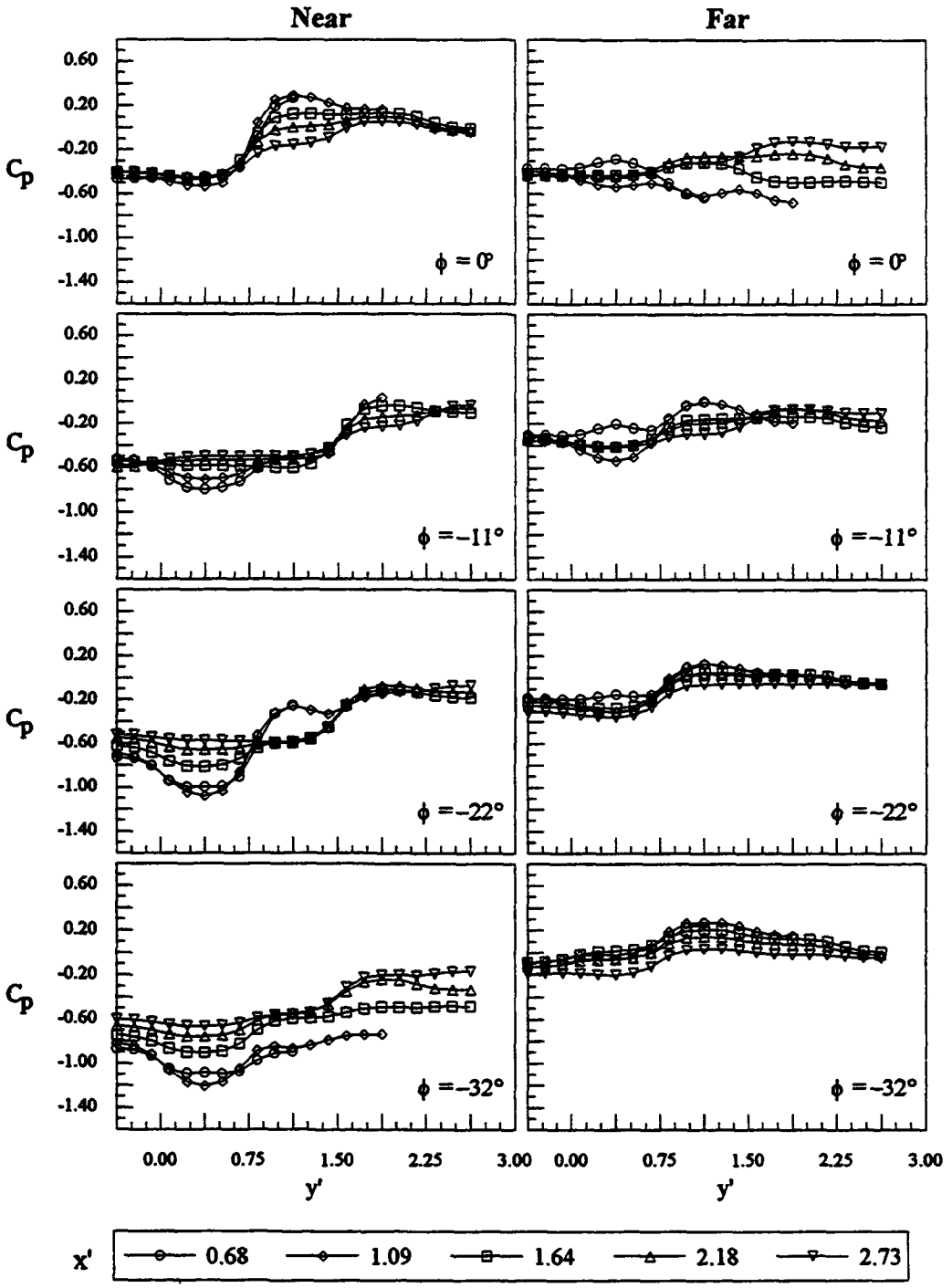

Figure 81. Spanwise Pressure Distributions on Fin ($\alpha = 45°$, $Re_d = 6000$, $(x/d)_f = 9.4$, negative ϕ).

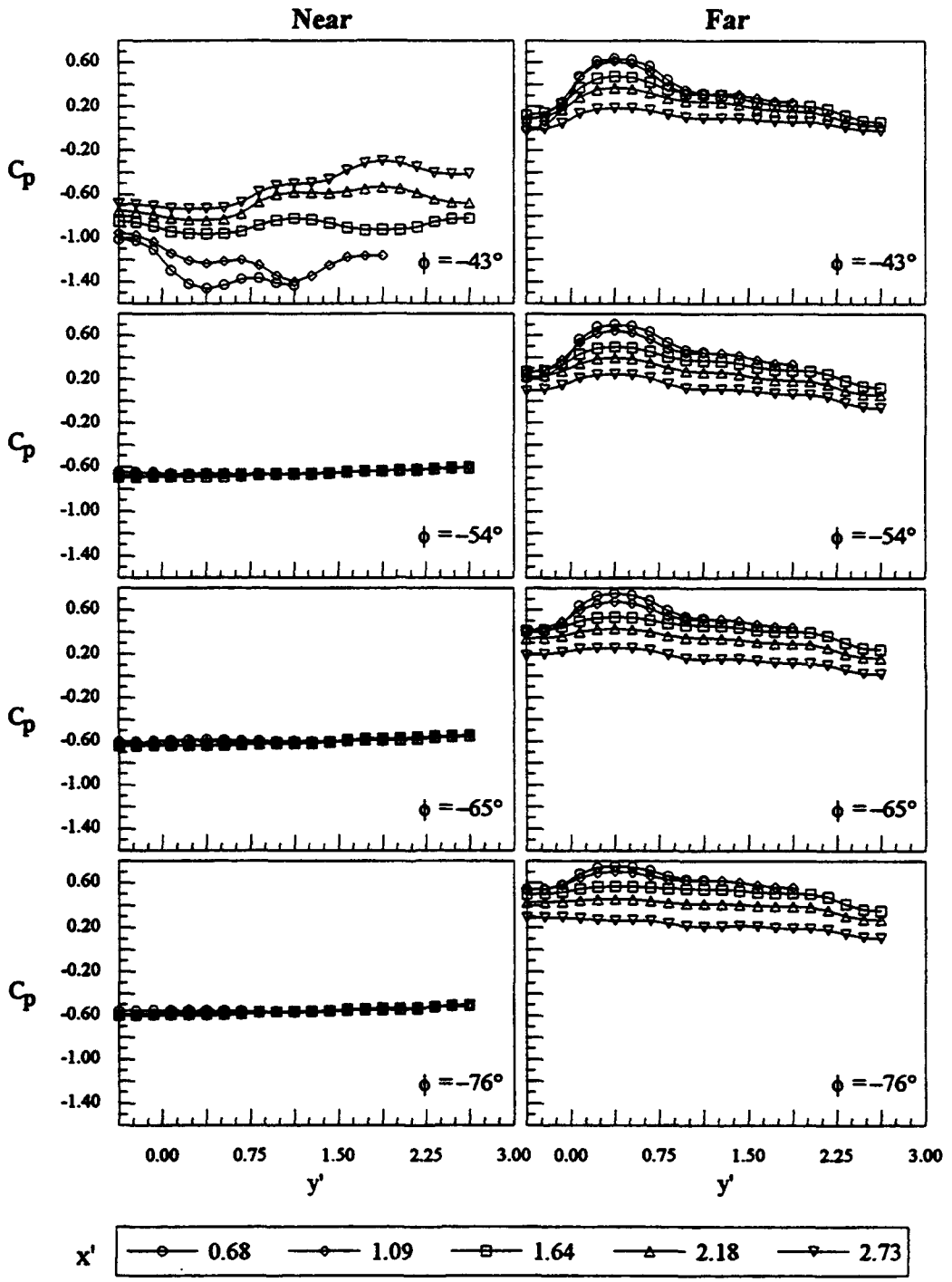

Figure 81. (Concluded)

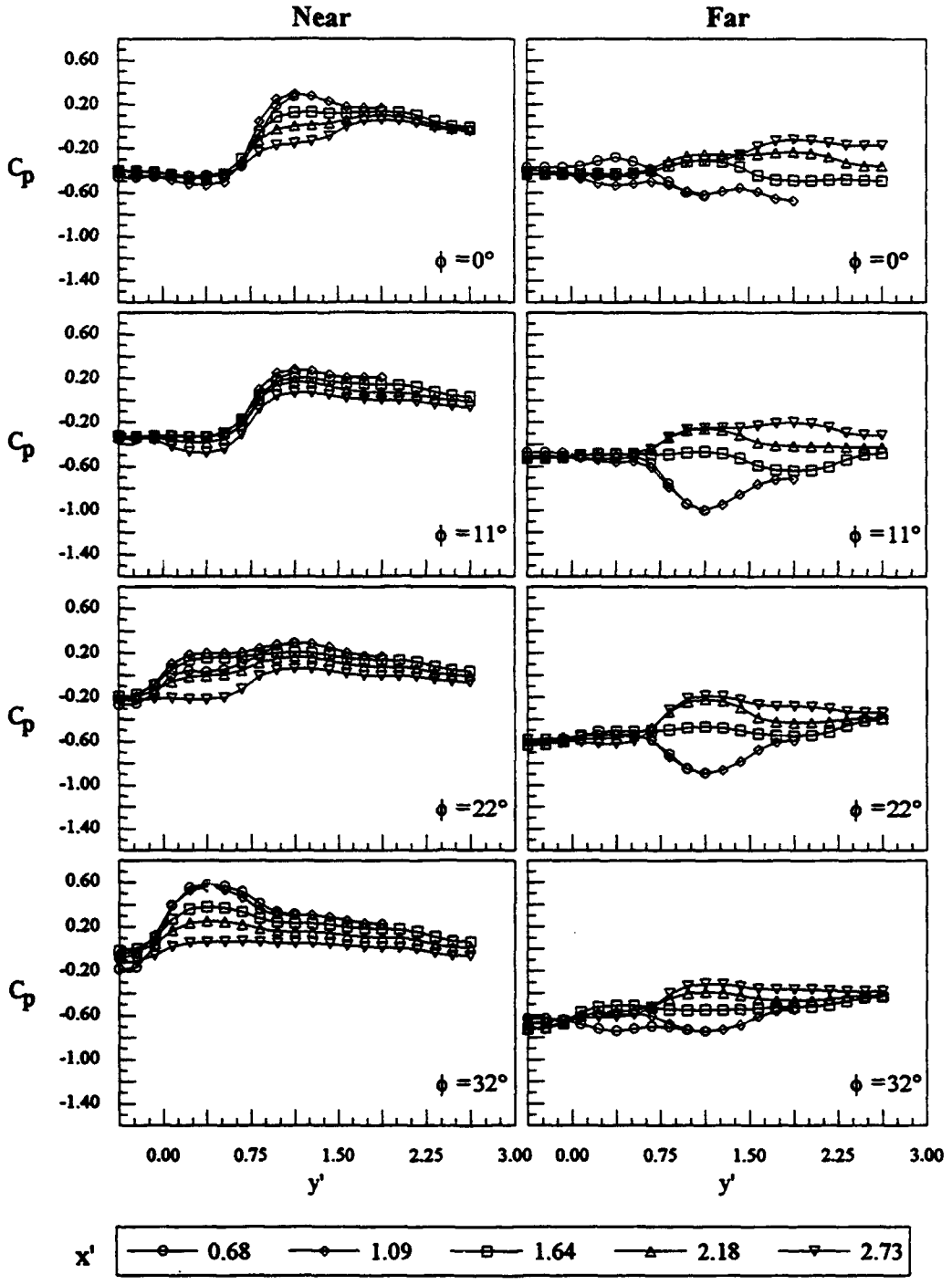

Figure 82. Spanwise Pressure Distributions on Fin ($\alpha = 45°$, $Re_d = 6000$, $(x/d)_f = 9.4$, positive ϕ).

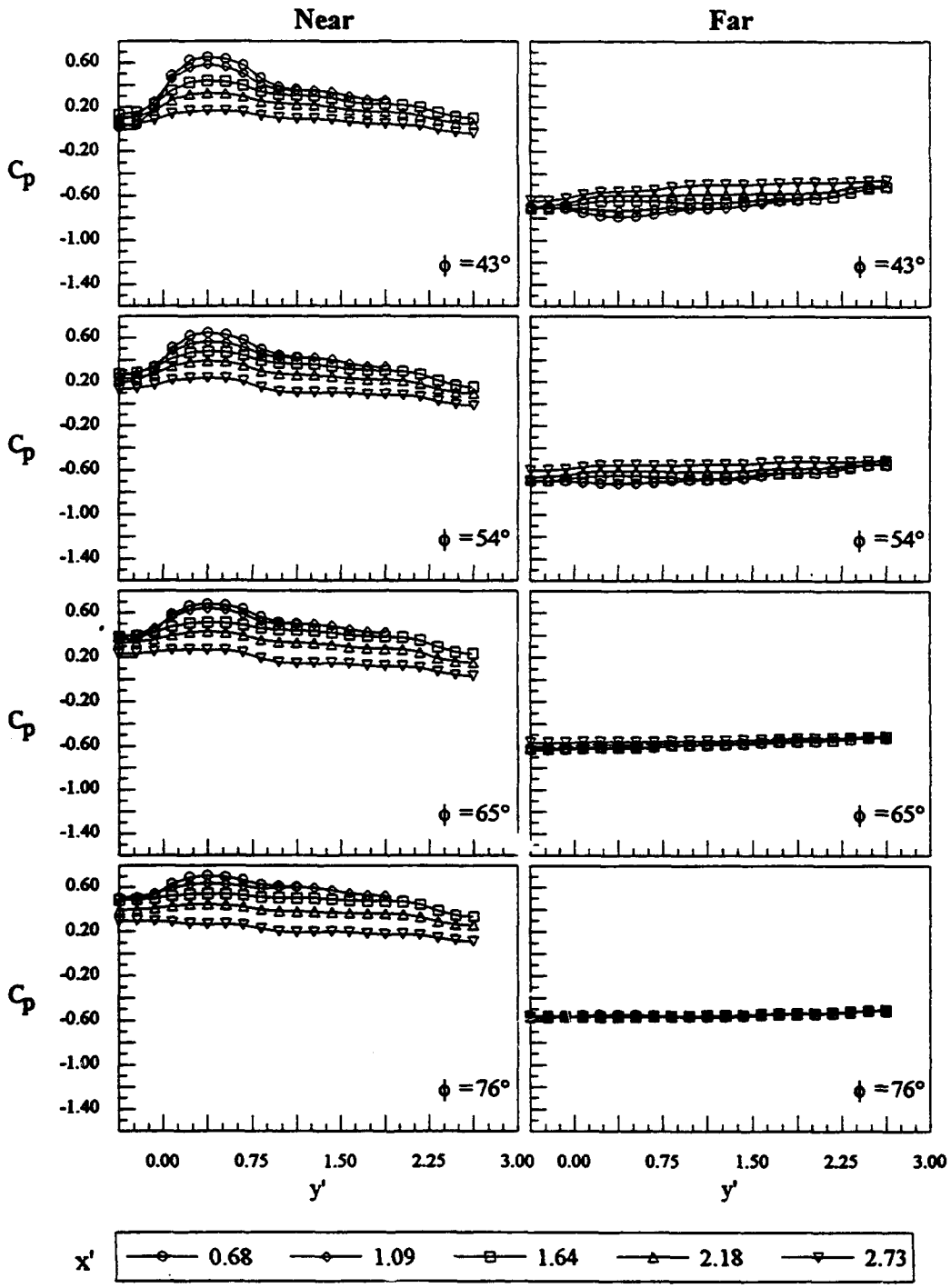

Figure 82. (Concluded)

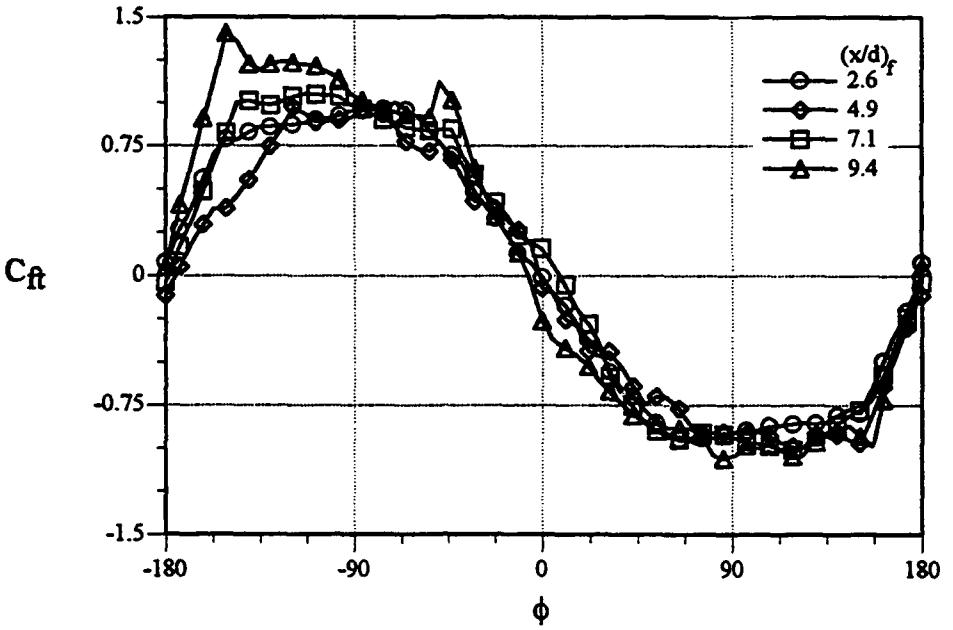

(a) $Re_d = 6000$

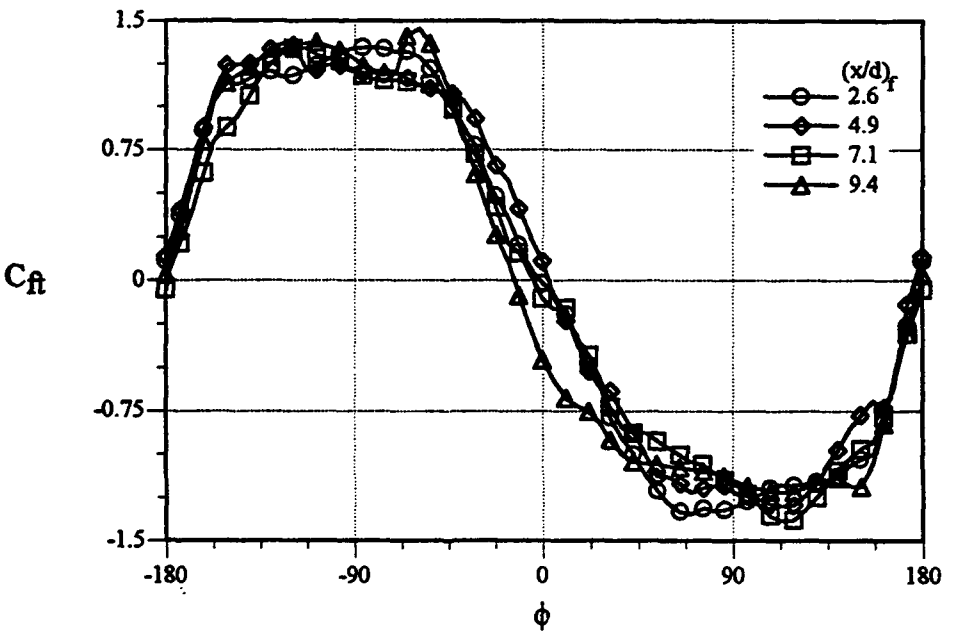

(b) $Re_d = 20000$

Figure 83. Normal Force Coefficient Variations with ϕ for Different $(x/d)_f$ ($\alpha = 45°$).

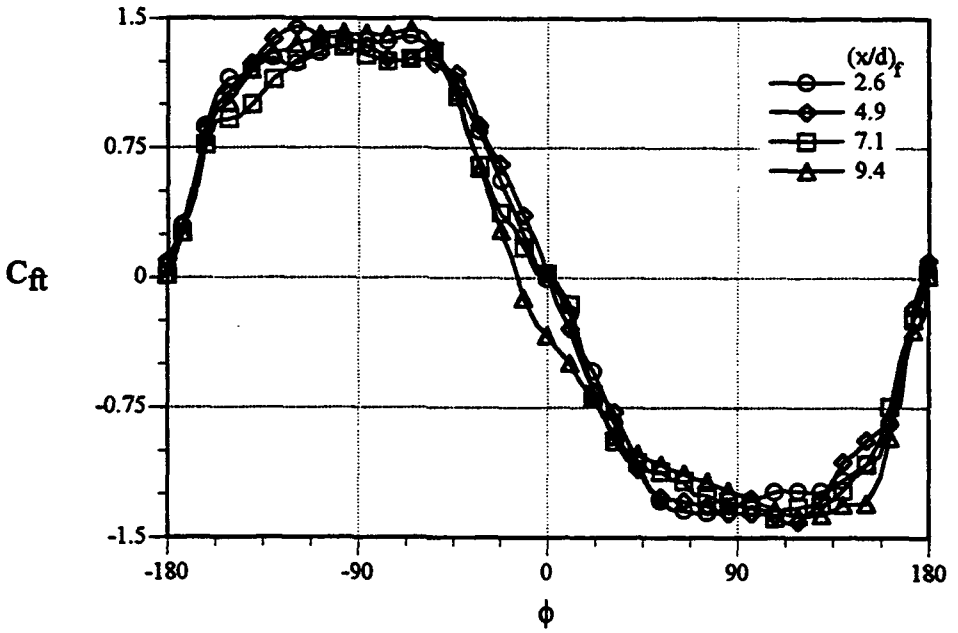

(c) $Re_d = 34000$

Figure 83. (Concluded)

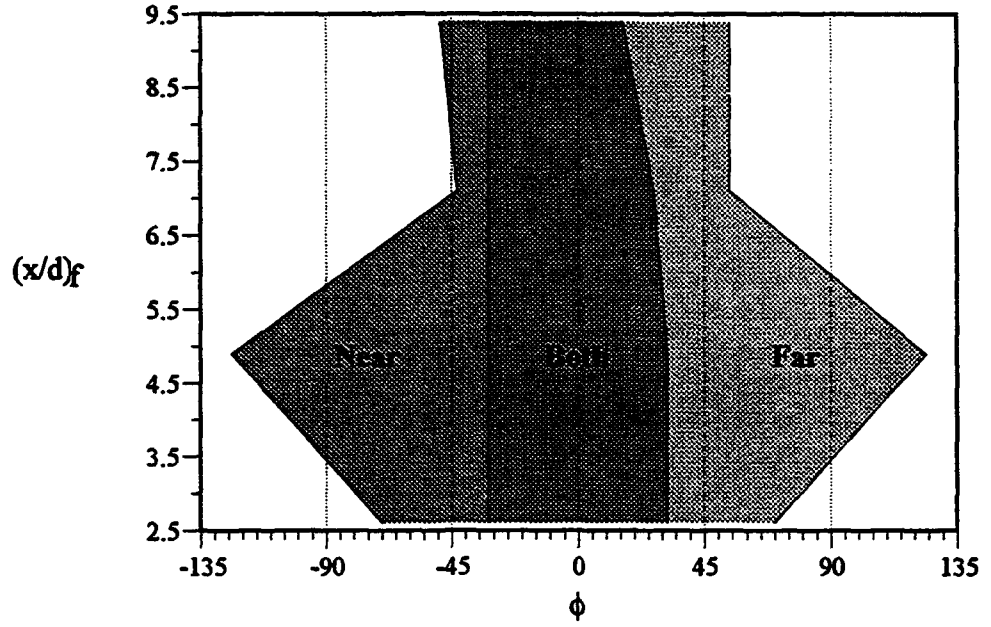

(a) $Re_d = 6000$

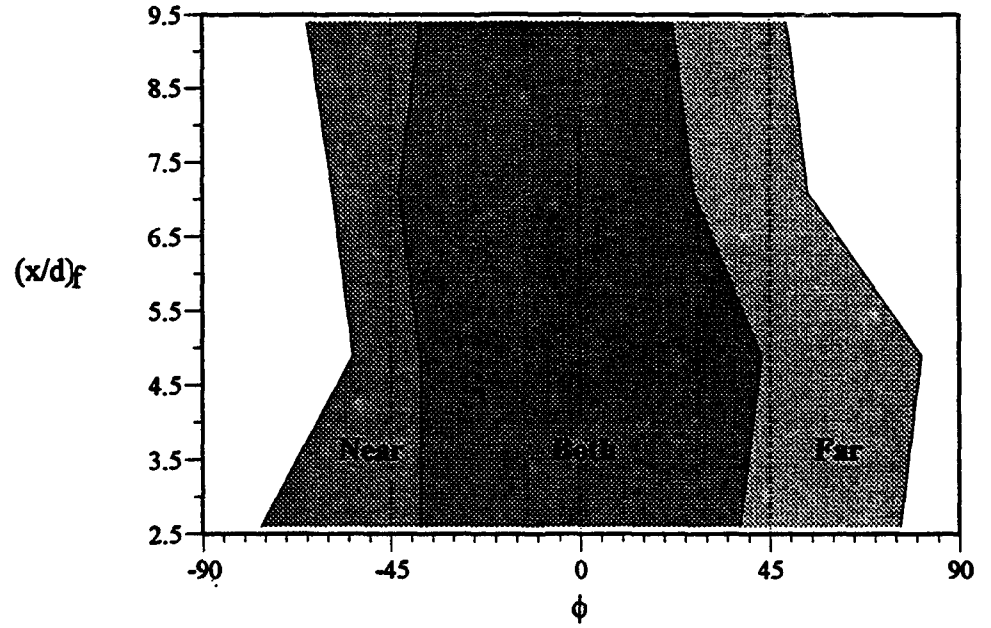

(b) $Re_d = 20000$

Figure 84. Range of Vortex Interaction with Fin for Different $(x/d)_f$ ($\alpha = 45°$).

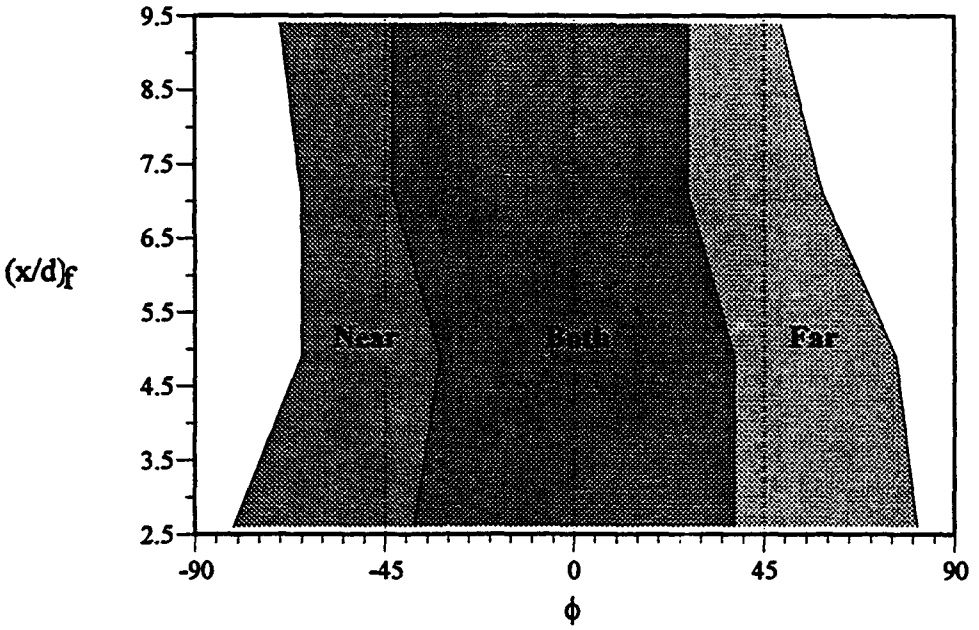

(c) $Re_d = 34000$

Figure 84. (Concluded)

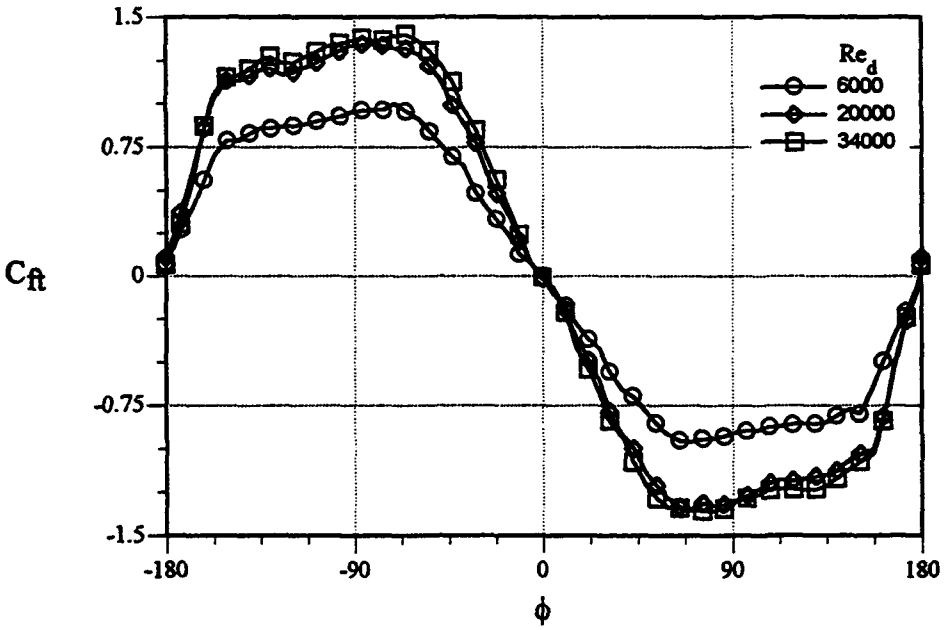

(a) $(x/d)_f = 2.6$

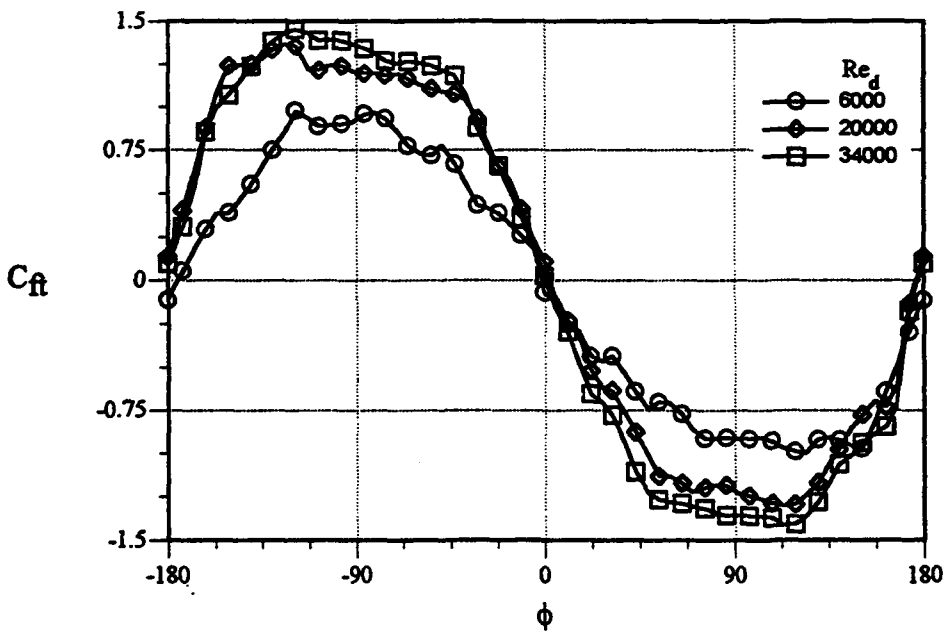

(b) $(x/d)_f = 4.9$

Figure 85. Normal Force Coefficient Variations with ϕ for Different Re_d ($\alpha = 45°$).

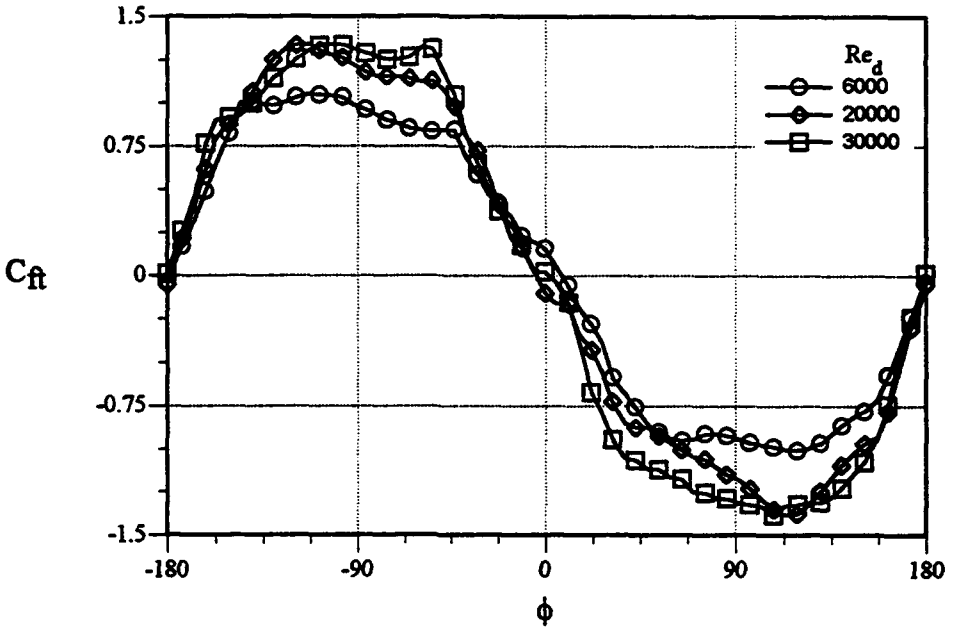

(c) $(x/d)_f = 7.1$

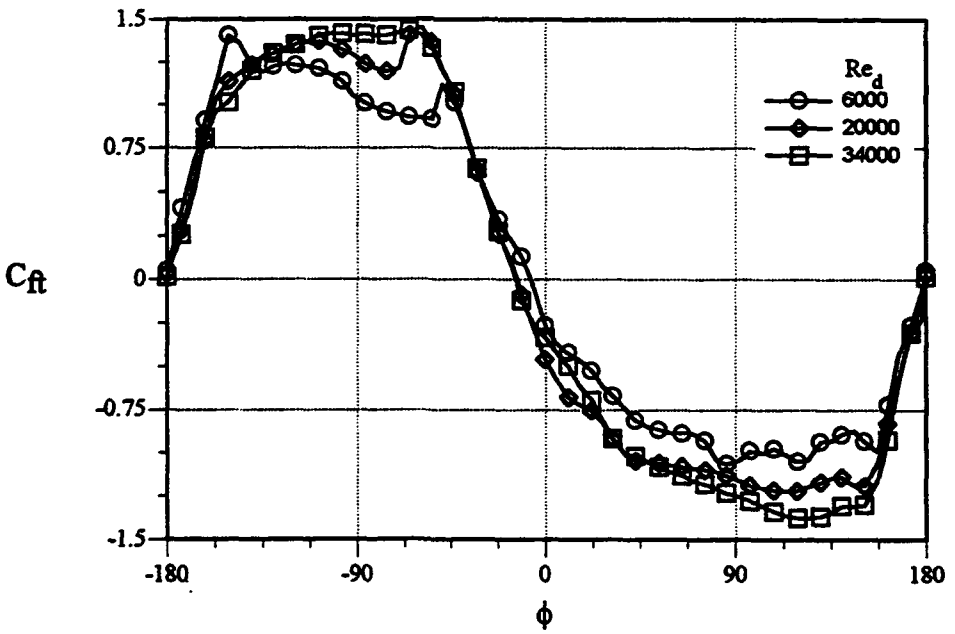

(d) $(x/d)_f = 9.4$

Figure 85. (Concluded)

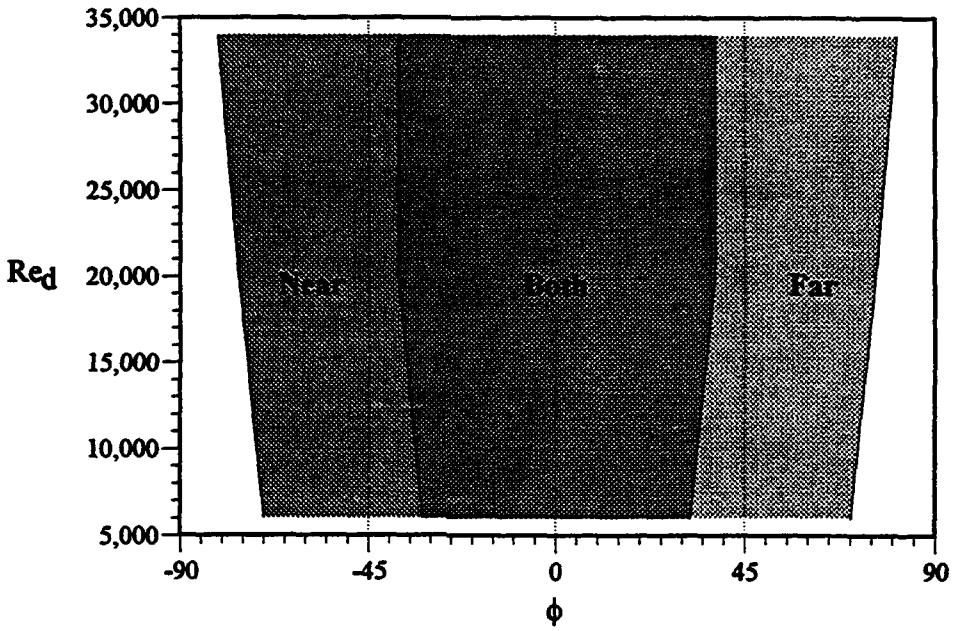

(a) $(x/d)_f = 2.6$

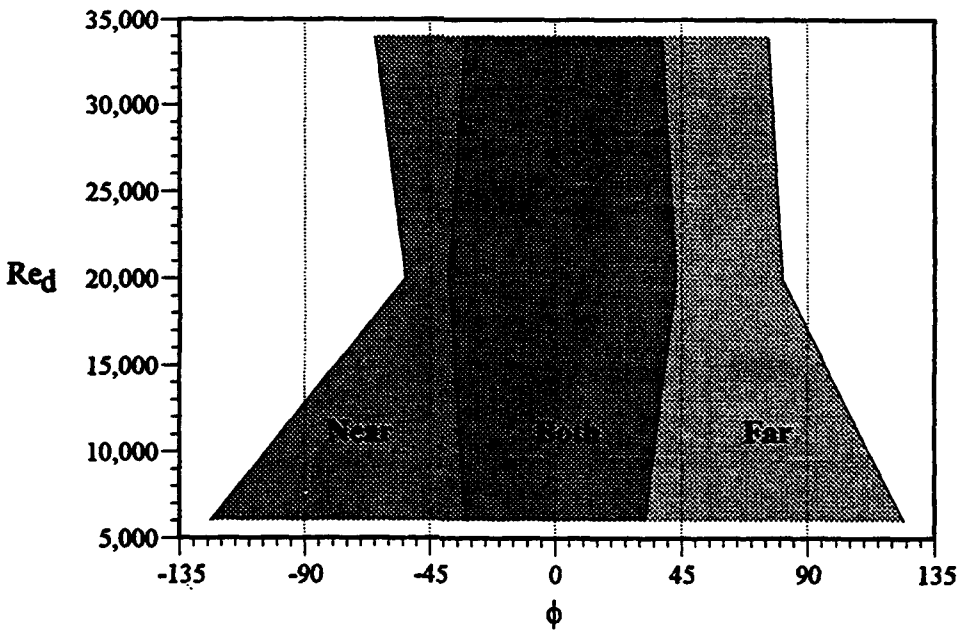

(b) $(x/d)_f = 4.9$

Figure 86. Range of Vortex Interaction with Fin for Different Re_d ($\alpha = 45°$).

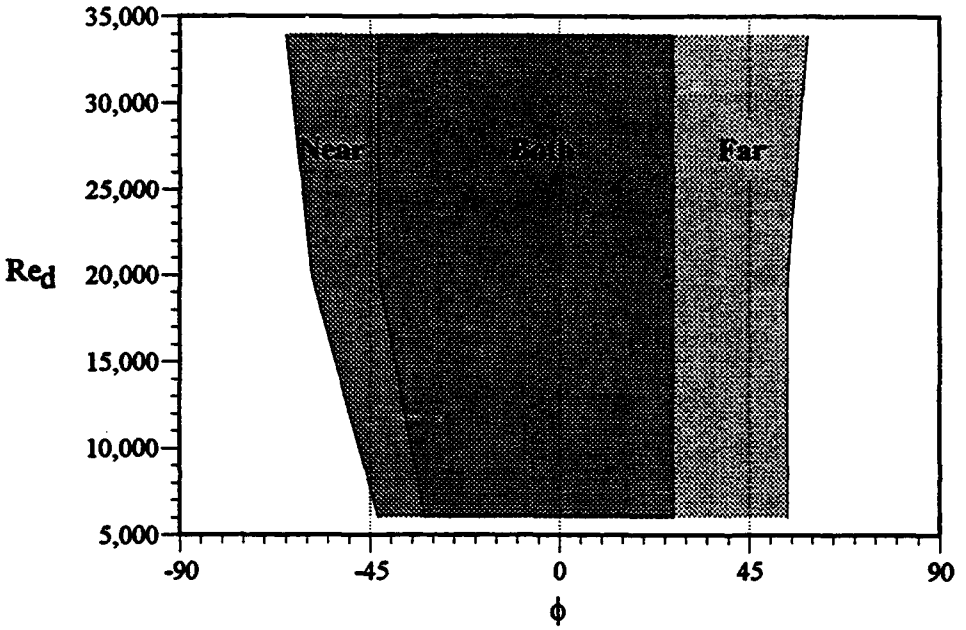

(c) $(x/d)_f = 7.1$

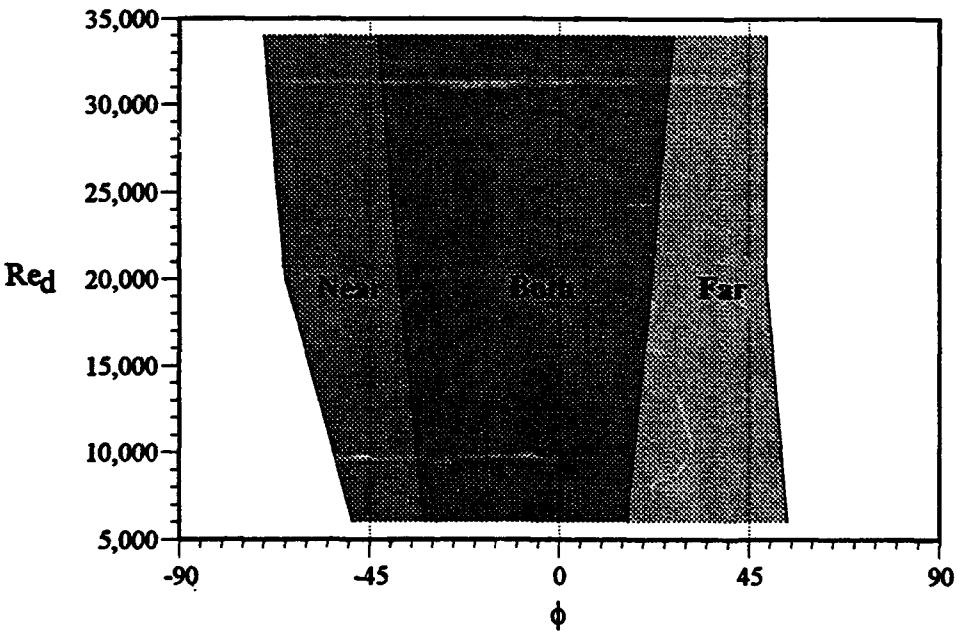

(d) $(x/d)_f = 9.4$

Figure 86. (Concluded)

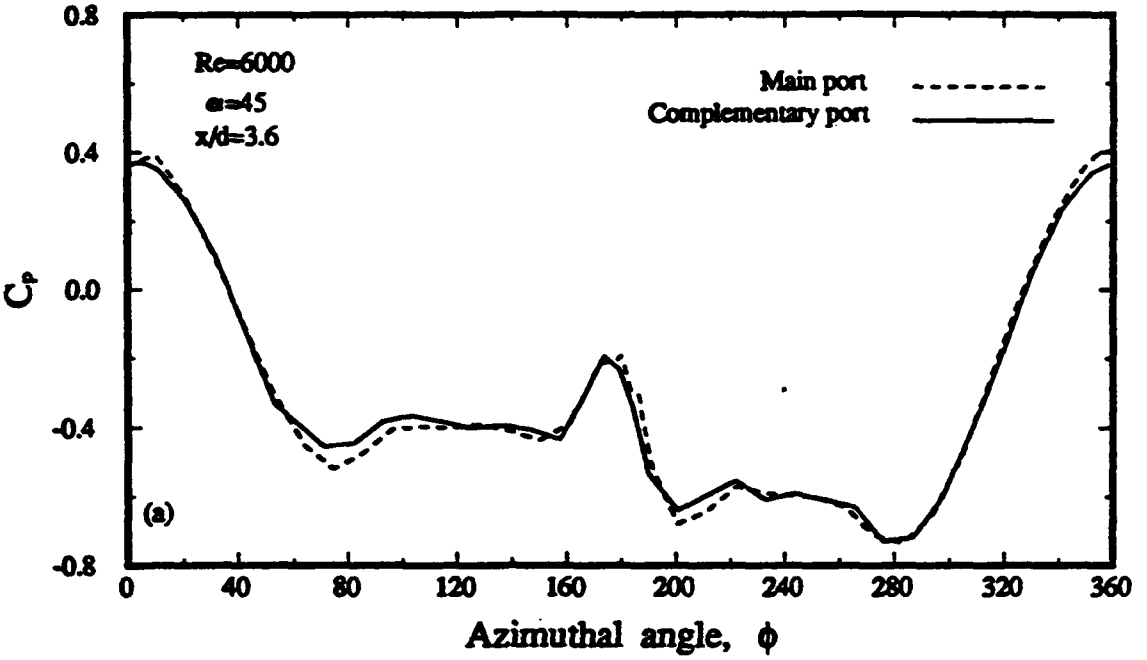

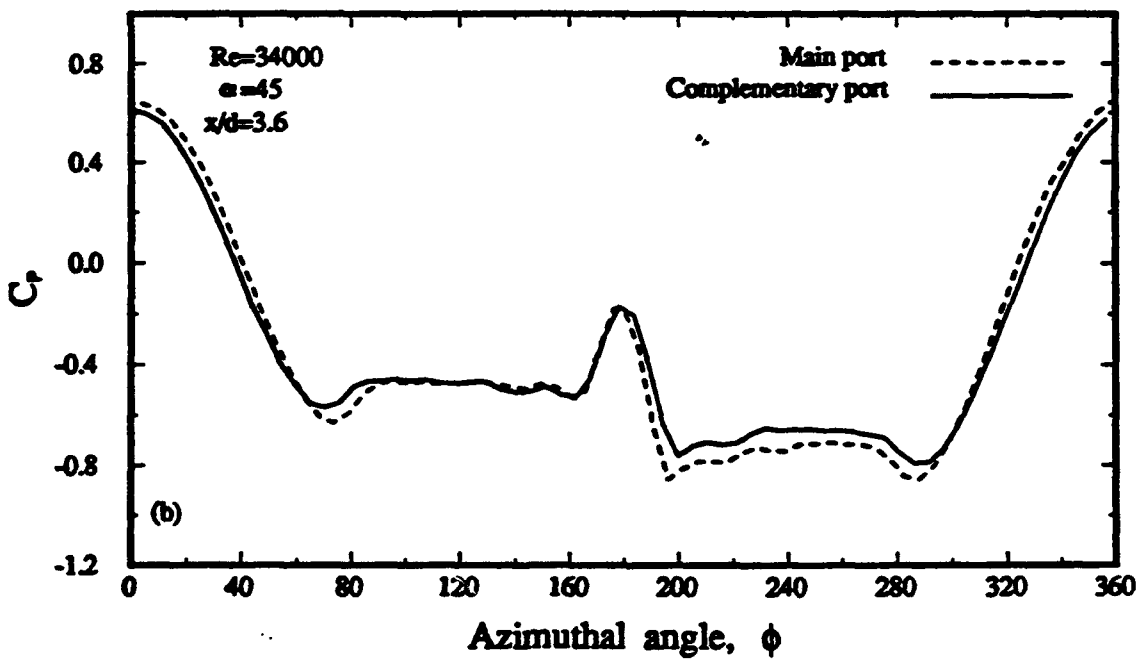

Figure 87. Comparison of Pressure Distributions Measured by Main Ray and Complementary Ports at α=45°, x/d=3.6, and Re (a) 6000 and (b) 34000

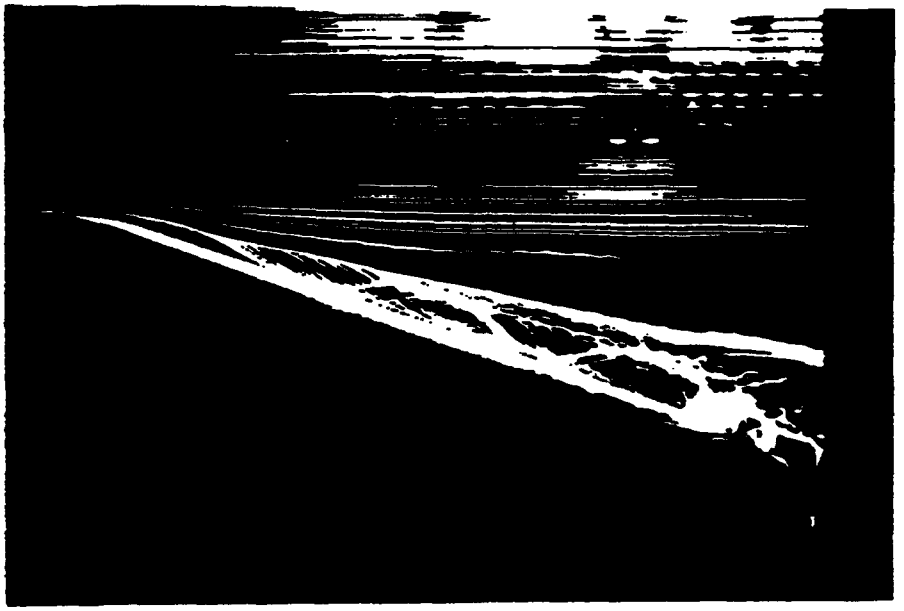

(a) Near Side

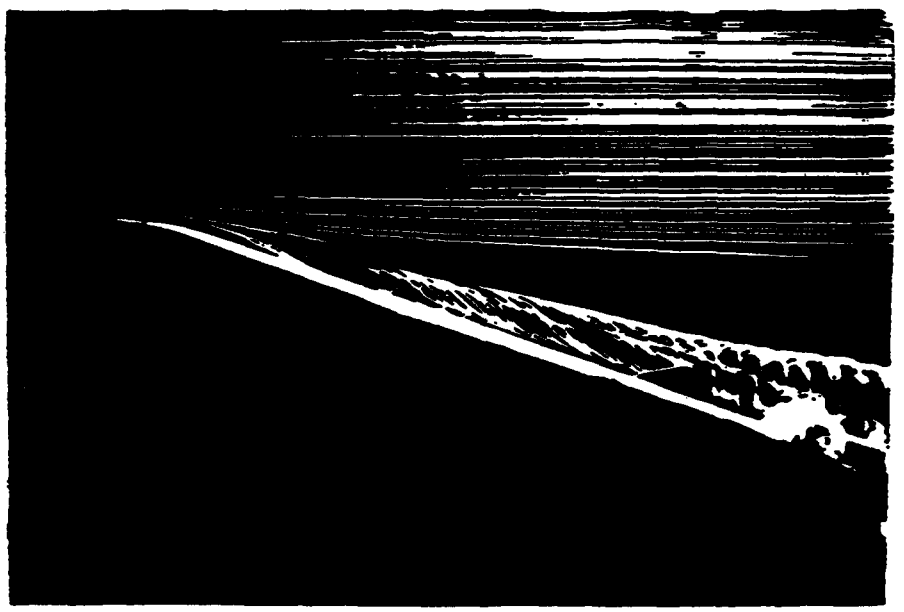

(b) Far Side

Figure 88. Smoke Wire Visualization at Re=6000, α=20°, (a) near side (b) far side

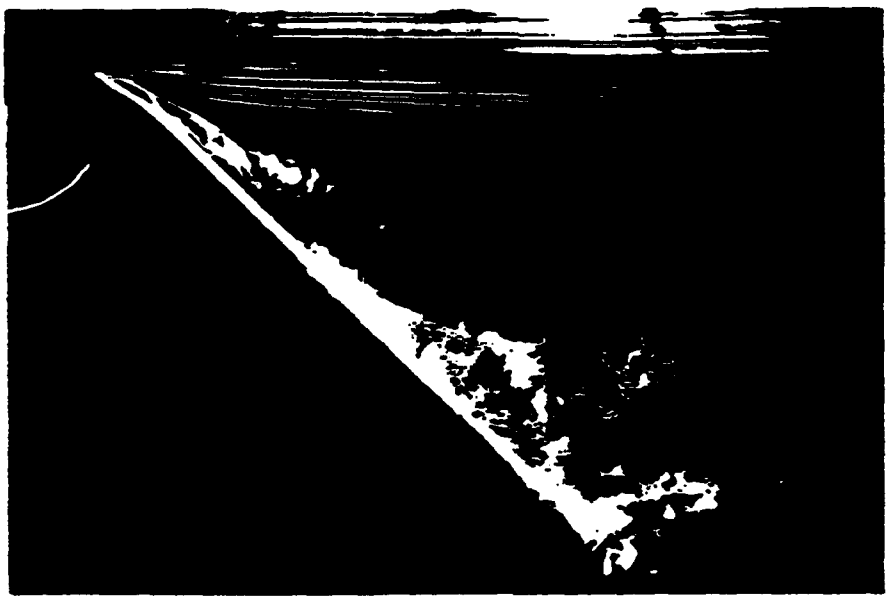

(a) Near Side

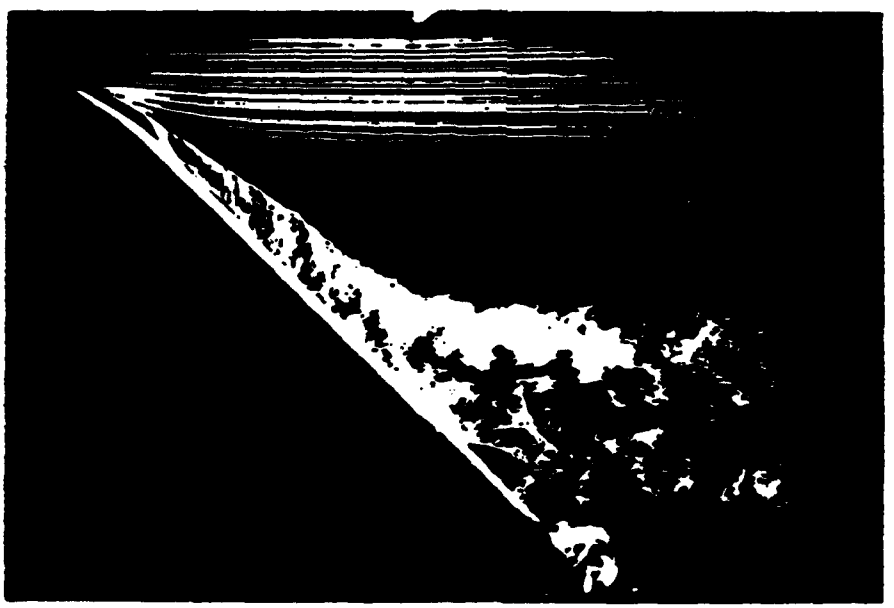

(b) Far Side

Figure 89. Smoke Wire Visualization at Re=6000, α=45°, (a) near side (b) far side

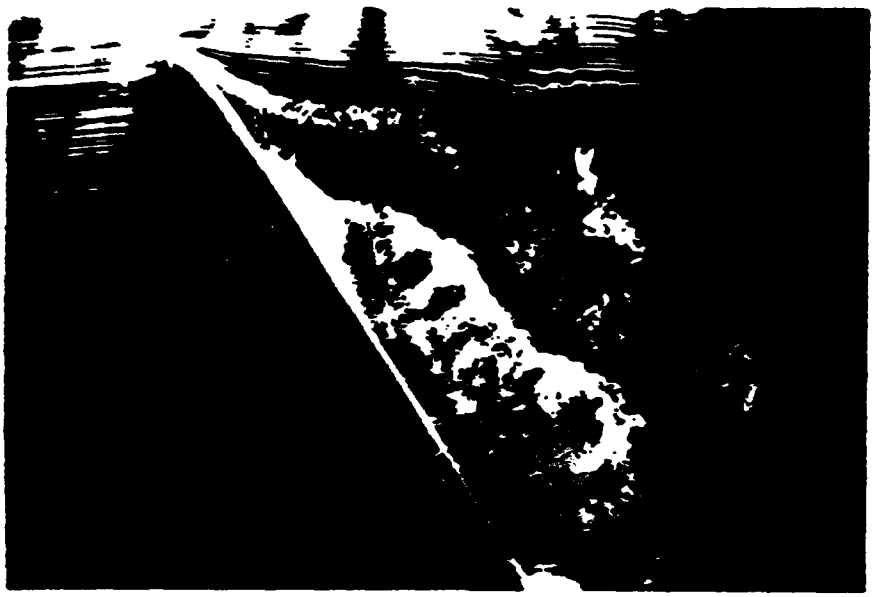

(a) Near Side

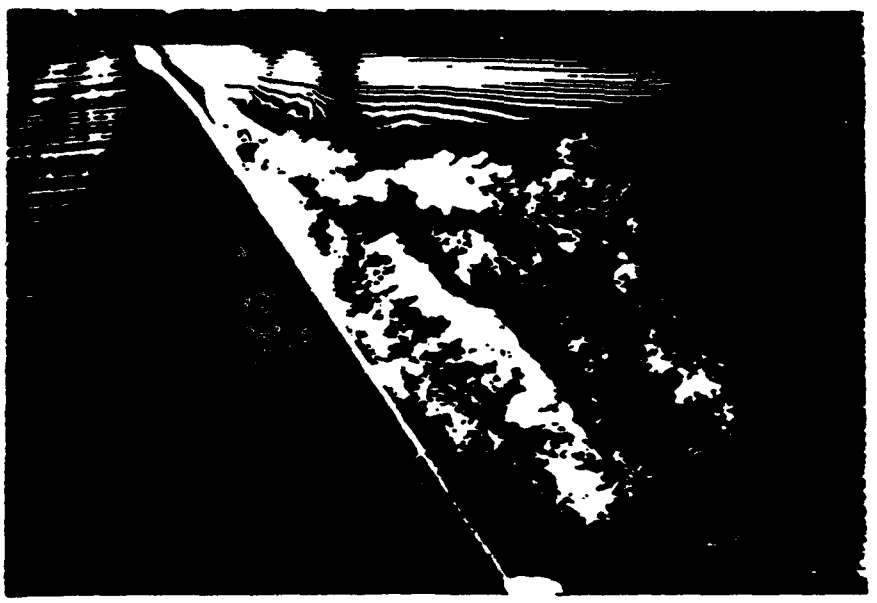

(b) Far Side

Figure 90. Smoke Wire Visualization at Re=6000, α=60°, (a) near side (b) far side

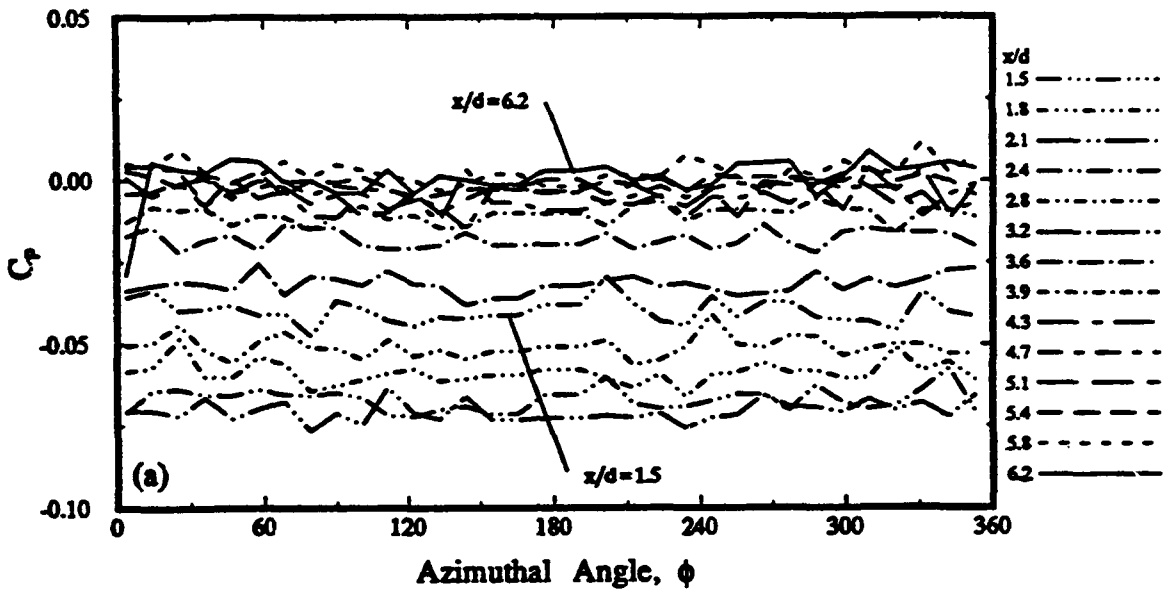

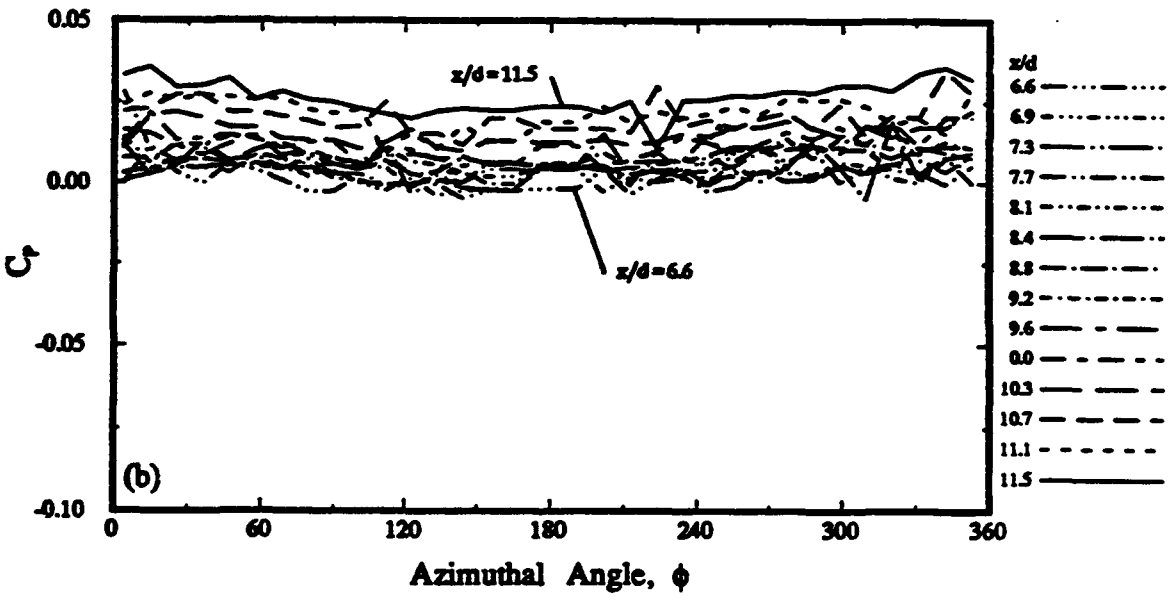

Figure 91. Pressure Distributions at Re=6000, α=0°, (a) 1.5≤x/d≤6.2 (b) 6.6≤x/d≤ 11.5 (c) for selected ϕ's along x/d

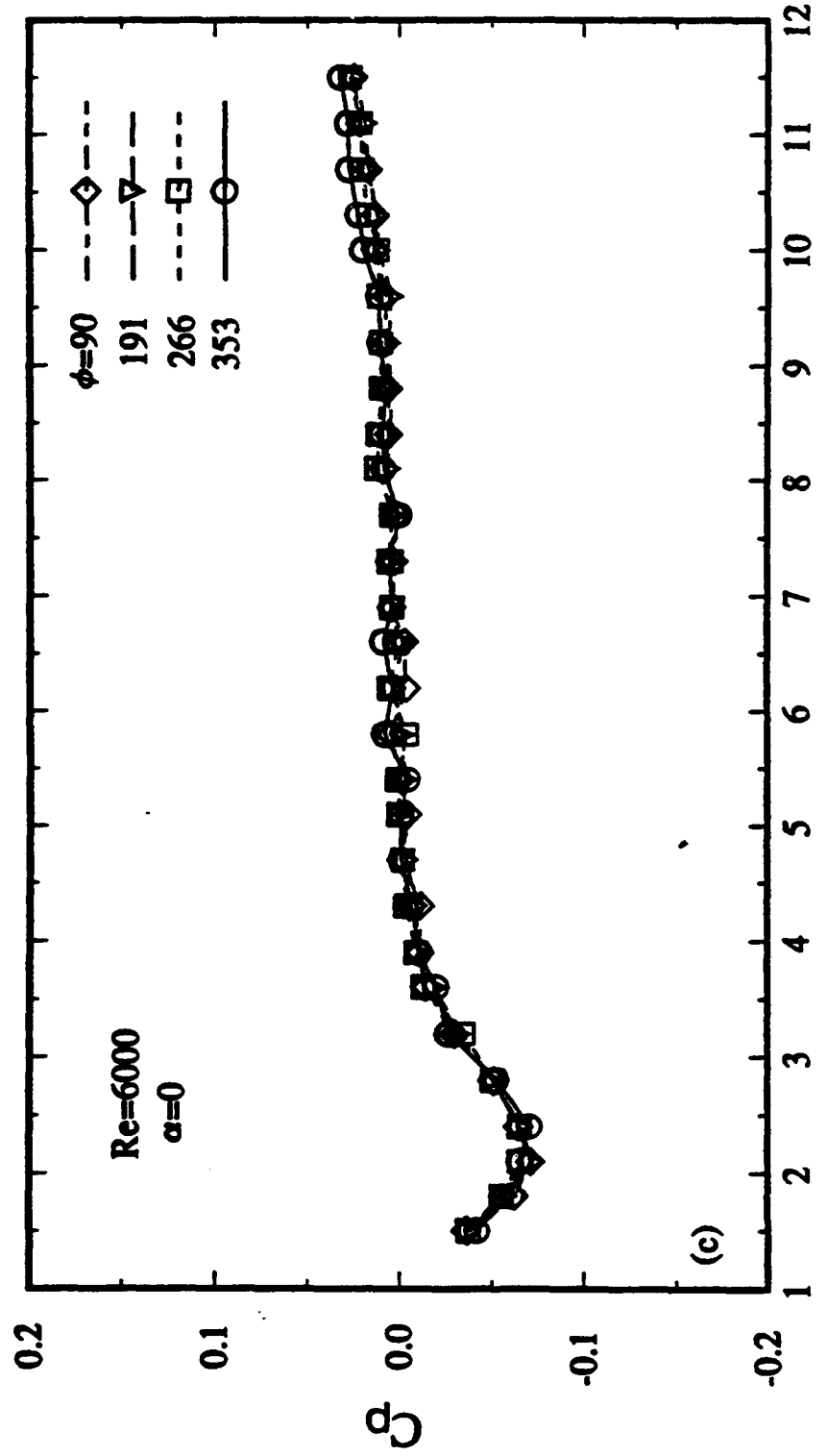

Figure 91 (concluded)

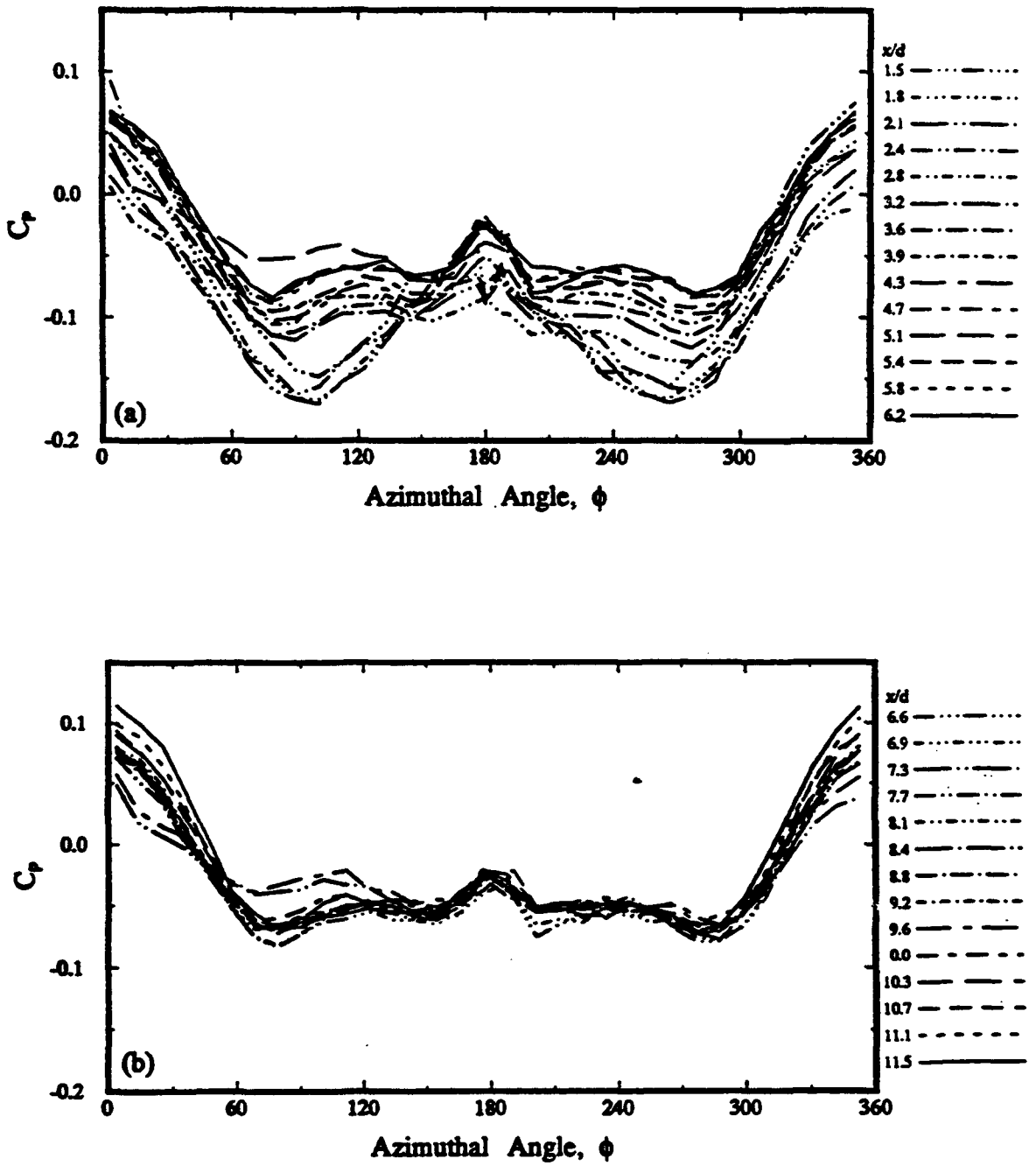

Figure 92. Pressure Distributions at Re=6000, α=15°, (a) 1.5≤x/d≤6.2 (b) 6.6≤x/d≤ 11.5

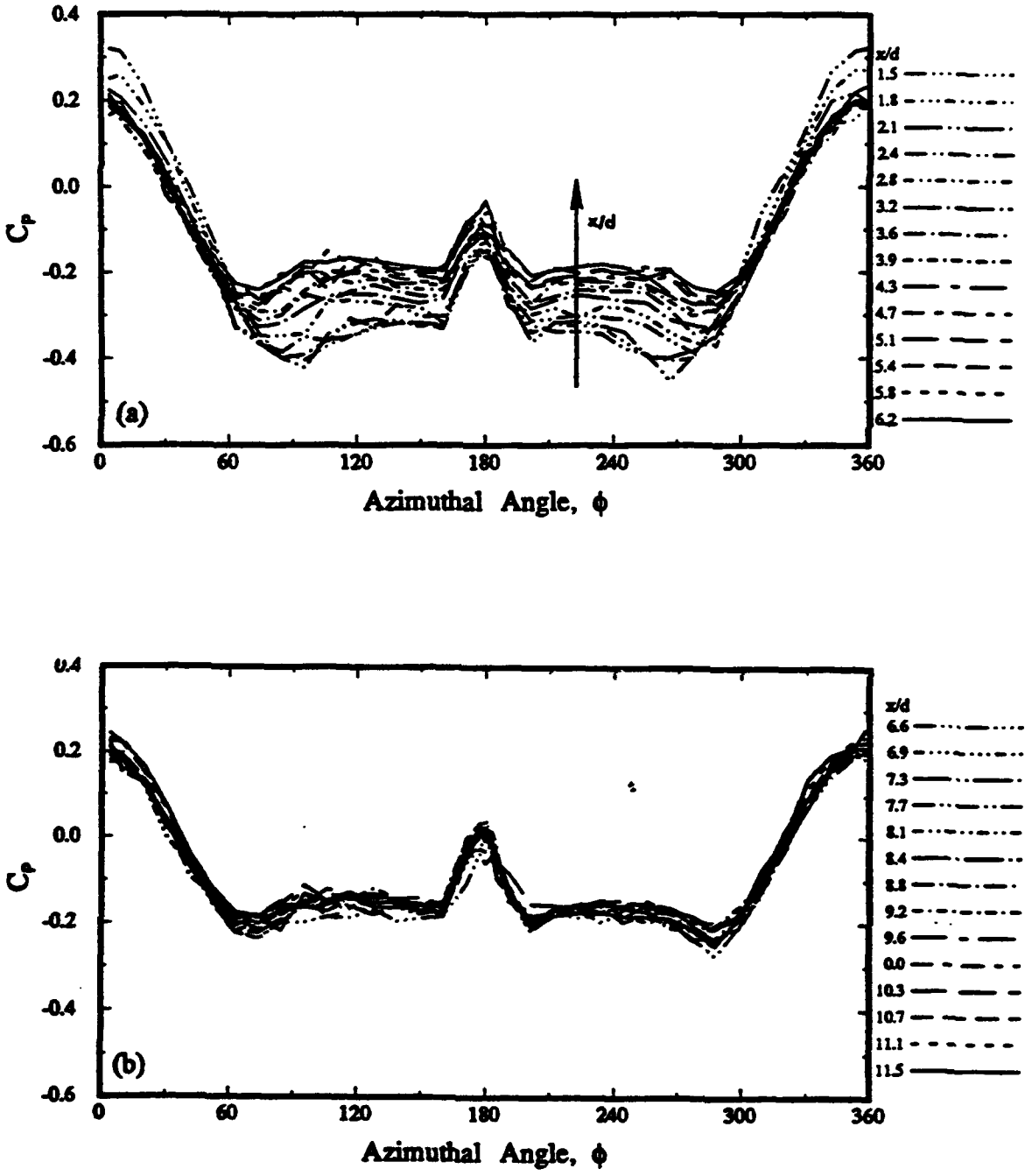

Figure 93. Pressure Distributions at Re=6000, α=30°, (a) 1.5≤x/d≤6.2 (b) 6.6≤x/d≤ 11.5

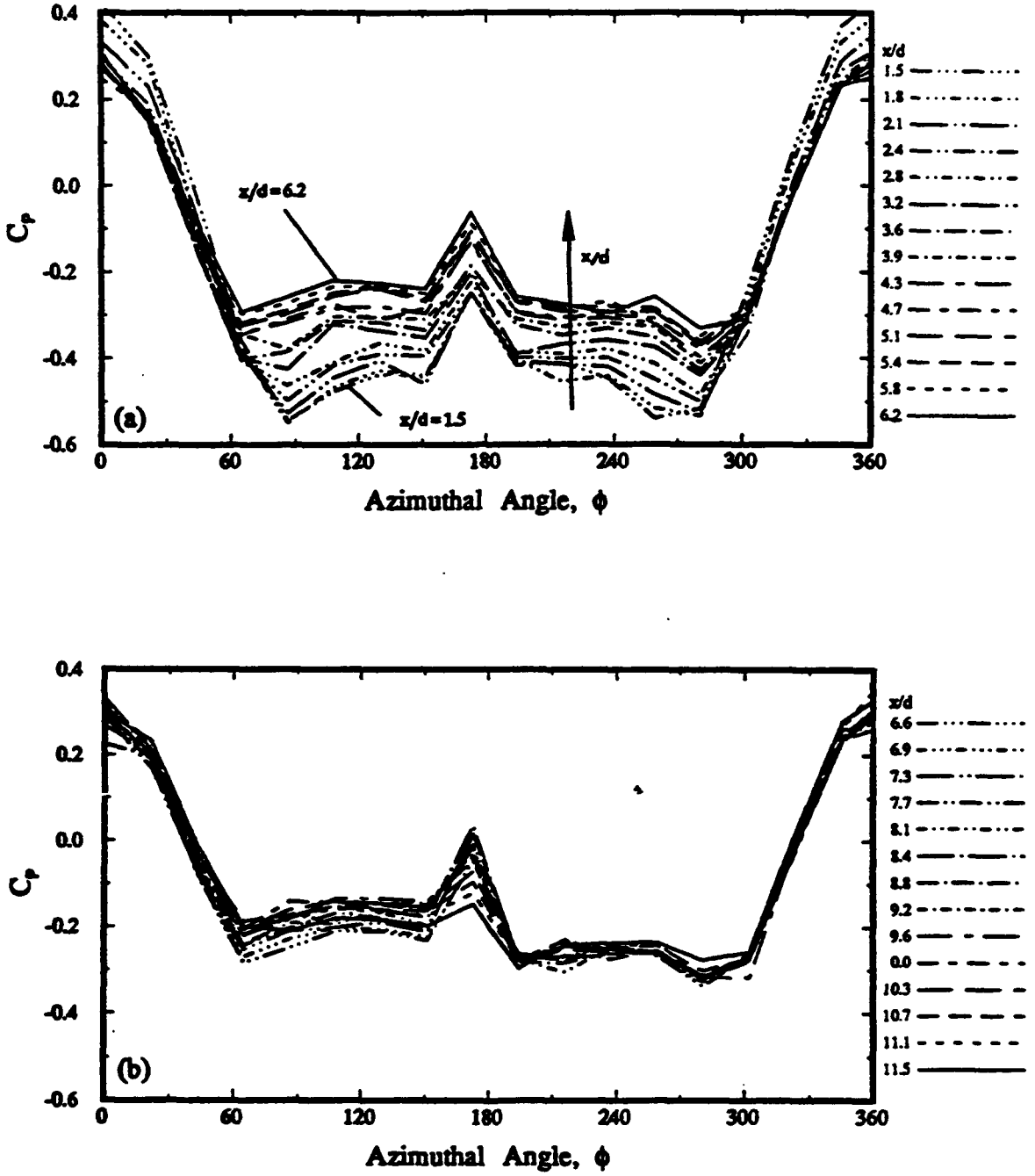

Figure 94. Pressure Distributions at Re=6000, α=37°, (a) 1.5≤x/d≤6.2 (b) 6.6≤x/d≤ 11.5

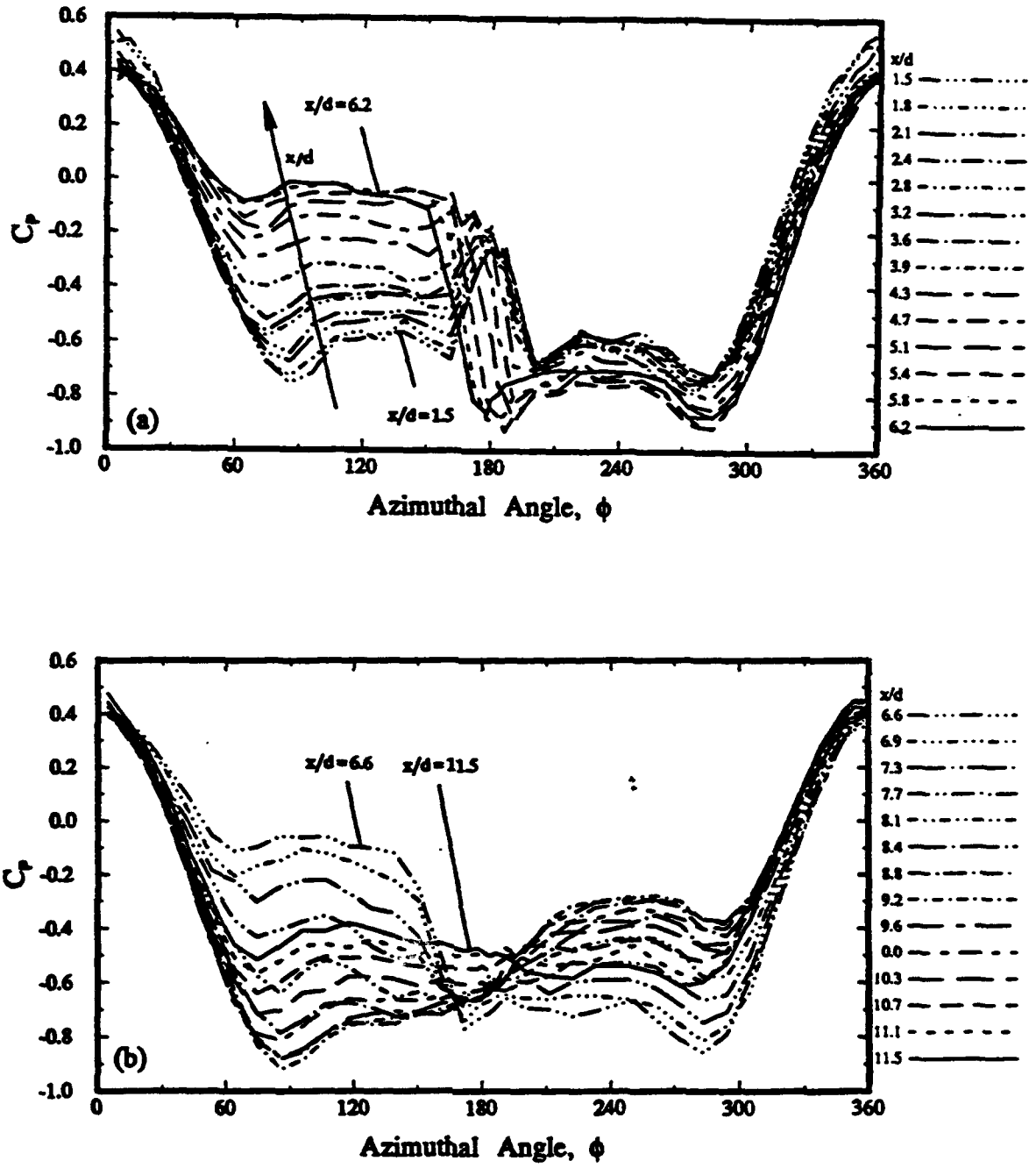

Figure 95. Pressure Distributions at Re=6000, α=45°, (a) 1.5≤x/d≤6.2 (b) 6.6≤x/d≤ 11.5

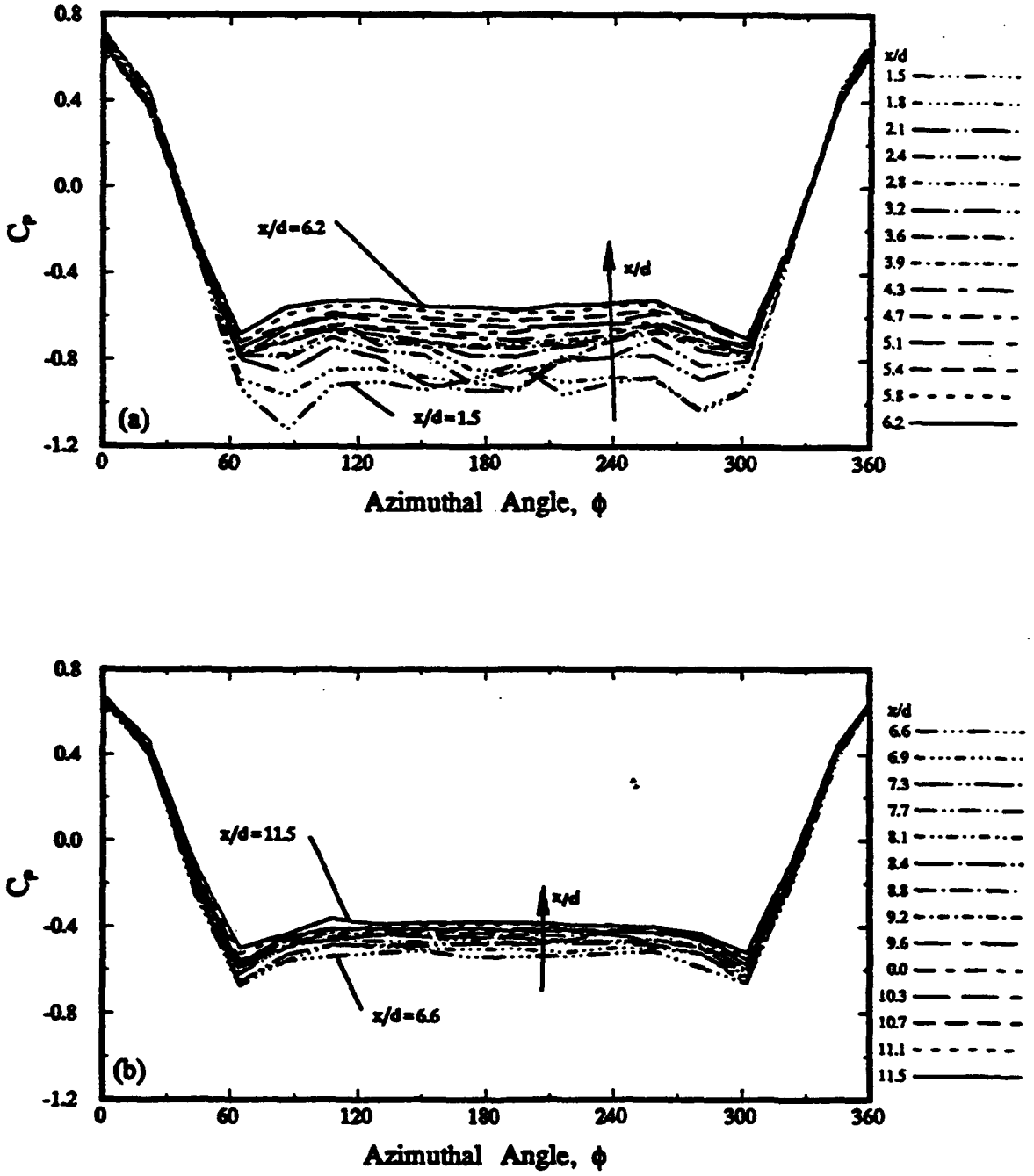

Figure 96. Pressure Distributions at Re=6000, α=70°, (a) $1.5 \leq x/d \leq 6.2$ (b) $6.6 \leq x/d \leq 11.5$

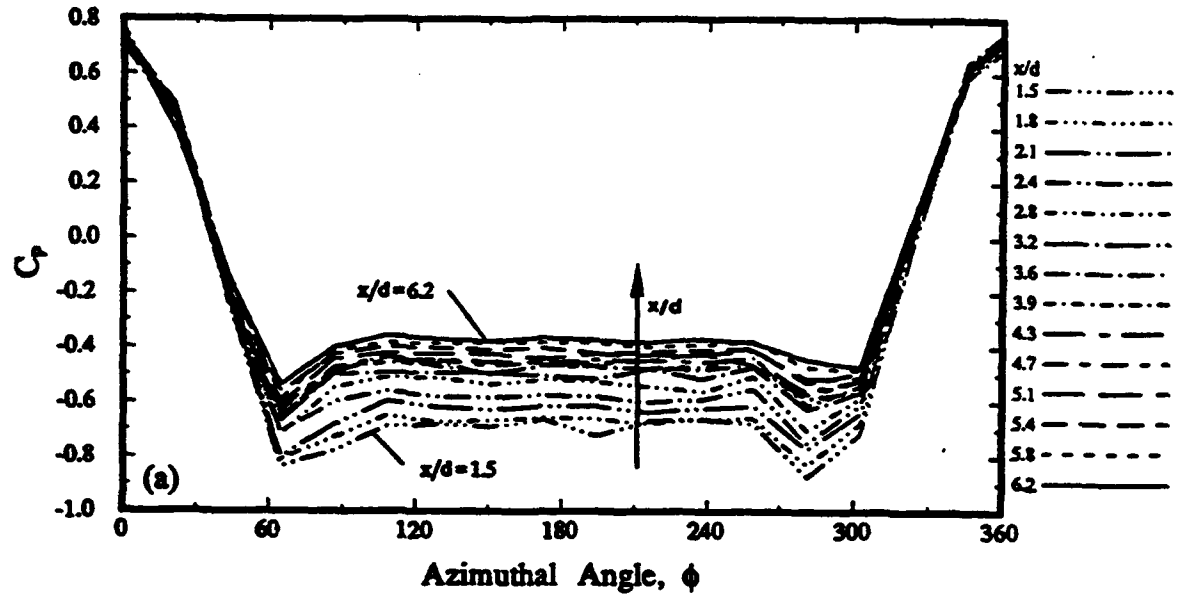

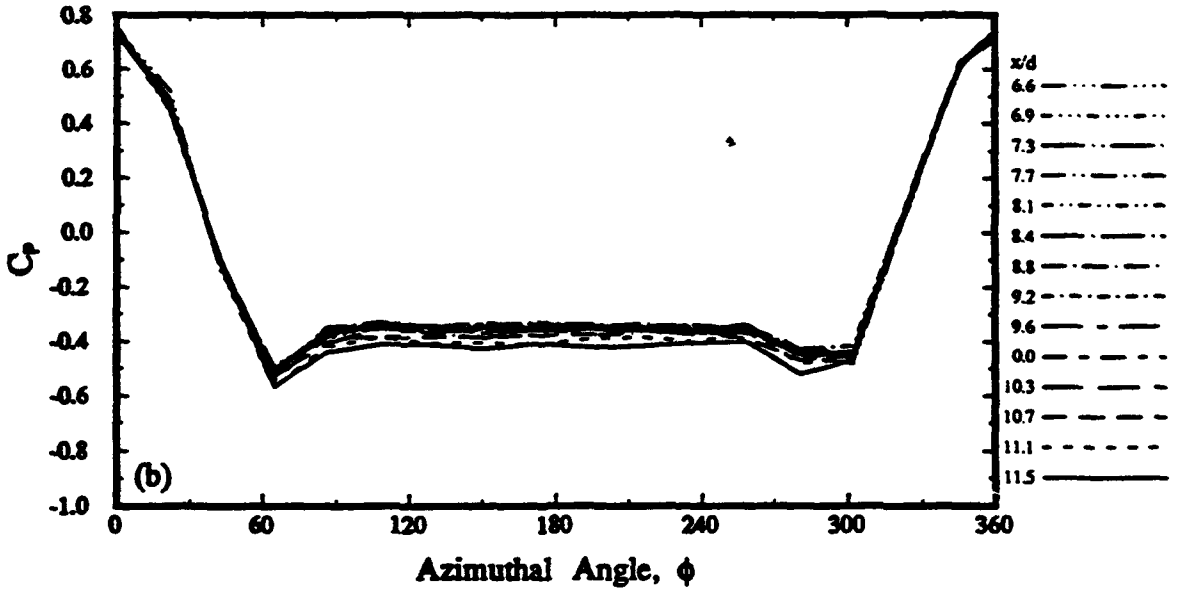

Figure 97. Pressure Distributions at Re=6000, α=85°, (a) 1.5≤x/d≤6.2 (b) 6.6≤x/d≤ 11.5

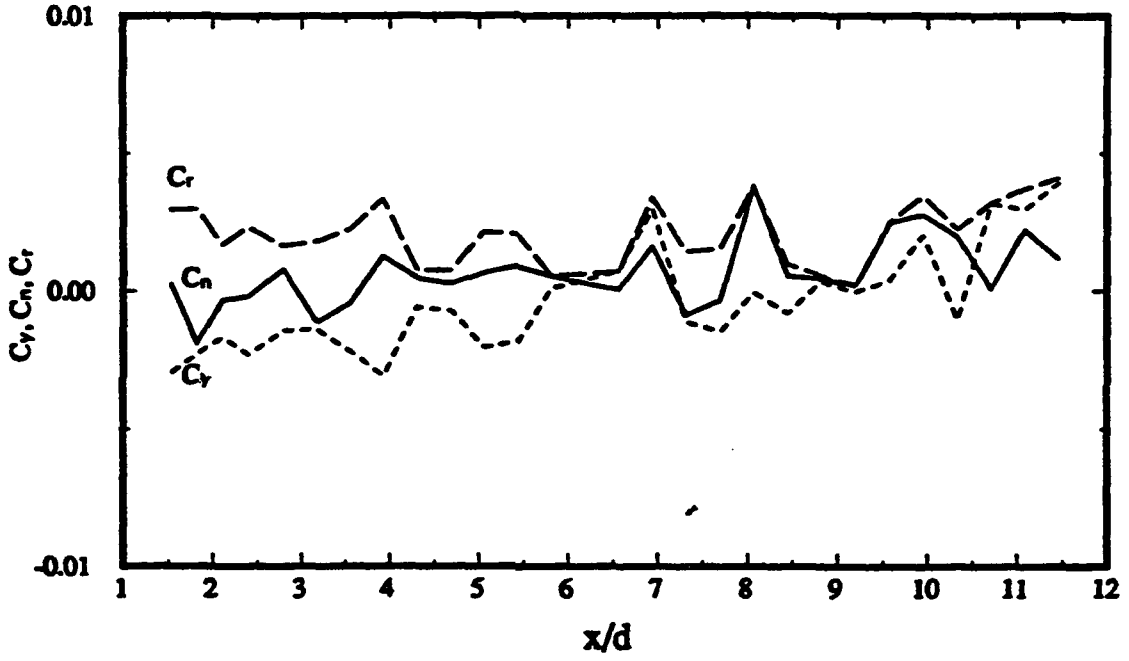

Figure 98. Local Force Distributions, C_y, C_n, C_r, at Re=6000, α=0° along x/d

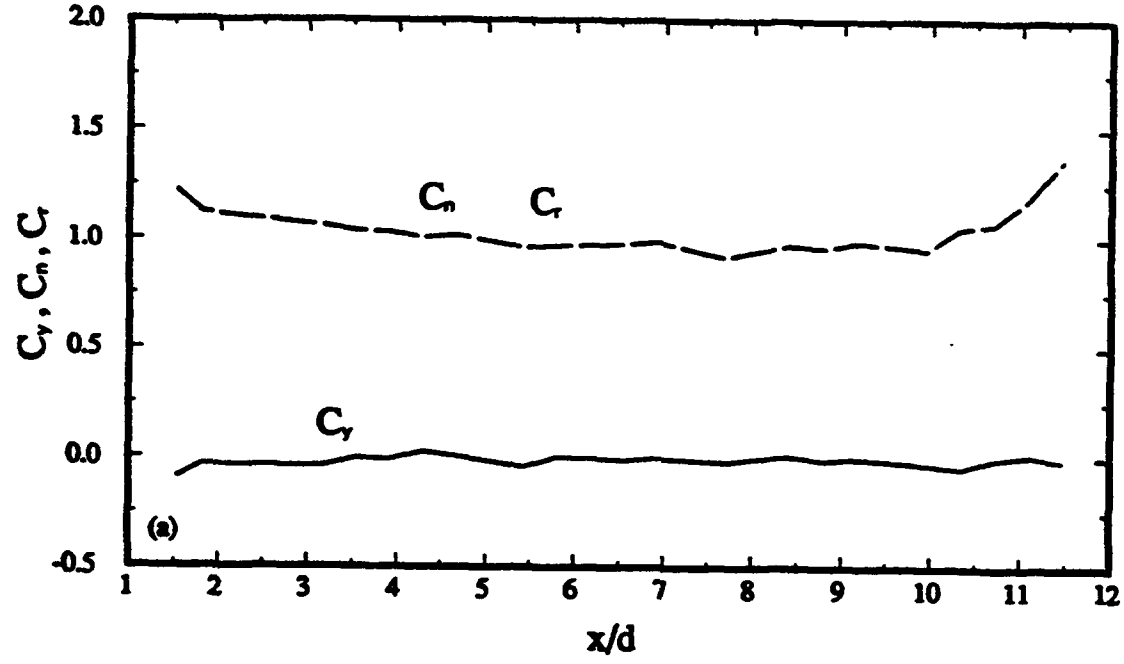

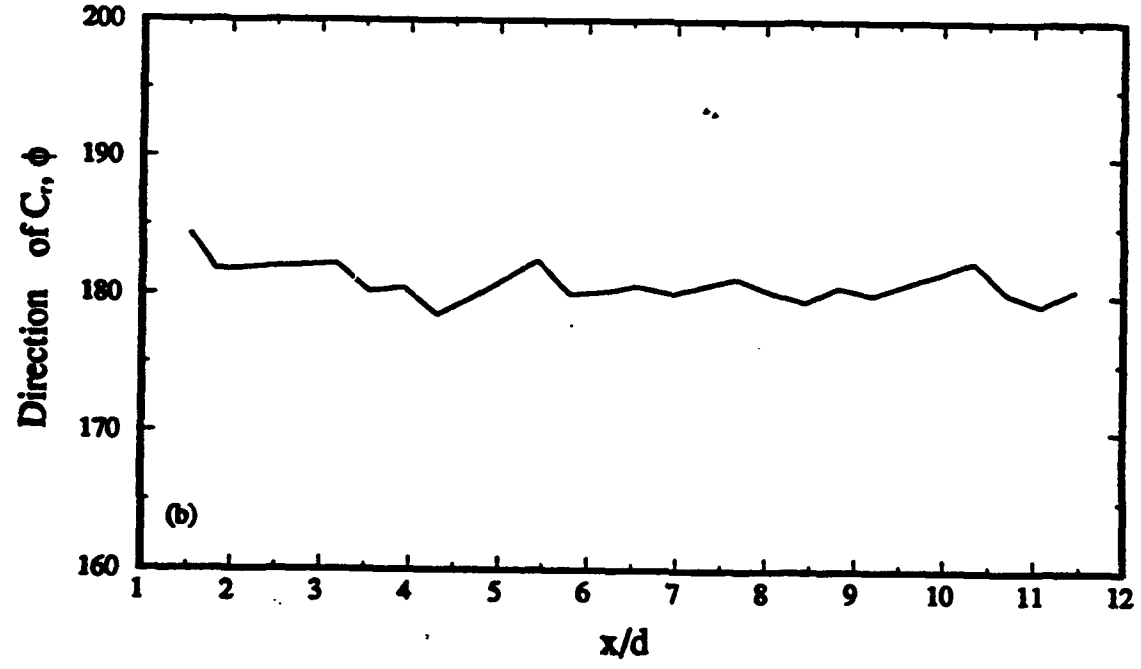

Figure 99. Local Force Distributions (a) C_y, C_n, C_r (b) Direction of C_r, ϕ, at Re=6000, α=15° along x/d

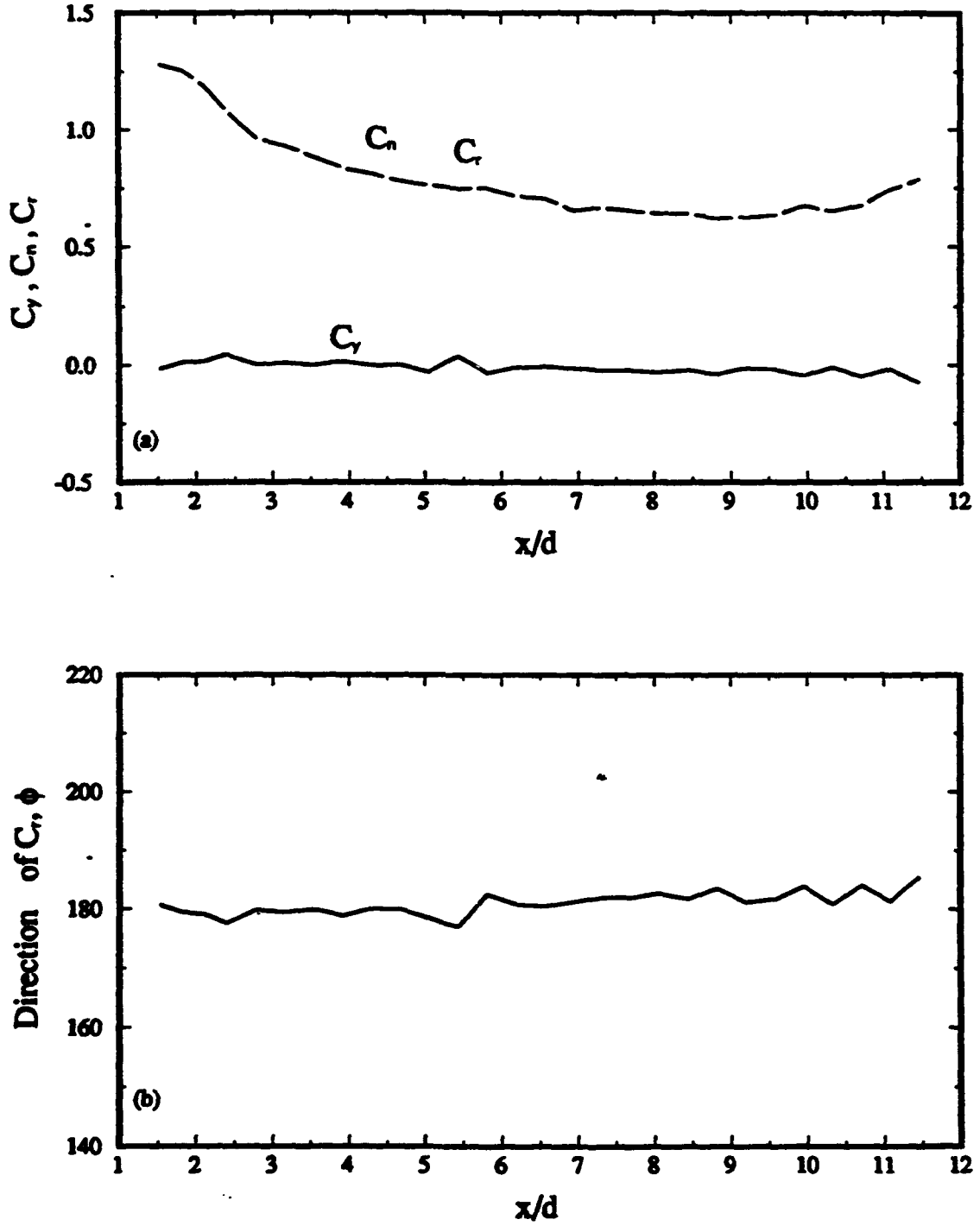

Figure 100. Local Force Distributions (a) C_y, C_n, C_r (b) Direction of C_r, ϕ, at Re=6000, α=30° along x/d

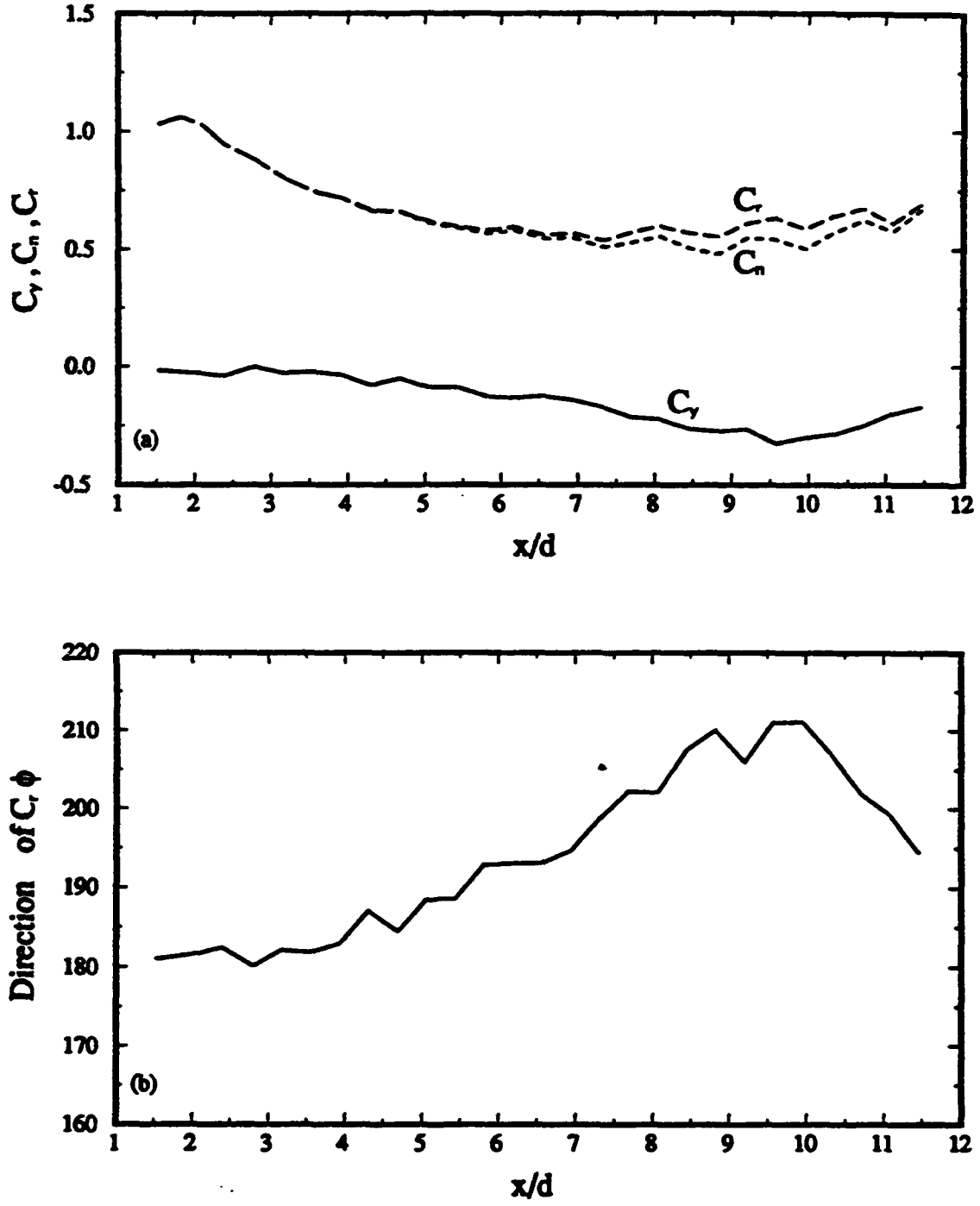

Figure 101. Local Force Distributions (a) C_y, C_n, C_r (b) Direction of C_r, ϕ, at Re=6000, α=37° along x/d

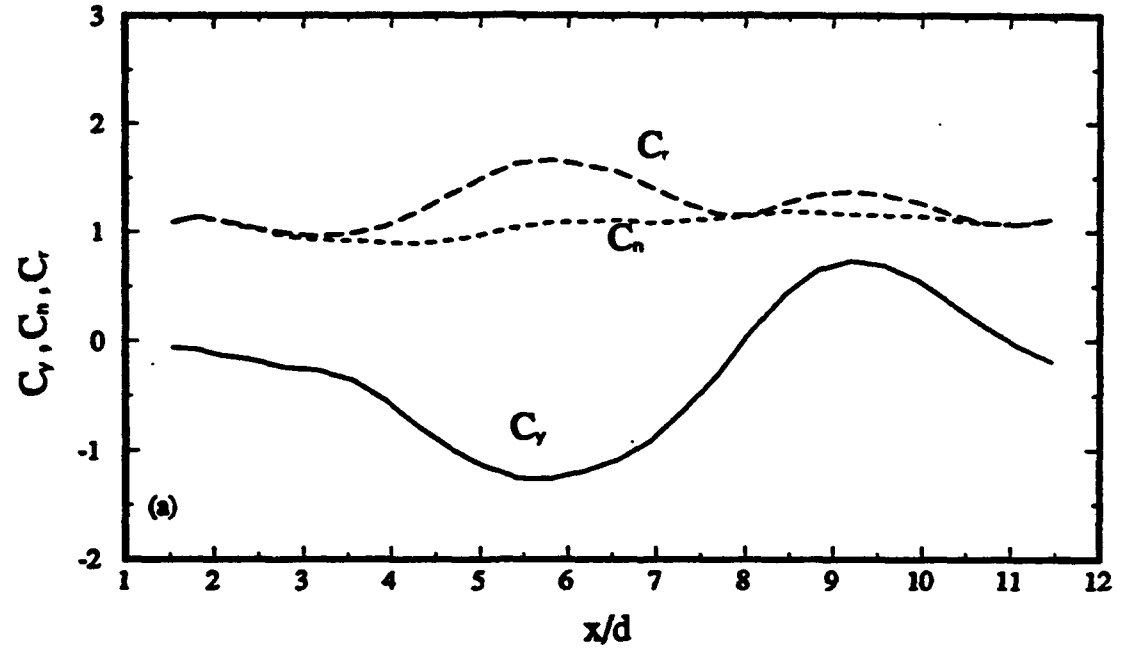

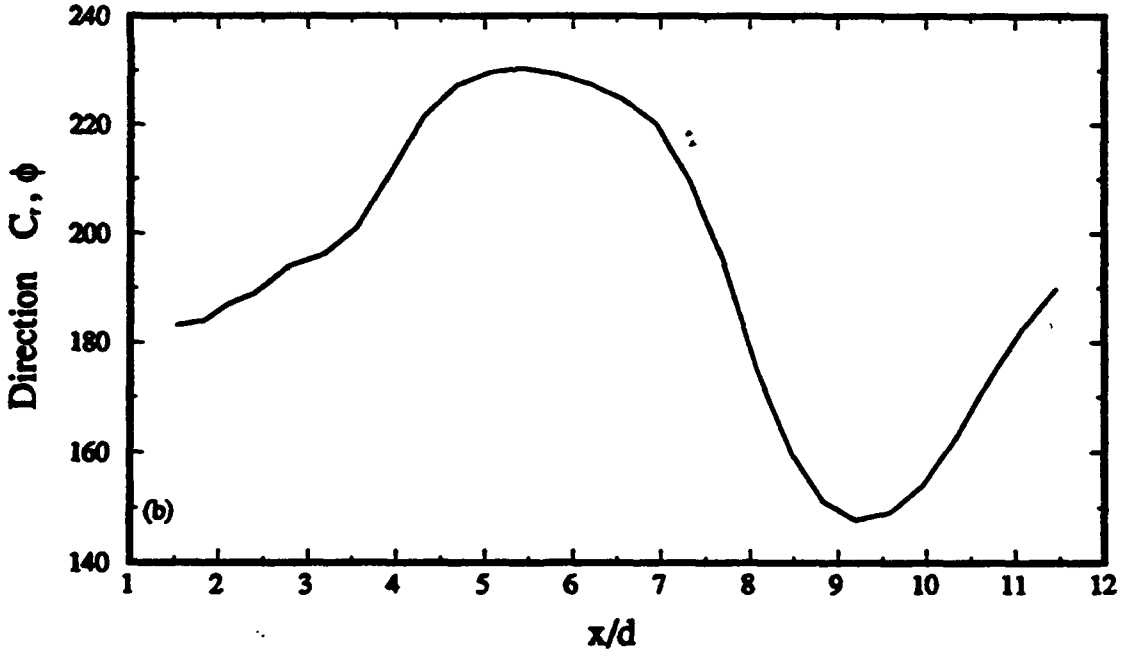

Figure 102. Local Force Distributions (a) C_y, C_n, C_r (b) Direction of C_r, ϕ, at Re=6000, α=45° along x/d

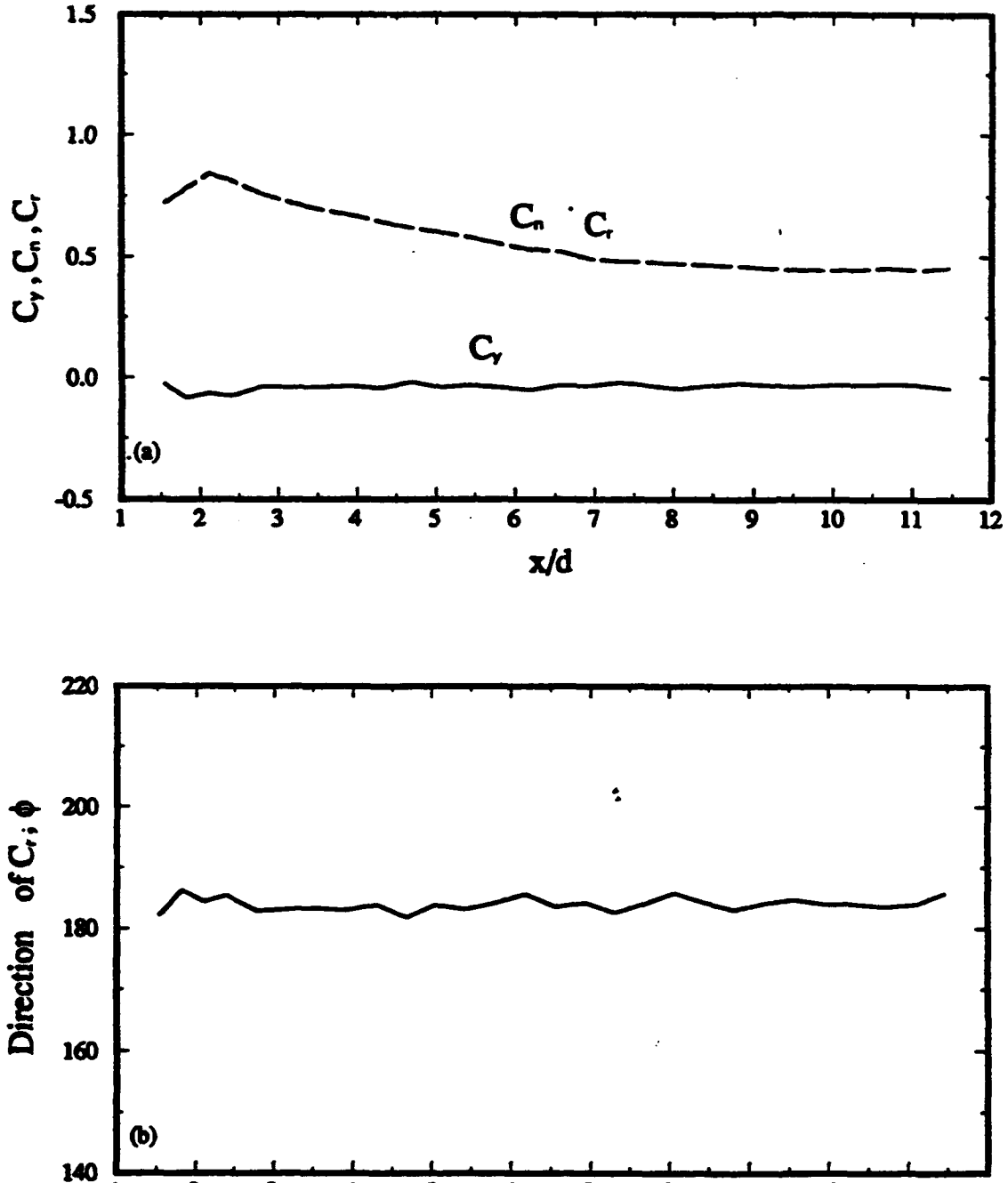

Figure 103. Local Force Distributions (a) C_y, C_n, C_r (b) Direction of C_r, ϕ, at Re=6000, α=70° along x/d

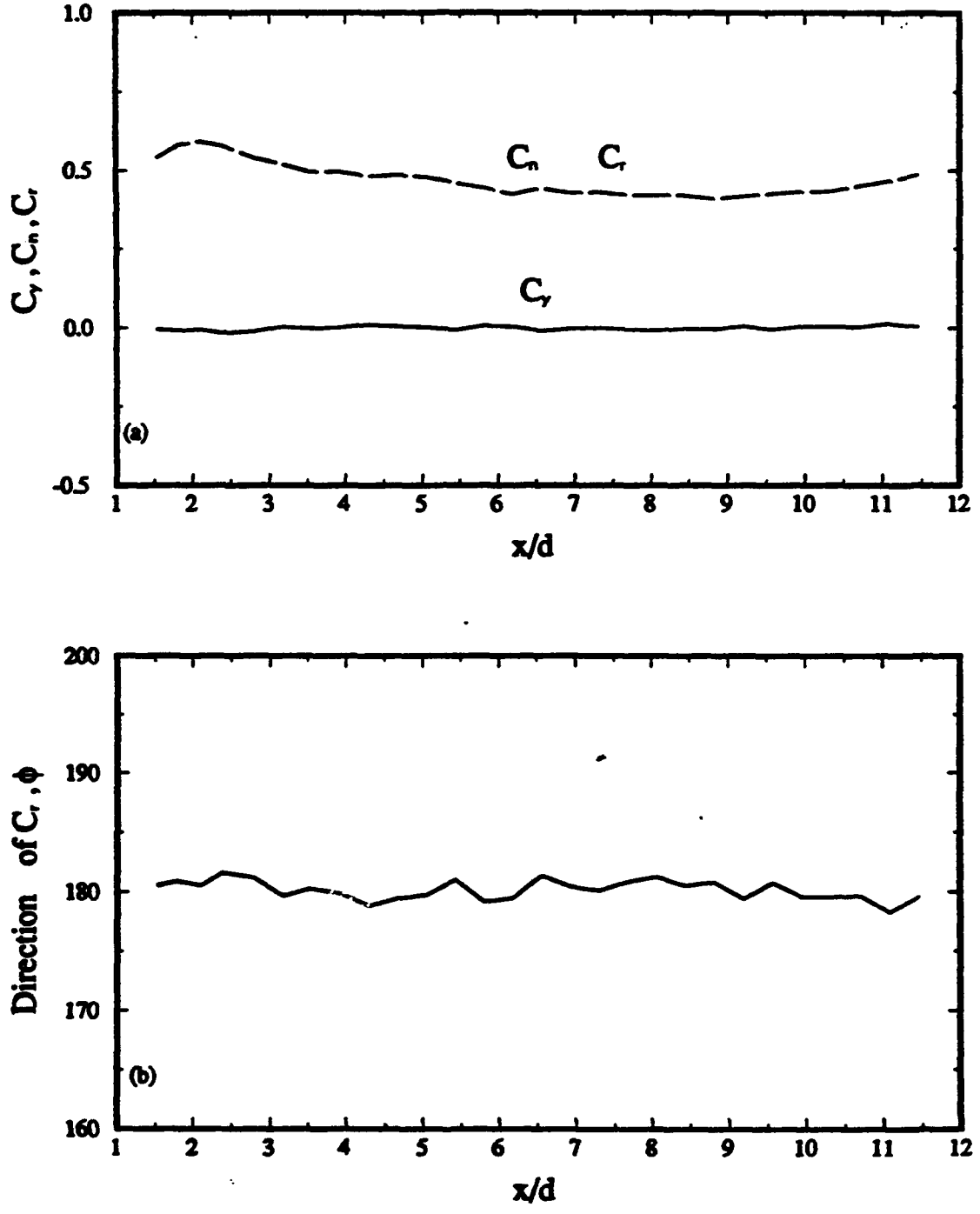

Figure 104. Local Force Distributions (a) C_y, C_n, C_r (b) Direction of C_r, ϕ, at Re=6000, α=85° along x/d

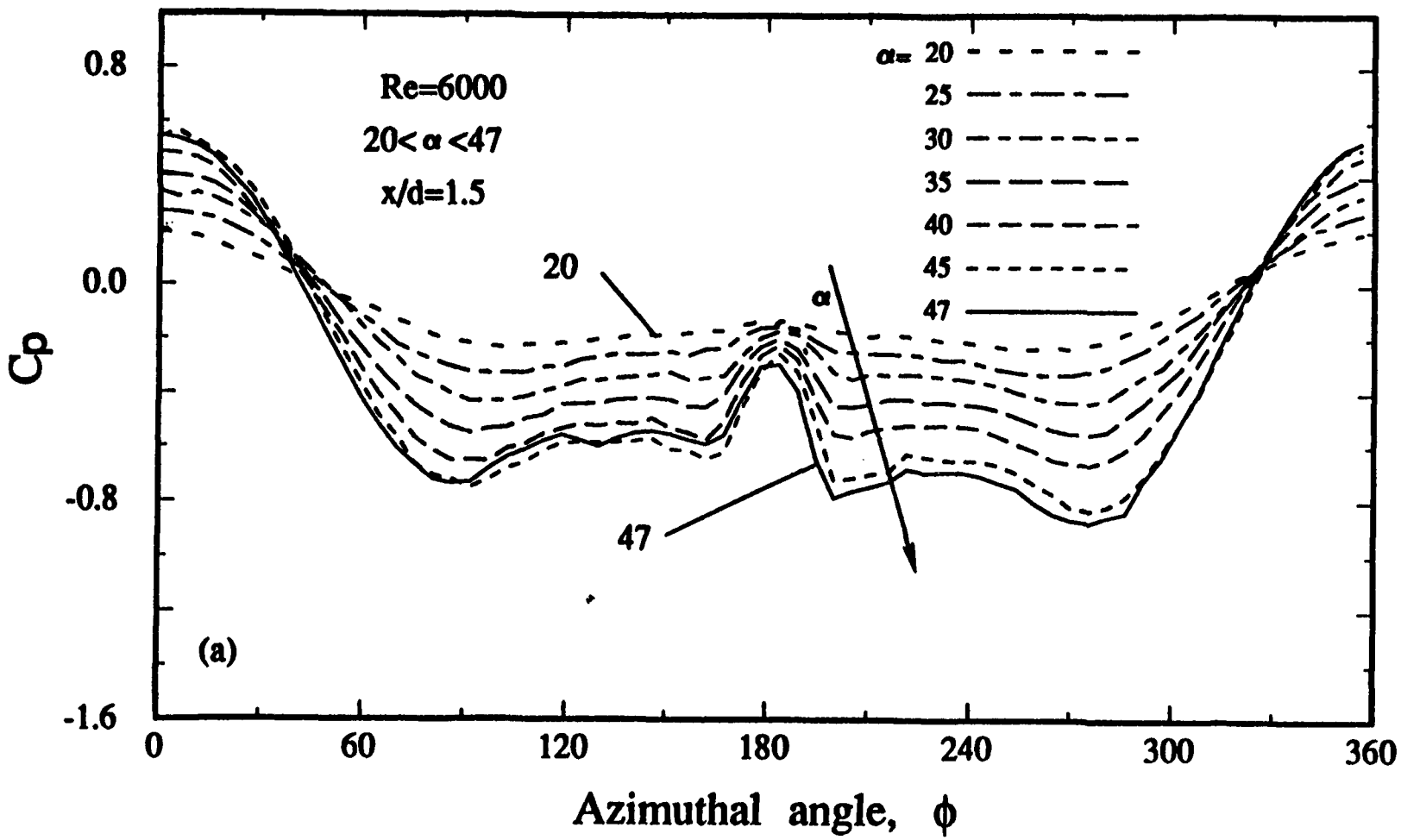

Figure 105. Pressure Distributions at Re=6000, x/d=1.5, (a) 20°≤α≤47° (b) 49°≤α≤57° (c) 59°≤α≤63° (d) 65°≤α≤69°

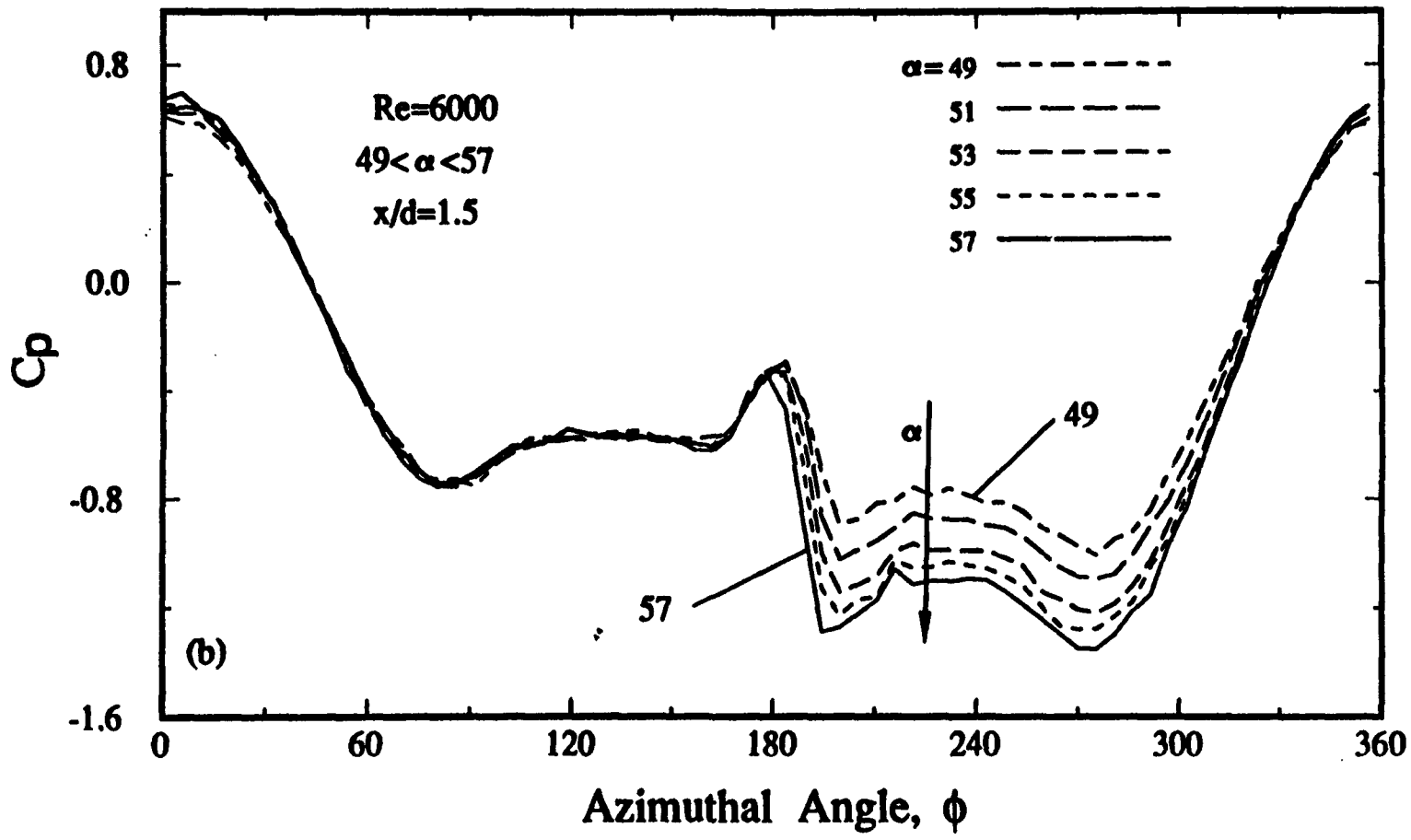

Figure 105 (continued)

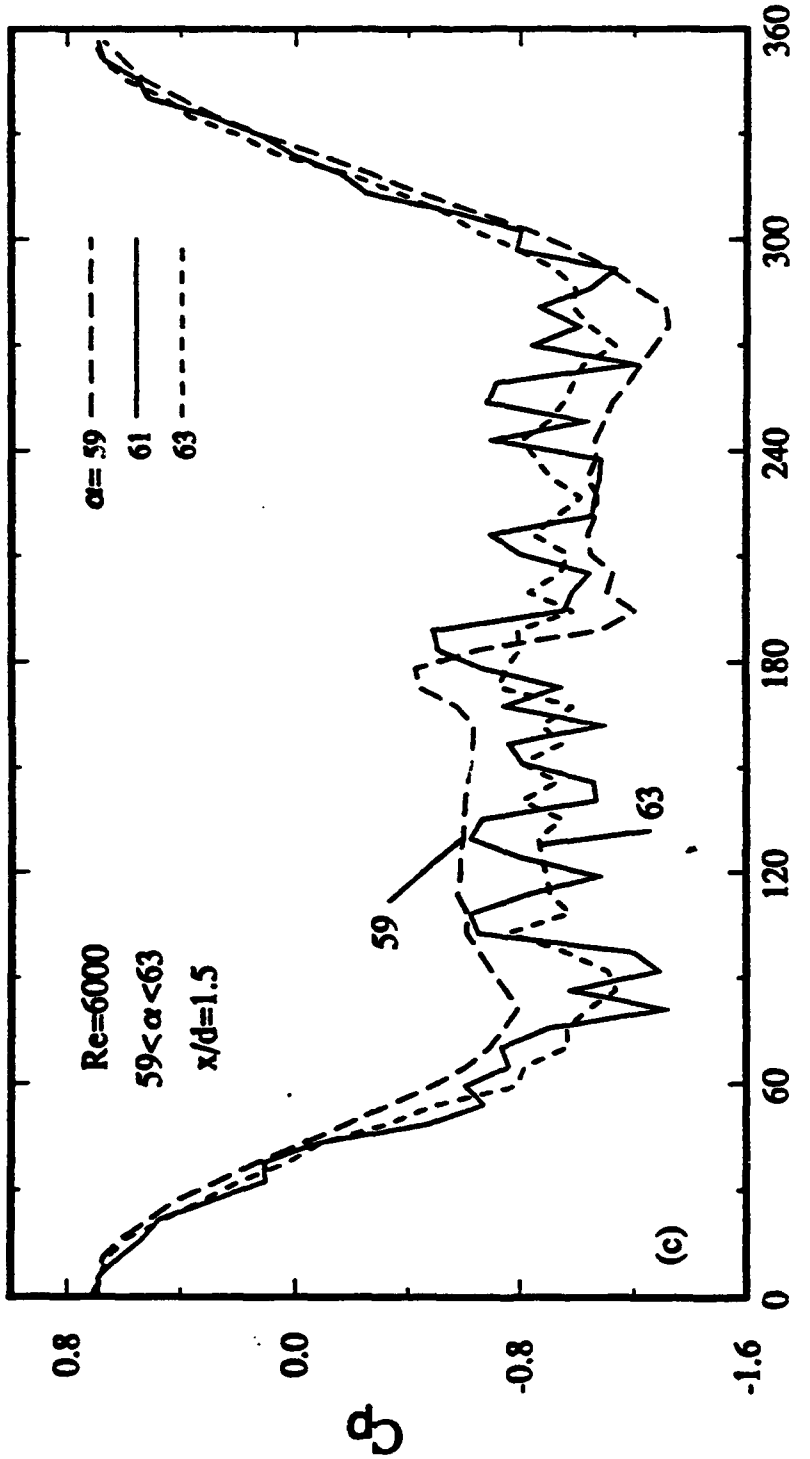

Figure 105 (continued)

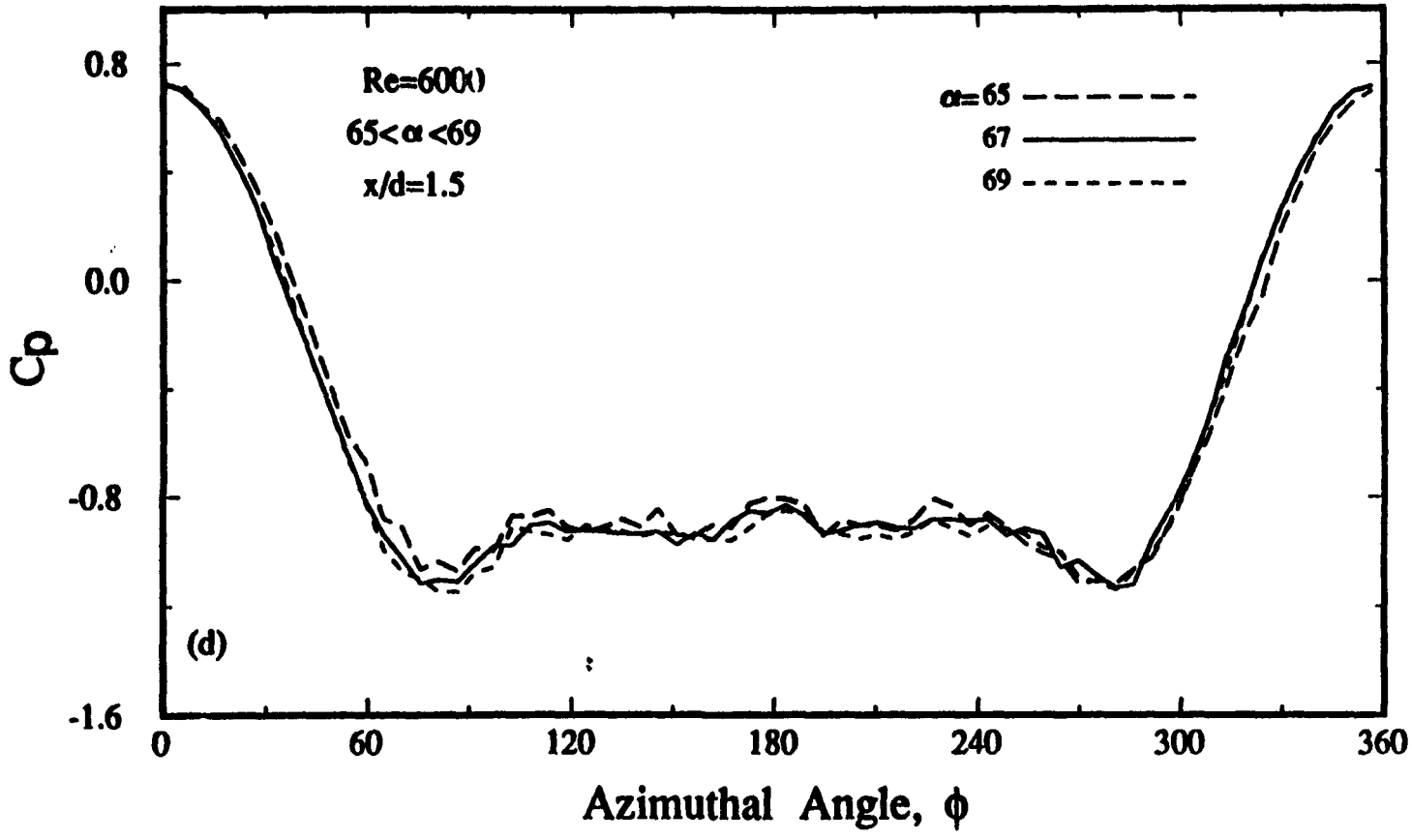

Figure 105 (concluded)

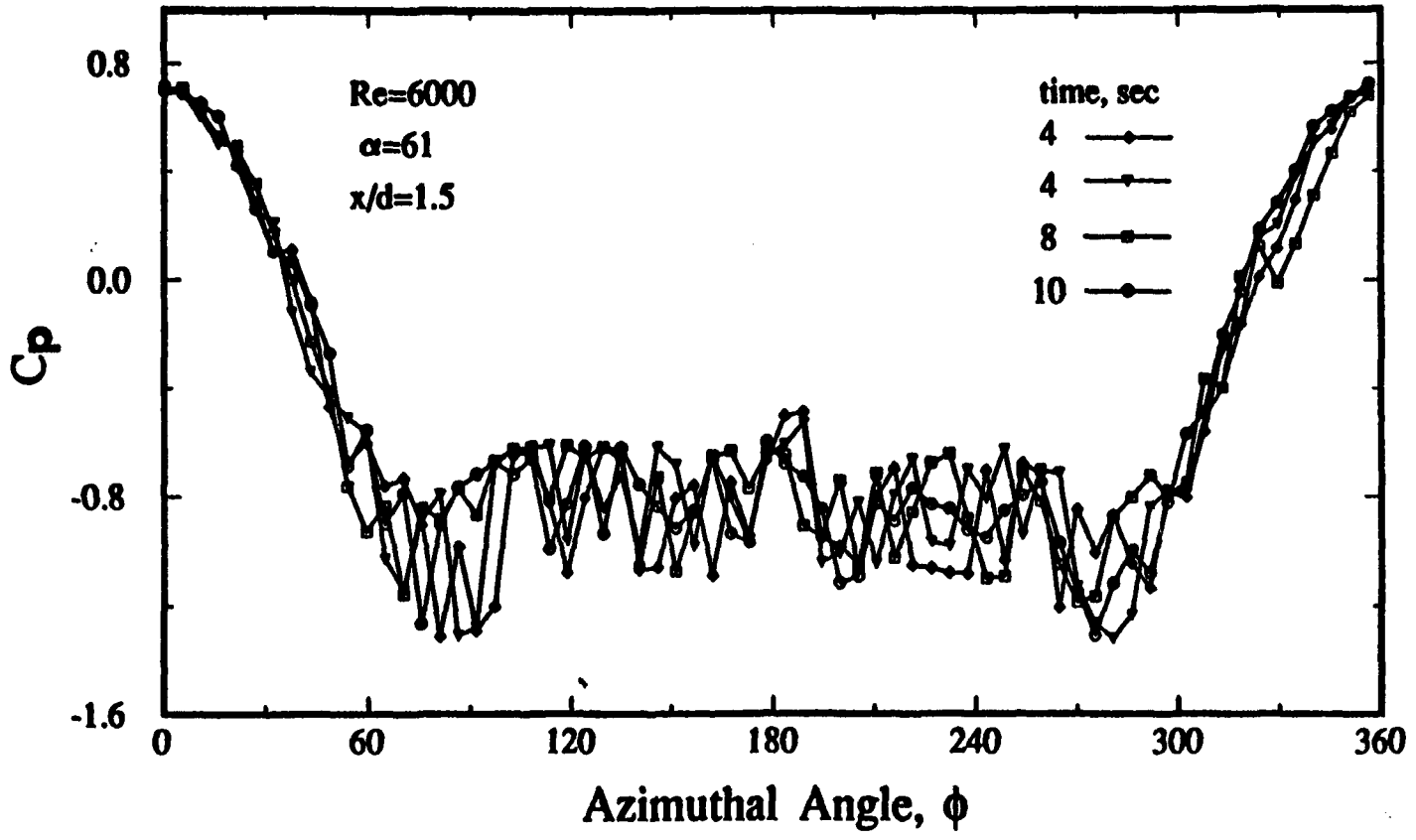

Figure 106. Pressure Distributions at Re=6000, α=61°, and x/d=1.5 Obtained at Four Different Acquisition Times

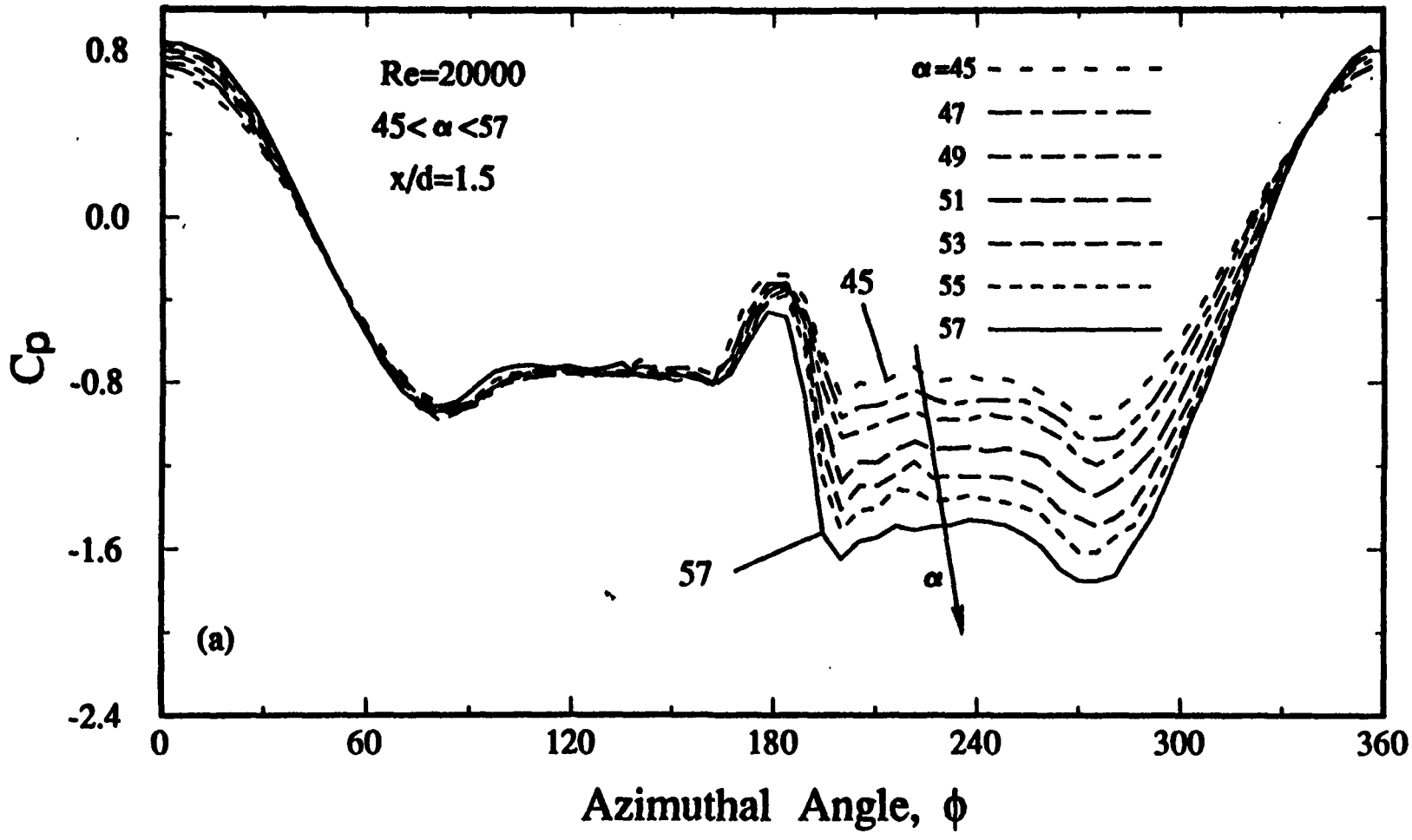

Figure 107. Pressure Distributions at Re=20000, x/d=1.5, (a) 45°≤α≤55° (b) 57°≤α≤65° (c) 67°≤α≤69°

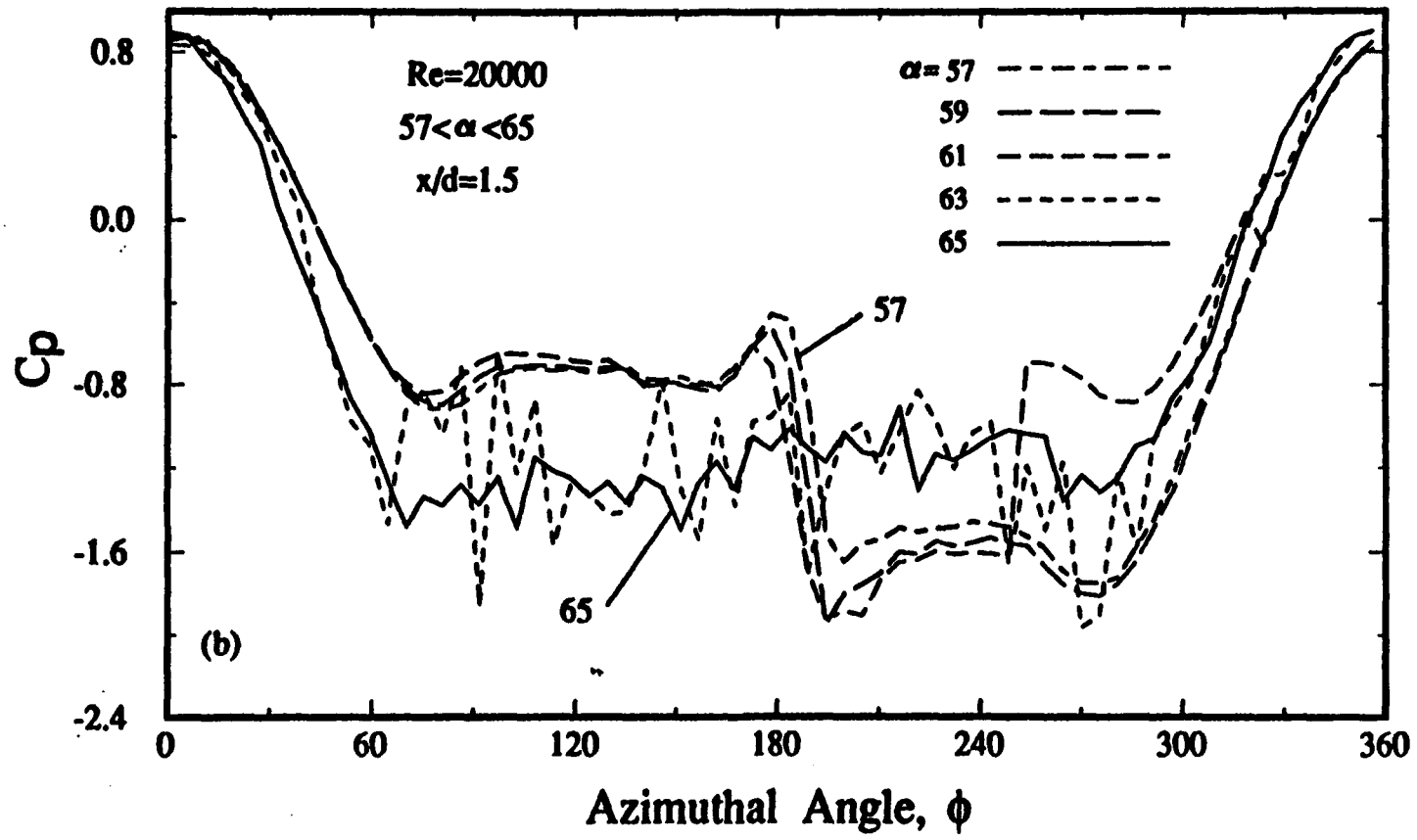

Figure 107 (continued)

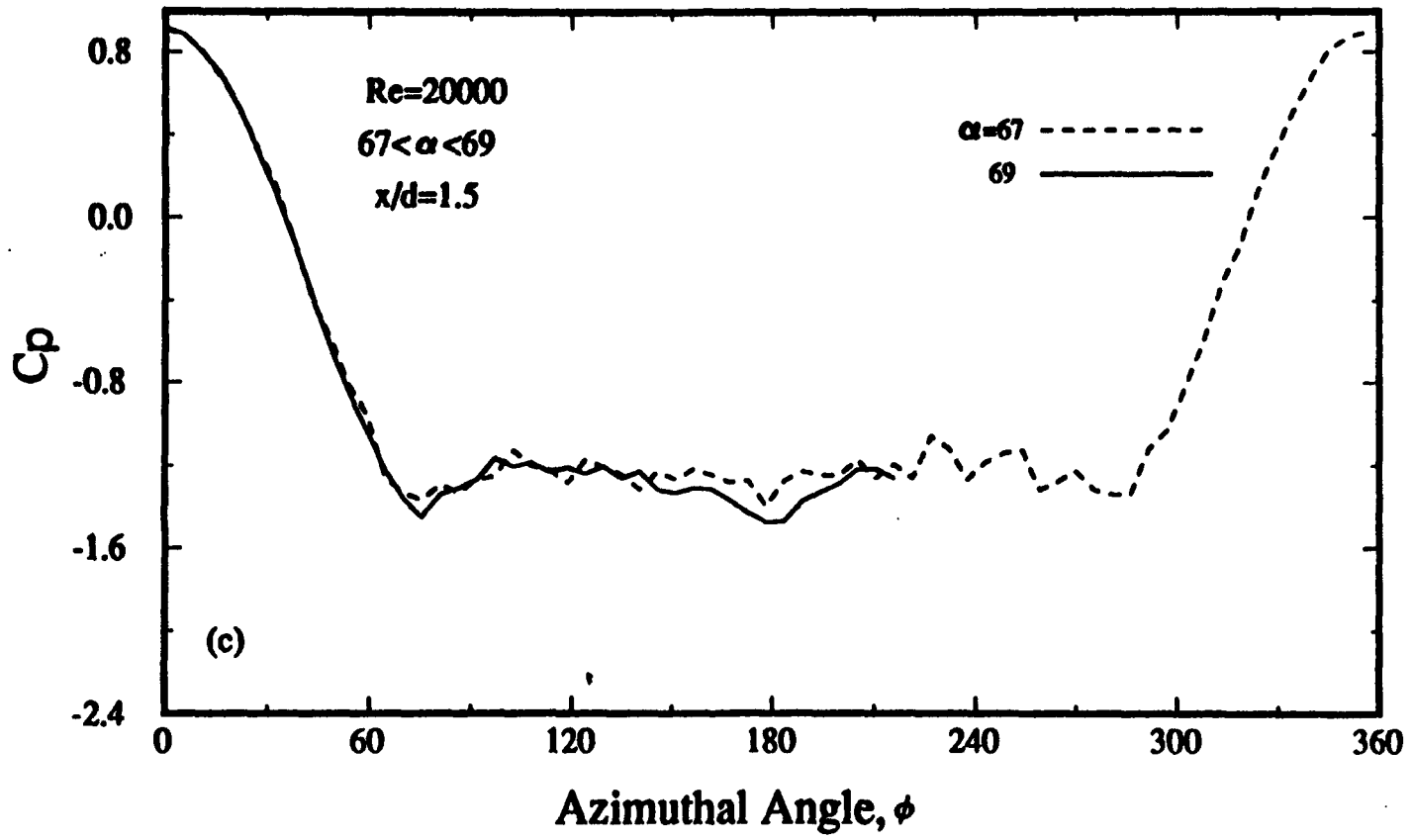

Figure 107 (concluded)

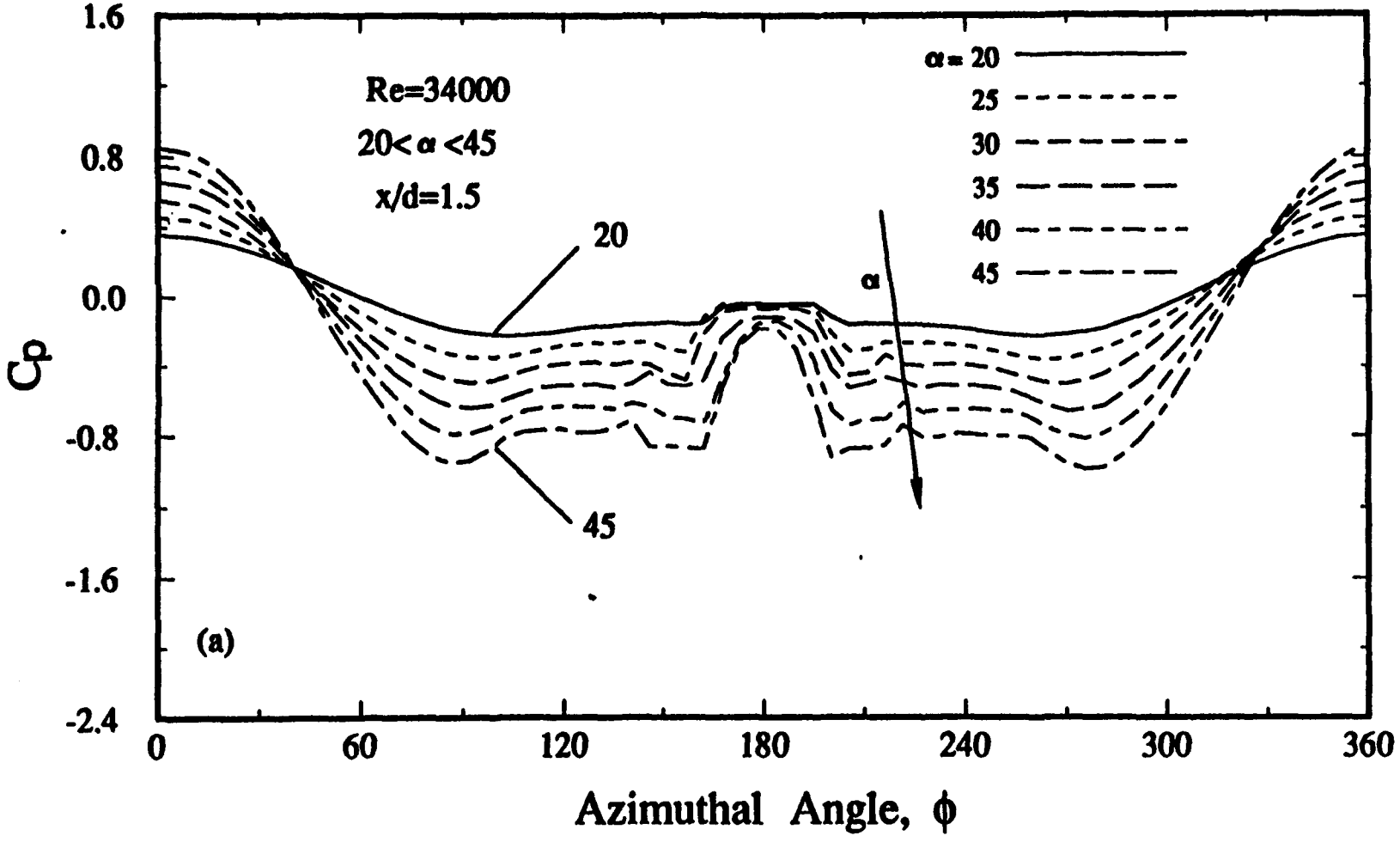

Figure 108. Pressure Distributions at Re=34000, x/d=1.5, (a) 20°≤α≤45° (b) 50°≤α≤66°

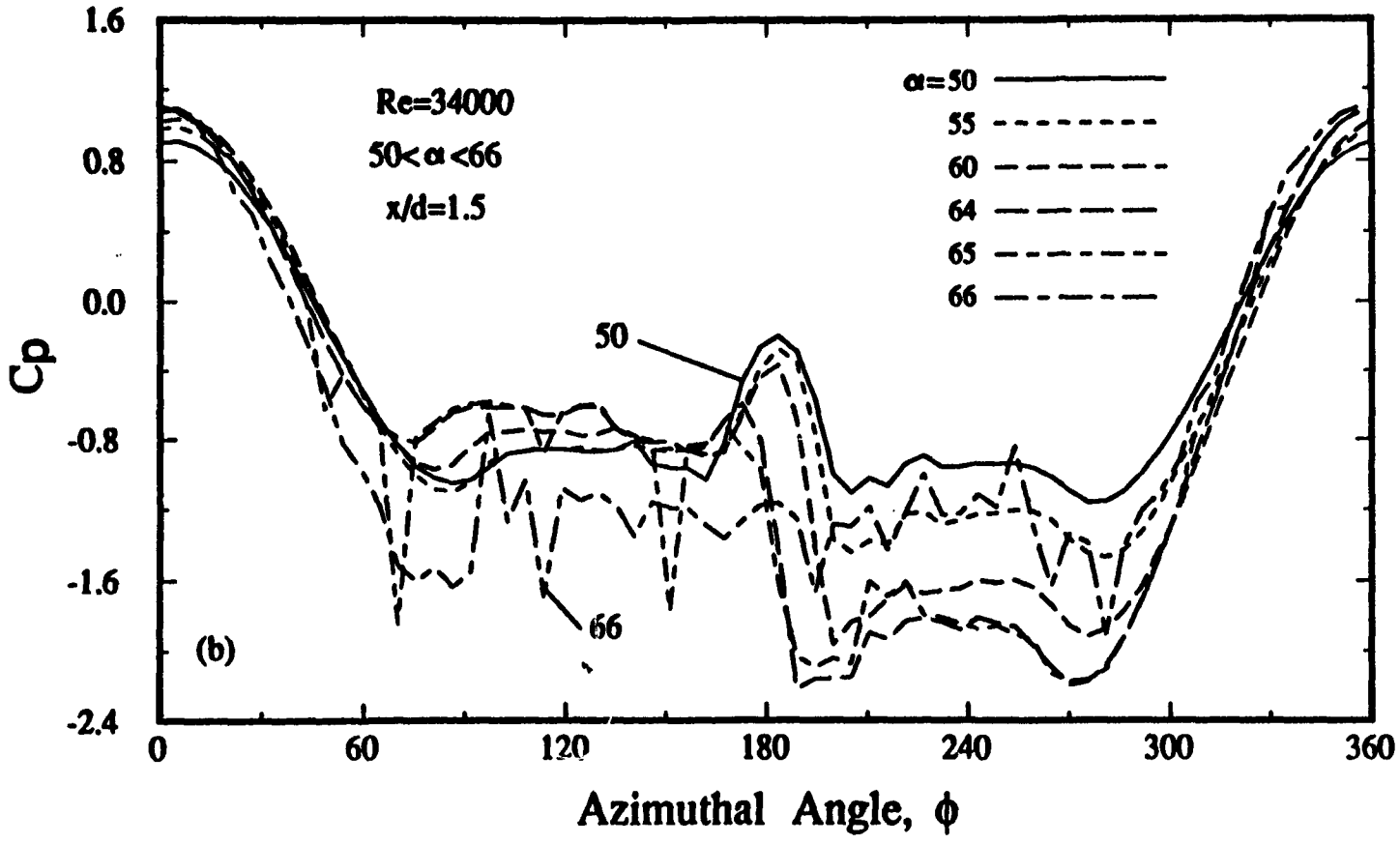

Figure 108 (concluded)

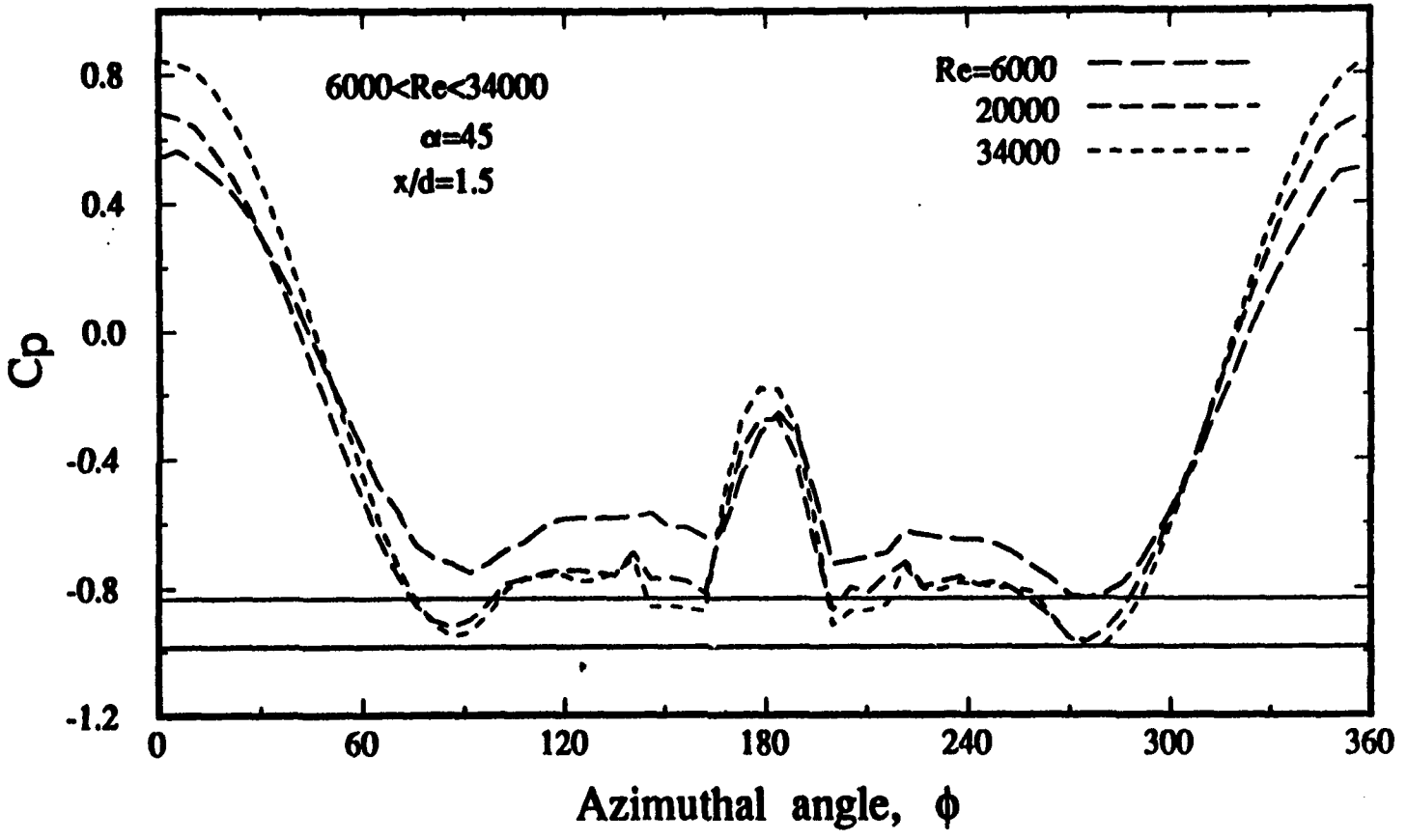

Figure 109. Pressure Distributions at α=45°, x/d=1.5, and Different Re's

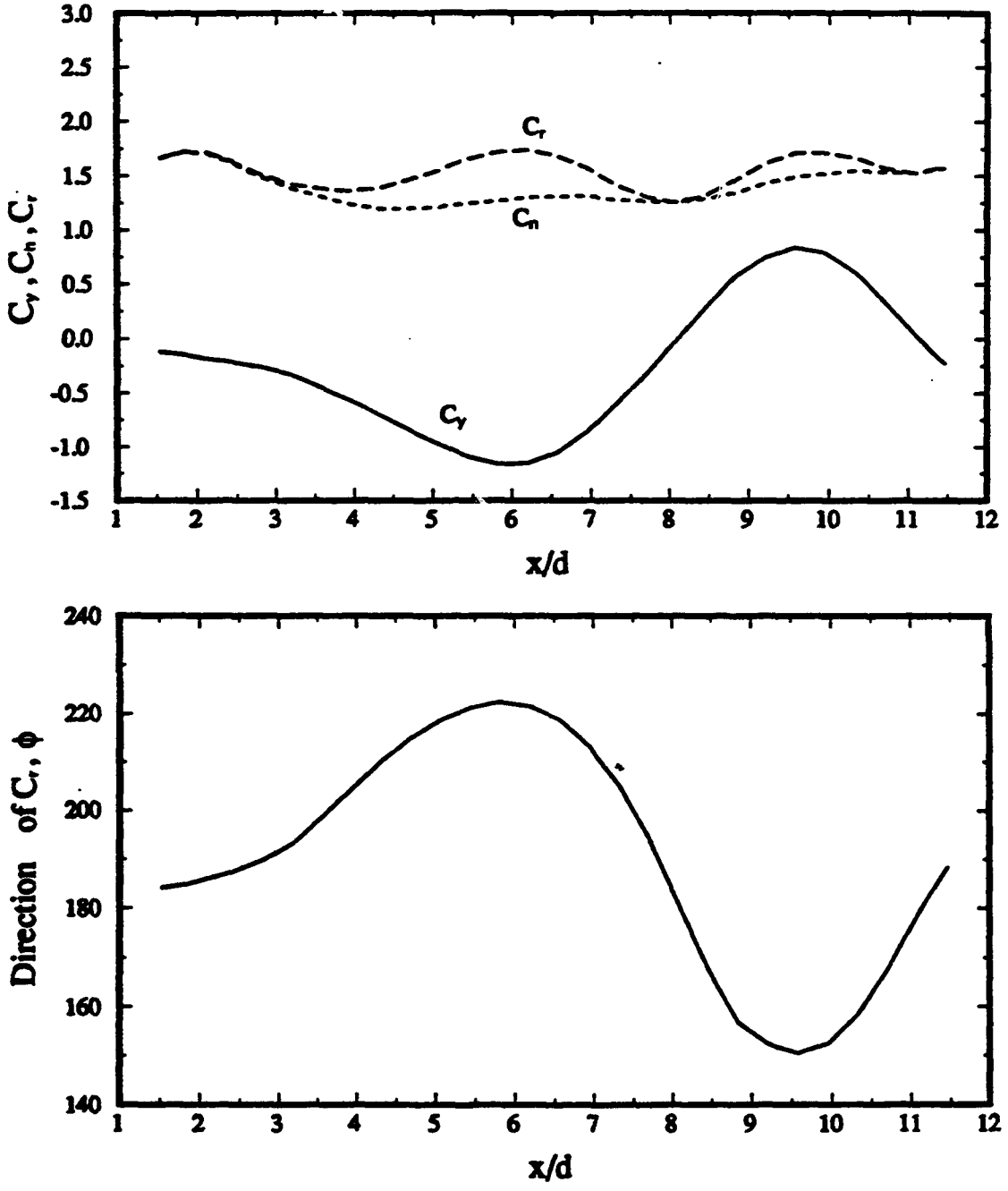

Figure 110. Local Force Distributions (a) C_y, C_n, C_r (b) Direction of C_r, ϕ, at Re=34000, α=45° along x/d

BIBLIOGRAPHY

Affes, H. and Conlisk, A. T., (1993) "Model for Rotor Tip Vortex-Airframe Interaction, Part 1: Theory," *AIAA Journal*, vol. 31, no. 12, pp. 2263-2273.

Affes, H., Conlisk, A. T., Kim, J. M., and Komerath, N. M., (1993) "Model for Rotor Tip Vortex-Airframe Interaction, Part 2: Comparison with Experiment," *AIAA Journal*, vol. 31, no. 12, pp. 2274-2282.

Bodstein, G. C. R., George, A. R., and Hui, C. Y., (1993) "Vortex/ Surface Interaction," AIAA Paper 93-0863, 31st Aerospace Sciences Meeting, Reno, NV.

Brand, A. G., McMahon, H. M., and Komerath, N. M., (1989) "Surface Pressure Measurements on a Body Subject to Vortex Wake Interaction," *AIAA Journal*, vol. 27, no. 5, p. 569.

Chapman, G. T. and Keener, E. R. (1979), "The Aerodynamics of Bodies of Revolution at Angles of Attack to 90 Degrees", AIAA Paper 79-0023.

Corke, T., Koga, D., Drubka, R., and Nagib, H., (1977) "A New Technique for Introducing Controlled Sheets of Smoke Streaklines in Wind Tunnels," Proc. Int. Cong. on Instrum. in Aerosp. Simulation Facilities, IEEE Publication 77-ch, 1251-8 AES., pp. 74-80.

Degani, D. and Zillliac, G. G. (1990), "Experimental Study of Nonsteady Asymmetric Flow Around an Ogive Cylinder at Incidence", *AIAA Journal*, v. 28, no. 4, pp. 642-649.

Ericsson, L. E. and Reding, J.P., (1986) "Asymmetric Vortex Shedding from Bodies Revolution," Tactical Missile Aerodynamics, Progress in Astronautics and Aeronautics, vol. 104, pp 243-296.

Hoeijmakers, H. W. M. (1989), "The Role of Computational Fluids Dynamics in Missile Aerodynamics", in Missile Aerodynamics: Proceedings of the NEAR Conference on Missile Aerodynamics, Monterey, CA.

Karim, M. A. (1992), "Experimental Investigation of the Formation and Control of the Dynamics Stall Vortex over a Pitching Airfoil", M.S. Thesis, MAE Dept., Illinois Institute of Technology, Chicago.

Lamont, P. J. (1982), "Pressure Around an Inclined Ogive Cylinder with Laminar, Transitional, and Turbulent Separation", *AIAA Journal*, v. 20, pp. 1492-1499.

Lee, B. H. K., and Tang, F. C., (1993) "Unsteady Pressure and Load Measurements on an F/A-18 Vertical Fin," *Journal of Aircraft*, vol. 30, no. 5, pp. 756-762.

Mendenhall, M. R., Nixon, D., and Dillenius, M. F. E. (eds.) (1989), Missile Aerodynamics: Proceedings of the NEAR Conference on Missile Aerodynamics, Monterey, CA.

Mendenhall, M. R., and Perkins, S. C., Jr., (1989) "Vortex Induced Characteristics of Missiles in Unsteady Maneuvers," AIAA Paper 89-0344, 27th Aerospace Sciences Meeting, Reno, NV.

Montividas, R. E., (1988) "The Scaling and Control of Vortex Geometry Behind Pitching Bodies of Revolution," M.S. Thesis, MAE Dept., Illinois Institute of Technology, Chicago, Illinois.

Montividas, R. E., Reisenthel, P., and Nagib, H., (1989) "The Scaling and Control of Vortex Geometry Behind Pitching Cylinders," AIAA Paper 89-1003, 2nd AIAA Shear Flow Conference, Tempe, AZ.

Peake, D. J. and Tobak, M. (1980), "Three Dimensional Interaction and Vortical Flows with Emphasis on High Speeds", NASA TM 81169.

Poling, D. R., Dadone, L., and Telionis, D. P., (1989) "Blade-Vortex Interaction," *AIAA Journal*, vol. 27, no. 6, p. 694.

Ramberg, S. E. (1983), "Vortex Wakes of Circular Cylinders", *Journal of Fluids Mechanics*, v. 128, pp. 81-107.

Reding, J. P. and Ericsson, L. E. (1984), "Re-examination of the Maximum Normalized Vortex Induced Side Force", *J. Spacecraft*, v. 21, no.5, pp. 433-440.

Ward, K. C. and Katz, J., (1987) "A Flow Visualization Study of the Vortex Structures Around an Inclined Body of Revolution," AIAA Paper 87-1247, 19th AIAA Fluid Dynamics, Plasma Dynamics and Lasers Conference, Honolulu, Hawaii.

Wardlaw, A. B. Jr. and Morrison, A. M (1975), "Induced Side Forces at High Angles of Attack", Technical Report NSWC/WOL/TR 75-17.

Washburn, A. E., Jenkins, L, N., and Ferman, M, A., (1993) "Experimental Investigation of Vortex-Fin Interaction," AIAA Paper 93-0050, 31st Aerospace Sciences Meeting, Reno, NV.

Williams, D. R. and Bernhardt, J., (1990) "Proportional Control of Asymmetric Forebody Vortices with the Unsteady Bleed Technique," AIAA Paper 90-1629, 21st AIAA Fluid Dynamics, Plasma Dynamics and Lasers Conference, Seattle, WA.

Wittmer, K. S., Devenport, W. J., Rife, M. C., and Glegg, S. A. L., (1994) "Perpendicular Blade Vortex Interaction," AIAA Paper 94-0526, 32nd Aerospace Sciences Meeting, Reno, NV.

Zilliac, G., Degani, D., and Tobak, M. (1990), "Asymmetric Vortices on Slender Bodies of Revolution", AIAA Paper 90-0388.